DEVELOPMENT OF MELCOR INPUT TECHNIQUES FOR HIGH TEMPERATURE GAS-COOLED REACTOR ANALYSIS

A Thesis

by

JAMES ROBERT CORSON, JR.

Submitted to the Office of Graduate Studies of
Texas A&M University
in partial fulfillment of the requirements for the degree of

MASTER OF SCIENCE

May 2010

Major Subject: Nuclear Engineering

DEVELOPMENT OF MELCOR INPUT TECHNIQUES FOR HIGH TEMPERATURE GAS-COOLED REACTOR ANALYSIS

A Thesis

by

JAMES ROBERT CORSON, JR.

Submitted to the Office of Graduate Studies of
Texas A&M University
in partial fulfillment of the requirements for the degree of

MASTER OF SCIENCE

Approved by:

Chair of Committee,	Karen Vierow
Committee Members,	Pavel Tsvetkov
	Devesh Ranjan
Head of Department,	Raymond Juzaitis

May 2010

Major Subject: Nuclear Engineering

ABSTRACT

Development of MELCOR Input Techniques for High Temperature Gas-Cooled Reactor Analysis. (May 2010)
James Robert Corson, Jr., B.S., Pennsylvania State University
Chair of Advisory Committee: Dr. Karen Vierow

High Temperature Gas-cooled Reactors (HTGRs) can provide clean electricity, as well as process heat that can be used to produce hydrogen for transportation and other sectors. A prototypic HTGR, the Next Generation Nuclear Plant (NGNP), will be built at Idaho National Laboratory.

The need for HTGR analysis tools and methods has led to the addition of gas-cooled reactor (GCR) capabilities to the light water reactor code MELCOR. MELCOR will be used by the Nuclear Regulatory Commission licensing of the NGNP and other HTGRs. In the present study, new input techniques have been developed for MELCOR HTGR analysis. These new techniques include methods for modeling radiation heat transfer between solid surfaces in an HTGR, calculating fuel and cladding geometric parameters for pebble bed and prismatic block-type HTGRs, and selecting appropriate input parameters for the reflector component in MELCOR.

The above methods have been applied to input decks for a water-cooled reactor cavity cooling system (RCCS); the 400 MW Pebble Bed Modular Reactor (PBMR), the input for which is based on a code-to-code benchmark activity; and the High Temperature Test Facility (HTTF), which is currently in the design phase at Oregon State University. RCCS results show that MELCOR accurately predicts radiation heat transfer rates from the vessel but may overpredict convective heat transfer rates and RCCS coolant flow rates. PBMR results show that thermal striping from hot jets in the lower plenum during steady-state operations, and in the upper plenum during

a pressurized loss of forced cooling accident, may be a major design concern. Hot jets could potentially melt control rod drive mechanisms or cause thermal stresses in plenum structures.

For the HTTF, results will provide data to validate MELCOR for HTGR analyses. Validation will be accomplished by comparing results from the MELCOR representation of the HTTF to experimental results from the facility. The validation process can be automated using a modular code written in Python, which is described here.

To my family, for their ever-present love and support

ACKNOWLEDGMENTS

I would like to thank Professor Karen Vierow for all of her advice and support. Her guidance and suggestions have made this research possible. I would also like to thank the members of the Laboratory for Nuclear Heat Transfer Systems for their advice and encouragement. I am especially indebted to Dr. Kevin Hogan, who introduced me to MELCOR and the PBMR.

In addition, I would like to thank my thesis committee: Professors Karen Vierow, Pavel Tsvetkov, and Devesh Ranjan. Their advice is greatly appreciated.

The code developers at Sandia National Laboratories have played a major role in this work. They have helped me a great deal by answering my questions about MELCOR and by offering suggestions about problems I encountered with the new models in the code. Their assistance has enabled me to complete this work.

Most of all, I would like to thank my family, including my parents, Jim and Donna Corson; my brothers, Andrew and Matthew Corson; and my fiancee, Holly Shepps. This thesis is a testament to their continued love and support.

ACRONYMS

AGR	Advanced gas-cooled reactor
AVR	Arbeitsgemeinshaft Versuchsreaktor
CFD	Computational Fluid Dynamics
CL	MELCOR clad component
CV	MELCOR control volume
DLOFC	Depressurized loss of forced coolant flow
ECCS	Emergency Core Cooling System
FL	MELCOR flow path
FSV	Fort St. Vrain
FU	MELCOR fuel component
GA	General Atomics
GT-MHR	Gas Turbine-Modular Helium Reactor
HS	MELCOR heat structure
HTGR	High Temperature Gas-Cooled Reactor
HTR-MODUL	HTR module
HTTF	High Temperature Test Facility
IHX	Intermediate heat exchanger
LOFC	Loss of forced coolant flow
LWR	Light Water Reactor

MHTGR	Modular High Temperature Gas-Cooled Reactor
MOX	Mixed oxide
NGNP	Next Generation Nuclear Plant
OECD	Organisation for Economic Co-operation and Development
PBMR	Pebble Bed Modular Reactor
PBR	Pebble bed reactor type in MELCOR
PCS	Power Conversion System
PIRT	Phenomena identification and ranking table
PLOFC	Pressurized loss of coolant flow
PMR	Prismatic reactor type in MELCOR
PTF	MELCOR plot file
PyC	Pyrolytic carbon
RCCS	Reactor Cavity Cooling System
RF	MELCOR reflector component
RPV	Reactor Pressure Vessel
SiC	Silicon carbide
SS	MELCOR supporting structure
THTR-300	Thorium high temperature reactor

TABLE OF CONTENTS

Page

Page

Page

Page

LIST OF TABLES

TABLE Page

TABLE Page

LIST OF FIGURES

FIGURE Page

FIGURE Page

FIGURE Page

FIGURE Page

FIGURE Page

1. INTRODUCTION

The United States nuclear energy industry is undergoing a major renaissance, fueled by an anticipated increase in electricity demand. While Advanced Light Water Reactors will make up the majority of the new reactors built in the immediate future [1], current efforts aim at deploying Generation IV reactors by 2030 [2]. One category of Gen IV reactors consists of Very High Temperature Reactors (VHTRs). VHTRs are designed to have outlet temperatures approaching 1000 °C, which makes these reactors ideal for producing both electricity and process heat for hydrogen production. VHTRs are a subset of High Temperature Gas-cooled Reactors (HTGR), which are thermal reactors moderated by graphite and cooled by helium gas with outlet temperatures exceeding 750 °C. HTGRs have been operated successfully in the past [3]. Because of this, and because of the potential of HTGRs – and thus, of VHTRs – to generate process heat for hydrogen production, a VHTR will be built at Idaho National Laboratory (INL) as the Next Generation Nuclear Plant (NGNP) [4].

New analysis tools must be developed to design and assess HTGRs. MELCOR, a severe accident code for Light Water Reactors (LWRs) developed at Sandia National Laboratories [5, 6], has been modified to include Gas-Cooled Reactor (GCR) models for HTGR design basis calculations [7]. The U.S. Nuclear Regulatory Commission (NRC) has chosen MELCOR as part of its code suite for HTGR analysis [8]. In order to use MELCOR to analyze HTGRs, the code must be validated using experimental results.

This thesis follows the style of International Journal of Heat and Mass Transfer.

1.1 Objectives

The objectives of this thesis are as follows:

- To assess the ability of MELCOR to model the Reactor Cavity Cooling System (RCCS) in an HTGR, particularly its ability to model radiation heat transfer, by comparing MELCOR results to results from other computational studies
- To develop new input techniques for MELCOR HTGR analyses
- To assess the ability of the GCR models in MELCOR to model an HTGR by comparing MELCOR results for the 400 MW Pebble Bed Modular Reactor (PBMR) to results from other computer codes
- To develop an input deck to model the High Temperature Test Facility (HTTF), to be built at Oregon State University (OSU)
- To develop methods by which to validate GCR models in MELCOR using experimental data gathered at the HTTF

1.2 Significance of Work

All commericial reactors in the United States must be licensed by the NRC. The NRC uses its own analysis tools to verify that the analyses performed by the licensee are appropriate and that the reactor poses no threat to the health and safety of the public [9]. To do so, the NRC must validate its analysis tools to ensure that results from these tools are appropriate.

The NGNP will be licensed by the NRC [10, 11]. MELCOR 2.1 will be used by the NRC in the licensing process, and so it must be validated against experimental data and other analysis tools.

This work represents the first efforts to model HTGRs with MELCOR 2.1. Previous attempts to model HTGRs with MELCOR [12, 13] were performed before the

addition of GCR models to the code. These efforts were performed to determine whether or not MELCOR could be applied to HTGR analysis. They represent the first step toward using MELCOR for performing HTGR studies.

The current work is the next logical step toward the ultimate goal of performing HTGR safety calculations with MELCOR. This thesis explains the development of modeling techniques that can be applied to future HTGR analyses. It also provides methods that can be adopted to validate MELCOR with experimental data from the HTTF.

1.3 Technical Approach

To meet the above objectives, three separate MELCOR input decks have been created. Each input deck represents a new application of MELCOR for HTGR analysis. The RCCS input model is the first effort to simulate a water-cooled RCCS with MELCOR. Particular focus is placed on radiation heat transfer modeling and natural circulation convective heat transfer because these are significant phenomena that affect RCCS performance. Methods developed to model radiation and natural convection are described in detail.

The PBMR-400 input model expands upon earlier attempts to model the PBMR with MELCOR [12, 13]. General guidance provided by these attempts was followed in creating the nodalization scheme for the PBMR-400. While the early efforts used only light water reactor code capabilities, the current effort applies new gas-cooled reactor models to the PBMR-400 input deck. Reflector input is described in detail to provide guidance for future HTGR studies with MELCOR. Additionally, MELCOR results are compared to results from other codes to determine how MELCOR fares with respect to the state of the art in HTGR analysis methods.

The availability of the problem definition and of results from the benchmark were key factors in choosing to base MELCOR input on the PBMR-400 benchmark. Since

experimental data is currently unavailable, the benchmark represents the best test case for the new GCR models in MELCOR.

The experience gained from the PBMR-400 activity is applied to modeling the HTTF, which will be built and operated to provide experimental data for code validation. This modeling effort marks the first step toward validating MELCOR for HTGR calculations. Since data from the HTTF will not become available until 2011 at the earliest, validation of MELCOR cannot be completed for a number of years. This thesis attempts to provide thorough documentation of the HTTF MELCOR input deck so that other researchers may continue this work. Clear distinctions are made between known and assumed parameters to facilitate this effort. Also, a validation plan has been developed, using the computer language Python, that can be adopted once experimental data becomes available. Modules written to perform the analyses presented in this thesis can be easily modified to perform the functions required in the validation process.

1.4 Thesis Overview

Section 2 of this thesis provides a review of High Temperature Gas-cooled Reactors, including the evolution of HTGR designs, general HTGR features, and analytical and experimental studies of HTGR behavior. An overview of MELCOR, highlighting code features utilized for this thesis, is presented in Section 3. Section 4 describes MELCOR input techniques developed to model a water-cooled RCCS and presents results from RCCS calculations. Section 5 contains the application of MELCOR to the PBMR-400 benchmark activity, including new input techniques for reflector modeling. Results from this study are compared to results from the benchmark. A MELCOR input model for the HTTF is described in Section 6. Preliminary results from this work, as well as suggestions on how to validate MELCOR using experimental results from the facility, are included. Conclusions from this work are

given in Section 7. Recommendations for future HTGR studies with MELCOR and for MELCOR code improvements are provided as well.

2. HIGH TEMPERATURE GAS REACTOR OVERVIEW

The Very High Temperature Reactor is a gas-cooled, graphite moderated nuclear reactor. The VHTR may utilize a pebble bed or prismatic (hexagonal) core. This reactor has a target outlet temperature of 900-1000 °C, making the reactor ideal for high-temperature process heat applications. In particular, the VHTR may be used to generate hydrogen for use in the transportation and other sectors to reduce dependence on fossil fuels and foreign energy supplies [14]. High Temperature Gas-Cooled Reactors (HTGRs) are similar in design to VHTRs but have lower outlet temperatures. HTGRs can be used to generate hydrogen with efficiencies comparable to those for VHTRs operating at higher temperatures [15]. HTGRs can also be used for electricity generation at an efficiency of up to 50%, salt water desalination, and coal gasification [16].

The VHTR is one of six Generation IV nuclear reactors, the other five being the Sodium-cooled Fast Reactor (SFR), the Super-Critical Water-cooled Reactor (SCWR), the Gas-cooled Fast Reactor (GFR), the Lead-cooled Fast Reactor (LFR), and the Molten Salt Reactor (MSR). Generation IV reactors must meet defined technological goals in the areas of sustainability, economics, safety and reliability, and proliferation resistance [2]. The Generation IV Internation Forum has been established to foster international cooperation in research and development efforts for these new energy systems [17].

The VHTR has been selected by the U.S. Department of Energy for the Next Generation Nuclear Plant. However, the NGNP target outlet temperature has been lowered from 1000 °C [4] to 700-850 °C due to high temperature material qualification concerns [18]. The long-term goal is to address these concerns so that the NGNP, and future VHTRs, can achieve the 1000 °C outlet temperature target [2, 19].

2.1 HTGR History

Commercialization of gas-cooled reactors began in 1956 at the Calder Hall plant in the United Kingdom. The UK continued its commitment to GCR technology, building a total of 26 Magnox and 14 advanced gas-cooled reactors (AGRs) [3]. Of these, 2 Magnox reactors and all 14 AGRs were still in operation as of 2008. In addition, 11 gas-cooled reactors were built, operated, and shut down in France, Italy, Japan, and Spain [20]. These early GCR designs were graphite-moderated, carbon dioxide-cooled systems [21].

High temperature gas-cooled reactor (HTGR) development began in the 1950s to improve GCR performance. These designs incorporated ceramic-coated fuel particles and helium gas coolant, and were able to operate at high temperatures due to an all-ceramic core. Early HTGRs include the Dragon Reactor Experiment, a 20 MWt reactor in the United Kingdom, which had a core exit temperature of 750 °C; the Arbeitsgemeinshaft Versuchsreaktor (AVR), a 15 MWe pebble bed reactor in Germany, which achieved a core outlet temperature of 950 °C [3]; and the 40 MWe Peach Bottom Unit 1, an HTGR that used annular fuel elements with a solid graphite spine and operated near Philadelphia, Pennsylvania, in the United States [22]. These three reactors used steel reactor vessels. All three have been shut down.

Later HTGRs were characterized by higher power and prestressed concrete reactor pressure vessels [3]. Fort St. Vrain (FSV), a 330 MWe [21] prismatic block-type reactor with a ^{235}U-thorium fuel cycle, operated in Colorado in the United States from 1979 to 1989, when it was permanently shut down [22]. While it had low availability due to problems with its steam and water-driven helium circulators, it successfully demonstrated the performance of TRISO-coated fuel particles in graphite blocks, once-through steam generators that produced superheated steam, and the fuel handling system. The thorium high temperature reactor (THTR-300), a 300 MWe pebble bed HTGR, operated in Germany from 1985 to 1989, when it was shut down and decommissioned due to a projected shortfall in funding for decommission-

ing in the future. THTR-300 successfully demonstrated the safety characteristics of the pebble bed and the fission product retention of the particle coatings. Other, higher power designs were developed in Germany, Russia, and the United States, but were never built for various reasons [3].

Instead, HTGR development focused on modular designs, beginning with the 80 MWe HTR module (HTR-MODUL) developed by Siemens/Interatom in the early 1980s. Many design features of the HTR-MODUL (1600 °C maximum fuel temperature limit, passive decay heat removal during accident conditions, and a steel pressure vessel, among others [3]) have been adopted by subsequent modular HTGR designs, including the Pebble Bed Modular Reactor (PBMR) and the Gas Turbine-Modular Helium Reactor (GT-MHR) designs described below. To date, no modular HTGRs have been built for commercial operation. However, the 30 MWt, prismatic block-type High Temperature Engineering Test Reactor (HTTR), and the 10 MWt pebble bed HTR-10, are currently operating as test facilities in Japan and China, respectively [23]. These reactors are described in some detail in Section 2.4.

2.2 HTGR Design

HTGRs are fueled by coated fuel particles dispersed in a graphite matrix [21]. Early HTGRs, including Peach Bottom and Fort St. Vrain in the United States, used slightly enriched uranium and thorium in the form of carbide or oxide particles [21, 22, 24]. More recent designs, including the Pebble Bed Modular Reactor developed by PBMR (Pty) Ltd in South Africa and the Gas Turbine-Modular Helium Reactor developed by General Atomics (GA) in the United States, plan to use TRISO-coated uranium dioxide or uranium oxycarbide fuel particles [23, 25]. GA has also proposed using a uranium-plutonium mixed oxide (MOX) or uranium-thorium fuel [3, 23].

TRISO coatings consist of the following concentric layers around a 0.8 mm-diameter fuel kernel: a porous carbon buffer layer, an inner layer of pyrolytic carbon (PyC), a layer of silicon carbide (SiC), and an outer layer of pyrolytic carbon. The

TRISO coating acts as a mini-containment for the fuel particle; the porous carbon buffer allows for thermal expansion of the fuel, PyC layers provide gaseous fission product retention, and the SiC layer provides solid fission product retention and structural support for the particle [26].

Fission product release from the fuel spheres increases with temperature. Experimental studies have shown that below 1600 °C, fission product releases are negligible. Above this temperature, TRISO coating failures have been observed, leading to significant releases of gaseous fission products [27]. For this reason, reactor operating conditions are selected in order to keep temperatures below 1600 °C to ensure that releases are negligible [3].

HTGRs use helium as the coolant. Helium has been selected due to its favorable heat transfer properties compared with other gases. It is also chemically inert and has a low neutron cross section [16]. Graphite is used as a moderator due to its very low neutron absorption cross-section [16, 28] and its favorable thermal properties. The high thermal conductivity of graphite reduces the temperature gradient between the fuel and the coolant and keeps fuel temperatures lower than in a typical LWR. The relatively high heat capacity and the large amount of graphite in an HTGR core slows the temperature response of the reactor during a transient. Graphite is also used as a structural material due to its high strength at high temperatures [21].

HTGRs have low power densities (~ 5 MW/m^3) and large thermal storage capacities. These features allow the reactors to withstand a depressurized loss of forced cooling (DLOFC) accident while maintaining fuel temperature below the 1600 °C limit [25]. The tall and narrow design allows heat to be transferred passively from the core outward, through the side reflector, to the vessel [23]. Heat is transferred from the vessel to the reactor cavity air volume by natural convection and to the reactor cavity cooling system (RCCS) by thermal radiation. The RCCS is a system used to maintain fuel, core, reactor pressure vessel (RPV), and reactor cavity component temperatures below design limits during accident conditions [29]. The low

power density and large thermal heat sink eliminate the need for an emergency core cooling system (ECCS).

Air ingress from a break in the primary system is a concern for HTGR operation. The presence of air can lead to graphite oxidation at high temperatures. This reaction is exothermic and can significantly damage the structural integrity of the graphite. Oxygen would likely not penetrate through graphite reflectors to the core, and so fission product retention would not be significantly impaired by air ingress [30]. However, oxidation can lead to failure of the bottom reflector [11]. In some cases, some oxidation may occur in the lower part of the core, which could lead to a release of fission products [31].

Two HTGR designs (the PBMR and GT-MHR) are described below. RCCS designs are described as well.

2.2.1 The Pebble Bed Modular Reactor

The Pebble Bed Modular Reactor is a 400 MWt HTGR designed by PBMR (Pty) Ltd for Eskom in South Africa. The reactor is shown in Figures 2.1 and 2.2. It is fueled by TRISO-coated uranium dioxide particles, encased in a graphite matrix, and formed into spheres, or pebbles, 6 cm in diameter. Fuel pebbles are packed in an annular core, bounded by central, side, top, and bottom reflectors. The reactor core is contained within a steel RPV designed to provide structural support for the core and to provide a heat transfer path to the RCCS.

The PBMR uses a direct Brayton cycle [32]. The reactor operates at a pressure of 9 MPa with coolant inlet and outlet temperatures of 500 °C and 900 °C, respectively. Helium coolant flows upward through helium channels drilled in the side reflector, into an upper inlet plenum. The helium is heated as it flows downward through the pebble bed to an outlet plenum in the bottom reflector [25]. From there, the coolant exits the reactor and flows to the remainder of the primary system, including the Power Conversion System (PCS).

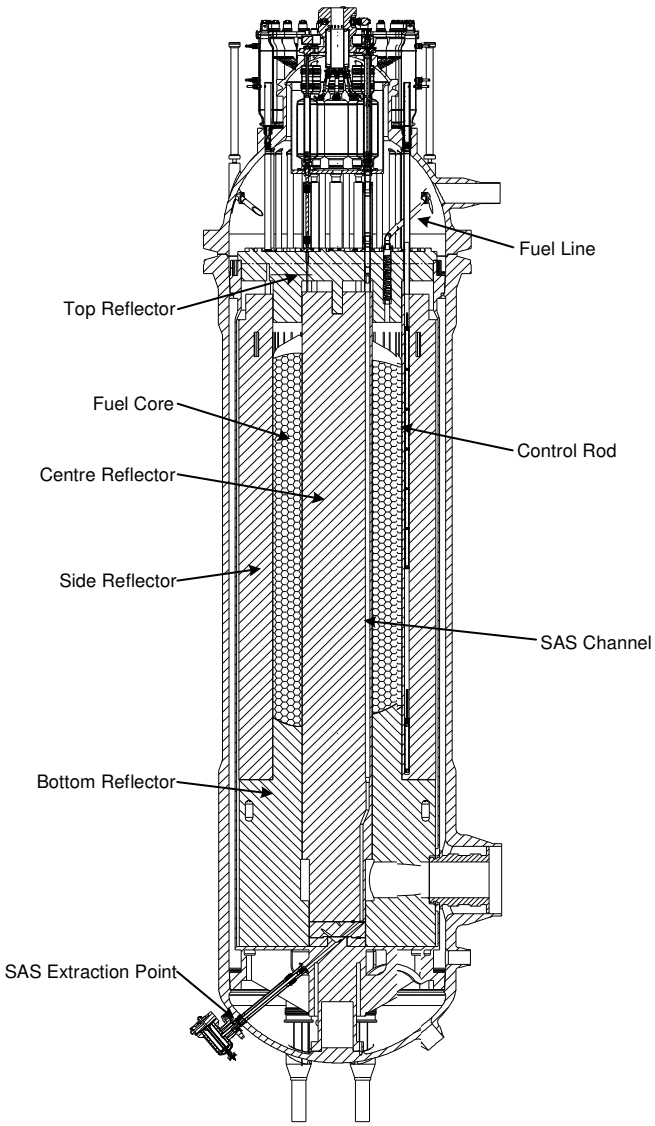

Fig. 2.1. Side view of the 400 MW PBMR [25]

Reactivity control is provided by control rods raised or lowered in channels in the side reflector. The reserve shutdown system provides long-term shutdown of the core by dropping neutron absorber spheres into channels in the central reflector [32].

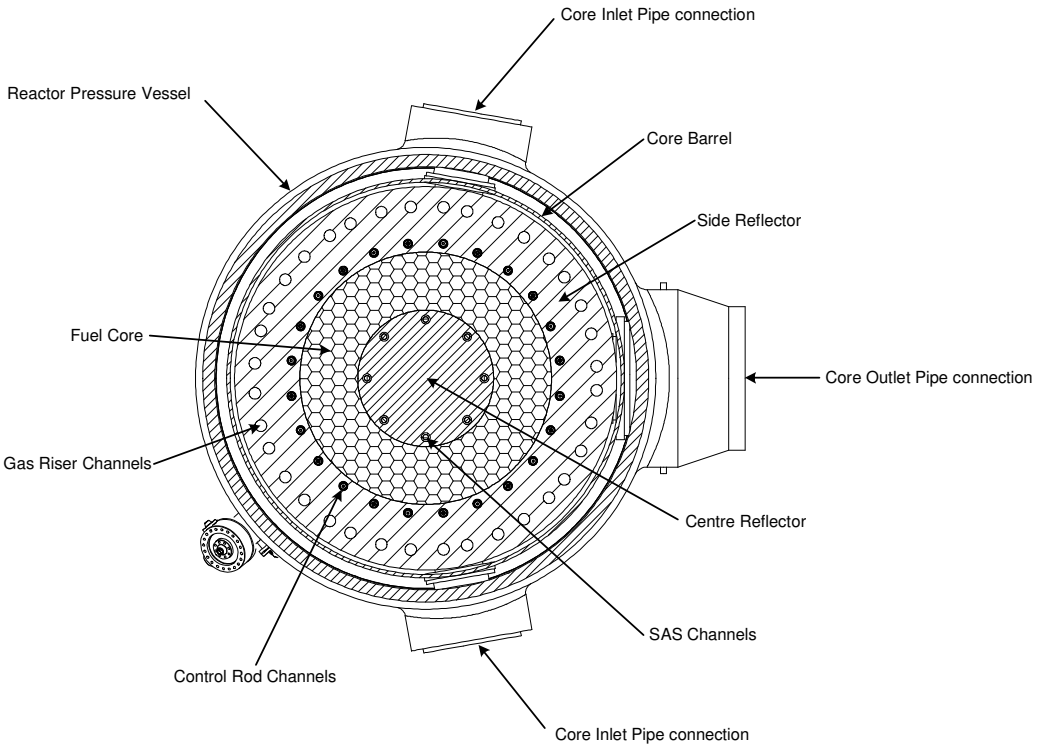

Fig. 2.2. Top view of the 400 MW PBMR [25]

The large negative temperature coefficient of the core provides a natural reactivity feedback effect in the event of an unexpected increase in temperature, such as during a loss of forced cooling (LOFC) accident [32].

The fuel particles and fuel pebbles in the reactor core are shown in Figure 2.3. The fueled region of the pebble is 5 cm in diameter. Each pebble contains approximately 15,000 TRISO particles [3] and 9 g of uranium. The pebble is encased in a 0.5 cm-thick graphite shell. There are approximately 452,000 pebbles in the reactor core at any time. These pebbles move downward through the core and are removed from the reactor at an average rate of 2833 spheres per day. Used pebbles are replaced by fresh fuel pebbles. On average, each sphere makes six passes through the core before being discharged to the spent fuel storage tanks [23].

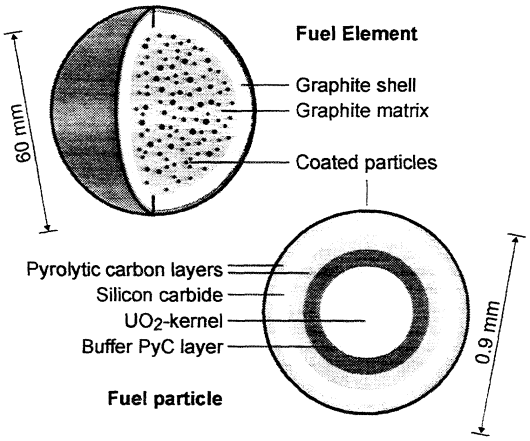

Fig. 2.3. PBMR fuel design [26]

2.2.2 The Gas Turbine-Modular Helium Reactor

The Gas Turbine-Modular Helium Reactor is a 600 MWt prismatic block-type HTGR designed by General Atomics in the United States. The reactor is shown in Figures 2.4 and 2.5. It is fueled by TRISO-coated uranium oxycarbide kernels encased in a carbonaceous matrix and formed into a cylindrical rod. These rods are placed in holes drilled in hexagonal graphite blocks. These fuel blocks are arranged in an annular core between central, side, top, and bottom reflectors made up of graphite blocks with the same dimensions as the fuel blocks. Like the PBMR, the modular helium reactor (MHR) is contained within a steel reactor pressure vessel. In accident conditions, heat is conducted through the side reflectors to the pressured vessel and radiated to the RCCS [23].

The GT-MHR uses a direct gas turbine (GT) and operates in a closed Brayton cycle. The reactor operates at a pressure of approximately 7 MPa with coolant inlet and outlet temperatures of 490 °C and 850 °C, respectively. Helium enters the reactor from the power conversion system through an annulus in the cross duct between the PCS and RPV. It flows upward through an annulus in the vessel to an upper inlet

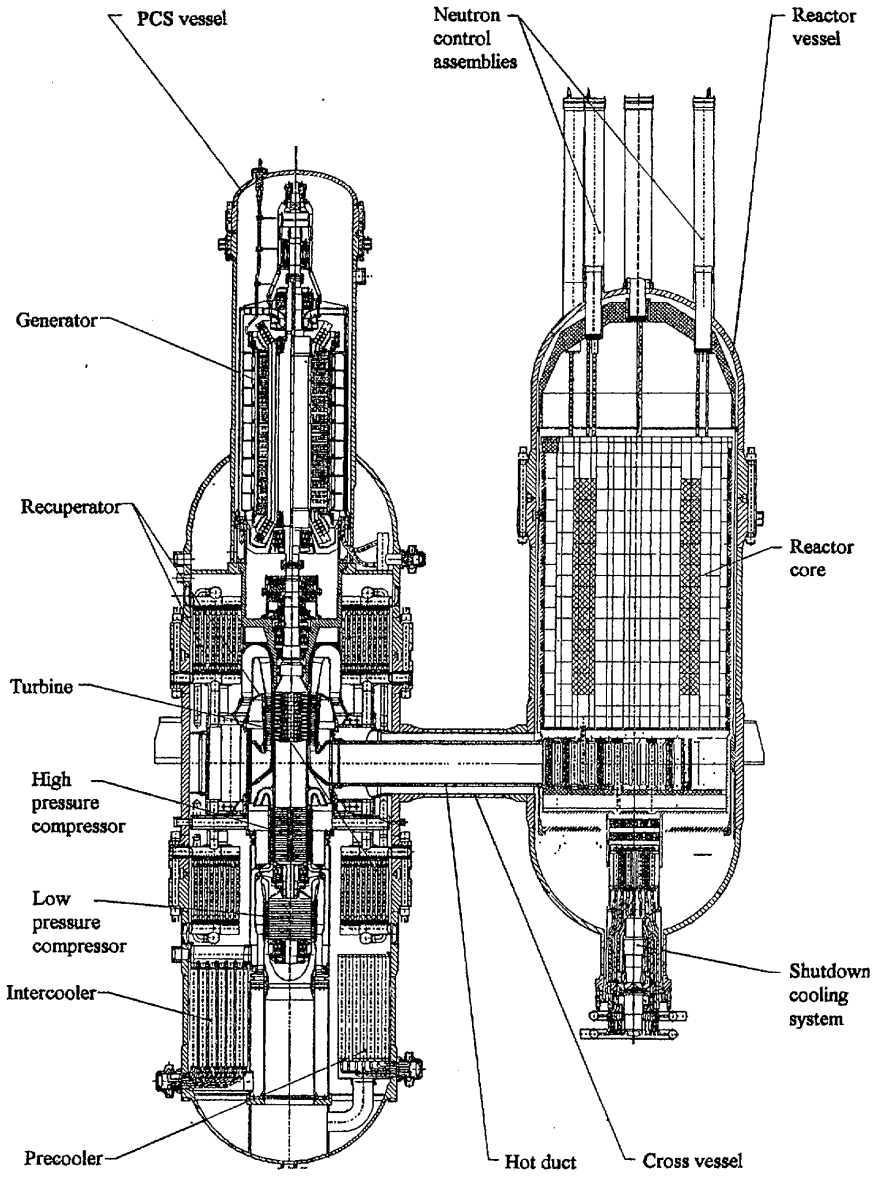

Fig. 2.4. Side view of the GT-MHR [3]

plenum, after which it flows downward through coolant holes drilled in the fuel and graphite blocks. The helium collects in an outlet plenum and flows through a circular pipe in the cross duct between the RPV and PCS [3].

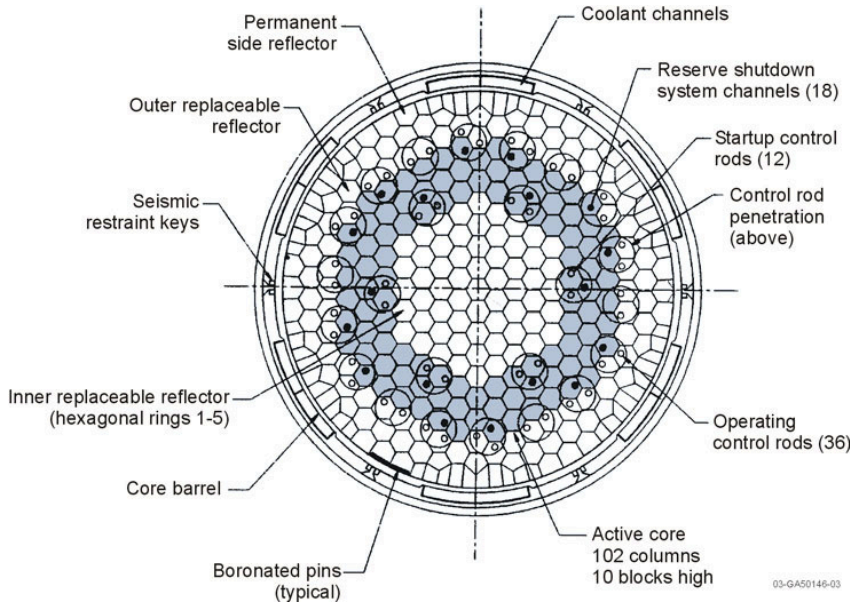

Fig. 2.5. Top view of the GT-MHR [4]

Reactivity control is provided by control rods that can be raised or lowered in the side reflector. Additional control rods in the reactor core are typically used for startup and shutdown of the reactor. The reserve shutdown system drops neutron absorbing materials into channels in the fuel blocks if the primary shutdown systems fail [23]. The large negative reactivity feedback of the reactor also provides natural reactivity control.

Fuel for the GT-MHR is shown in Figure 2.6. TRISO-coated particles are contained in fuel compacts 12.5 mm in diameter. There are nearly 3,000,000 of these fuel compacts in the core. The reactor core is 8 m in height with equivalent inner and outer diameters of 2.96 m and 4.84 m [3].

The GT-MHR uses a buoyancy-driven, air-cooled RCCS, which is described below.

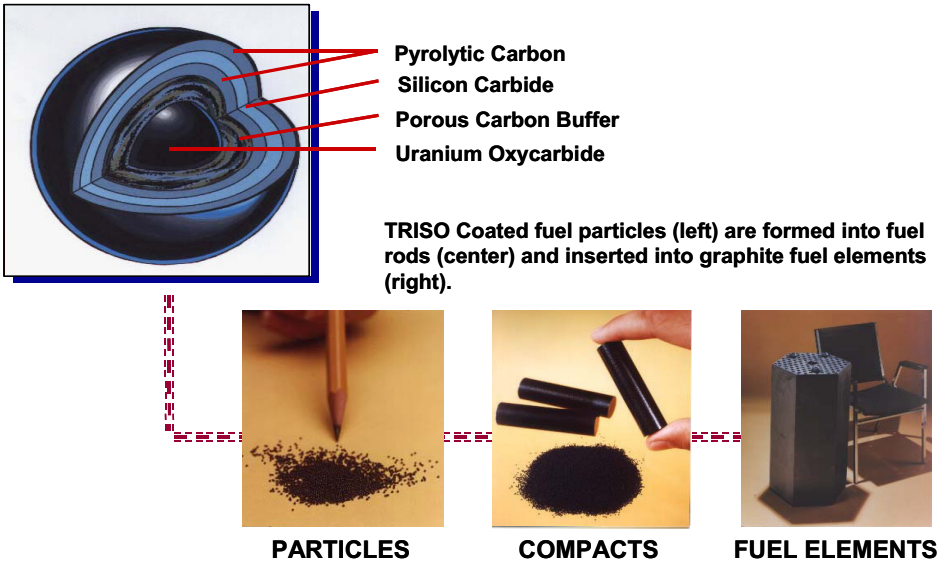

Fig. 2.6. GT-MHR fuel design [4]

2.2.3 Reactor Cavity Cooling System Designs

The reactor cavity cooling system is designed to remove core decay heat in the unlikely event where all main and shutdown cooling systems are lost. Heat is radiated from the reactor pressure vessel to RCCS pipes along the reactor cavity wall and convected from the pipes by flowing coolant. Designs have been proposed that use water or air as the coolant and natural buoyancy forces or pumps to drive the flow [29]. Specific features of water-cooled and air-cooled RCCS designs are described below.

Water-Cooled Reactor Cavity Cooling Systems

Water-cooled reactor cavity cooling systems use water flowing through cylindrical or ovular pipes to remove heat from the reactor pressure vessel. Water-cooled designs have been proposed by Westinghouse and PBMR (Pty) Ltd and by AREVA for their pebble bed and prismatic pre-conceptual designs for the NGNP [10], and for the

Russian VGM reactor design [29]. Water-cooled systems are used in the HTTR [33] and the HTR-10 [34].

The Westinghouse RCCS is an active system consisting of water-filled tanks and ovular standpipes. Water is pumped from the equipment protection cooling circuit (EPCC) to a common header, which directs flow to the bottom of each standpipe. Water flows upward through the standpipes, and exits to the water storage tanks. The coolant continues to the EPCC, where it is cooled and pumped back to the common inlet header for the RCCS. This system can also operate in passive mode. In passive cooling mode, water drains from the water storage tanks to the bottoms of the standpipes. Flow through the standpipes is driven by buoyancy forces due to density differences between the water in the drain line and the heated water in the standpipe [35]. The water storage tanks are sized to operate in passive, boil-off mode for approximately 72 hours [10].

The AREVA RCCS design is a natural circulation-driven system. The RCCS consists of riser and downcomer pipes filled with water and connected at the bottom by an inlet header and at the top by a water storage tank. Buoyancy forces resulting from density differences between the warmer water in the risers and the cooler water in the downcomer causes water to flow upward, through the risers, and into the water storage tank. Heat is removed from the water storage tank by a forced convection loop in a water-to-water heat exchanger in the tank. The forced convection loop rejects heat to the atmosphere in a water-to-air heat exchanger [10].

The VGM RCCS [29] is similar to the AREVA design. This system will be discussed in more detail in Section 4.

Air-Cooled Reactor Cavity Cooling Systems

Air-cooled systems use air flowing through ducts to remove heat from the RPV. General Atomics has proposed an air-cooled RCCS design for its GT-MHR and MHTGR. The GA RCCS is a natural circulation-driven system. It consists of two

inlet/outlet structures open to the atmosphere, rectangular cooling ducts around the reactor vessel to remove heat, and concentric ducts to transport air between the cooling panels and inlet/outlet structures [36, 37]. Like the passive water-cooled systems, air flow is driven by buoyancy forces due to the density difference between the cold air in the downcomer and the heated air in the risers. The GA RCCS has a total heat removal capacity of 4 MW, which is sufficient to maintain vessel and cavity concrete temperatures below design limits [3].

2.3 Next Generation Nuclear Plant

The NGNP project was established to demonstrate the use of nuclear technology for electricity and hydrogen co-generation [4]. Three contractor teams led by Westinghouse Electric Company, LLC; AREVA NP, Inc.; and General Atomics performed studies to address key aspects of the NGNP, including the reactor type, power level, heat removal systems, and power conversion system. Results from these studies were translated into pre-conceptual designs that were used to provide schedule and cost estimates for NGNP licensing, construction, startup and testing, and operation. Westinghouse proposed a pebble bed reactor with an active, water-cooled RCCS; AREVA proposed a prismatic reactor with a passive, water-cooled RCCS; and GA proposed a prismatic reactor with a passive, air-cooled RCCS. These reactors have target outlet temperatures and core powers set at 900-950 °C and 500-600 MWt, respectively [10]. However, conceptual designs will likely operate at lower temperatures (700-850 °C) [18]. The long-term goal is to address technical issues so that the outlet temperature of the NGNP can be increased to the target of 900-1000 °C [2, 19].

A phenomena identification and ranking table (PIRT) process was conducted for the NGNP [11] by panels of experts in five topical areas: Accident and Thermal Fluids, Fission-Product Transport and Dose, High-Temperature Materials, Graphite, and Process Heat and Hydrogen Co-Generation Production. Each panel identified the most significant phenomena, defined as those phenomena with a low or medium

associated knowledge level and a high importance in regards to the specified figures of merit. Figures of merit include doses at the site boundary and worker doses due to releases of radioactivity; fuel failure rates or conditions that would impact fuel failure; and conditions that would affect vessel failure. Each significant phenomenon represents an important research need.

The Accident and Thermal Fluids panel identified a number of significant phenomena, including the following [11]:

- Bypass and core flows
- Decay heat and distribution
- Graphite temperature profiles
- Graphite thermal conductivity
- Coolant flow
- RPV and RCCS emissivity

All of these phenomena have a significant impact on fuel failure and fission product release. Bypass flow – defined as the fraction of the primary coolant flow that does not directly cool the fuel elements [11] – impacts fuel temperatures, and hence the fission product release rate from the fuel kernels. Bypass flow changes as a function of thermal expansion and irradiation damage of the graphite. Uncertainties in the core power and flow profiles in both time and space complicate the determination of, for instance, the size of the gaps between blocks in prismatic block-type reactors, or the near-wall pebble bed void fraction in pebble bed reactors [38]. Similarly, graphite thermal conductivity and coolant flow distribution influence fuel temperature profiles during normal operation and transient scenarios, which affect fission product releases from the fuel. The decay heat power and distribution affect temperature profiles and fission product releases during accident scenarios, while RPV and

RCCS emissivities affect RPV temperatures and hence the structural integrity of the RPV. High RPV temperatures can lead to vessel failure and a subsequent release of radioactivity from the primary system. These phenomena must be studied further in order to quantify their effects on the figures of merit identified in the Accident and Thermal Fluids PIRT.

2.4 Thermal Hydraulic Evaluations of HTGRs

The PIRT findings emphasize the need for additional HTGR thermal hydraulics research. Research efforts can be broken into analytical (computational) studies and experiments.

2.4.1 Computational Analysis of HTGRs

Computer codes used to analyze HTGR thermal hydraulics can be divided into three categories: gas-cooled reactor codes, LWR systems codes, and computational fluid dynamics (CFD).

GCR codes have been developed specifically for GCR applications, and lack the capabilities to model LWRs. GRSAC is a code that can model design basis accidents and severe accidents in pebble bed and prismatic reactors. The code uses a 3D thermal hydraulics model of the core and RCCS and includes a point kinetics model to analyze transients without SCRAM [39]. GRSAC has been used extensively for over 25 years. However, the numerical architecture has not been update. Furthermore, the code cannot model rapid transients and does not model the balance of plant [40]. THERMIX is a code used to analyze HTGRs with pebble fuel and has been validated with experiments for steady-state and burnup calculations [40, 41]. The code has not been validated for transient analyses [40]. THERMIX is used in Germany and South Africa for pebble bed reactor design calculations [42]. GAMMA has been developed specifically for air ingress accident analysis [43] and has been validated against

Japanese diffusion data [40]. AGREE was developed for HTGR analysis and is part of the NRC's HTGR code suite [8]. AGREE has been coupled to the neutronics code PARCS to analyze feedback mechanisms between reactor neutronic and thermal hydraulic conditions [44]. TINTE was developd to study the transient behavior of high temperature reactors. The code has the capability to solve time-dependent coupled neutronic, thermal-hydraulic, and chemical calculations. TINTE is one of the codes used by the developers of the PBMR [32]. GCR codes are advantageous because they have been developed specifically for HTGR analysis. However, many of these codes require additional validation. A second disadvantage is that these codes do not have the extensive user experience enjoyed by LWR systems codes like RELAP5 and MELCOR [40].

A number of these LWR systems codes are being modified to analyze HTGRs. ATHENA-3D, based on RELAP5-3D, has been used to analyze HTGRs [4,45,46]. In addition, RELAP5 has been used to analyze the RCCS of an HTGR [47]. Graphite oxidation and molecular diffusion models were added to MELCOR 1.8.2 by Idaho National Laboratory. The code has been used to model air ingress in a pebble bed reactor [31]. MELCOR 1.8.5 and 1.8.6 have been used to analyze a pebble bed reactor using the particulate debris core component as the fuel [12,13]. This version of MELCOR did not include gas-cooled reactor models. Calculations tended to significantly overpredict fuel and coolant temperatures. Still, this work concluded that MELCOR has many of the capabilities needed for PBMR calculations, and that additional models needed for PBMR analysis could reasonably be implemented into the code [12]. Extensive user experience with the code makes an improved MELCOR a useful tool for HTGR studies. For this reason, GCR models have been incorporated into MELCOR 2.1 [7].

Computational fluid dynamics codes provide a more detailed analysis of heat transfer and fluid flow in complex geometries than systems codes can provide. Air ingress studies have been performed using the commercial CFD code FLUENT.

These calculations were benchmarked against experimental data [48]. STAR-CD has been used to simulate steady-state and PLOFC and DLOFC transients in a prismatic reactor. A symmetrical 30° slice of the reactor was used in the calculations, which assumed a constant temperature for the RCCS rather than simulate its behavior [49]. Flownex is a systems CFD code with the capability to perform steady-state or transient calculations of a full HTGR plant, integrated with neutronics and controller algorithms [50, 51]. Flownex, Star-CD, and Fluent are all used by PBMR (Pty) Ltd in the PBMR design process [32]. CFD has also been used to analyze RCCS performance [52,53] and core bypass flow [38]. However, CFD codes take much longer to execute and typically cannot be used to analyze an entire reactor system [51]. CFD analyses should only be used for specific components for which the added computational burden is justified. The NRC will use CFD if needed to analyze HTGRs, but its use will be limited by the large computational times required for a CFD solution [8].

The large computational time and power required by CFD, combined with the lack of experience with GCR systems codes, makes MELCOR a good choice as an HTGR analysis tool. MELCOR enjoys the benefits that come with a widely executed software package; namely, the code is actively under development and has an extensive bug tracking system for licensed users. The code has also been used successfully to model the PBMR. For these reasons, MELCOR has been chosen for the HTGR studies presented in this thesis.

2.4.2 Experimental Studies of HTGRs

All codes used to analyze HTGRs must be validated against experimental data to ensure that reactor behavior can be accurately predicted [17]. Experimental data is especially necessary for the significant phenomena identified in the NGNP PIRT.

A number of separate effects and integral tests are being performed to increase the knowledge base of these important phenomena. Separate effects tests include

experiments for flow mixing in the lower plenum of an HTGR [54] and for flow through a pebble bed [55]. Idaho National Laboratory is currently performing or designing separate effects tests in order to obtain thermal fluids data for validation of CFD and systems analysis codes [19].

A number of integral facilities have been, and are currently being used to study HTGR behavior. The SANA facility in Germany was built and operated to study heat transport in a pebble bed reactor. The facility featured a pebble bed 1 m high and 1.5 m in diameter, a central 20 kW graphite heating element, and three 10 kW radial heating elements, all enclosed in a steel pressure vessel. The facility could reach temperatures of 1600 °C and could establish radial temperature profiles in the core. Data from the facility was used for validation of computer codes, including THERMIX [56].

HTTR in Japan and HTR-10 in China are two test reactors currently in operation. HTTR is a 30 MWt, prismatic block-type reactor with an operating pressure of 4 MPa. The reactor coolant outlet temperature is 850 °C during "rated operation" and can reach 950 °C during "high temperature test operation" [33]. HTTR reached an outlet temperature of 950 °C in April 2004 [43]. The reactor is fueled with TRISO coated uranium dioxide fuel particles encased in cylindrical graphite compacts placed in fuel holes drilled in hexagonal graphite blocks. The HTTR removes heat from the primary helium coolant using the primary pressurized water cooler (PPWC) and an intermediate heat exchanger (IHX). The PPWC is a steam generator that could be used with a Rankine cycle for electricity production, while the IHX is a helium-to-helium heat exchanger to provide clean, high-temperature helium for process heat applications. The HTTR is being used to demonstrate the safety characteristics of HTGRs [33].

HTR-10 is a 10 MWt, pebble bed reactor with an outlet temperature of 700-900 °C [57] and an operating pressure of 3 MPa. The reactor features fuel pebbles similar to those used in the AVR and planned for use in the PBMR, arranged in a cylindri-

cal (as opposed to annular, like in some PBMR designs) packed bed, based on the HTR-MODUL design. The HTR-10 features both a steam generator and an IHX. Initially, the reactor will operate with an outlet temperature of 700 °C and will use only the steam generator to remove heat from the primary coolant. In the second test phase, the reactor will operature with an outlet temperature of 900 °C and will utilize both the IHX and the steam generator to demonstrate a combined gas turbine and steam turbine cycle. Tests will be performed during both phases of operation to demonstrate the safety characteristics of HTGRs and HTGR components [3].

2.4.3 High Temperature Test Facility

Data from the HTTR and HTR-10 are being used to demonstrate HTGR safety and to validate HTGR analysis tools in code-to-experiment benchmark activities [29, 58]. However, due to insufficient instrumentation and/or the limited availability of the data from these experimental reactors and from historical HTGRs (such as Peach Bottom, Fort St. Vrain, and AVR), additional test facilities are needed [57]. For this reason, design and fabrication of an integral test facility is in progress at Oregon State University.

The High Temperature Test Facility (HTTF) is a full temperature, quarter scale, integral test loop that will be used to study HTGR thermal hydraulics. The HTTF is based on the Modular High Temperature Gas-cooled Reactor (MHTGR), designed by General Atomics, which is an early iteration of GA's GT-MHR. Electric heater rods are used to provide power to the HTTF. These heater rods are surrounded by coolant channels and arranged in a hexagonal lattice [59].

A detailed scaling analysis was performed for the facility. The dimensions of the HTTF were chosen to preserve kinematic and friction and form loss similarity. Helium was chosen to preserve kinematic similarity for depressurized loss of forced cooling tests. Quarter scale was chosen because fluid volume and core power require-

ments for this scale are reasonable. Also, this scaling choice makes it possible to outfit the facility with readily available piping and drawn tubing [60].

The HTTF will operate at coolant inlet and outlet temperatures of 490 °C and 1000 °C and at a maximum pressure of 0.8 MPa [61]. Pressure is limited by the cost and availability of high temperature, high pressure vessels.

Core power is limited to 600 kW [61]. This is sufficient for simulating decay heat, for which a maximum power of approximately 300 kW is needed. However, to simulate full-power operations, more than 10 MW would be required. This power level is impractical, and so the HTTF cannot be used for full-power tests [60].

The HTTF will be used primarily for DLOFC tests but may also be used for PLOFC and low-power, steady-state experiments. Data from the HTTF will be used to gain an increased understanding of HTGR thermal hydraulic phenomena, especially those phenomena identified by the NGNP PIRTs as significant. In particular, the HTTF will be used to study the distribution of flow through the core and bypass, the effects of the decay heat profile on reactor temperatures, the graphite temperature profile, and the effects of RPV and RCCS emissivity on heat removal from the reactor during accident conditions. In addition, data from the HTTF will be used to validate analytical tools and methods for gas-cooled reactor analysis [60].

3. MELCOR OVERVIEW

MELCOR is a systems code that models the progression of severe accidents in light water reactors. It was originally conceived as a parametric tool that could execute quickly and could model complicated physical phenomena for which there was a low knowledge base. Parameters called "sensitivity coefficients" can be used to adjust models used by the code, which allows for greater code flexibility and for sensitivity studies. As both available computing power and understanding of severe accident behavior have been increasing, mechanistic models that are increasingly best estimate in nature are being added to the code [5].

MELCOR is widely used in the United States and abroad for severe accident analysis of light water reactors. The code determines severe accident progression up through release of radioactivity to the environment [5]. MELCOR can be coupled to the MACCS code to perform public health and environmental consequence analysis calculations based on the calculated releases [62]. Comparisons have been made between MELCOR and two other severe accident codes used in the United States, MAAP [63] and SCDAP/RELAP [64,65]. Good agreement of predicted thermal hydraulic and major in-vessel severe accident phenomena in LWRs has been shown between MELCOR, SCDAP/RELAP, and MAAP [65]. Modified versions of MELCOR have used to analyze the Russian RBMK [6], fusion reactors [66], and the sulfur-iodine cycle for cogeneration of hydrogen with heat from a VHTR [67]. The code has also been used to model pebble bed reactors using the capabilities built in for light water reactors [12, 13].

MELCOR is part of the Nuclear Regulatory Commission's HTGR analysis code suite and will be used for HTGR design basis calculations [8].

3.1 Code Overview

The MELCOR code consists of two executables, MELGEN and MELCOR, shown schematically in Figure 3.1. MELGEN is responsible for processing and checking code input. It generates a diagnostic file that includes error and warning messages and a restart file containing the initial conditions and boundary conditions for the calculation. MELCOR reads this restart file, as well as additional user input, and moves the calculation forward in time. It writes output to a text file and to a plot file. The plot file, referred to as the PTF file, can be used to generate plots using the EXCEL® plugin PTFREAD or a plotting tool such as AcGrace. MELCOR also writes diagnostic and message files that contain error and warning messages and any messages about special events during code execution [5].

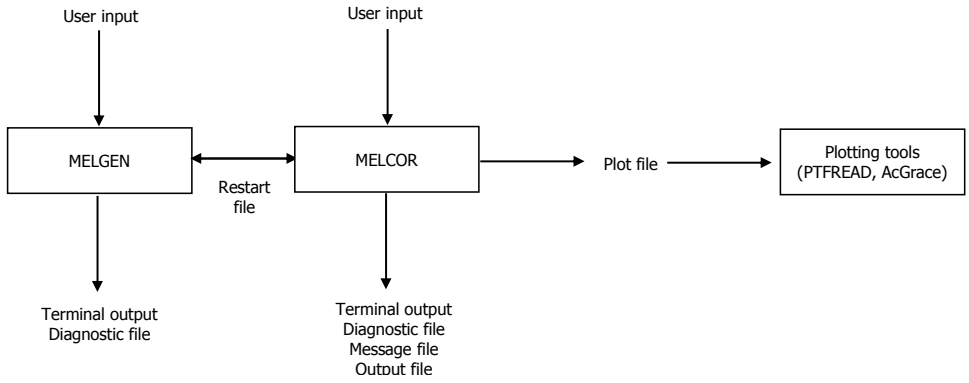

Fig. 3.1. MELCOR program flow diagram (based on [5])

3.2 Code Architecture

MELGEN and MELCOR are broken into major modules, called packages. For HTGR analysis, the following packages are significant:

- Executive (EXEC): controls execution of MELGEN and MELCOR and passes information between packages
- Core (COR): models the thermal response of the reactor core and lower plenum structures
- Control Volume Hydrodynamics (CVH) and Flow (FL): model the thermal hydraulic behavior of fluids, using flow paths to transfer mass and energy between control volumes
- Heat Structure (HS): calculates heat conduction through solid structures and energy transfer at surface boundaries
- Control Function (CF): allows the user to define functions of MELCOR variables, which can be used for reactor control logic, valve movement, or pump control, or to create a new variable to add to the plot file
- Noncondensible Gas (NCG): treats gases as ideal gases
- Material Properties (MP): includes material properties used by other packages
- Decay Heat (DCH): models decay heat from fission products
- Tabular Function (TF): allows the user to create one-dimensional tables that can be used to define material properties, create a decay heat curve, provide heat transfer coefficients to the HS package, or define mass and energy sinks

These packages exchange information such that all phenomena are explicitly coupled at each time step [5, 6]. Overviews of several of the above packages are provided in the following sections.

3.2.1 COR Package Overview

The MELCOR COR package models heat generation, heat transfer, chemical interactions, and material relocation of core structures in the core and lower plenum. The core and lower plenum are divided into a user-specified number of axial levels and radial rings. Radial rings are numbered consecutively from the core centerline outward. Axial levels are numbered from the bottom to the top of the core. A particular axial level and radial ring create a COR cell, which is azimuthally symmetric about the core centerline. Each COR cell must be coupled to a control volume in the CVH package. The COR package provides energy sources to CVH volumes [6].

A number of input options are available to the user for the COR package. The user can specify one of several reactor types, including Pressurized Water Reactor (PWR), Boiling Water Reactor (BWR), Pebble Bed Reactor (PBR), and Prismatic Reactor (PMR). Choosing one of these types sets default geometric parameters, such as fuel and cladding radii, and makes available additional modeling options, such as reflector modeling for PBRs and PMRs or pebble bed effective conductivity for PBRs [5].

The user must specify the mass and surface area of each COR component (such as fuel, clad, and supporting structure) for each COR cell. The user must also specify axial and radial relative power profiles, which are normalized and multiplied by the user-specified total core power (or decay heat power after reactor shutdown) to determine the power produced in each cell [5].

The user must also specify lower plenum and lower head geometry. MELCOR can model lower head failure using a number of parametric models and can model debris ejection from the lower plenum into the reactor cavity based on this user input [6].

3.2.2 CVH and FL Package Overview

MELCOR uses a control volume/flow path approach in modeling the thermal hydraulic behavior of fluids. CVH volumes contain mass and energy, which can be transferred to other volumes by flow paths using the FL package. MELCOR solves integrated, linearized-implicit finite difference equations for the conservation of mass, momentum, and energy in each control volume. Unlike MAAP, MELCOR does not have a built-in nodalization scheme. Instead, users must create pipes, vessels, valves, pumps, and other components using control volumes, flow paths, and heat structures [6].

The CVH and FL packages interface with the COR package to model heat transfer between core structures and control volumes and to model volume changes and flow blockage due to core material relocation. The CVH package also interfaces with the HS package to model heat transfer between control volumes and heat structure surfaces [6].

Networks of control volumes connected by flow paths can be used to approximate two- or three-dimensional behavior. However, since each flow path is only one-dimensional, multidimensional effects like advection of momentum cannot be correctly calculated [6].

The thermodynamic state of a control volume is defined by one pressure, evaluated at the interface between the liquid "pool" and the "atmosphere" in the control volume, and by the temperatures of the pool and atmosphere. If a control volume contains only noncondensible gases (such as in an HTGR core), its state is specified by one pressure and one temperature, corresponding to the average temperature in that volume. Equations of state for the fluids in CVH volumes are contained in the water properties (H2O) and Noncondensible Gas (NCG) packages [6].

CVH volume is specified using altitude/volume tables. Each row in an altitude/volume table consists of an elevation and the total volume between that elevation and the bottom elevation specified in the first row of the table. Thus, using these

tables, control volumes of various shapes can be constructed. Specified volumes do not include "virtual volume," defined as volume occupied by components from other packages (like fuel in the COR package) [5]. MELCOR uses specified volumes and altitudes to calculate elevation differences between two control volumes connected by a flow path for use in determining gravitational head [6].

The user must specify the initial thermodynamic state of each control volume used in the calculation. The control volume can be active, meaning properties are advanced through time by integrating the conservation equations; time-independent, meaning properties are constant with respect to time; or property-specified, meaning properties are specified as a function of time or any other variable available to the control function package [5].

Flow path geometry is specified by user input. Flow paths can be broken into segments, which can be used to model expansions and contractions. MELCOR uses hydraulic diameters, segment lengths, and elevation changes to calculate pressure changes used in the momentum equation. Frictional losses due to blockage in the flow path from degraded core structures or from a pebble bed are also treated [5].

The user can also create time-dependent flow paths, where coolant velocity is specified using a control function. Such a flow path can be used to provide constant flow for simulations of reactor steady-state behavior [5].

3.2.3 HS Package Overview

The HS package calculates one-dimensional heat conduction through solid "heat structures" and convective and radiative transfer at heat structure boundaries. Heat structures can be used to model vessels, pipe walls, or floors and walls in the containment building [6].

The user must specify the heat structure geometry. Heat structures can be rectangular, cylindrical, spherical, or hemispherical. Heat structure orientation, elevation, height, and surface area are specified by the user [5].

Energy transfer at heat structure boundaries is governed by user input. The user can choose to model convective heat transfer to an adjacent control volume, using heat transfer coefficients calculated using correlations in MELCOR or using control or tabular functions specified by the user. Radiative heat transfer to carbon dioxide, carbon monoxide, and steam in the atmosphere of an adjacent control volume can be modeled. Radiative heat transfer between surfaces can also be modeled by specifying view factors for pairs of heat structures [6].

3.3 Changes to MELCOR 2.1 for HTGRs

Two new reactor types, PBR and PMR, have been added to MELCOR 2.1 to model pebble bed and prismatic HTGRs. Selection of either of these reactor types enables graphite oxidation, activates user input records for graphite reflector modeling, and allows for axial and radial heat conduction in the core using an effective conductivity for a pebble bed or prismatic core.

In addition to the above changes, selecting PBR as the reactor type switches to heat transfer for a sphere with internal heat generation. Fuel is defined as the fueled region of the pebble, which contains TRISO-coated fuel particles in a graphite matrix. Cladding is defined as the graphite shell around the fueled reigon of the pebble. Heat transfer from the coolant to the clad is changed from that for cylindrical rods to that for a pebble bed. A correlation based on flow over an isolated sphere is used for convection from the pebble bed. Two new flow blockage models, PBR-A and PBR-R, are activated to model frictional losses for axial ('A') or radial ('R') flow through a packed bed.

For PMRs, the fuel component represents the fuel compacts, and the clad component represents part of the graphite block associated with a fuel compact and coolant channel. The cladding is treated as a thick cylinder with an assumed radial temperature profile [7].

4. RCCS CALCULATIONS

As the ultimate heat sink for HTGRs, the RCCS serves an important purpose during accident scenarios, particularly when active core cooling systems are lost. For this reason, an accurate prediction of RCCS behavior is a key component of HTGR accident analysis.

Several studies of the effects of the RCCS on vessel temperatures have been performed using CFD [52, 53] and systems codes, including THERMIX, GAMMA, TAC2D, and RELAP5 [29,43,47,68]. CFD is a useful tool for modeling the RCCS but has large computational requirements. THERMIX has not been validated against experimental data for transient calculations [40]. GAMMA is a relatively new tool with a rather limited scope (it was designed for air ingress studies) [43], while TAC2D is a legacy code developed by General Atomics in the 1970s [68]. Neither code is widely used. RELAP5 boasts extensive experience with LWR analysis but lacks the ability to model an HTGR.

Most studies of HTGR behavior [12, 13, 69–71] do not include an explicit model of the RCCS. Instead, a fixed-temperature boundary condition is used for the calculation. Such an assumption is sufficient for studies of core behavior because the RCCS has little impact on fuel temperatures. However, since the vessel temperature is strongly dependent upon RCCS performance [52, 69], RCCS behavior must be accurately predicted to guarantee the integrity of the reactor pressure vessel during and following an accident scenario.

Because of the need to simulate RCCS performance, and because of the limitations of the computer codes mentioned above, MELCOR has been used to study a water-cooled reactor cavity cooling system. Since MELCOR has not been used to model a water-cooled RCCS, this effort primarily focuses on modeling techniques developed for this activity. Less emphasis is placed on validation of the results, due to

large uncertainties in the RCCS design and in selection of appropriate heat transfer correlations.

The modeling approach used in this analysis is described below. Results from this study are compared to results from a code-to-code benchmark activity. Trends predicted by MELCOR are shown to be reasonable.

4.1 Modeling Approach

The purpose of this activity is to assess MELCOR's ability to simulate a water-cooled RCCS for an HTGR. Note that MELCOR has already been used to analyze the GT-MHR's air-cooled RCCS [72].

The RCCS input model was initially intended to replace the radial boundary condition for the 268 MWt PBMR input deck [12], developed at Purdue with MELCOR 1.8.5 and converted to MELCOR 2.1 by Sandia National Laboratories. However, the coupled reactor-with-RCCS input deck required a small time step, and hence an impractical amount of computing power for its intended purpose as a simplified case study. The PBMR model was replaced by a fixed temperature boundary condition to simulate the reactor pressure vessel.

Input for this activity is based on the RCCS of the Russian VGM pebble bed reactor [29], shown in Figures 4.1 and 4.2. This RCCS design was chosen due to the availability of design dimensions, and due to the comparable RPV dimensions and reactor powers of the VGM and the 268 MWt PBMR. Since little information was available on the source of the water in the RCCS, it was assumed that water flows from a water storage tank with a fixed temperature. This corresponds to the AREVA RCCS design when the heat removal loop through the water tank is functioning properly.

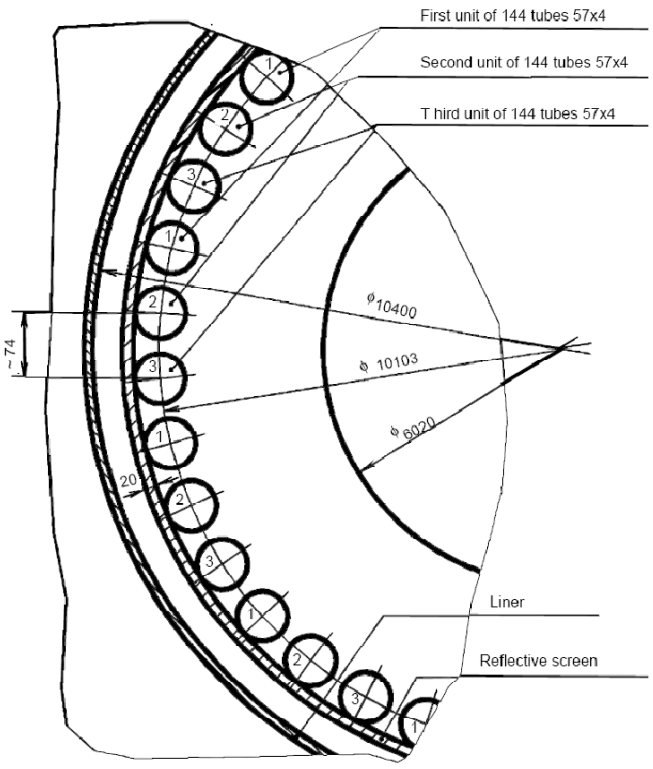

Fig. 4.1. Top view of the VGM RCCS [29]

4.2 Input Description

An overview of the input for a water-cooled RCCS is given here. This model describes the steady-state operation of a water-cooled RCCS for an HTGR, represented here as a fixed-temperature cylinder, divided into several shorter cylindrical heat structures. The nodalization scheme for this model is shown in Figure 4.3.

Input is included for the following components: reactor pressure vessel heat structures, cavity atmosphere control volumes, RCCS pipe heat structures, RCCS riser control volumes, RCCS downcomer control volumes, and the RCCS water storage tank. The reactor cavity atmosphere is divided into two rings and seven axial levels.

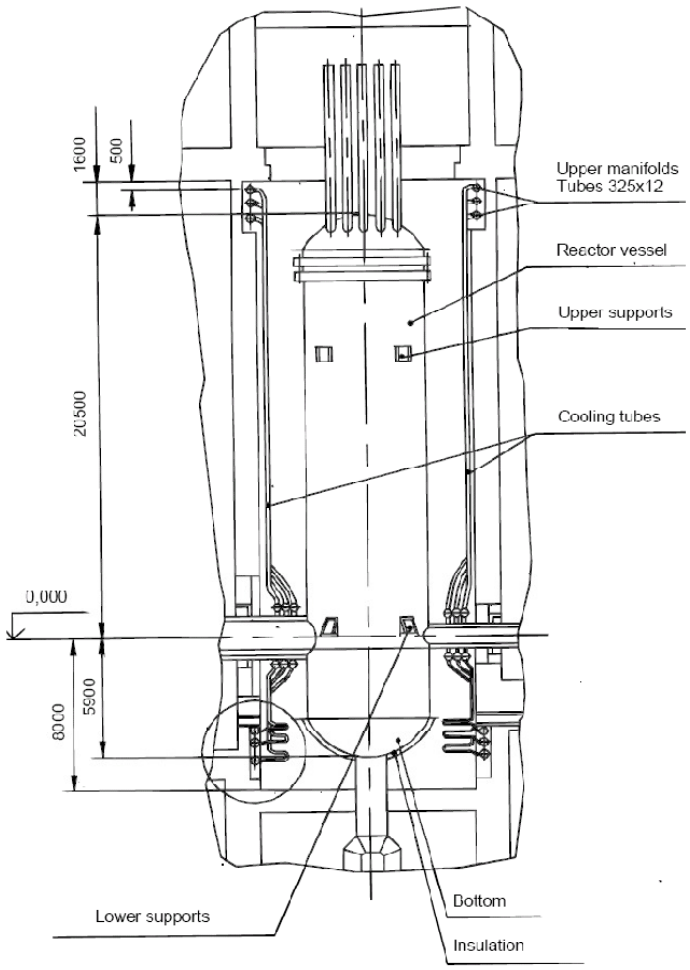

Fig. 4.2. Side view of the VGM RCCS [29]

It was divided to model natural circulation patterns in the reactor cavity, between the heated RPV and RCCS pipes. The cavity is connected to a time-independent control volume (CV) (CV350) that corresponds to the containment/confinement atmosphere. The confinement atmosphere is assumed to be at atmospheric pressure and at room temperature. Downcomer (CV55x) and riser (CV50x) CVs are likewise divided into several axial pieces. The division of the RCCS riser pipes into several control volumes provides a crude axial temperature profile, which is used to

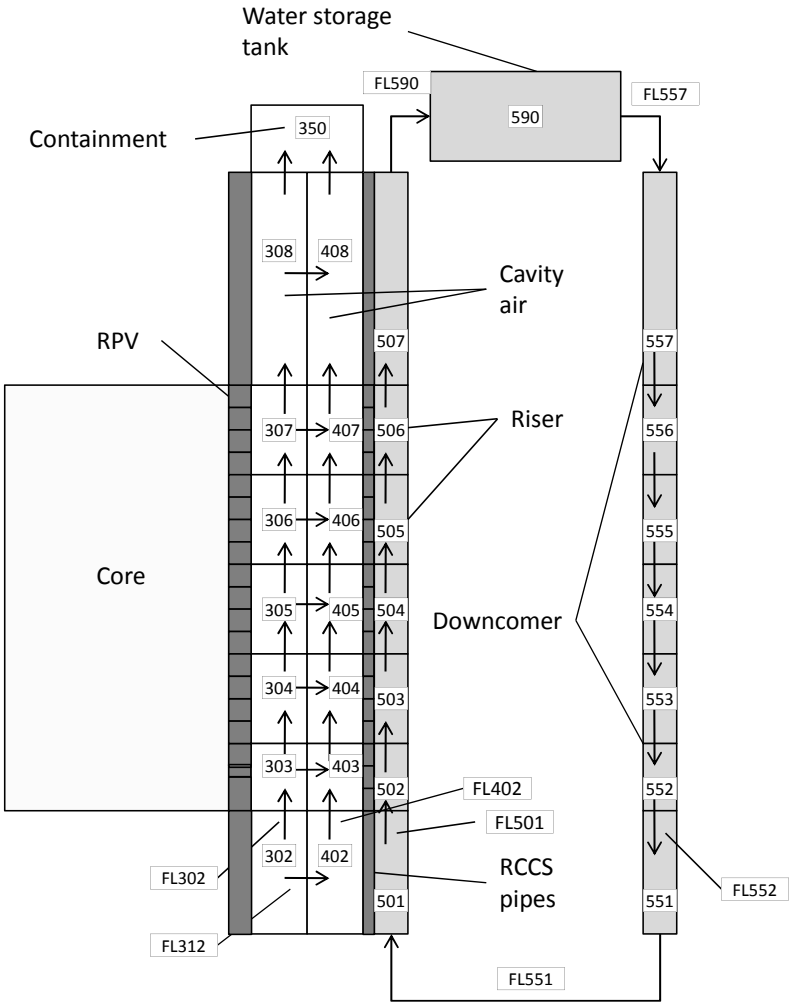

Fig. 4.3. Nodalization diagram for a water-cooled RCCS

determine buoyancy forces in the RCCS. Cavity and riser CVs are each coupled to multiple heat structures to decrease the number of flow paths (FLs), which simplifies the input and the analysis and speeds up runtime. This choice is justified since a fine spatial resolution of temperatures in the cavity and RCCS is not needed. Temperatures are expected to increase by no more than 5 °C between two adjacent control

volumes or heat structures. The water storage tank (CV590) above the RCCS riser and downcomer pipes is modeled as a time-independent control volume. For the tank, pressure is assumed to be atmospheric, and temperature is assumed to be 43 °C per the specifications for the VGM bencmark [29].

The RPV is broken into a large number of heat structures to match the vessel nodalization used for the 268 MW PBMR input. These heat structures are cylindrical, with a fixed temperature boundary condition at the inner surface and a convective boundary condition at the outer surface. The outer surface is coupled to the inner ring of reactor cavity control volumes (CV30n). The RCCS pipes are replaced by a cylindrical heat structure, such that the RPV and RCCS heat structures are concentric cylinders. The HS heights correspond to the heights of the RPV heat structures. These two modeling decisions were made to simplify the determination of view factors, for reasons explained below. The heat structures have convective boundary conditions at both the inner and outer surfaces, which are coupled to the cavity (CV40n) and riser (CV50n) CVs, respectively.

In this input model, heat is tranferred from the heated RPV surface to the cavity atmosphere by convection and to the RCCS pipes by radiation. Heat is transferred from the RCCS pipes by convection to the cavity and to the RCCS riser CVs. Natural circulation patterns in the cavity develop due to temperature gradients caused by heat transfer from the RPV and RCCS. At the same time, water flows from the RCCS storage tank to the downcomer CVs, from the downcomer CVs to the riser CVs, and back to the water storage tank. Initial pressures were carefully calculated and implemented such that calculated flow is negligible for an adiabatic calculation. Thus, all calculated flows in the cavity and RCCS are driven by density gradients resulting from heat transfer from the RPV.

4.2.1 View Factors

In radiation heat transfer, a view factor is defined as the fraction of radiation leaving one surface that reaches another surface [73]. View factors for pairs of surfaces can be specified in a MELCOR input deck.

For this calculation, view factors (F_{21}) were determined for radiation heat transfer from a "shell" (i.e. a portion of the inside of the outer cylinder) to a "tube" (i.e. a portion of the outside of the inner cylinder). Here, the RCCS heat structures are the "shells" and the RPV heat structures are the "tubes." This configuration is shown in Figure 4.4.

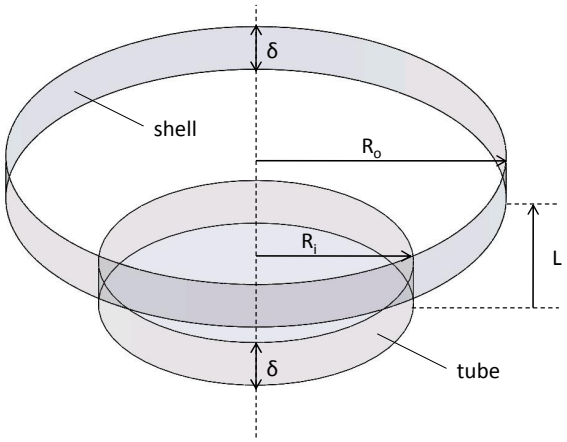

Fig. 4.4. Illustration of radiation heat transfer between a shell and tube

The following formula can be used when the shell and tube have the same height [74]:

$$F_{21} = \frac{1}{R_o \delta} \int_o^c \left(\frac{B}{a^{3/2}} \left[(L-\delta) \tan^{-1} \frac{L-\delta}{a^{1/2}} + (L+\delta) \tan^{-1} \frac{L+\delta}{a^{1/2}} - 2L \tan^{-1} \frac{L}{a^{1/2}} \right] \right) d\theta \tag{4.1}$$

where

$$a = R_o^2 + R_i^2 - 2R_oR_i\cos\theta$$

$$B = \frac{R_oR_i}{\pi(R_o - R_i)^2}\left[R_o^2+R_i^2 - R_oR_i(1+\cos\theta) - 2R_i^2\sin^2\frac{\theta}{2}\right]\times \left[R_o^2 + R_i^2 - R_oR_i(1+\cos\theta) - 2R_o^2\sin^2\frac{\theta}{2}\right]$$

$$c = \cos^{-1}(R_i/R_o)$$

R_o is the radius of the shell, R_i is the radius of the tube, δ is the height of the tube, and L is the distance from the bottom of the tube to the bottom of the shell. L must be an integral multiple of δ. When the base of the tube and shell are at the same elevation, the above expression simplifies to the following equation [75]:

$$F_{21} = \frac{1}{\pi R_2}\left[\frac{1}{2}(R_2^2 - R_1^2 - 1)\cos^{-1}\frac{R_1}{R_2} + \pi R_1 - 2R_1\tan^{-1}(R_2^2 - R_1^2)^{1/2} + (1+A^2)(1+B^2)^{1/2}\tan^{-1}\left(\frac{(1+A^2)B}{(1+B^2)A}\right)^{1/2} - \frac{\pi}{2}AB\right] \tag{4.2}$$

where $R_1 = R_i/\delta$, $R_2 = R_o/\delta$, $A = R_2 + R_1$, and $B = R_2 - R_1$. The view factor from the tube to the shell can be determined using a simple view factor relationship [73]:

$$F_{12} = \frac{A_o}{A_i}F_{21} \tag{4.3}$$

Numerical integration of Equation 4.1 was performed using MATLAB. Correct implementation of Equation 4.1 was verified by comparing results from several test cases to results presented in [74], and by comparing results for which $L = 0$ to results from Equation 4.2.

View factors for the RCCS input deck were determined by numerically integrating Equation 4.1 for a range of values for L. The view factor for each RPV and RCCS HS pair was determined using the appropriate value for each separation distance L.

Figure 4.5 shows the view factor F_{12} as a function of L/δ for three values of δ found in the RCCS nodalization scheme.

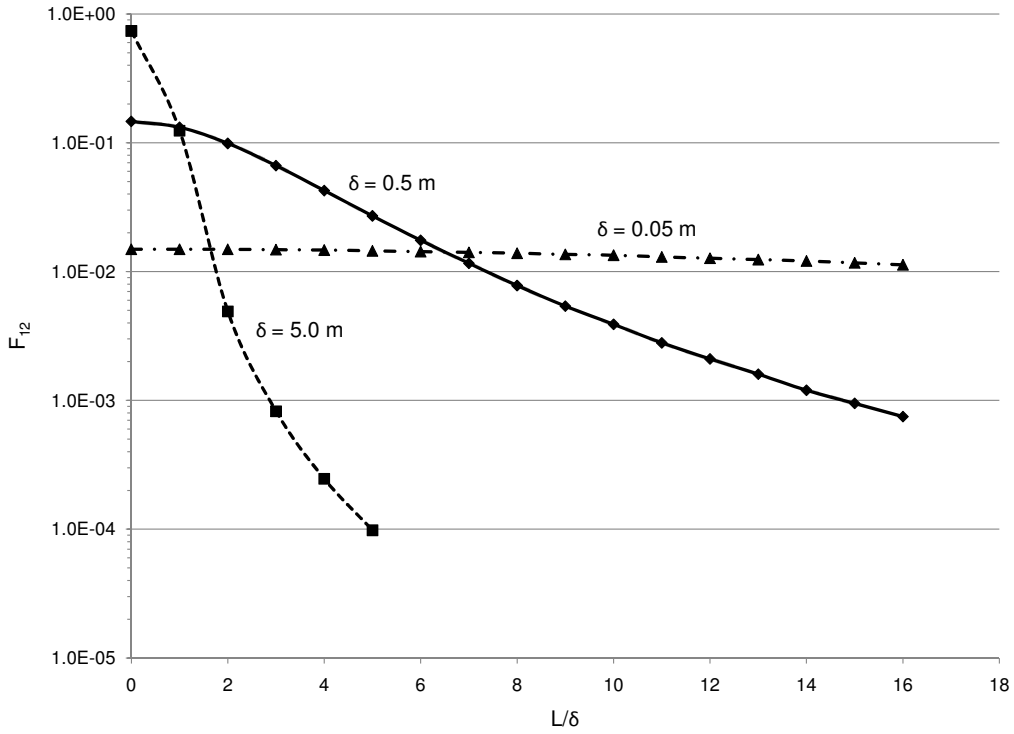

Fig. 4.5. View factors as a function of L/δ

For any pair in which the height of the shell is greater than the height of the tube, the view factor is determined by breaking the shell into pieces equal to the height of the tube, determining the view factor for each piece, and summing these values to obtain the view factor for the pair. If any of these pieces has a height less than the height of the tube, the view factor for that piece is found by interpolating, as illustrated in Figure 4.6. This assumes that each point on that portion of the shell receives the same heat flux. In reality, the heat flux from the tube decreases as the distance from the tube increases. However, using simple interpolation results in small errors, which are acceptable for this calculation.

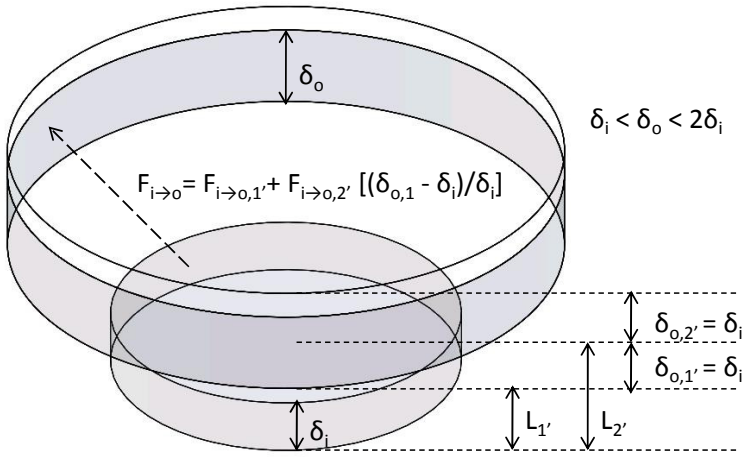

Fig. 4.6. Interpolation scheme used to calculate radiation heat transfer. Here, $\delta_{tube} \neq \delta_{shell}$.

MELCOR uses these view factors to determine the heat transfer rate from one surface to another using the following equation [6]:

$$q_{12} = \frac{\sigma(T_1^4 - T_2^4)}{\frac{1-\epsilon_1}{\epsilon_1 A_1} + \frac{1}{A_1 F_{12}} + \frac{1-\epsilon_2}{\epsilon_2 A_2}} \tag{4.4}$$

For this calculation, subscript "1" refers to the RPV heat structures and subscript "2" refers to the RCCS riser heat structures. The emissitivities of the RPV and RCCS risers (ϵ_1 and ϵ_2) are user input parameters. The emissivities for all surfaces in this problem are set to 0.8 as per the VGM benchmark description [29]. Equation 4.4 is applied for each heat structure pair defined in the input.

4.2.2 Flow Losses

Coolant flow through the RCCS is driven by buoyancy forces. Flow is governed by the following equation:

$$\rho\frac{D\mathbf{v}}{Dt} = (-\bigtriangledown p + \bar{\rho}\mathbf{g}) - [\bigtriangledown \cdot \tau] - \bar{\rho}\mathbf{g}\bar{\beta}(T - \bar{T}) \tag{4.5}$$

For one-dimensional flow (as in MELCOR) in the z-direction, this simplifies to

$$\frac{\partial}{\partial t}(\rho v) + v\frac{\partial}{\partial z}(\rho v) = \left(-\frac{dp}{dz} + \bar{\rho}g\right) + \mu\frac{\partial^2 v}{\partial z^2} - \bar{\rho}g\bar{\beta}(T - \bar{T}) \tag{4.6}$$

Here, v is the speed of fluid in the flow path. A positive value indicates flow from the "from" CV to the "to" CV. The above equations are derived using the Boussinesq approximation, which assumes that the density can be expanded in a Taylor series about the average fluid temperature [76].

The momentum equation for single phase flow from volume i to volume k in MELCOR includes all of the above terms in a modified form:

$$\rho L\frac{\partial v}{\partial t} = (p_i - p_k) + \rho g\Delta z + \Delta p - \frac{1}{2}K\rho|v|v + \rho v(\Delta v) \tag{4.7}$$

where ρ is the density of the upstream CV, L is the flow path length, p_i and p_k are the pressures of the "from" and "to" CVs, Δz is the change in elevation in the flow path, Δp is the pump head developed in the flow path, K is the net form- and friction-loss coefficient (explained below), and Δv is the change in velocity through the flow path (the "momentum flux") [6]. In this formulation, spatial derivatives ($\partial v/\partial z$) are replaced by simple differentials ($\Delta v/L$ or $\Delta v/\Delta z$), and the $K/2$ term is analogous to the viscous force term ($\mu(\partial^2 v/\partial z^2)$). For natural circulation conditions, the pump head term is equal to zero. The Boussinesq approximation does not appear directly in MELCOR's momentum equation. Instead, buoyancy forces are captured in the pressure difference ($p_i - p_k$) rather than in the fluid density. In order to accurately

predict natural circulation, problem nodalization should be as fine as is feasible so that the donor density is close to the average density used for the Boussinesq approximation.

The last term in Equation 4.6 describes the buoyancy force. Since there are no pumps to maintain flow, buoyancy drives any flow that may exist in the RCCS. To drive the flow, the buoyancy force must overcome flow resistances due to viscous forces (the $K/2$ term in Equation 4.7). While the pressure losses may be small in comparison to the buoyancy forces, they play an important role in determining the velocity of the fluid.

Flow losses can be divided into major and minor losses. Major losses are frictional head losses in the fully-developed regions of a piping network and are described by the following equation [77]:

$$\Delta p_{major} = f \frac{L}{D_h} \frac{\rho v_{avg}^2}{2} \tag{4.8}$$

The flow path length L and hydraulic diameter D_h are user inputs in MELCOR. The fluid density ρ, average velocity v_{avg}^2, and friction factor f are calculated by the code. Since the RCCS riser height and diameter are well-defined in the problem input, there are no uncertainties in the determination of major losses that are related to user input.

Minor losses are caused by components – such as expansions, contractions, inlets, outlets, valves, bends, and tees – that interrupt the smooth flow of fluid in a piping network. In a network with several of these components within a short distance, the minor losses may exceed the major losses.

Minor losses are described by a loss coefficient K_L. Minor loss coefficients must be determined experimentally. As a result, they often have large uncertainties due to variations in problem geometry and flow conditions.

Minor loss coefficients can be combined to yield a total minor loss coefficient for the system. The pressure drop caused by these losses is as follows [77]:

$$\Delta p_{minor} = \frac{\rho v_{avg}^2}{2} \sum K_L \tag{4.9}$$

Equations 4.8 and 4.9 can be combined the give the total frictional pressure loss. This can be combined with the gravitational pressure drop ($-\bar{\rho}\mathbf{g}$) to give the total pressure drop in Equation 4.5.

The minor loss coefficient for a flow path is a user input parameter. Since the document referenced for the RCCS input does not include information on the geometry of the system beyond the RCCS riser pipes, only a very rough estimate of the minor loss coefficients used in this calculation is possible. Several assumptions must be made. First, it is assumed that there is an inlet header to direct flow from the downcomer pipes to the riser pipes. Water would flow from the downcomer into this header, and from the header to the riser pipes. Thus, there would be both a pipe entrance ($K_L = 0.5$) and exit ($K_L = 2$) in this header. There must also be at least two 90° bends to connect the downcomer to the riser pipes. The loss coefficient depends strongly on whether the bend is smooth or rough, flanged or threaded, or whether or not it has vanes. Assuming flanged, smooth bends, the loss coefficient for each bend is 0.3. Combining these losses gives a loss coefficient of 3.1 for the flow path between the bottom of the downcomer and riser pipes. There may be additional components, such as valves, so the loss coefficient for this flow path is set as 5.0 in the user input. Similar reasoning can be used to determine the minor loss coefficient between the top of the riser pipes and the top of the downcomer.

It is clear that there are large uncertainties in the determination of the pressure drop in the RCCS due to user input. However, these uncertainties can be significantly reduced if accurate geometric data is given for the entire RCCS. Since this particular calculation is a proof of concept for MELCOR's ability to model the RCCS, accurate geometric data is not necessary.

4.2.3 Natural Convective Heat Transfer

As previously mentioned, flow through the RCCS risers and in the reactor cavity is driven by buoyancy forces. Buoyancy forces result from the presence of a density gradient and a body force, such as gravity, that is proportional to density. Flow driven by buoyancy is referred to as natural or free convection. This is different from forced convection, in which flow is driven by an external forcing condition, such as a pump or a fan [73].

The buoyancy forces at work in this particular problem may be large enough to create high flow rates, such that inertial forces become important. When inertia forces become more important than buoyancy forces, the flow behaves as a forced convective flow. This is important because the dominant heat transfer phenomena differ between natural and forced convective flows. For instance, in flows dominated by inertial forces, the thermal boundary layer is typically thin, resulting in a low temperature difference between the heated surface and the bulk fluid temperature. In flows dominated by buoyancy forces, the boundary layer is much thicker, resulting in a larger temperature gradient between heated surface and coolant, and thus poorer heat transfer.

The difference in heat transfer phenomena is reflected in experimentally-derived heat transfer correlations. Thus, one must know the heat transfer regime in order to choose an appropriate heat transfer correlation.

To determine whether a particular flow is in the natural convection or forced convection regime, one can compare two non-dimensional numbers, the Reynolds number (Re) and the Grashof number (Gr), defined as follows:

$$\mathrm{Re} = \frac{\rho v L}{\mu} \tag{4.10}$$

$$\mathrm{Gr} = \frac{g\beta(T_s - T_\infty)L^3}{\nu^2} \tag{4.11}$$

The Reynolds number is a ratio of inertial forces to viscous forces, while the Grashof number is a ratio of buoyancy forces to viscous forces [73].

MELCOR uses the following criteria to determine whether or not the flow is in a forced convection, mixed convection, or natural convection heat transfer regime [6]:

$$\text{Natural convection: } \mathrm{Re}^2 < \mathrm{Gr} \tag{4.12}$$

$$\text{Forced convection: } \mathrm{Re}^2 > 10\mathrm{Gr} \tag{4.13}$$

$$\text{Mixed convection: } \mathrm{Gr} < \mathrm{Re}^2 < 10\mathrm{Gr} \tag{4.14}$$

Substituting the relevant thermophysical properties of water and geometric properties of the RCCS risers into Equations 4.10 and 4.11, using an expected flow rate [29] to determine the coolant velocity, and assuming that the temperature difference between the RCCS riser tube and the fluid is approximately 10 °C, $\mathrm{Re}^2 = 6.3 \times 10^6$ and $\mathrm{Gr} = 1.9 \times 10^7$ for the RCCS risers. This shows that flow through the risers is expected to be in the natural convection heat transfer regime. However, if the flow rate is higher than expected, or if the temperature difference between the risers and the coolant is lower, then the flow may be in a mixed convection heat transfer regime. In this regime, inertial forces are as important as buoyancy forces.

The heat transfer regime in the cavity can be determined as well. In this case, the characteristic length is the height of the RPV, which is approximately 20 m [3]. The temperature difference between the heated vessel and the cavity is no less than 120 °C, which would occur in the lower third of the RPV. (The temperature difference from the RPV to the cavity in the upper two-thirds of the vessel would be much greater than 120 °C because the reactor core is at these elevations. The core is at much higher temperatures than the lower plenum during accidents.) Using relevant thermophysical properties of air, the minimum value of the Grashof number is 6.0×10^{13}. To be in the mixed convection heat transfer regime, the air velocity in the cavity must be greater than 10 m/s. It is unlikely that the velocity at some

point along the RPV would exceed 10 m/s. Furthermore, it is most likely that the highest velocities will occur along the upper half of the RPV, at which point the wall temperature (and thus the Grashof number) is higher. Thus, it is expected that flow along the RPV will be in the natural convection heat transfer regime. MELCOR results will be analyzed to determine whether calculated flow regimes are as expected.

The natural convection heat transfer correlations in MELCOR take the following form [6]:

$$\mathrm{Nu} = C\mathrm{Ra}^m + D \tag{4.15}$$

where

$$\mathrm{Nu} = \frac{kL}{h} \tag{4.16}$$

is the Nusselt number,

$$\mathrm{Ra} = \mathrm{GrPr} \tag{4.17}$$

is the Rayleigh number,

$$\mathrm{Pr} = \frac{\nu}{\alpha} \tag{4.18}$$

is the Prandtl number, and C, m, and D are constants. The heat transfer coefficient h is used to relate the heat flux at the heated surface to the temperature difference between the heated surface and the bulk fluid:

$$q'' = h(T_w - T_\infty) \tag{4.19}$$

An accurate prediction of the heat transfer coefficient is important in determining the heat removal rate from the RPV and the temperature rise in the RCCS risers. The temperature increase from the bottom to the top of the RCCS risers directly impacts the coolant flow rate through the RCCS, which in turn affects the temperature increase in the system. The RCCS coolant flow rate and the fraction of heat removed from the vessel by convection calculated by MELCOR will be compared to results from the VGM benchmark.

4.2.4 Boundary Conditions

In this calculation, vessel temperature, RCCS water tank temperature and pressure, and containment atmosphere temperature and pressure are specified as boundary conditions. The water tank temperature is set as 43 °C, as per VGM benchmark specifications [29]. The containment atmosphere is assumed to contain dry air at room temperature. The containment atmosphere and the water tank are both assumed to be at atmospheric pressure.

Pressure vessel temperatures are based on the VGM benchmark specifications found in Reference [29]. Figure 3-4 in the benchmark document contains a plot of RPV temperature versus height for both pressurized and depressurized conduction cooldown scenarios. The temperature for each RPV heat structure has been determined by estimating the average temperature for the corresponding axial location using the benchmark figure.

Temperatures used in this calculation are for depressurized conditions. While the temperature of the vessel would change throughout the transient, the thermal response of the vessel is slow, and so a quasi-steady condition would be reached. RCCS performance at this quasi-steady condition is studied using MELCOR.

4.3 Calculations

Steady-state calculations were performed with the input deck described above. Initially, the deck was run without a heat source. This was done to verify that there is no flow in the cavity or through the RCCS due to an error in control volume pressure input. The deck was then run with the heat source, with simplified view factors from the RPV to the RCCS. The view factor between each RPV heat structure and the RCCS heat structure at the same level was set to one. This was done to verify that heat structure and view factor input was correct. Once this was done, the simplified view factors were replaced by the detailed view factors described above.

Input for these calculations is described above. Additional cases tested the effects of minor losses in the RCCS on the coolant flow rate. This was done to address uncertainties in the determination of minor losses, as described in Section 4.2.2. All cases were run for 3000 s, which is sufficient for flow rates and heat transfer rates to reach an equilibrium condition.

4.4 Results

Results from MELCOR calculations using the water-cooled RCCS input deck are presented here. It must be understood that, since there were large uncertainties in the creation of the input deck, especially in regards to loss coefficients in the RCCS and the RPV temperature profile, these calculations are not meant to simulate the behavior of a particular RCCS design. Nevertheless, these results can be used to assess MELCOR's ability to model a water-cooled RCCS. This will be done by comparing MELCOR results to results from the VGM RCCS benchmark activity.

Table 4.1 shows the radiative and convective heat fluxes for each RPV heat structure. As the heat structure temperature increases, the fraction of heat transferred by radiation increases, since radiation heat transfer is proportional to T^4. The total radiative and convective heat transfer rates from the RPV are listed at the bottom of the table.

Radiation heat transfer results compare reasonably well with VGM benchmark results. Radiative heat transfer rates ranged from 860 kW to 1130 kW [29]. MELCOR results are 20-60% greater than results presented in the benchmark; however, heat source input for MELCOR calculations was based on a graph in the benchmark description. Thus, the discrepancy between MELCOR and VGM benchmark results is largely due to poor data interpolation for the MELCOR input.

Convective heat transfer rates are much higher than those reported for the VGM benchmark, which ranged from 70 kW to 220 kW [29]. MELCOR results are two to eight times greater than benchmark results. Furthermore, the percentage of heat

Table 4.1
Radiation heat flux from the RPV to the RCCS

		Heat flux (W/m^2)	
Heat structure	HS Temperature (K)	Radiation	Convection
33001	423	857	638
33002	532	3622	1625
33003	556	4574	1892
33004	561	4762	1947
33005	561	4766	1947
33006	571	5168	2024
33007	576	5374	2080
33008	586	5796	2193
33009	596	6238	2309
33010	601	6467	2325
33011	611	6944	2442
33012	620	7445	2560
33013	620	7446	2560
33014	615	7194	2439
33015	611	6948	2381
33016	596	6242	2209
33017	586	5799	2096
33018	571	5170	2051
33019	551	4401	1831
33020	532	3699	1618
33021	522	3345	1515
33022	482	1994	1098
Total (kW)		**1380**	**596**

transferred from the vessel by convection calculated by MELCOR (30%) is significantly higher than values reported in the benchmark (7.5-17%). The benchmark results are in line with the general consensus among experts in HTGR thermal hydraulics that radiation heat transfer accounts for 80-90% of the total heat transfer from the reactor vessel during a loss of flow transient [11]. Thus, results suggest MELCOR is significantly overpredicting convective heat transfer from the vessel. This may be due to a difference among the codes in the natural convection heat transfer correlations used. Experimental results are needed to determine which natural con-

vection heat transfer correlation is appropriate for RCCS calculations. It may also be due to the modeling choices made for the reactor cavity. Increasing the containment temperature would decrease convective heat transfer. Also, the containment temperature may not be constant throughout the transient. However, without more information about the containment design used in the VGM benchmark activity, it is impossible to say how the MELCOR model of the cavity compares to the model used in the benchmark activity.

Water flow through the RCCS is also significantly higher than expected. MELCOR calculates a flow rate of 95 kg/s through the RCCS, which is three times greater than the flow rate reported in the benchmark [29]. The high flow rate calculated by MELCOR may be due to an inaccurate estimation of flow losses in the RCCS piping. Calculations performed with higher flow loss coefficients show lower flow through the RCCS. Uncertainties in the loss coefficients are a result of insufficient data and do not reflect upon MELCOR's ability to treat buoyancy-driven flow. More information is needed about the RCCS piping layout in order to fully assess MELCOR's treatment of natural circulation.

The higher flow rates increase the importance of inertial forces in convective heat transfer. For this reason, MELCOR has determined that flow through the RCCS is in the mixed convective heat transfer regime, resulting in improved heat transfer from the RCCS pipes to the coolant. Heat is removed from the RPV by turbulent natural convection, as predicted above. The maximum calculated air velocity in the cavity is 1.9 m/s ($\sim$ 4 mph), which occurs at the top of the vessel. This result seems reasonable; however, it is impossible to say whether or not this result is correct without experimental validation.

4.5 Summary

A MELCOR 2.1 input deck has been created to model a water-cooled reactor cavity cooling system. The RCCS modeled in this study is based on the RCCS of the VGM pebble bed reactor.

The primary reactor vessel heat removal mechanism is radiation. This radiation is absorbed by RCCS riser pipes. Detailed view factors from reactor vessel heat structures to riser pipe heat structures have been developed based on a formula for heat transfer from the outer surface of an inner cylinder to the inner surface of an outer cylinder. The formula was implemented in a MATLAB script. Calculated view factors were incorporated into the MELCOR input model. The methodology developed here can be applied in future HTGR calculations.

Additional attention is given to modeling natural circulation heat transfer and pressure losses. Form loss coefficients play a major role in determining flow rates for buoyancy-driven flows. Care must be taken when selecting form loss coefficients so that natural circulation flow rates, and thus convective heat transfer rates, are accurately predicted.

Results show that MELCOR accurately predicts radiative heat transfer rates from the reactor vessel heat structures, but overpredicts convective heat transfer in the reactor cavity and coolant flow rates in the RCCS pipes. The high flow rates are likely a result of underestimating the form loss coefficients due to a lack of RCCS geometric data. Both the modeling approach and the natural circulation heat transfer correlation should be re-assessed to explain why convective heat transfer rates are higher than expected.

Overall, the positive results indicate that an approach similar to that used here to model a water-cooled RCCS can be adopted for future HTGR studies.

5. PBMR-400 CALCULATIONS

To assess the new gas-cooled reactor models in MELCOR 2.1, and to apply MELCOR 2.1 to model a high temperature gas-cooled reactor, input has been developed for the 400 MW Pebble Bed Modular Reactor. MELCOR input for the PBMR is based on the PBMR-400 benchmark activity sponsored by the Organisation for Economic Co-operation and Development (OECD). The PBMR-400 benchmark was a code-to-code, coupled neutronics and thermal hydraulics activity organized to compare methods and tools for gas-cooled reactor analysis, featuring participants from around the world [71]. The availability of the problem definition and of results from the benchmark were key factors in choosing to base MELCOR input on the PBMR-400 benchmark. Since experimental data is currently unavailable, the benchmark represents the best test case for the new GCR models in MELCOR.

The current use of MELCOR to model an HTGR is an extension of previous efforts using earlier versions of the code [12, 13]. These efforts demonstrated that MELCOR could be used to analyze an HTGR, provided certain modifications were made to the code. The new GCR models are a response to this work. The current effort expands upon that work by developing new input techniques for modeling HTGRs and by comparing MELCOR results to results from other codes.

5.1 Modeling Approach

The primary objective of this work is to develop input techniques for simulating PBMR behavior during steady-state and accident conditions. Input is based on the PBMR geometry and operating parameters, as described in the OECD PBMR-400 benchmark.

Input for the PBMR-400 is contained in the following files: **pbmr400.inp**, **pbmr400-src_sink.inp**, **viewfactors.inp**, and **decay-heat.inp**. **pbmr400.inp** contains control volume, flow path, and COR cell input for the reactor core; thermo-

physical properties for materials used in this problem; heat structures representing the core barrel, reactor pressure vessel, and RCCS pipes; and control functions to calculate parameters that are not included in standard output. **pbmr400-src_sink.inp** includes input for the coolant mass source and mass sink, as well as control logic for the coolant source flow rate and reactor inlet and outlet pressure. **viewfactors.inp** includes view factor input for structure-to-structure radiation heat transfer. **decayheat.inp** includes a decay heat curve, as well as simple control logic for the reactor. Additional files are used for transient calculations. The input contained in these files is described in the following section. A detailed explanation of code input can be found in Appendix B.

A number of assumptions were made as part of the benchmark problem definition. Thermal hydraulics assumptions and stipulations are as follows:

- The reactor is azimuthally symmetric about the reactor centerline.
- The coolant flow is simplified to the main coolant flow path. In other words, all flow is assumed to pass through the pebble bed core, and bypass flow is neglected. This assumption is justified because there are large uncertainties in bypass flow paths and flow rates. The goal of the benchmark was not to resolve the complex issue of bypass flow, but to compare analysis methods for phenomena that are better understood.
- The coolant flows through an open loop. No effort is made to model the balance of plant.
- Adiabatic boundary conditions are applied at the top and bottom plates. Thus, heat transfer through structures above and below the top and bottom plates is neglected. Notably, radiation heat transfer from the upper and lower heads to the RCCS is not considered. This assumption is conservative because it decreases the total heat removal from the core.

- A constant temperature boundary condition is applied at the reactor cavity cooling system pipes.
- The helium between the side reflector and core barrel and the core barrel and reactor pressure vessel is static. Also, the air in the reactor cavity is static.
- The pebbles are stationary. Pebble flow through the core is not considered.
- The pebble bed porosity is constant at 0.39 throughout the reactor core. This value represents the average porosity determined by the developers of the PBMR [32].
- Material properties for graphite and steel are specified. This was done because there are large variations in graphite and steel properties. Specifying the properties benchmark participants should use allows for a better comparison of HTGR analysis methods.

5.2 Steady-State Input Description

A description of MELCOR input for the 400 MW PBMR is given here. A more detailed description can be found in Appendix B.

Input has been created for steady-state and transient calculations, using GCR models included in MELCOR 2.1. The nodalization diagram representing this input deck is shown in Figure 5.1. Input for the CVH, FL, HS, and COR packages is represented on the diagram. Like the RCCS model, this model is azimuthally symmetric about the centerline. Note that the diagram is not to scale.

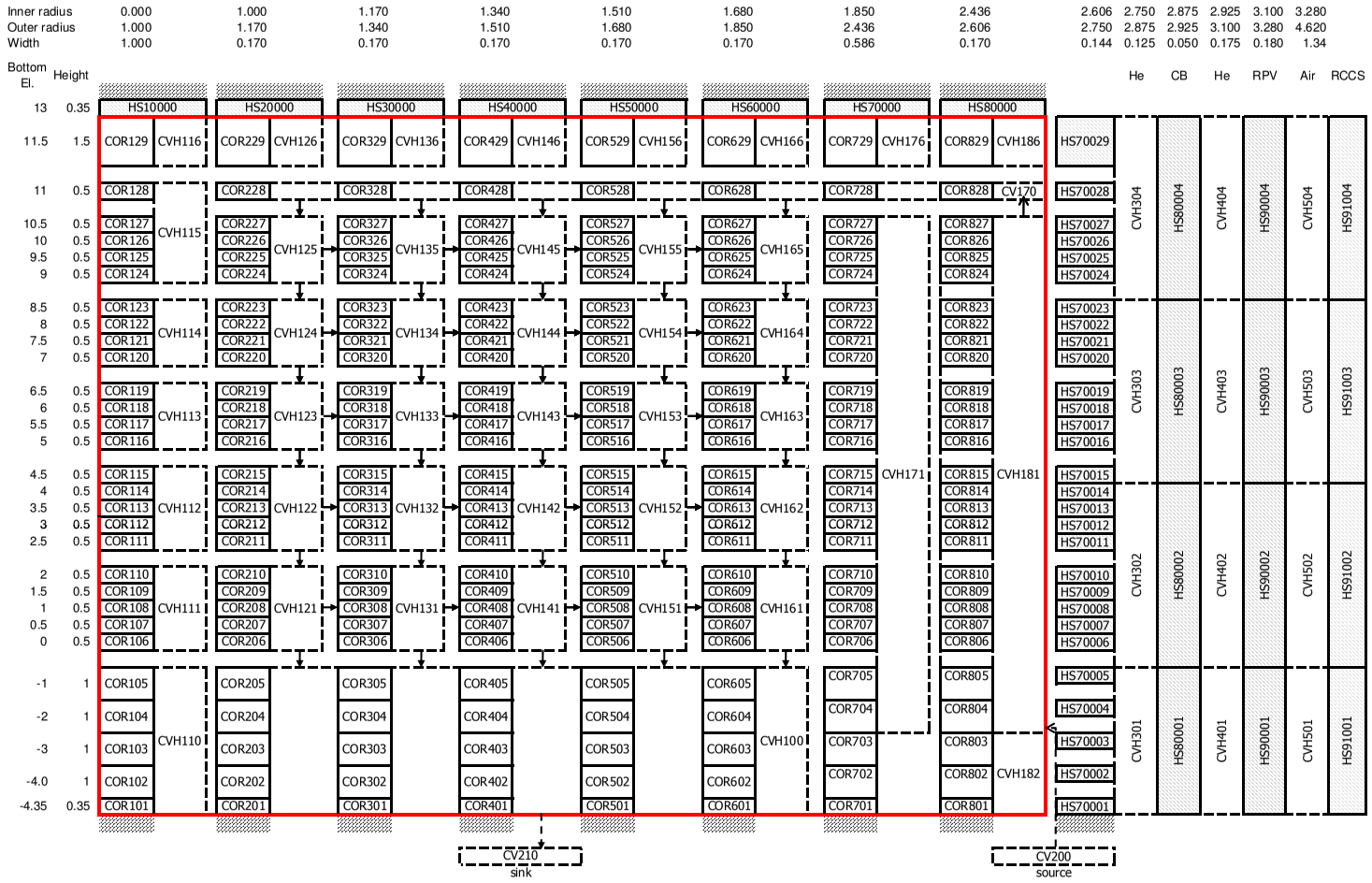

Fig. 5.1. Nodalization diagram for the PBMR-400 MELCOR input deck

5.2.1 COR Input

The input model for the COR package includes the pebble bed core; top, bottom, central, and side reflectors; the bottom plate; and the lower head. The core is divided into 8 radial rings and 29 axial levels. Ring 1 represents the central reflector; rings 7 and 8 represent the side reflector; level 1 represents the bottom plate; levels 2-5 represent the bottom reflector; level 28 represents the void region above the pebble bed core; level 29 represents the top reflector; and levels 6-27 of rings 2-6 represent the pebble bed core. The active core nodalization follows the active core nodalization of the benchmark definition.

The reactor type for this input model is chosen as PBR. This automatically treats heat transfer from the clad to the coolant for a packed bed, changes the fuel internal temperature profile to that of a sphere with internal heat generation, allows radial and axial heat conduction between rings and axial levels using an effective bed conductance correlation, and enables reflector modeling and graphite oxidation. It also considers the graphite in the fueled region of a pebble to be part of the fuel (FU) component. Note that for PBRs, the "clad" is the graphite shell around the fueled region of the pebble.

The mass of uranium dioxide and graphite in the fuel and graphite in the clad is required for each COR cell. The mass of UO_2 in cell rzz was determined by first calculating the total number of pebbles present in rzz, which is equal to the volume of rzz occupied by pebbles divided by the volume of one pebble:

$$N_{rzz} = \frac{V_{rzz}(1-\varepsilon)}{V_p} \tag{5.1}$$

Here, ε is the bed porosity, defined as the fraction of the volume occupied by gas. The mass of UO_2 in rzz is then equal to the number of pebbles in rzz times the mass of UO_2 per pebble. (Each pebble contains 9 g of uranium [71], so the mass of UO_2 per pebble is 10.2 g). This mass is input for each COR cell.

Assuming that the TRISO coatings can be treated as graphite, the volume of graphite in the 5 cm-diameter fueled region of a pebble can be calculated as follows:

$$V_{g,fr} = V_{fr} - \rho_{UO2} m_{UO2,fr} \tag{5.2}$$

where the subscript fr stands for fueled region. Multiplying this quantity by the density and by the number of pebbles in cell rzz gives the mass of graphite in the fueled region of the pebble. This is input as the mass of graphite in the FU component, since MELCOR considers this graphite to be part of the fuel.

The mass of graphite in the clad (CL) component of cell rzz is simply equal to the volume of graphite cladding in each cell, multiplied by the density of graphite and by the number of pebbles in rzz.

The masses of UO_2 and graphite in the fuel and graphite in the cladding calculated using the methods described above were input for each active core cell; for all other COR cells, these masses were input as 0.0.

The bottom plate in level 1 was modeled as a steel PLATEG type of supporting structure (SS). Little information about the lower plate for the PBMR is available, so the input parameters used in stress calculations for this SS were chosen such that the SS will not fail under the conditions expected in these calculations. Since the main focus of this activity is to assess MELCOR's capabilities as an analysis tool for HTGR thermal hydraulics, and since the lower plate simply acts as an adiabatic boundary for this problem, an accurate simulation of stresses in the lower plate is unnecessary. The mass of steel in the supporting structure in each cell in level 1 was calculated by multiplying the volume of that cell by the density of steel specified in the benchmark definition.

The top reflector in level 29 and the portion of the bottom reflector in level 5 were modeled as supporting structures due to limitations in the code. In MELCOR, FU must be supported from below by FU or by a supporting structure. The same is true of the CL component. In other words, the reflector (RF) component cannot

support the FU component. For this reason, the portion of the bottom reflector in level 5 must be modeled as a supporting structure; otherwise, the pebble bed core would collapse. A new type of supporting structure (RFLCT) was created for this input deck. RFLCT is able to support any COR component above it and will not fail unless its temperature exceeds 5000 K. Since the reflector is not expected to fail for the steady-state and transient conditions analyzed in these calculations, this method is acceptable. The top reflector must be modeled as a supporting structure because the reflector component (RF) must be supported by RF or by a supporting structure. Since rings 2-6 of level 28 represent the void region above the pebble bed core, rings 2-6 of level 29 must be modeled as a supporting structure. Again, this supporting structure is modeled as RFLCT. In reality, the top reflector would be connected to the top plate and supported from above. Both RFLCT supporting structures are modeled as zirconium because graphite cannot be used as a supporting structure. Instead, zirconium properties are redefined to match those of graphite.

The central and side reflectors and levels 2-4 of the bottom reflector are modeled as reflectors (RF). The user must define reflector geometry, including the hydraulic diameter of the inner and outer surfaces, the radius of the channel side of the reflector, the reflector thickness, and the reflector orientation (flat or cylindrical).

The central reflector is cylindrical, with a thickness equal to the physical radius of the reflector. In the input deck, the thickness is negative to signify to the code that the outer surface is the "channel" side. (MELCOR differentiates between the "channel" and "bypass" region of each COR cell. Per the benchmark assumptions, bypass flow is not considered in this analysis.) The channel side hydraulic diameter is set as 2 m, which is equal to the physical diameter of the reflector. The bypass hydraulic diameter has no significance because bypass flow is not modeled. The mass of RF in each central reflector cell is simply equal to the volume of the cell times the density of graphite. In other words, there are no gaps or holes in this model of the central reflector. Physically, there would be small channels drilled into the

central reflector, into which balls containing a neutron-absorbing material would be dropped if the control rods fail to shut down the reactor in the event of a transient. However, since bypass flow through the reflector is not considered, and since these channels occupy a small, but unspecified, fraction of the total reflector volume, the channels are not modeled. The reflector surface area in each cell is equal to the outer surface area of the reflector. Again, the surface area of the shutdown absorber sphere channels is not considered. Each central reflector cell is coupled to a CVH cell with negligible volume. These volumes are used to satisfy the input requirement that each COR cell be coupled to a CVH cell, even though in this case no helium volume is present.

Levels 2-4 of rings 2-6 are modeled as flat reflectors, whose thicknesses are equal to their COR level height. Level 3 contains the coolant outlet plenum and is considered a porous medium in the language of the benchmark. The exact configuration of the outlet plenum is not provided, but the graphite porosity and the hydraulic diameter for this region is defined in the benchmark document. Level 2 is considered to be solid graphite, meaning there is physically no helium volume in this portion of the reflector. Level 4 is considered to be a porous medium, through which coolant flows from the pebble bed core to the outlet plenum in level 3. The reflector thicknesses in levels 2-4 are input as negative numbers to signify that the channel side is at the upper surface (i.e. they are bottom reflectors). Channel side hydraulic diameters are set equal to 0.07 m for level 4, 0.144 m for level 3, and 0.01 m for level 2. The hydraulic diameter for level 2 has no physical significance, since the CVH cells coupled to these core cells have negligible volume and are not connected by flow paths. Hydraulic diameters for levels 3 and 4 are specified in the benchmark definition. The mass of graphite in each cell was determined by multiplying the volume of each cell by the mass of graphite. In levels 3 and 4, this value was multiplied by the fraction of the cell occupied by graphite, defined as 0.8 in the benchmark definition. To determine the surface area of the reflector in levels 3 and 4, it was assumed that helium flows through cylindrical

channels with a diameter equal to the hydraulic diameter given in the benchmark. This is a reasonable assumption for the reflector in level 4, though it is certainly not true for level 3, which contains the outlet plenum. Still, since little heat transfer from the coolant to the reflector is expected, this is an acceptable assumption. The surface area is calculated by determining the number of these channels that would be present in each bottom reflector cell, using the calculated volume of helium in each cell. The channel side surface area in each cell in the bottom reflector is equal to this estimated number of channels times the surface area of one channel.

The side reflector in ring 7 is modeled as a cylindrical reflector, whose thickness is equal to the thickness of ring 7. The channel side surface area for the levels adjacent to the pebble bed (levels 6-27) is equal to the surface area of the inner face of the reflector. Channel side hydraulic diameters for these levels were set equal to their axial lengths. For level 28, which contains part of the upper inlet plenum, the hydraulic diameter is set equal to 0.335 m per the benchmark specifications. The surface area of this porous area was calculated using the methods described above for the porous regions of the bottom reflector. The mass of graphite in level 28 was calculated using the methods described above for porous media. The mass of graphite in the other levels of ring 7 were calculated assuming zero porosity. Control volumes coupled to these cells have negligible volume.

The side reflector in ring 8 is modeled as a cylindrical reflector, whose thickness is equal to the thickness of ring 8. This portion of the side reflector contains the helium riser channels pictured in Figure 2.2. Levels 4 and 5 and level 28 contain the lower and upper inlet plena ($D_h = 0.335$ m). Levels 6-27 contain the riser channels ($D_h = 0.07$ m). Channel side surface areas were calculated using the methodology described for the porous regions of the bottom reflector. Graphite masses for these cells were calculated using the methods described above for porous media. The remaining levels of the side reflector have zero porosity. Surface areas and hydraulic diameters input for these levels are arbitrary. Masses are calculated as above.

A flat lower head was chosen for this modeling effort. In reality, the lower head of the PBMR is hemispherical; however, the benchmark specifies that the bottom plate forms the lower boundary of the system. To simulate an adiabatic boundary condition, the heat transfer coefficient between the lower head and the atmosphere outside of the lower head was set to zero. The temperature of the control volume around the lower head was set equal to the temperature of the bottom plate. The rest of the lower head input is arbitrary, so long as all input requirements are satisfied and the lower head does not fail during the calculation.

The relative core power was input for each radial ring and for each axial level. The relative power in each cell is equal to the radial profile times the axial profile, evaluated for that cell. MELCOR determines the core power in each cell by multiplying the normalized relative power by the total core fission power specified in the user input. This approach differs from the approach used in the benchmark. For the benchmark, the power density in each cell was calculated using the neutronics code PARCS. Results are tabulated for use in thermal hydraulic steady-state exercises. The user can specify the power in each COR cell in MELCOR using control functions; however, this significantly complicates the required input and makes it more difficult to simulate decay heat production during transients. For this reason, a separable power profile was created from the cell-specified power densities given in the benchmark. The axial power profile was created by calculating the average power density for each axial level and dividing by the average power density for the core. The radial profile was created by first calculating the average power density for each ring and dividing by the core average power density. The radial power profile was then adjusted slightly to preserve the total core power. The resulting separable profile shown in Figures 5.2 and 5.3 compares well with the profile specified in the benchmark. The relative errors in the power for each cell are listed in Table 5.1. Negative errors indicate that the power specified in the benchmark is greater than the power specified in the MELCOR input.

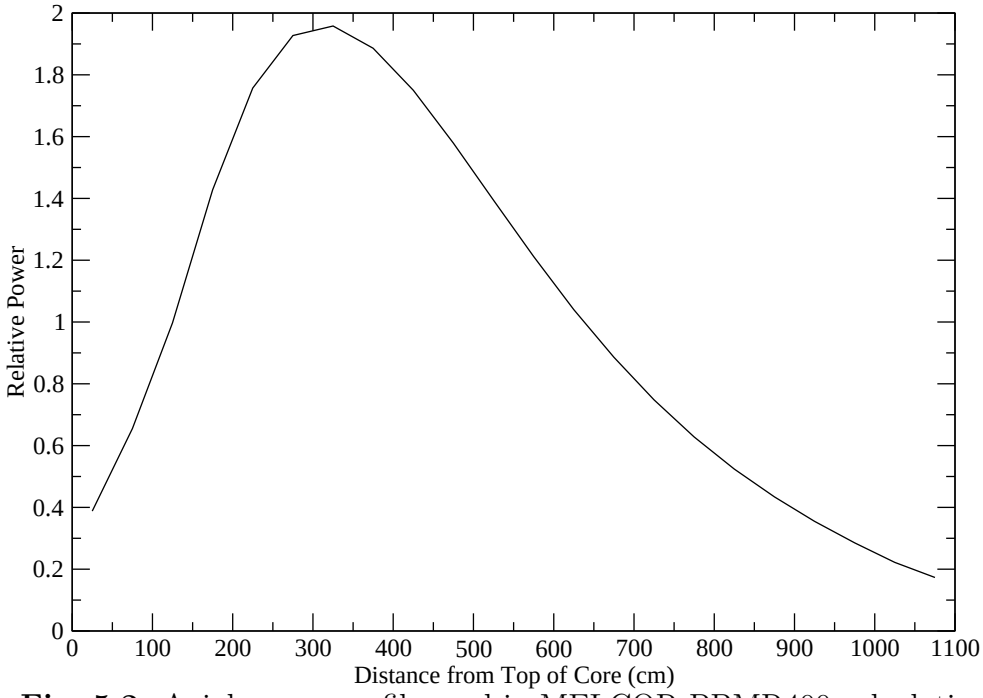

Fig. 5.2. Axial power profile used in MELCOR PBMR400 calculations

5.2.2 Core CVH-FL Input

Control volume and flow path input simulates the flow of coolant from a helium source (see Section 5.2.3) to a lower inlet plenum, up through riser channels in the side reflector to an upper inlet plenum, into a void region above the core, downward through the pebble bed core and the bottom reflector, into an outlet plenum, and out of the reactor to a helium sink. Control volumes and flow paths in the active core are designed to allow for both axial and radial flow, which allows for the simulation of natural circulation flow in the core.

Figure 5.1 shows the control volumes and flow paths for the PBMR-400 input deck. Note that the arrows indicate the direction of positive flow, not the flow direction. Also note that each COR cell is coupled to a control volume. In most cases, several COR cells are coupled to one control volume. This still allows for the prediction of the core temperature profile without an impractical one-to-one

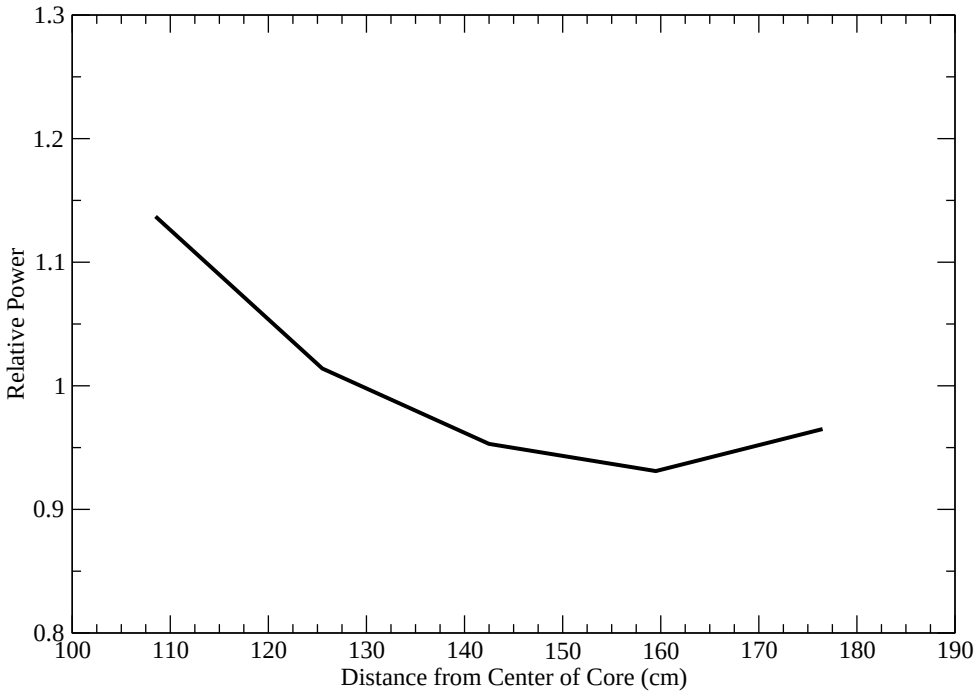

Fig. 5.3. Radial power profile used in MELCOR PBMR400 calculations

correspondence between COR cells and CVH volumes. Such a correspondence would require an excessively large number of control volumes, and subsequently a large number of flow paths, which would significantly slow down code execution. For this reason, each control volume in the active core (CVH121-125, 131-135, 141-145, 151-155, 161-165) is coupled to four or five COR cells, resulting in control volumes 2 m or 2.5 m high.

The temperature within each control volume is uniform; however, the dT/dz model in MELCOR estimates the coolant temperature in each COR cell based on the COR cell power, control volume temperature, and coolant flow direction. These local temperatures are reported in MELCOR output and plot files. This makes it possible to shorten runtime by decreasing the number of control volumes while still having sufficient data to compare with the benchmark results.

Input required for each control volume includes its volume, specified as a table with pairs of altitudes and volumes, and its thermodynamic state. For each CVH

Table 5.1
Relative error in cell powers specified in the MELCOR input deck

Level	Ring 2	Ring 3	Ring 4	Ring 5	Ring 6
27	18.1%	7.9%	-0.8%	-12.8%	-30.4%
26	17.6%	7.9%	-0.6%	-12.6%	-29.8%
25	13.6%	5.5%	-0.6%	-8.7%	-19.7%
24	5.7%	-0.1%	-2.6%	-3.8%	-1.0%
23	1.8%	-2.0%	-2.6%	-1.3%	3.4%
22	0.3%	-2.0%	-1.9%	-0.4%	3.8%
21	-0.8%	-1.7%	-1.2%	0.2%	3.5%
20	-1.7%	-1.3%	-0.6%	0.8%	3.0%
19	-2.5%	-1.0%	0.0%	1.2%	2.5%
18	-3.1%	-0.7%	0.5%	1.6%	2.1%
17	-3.7%	-0.5%	0.9%	1.9%	1.8%
16	-4.2%	-0.2%	1.3%	2.2%	1.4%
15	-4.6%	0.0%	1.6%	2.4%	1.2%
14	-5.0%	0.1%	1.9%	2.6%	0.9%
13	-5.3%	0.2%	2.1%	2.8%	0.7%
12	-5.6%	0.4%	2.3%	2.9%	0.5%
11	-5.8%	0.5%	2.5%	3.0%	0.4%
10	-6.0%	0.5%	2.6%	3.1%	0.2%
9	-6.2%	0.6%	2.8%	3.2%	0.1%
8	-6.2%	0.7%	2.8%	3.3%	0.0%
7	-6.4%	0.8%	3.0%	3.3%	-0.3%
6	-7.6%	2.0%	4.8%	3.8%	-2.8%

volume, an entry in the altitude/volume table is included for each elevation corresponding to the elevation of an axial level coupled to the control volume. Initially, all control volumes contain helium at 9.0 MPa and 500 °C, which corresponds to the conditions of the outlet when the reactor is at zero power.

Volumes for cells in the active core are calculated by multiplying the empty cell volume by the bed porosity. The same methodology applies for control volumes in porous graphite regions in the bottom and side reflectors (CVH100, 170, 181), except here the empty volume is multiplied by the reflector porosity (0.2) instead of the bed porosity (0.39). Several control volumes (CVH110-116, 126, 136, 146, 156,

166, 171, 176, 182, 186) are coupled to COR cells where no helium volume should be present. This is done to satisfy user input requirements as explained in Section 5.2.1. These CVH cells have negligible volume and are not connected by flow paths. Other CVH cells (CVH301-304, 401-404, 501-504) represent volumes between heat structures where a "no flow" condition has been specified in the benchmark. These control volumes are not connected by flow paths to prevent flow in these regions.

Input required for each flow path includes "to" and "from" control volume names and junction elevations, flow area, segment hydraulic diameters, and segment lengths. For flow paths in the core, segment lengths are set equal to the distance between the centers of the "to" and "from" control volumes. For axial flow through a ring, the hydraulic diameter is equal to $2(R_o - R_i)$, where R_o and R_i are the ring inner and outer radii. This formulation also applies for flow from one ring to another, except the radii in the above equation are replaced by the top and bottom elevations of the control volumes connected by the flow path. Flow areas are set equal to the empty bed flow areas. MELCOR adjusts the flow area for "blockage" due to fuel pebbles. PBR-A and PBR-R are selected as the blockage models for axial and radial flow in the pebble bed. When either of these options is selection, MELCOR uses a packed bed correlation (the default is the Ergun equation) to calculate the pressure drop across the flow path.

Flow paths from the lower inlet plenum to the upper inlet plenum, from the upper inlet plenum to the void region above the core, and from the bottom of the core to the outlet plenum assume flow through channels drilled into the graphite in these regions. Hydraulic diameters are taken from the benchmark specifications. Flow areas were calculated by multiplying the total cross sectional area of the appropriate COR cell by the graphite porosity, specified as 0.2 in the benchmark [71].

5.2.3 Coolant Source and Sink Input

As per the benchmark specifications, the balance of plant for the 400 MW PBMR is not modeled. Instead, helium flows into the reactor from a property-specified source and exits the reactor to a property-specified sink. During steady-state calculations, the helium sink is at a pressure of 9 MPa. The specified control volume temperature has no effect on the calculation, since it simply acts as a mass and energy sink. The specified pressure does, however, affect the pressure in the reactor. The helium source is at a temperature of 500 °C. The helium velocity from the helium source to the reactor is set at a constant value of 62.7 m/s, which corresponds to the benchmark mass flow rate of 192.7 kg/s. The source pressure is specified as 9.3 MPa. The specified pressure has no effect on the flow rate or on the pressure in CVH181; it only affects the density used to calculate the helium velocity from the source. The pressure in CVH181 is determined by MELCOR by adding the pressure drop from inlet to outlet to the outlet pressure.

5.2.4 Heat Structure Input

Heat structures represent the top plate, the portion of the side reflector beyond the helium risers, the core barrel, the RPV, and the RCCS. The top plate and side reflector heat structures act as boundaries for the core package. Code requirements dictate that a heat structure serve as the top boundary for each radial ring and the side boundary for each axial level. The top plate heat structures (HSr0000) are modeled as flat plates, with surface areas equal to the areas of their respective radial rings. Convective boundary conditions, with heat transfer coefficients calculated by MELCOR, are specified at the bottom surfaces. However, since the control volumes adjacent to the top plate have negligible volume and are not connected by flow paths, heat transfer by convection is expected to be negligible. Adiabatic boundary conditions are applied at the top surface of the heat structures.

The side reflector heat structures (HS700zz) are modeled as cylindrical heat structures, with heights equal to the heights of their respective axial level. Convective boundary conditions are applied at both surfaces. However, since there is no control volume adjacent to the inner surface, and since helium in the control volumes adjacent to the outer surface is stagnant, convection is expected to be negligible.

The core barrel, RPV, and RCCS are each divided into four heat structures with equal heights of 4.5 m. The number of heat structures was chosen to reduce input requirements while still preserving some axial temperature variation in these components. Future studies can include more heat structures for a more detailed analysis. Convective boundary conditions are applied at both surfaces, though no convection is expected because boundary control volumes contain static gas.

Radiation heat transfer between the side reflector and core barrel, the core barrel and RPV, and the RPV and RCCS is modeled using the view factors explained in Section 4.2.1. Emissivities are set at 0.8 for all heat structure surfaces per the benchmark specifications.

5.2.5 Control Logic

Control logic has been provided through CF package input. These control functions allow linear changes in helium source velocity, helium source pressure, and helium sink pressure for transient calculations. A control function 'TransientDT,' defined as the difference between the problem time and the value specified as the initial time ('TransientTime'), is applied together with control functions for rates of change in source velocity, source pressure, and sink pressure, to determine the source velocity or source or sink pressure. For example, the helium velocity is determined as follows. The value of 'TransientDT' is multiplied by the linear rate of change in the mass flow rate 'dMdot-dt' to give the total change in flow 'FlowLoss.' The flow rate 'MFlow' is determined by subtracting 'FlowLoss' from a user-defined initial flow rate 'SS_MFlow.' The helium velocity 'CF_HeSource' is then calculated

by dividing 'MFlow' by the flow area and the source density. If 'CF_HeSource' is negative, function 'SourceCheck' becomes FALSE and latches for the duration of the calculation. When 'SourceCheck' changes state to FALSE, the helium velocity is set equal to zero. Similar methodology has also been used to determine the source and sink pressure. When 'SourceCheck' becomes FALSE, the source and sink pressures are set equal to a specified value (6 MPa for the PLOFC transient, 0.1 MPa for the DLOFC transient) for the remainder of the calculation. Note that during steady-state calculations, the rates of change and the time since the start of the transient are set to constant values of 0.0.

Two other functions define the source and sink temperatures. During steady-state calculations, 'SourceTemp' and 'SinkTemp' are constants equal to 773 and 1173, respectively. If 'SourceCheck' latches FALSE, source and sink temperatures are set equal to the temperatures of CVH181 and CVH100, respectively. This is done to prevent any non-physical flows that could develop as a result of non-physical source and sink temperature specifications.

Additional control functions have been included to turn off fission power and simultaneously activate decay heat. These functions trip the reactor and activate decay heat when 'SourceCheck' latches FALSE.

5.2.6 Decay Heat

Decay power is given as a table in the benchmark problem definition. This data has been incorporated into a tabular function in the MELCOR input deck. Log-log interpolation was employed by the benchmark codes to interpolate between data points. In contrast, MELCOR linearly interpolates between data points, and so there is some error in MELCOR's estimation of decay heat generation from the tabular function. However, since a large number of data pairs are included in the tabular function, the change in decay power between two data points is small, and so the interpolation error is low (approximately 0.2%).

The decay heat package is activated when it receives a trip signal from a control function. DCH is not activated during steady state calculations for the PBMR, but DCH input must be included in the steady state input deck because the restart file generated by the steady-state calculation is used in transient calculations.

5.3 Transient Input Description

The pressurized loss of forced cooling with SCRAM and depressurized loss of forced cooling with SCRAM transient benchmark exercises have been performed with MELCOR. The restart file generated by the steady-state calculation is used to provide the initial conditions for the transient calculations. Input for each transient calculation is described below.

5.3.1 PLOFC Input

At the start of the PLOFC transient, the helium velocity – and thus the mass flow rate – decrease linearly over thirteen seconds per the benchmark specifications. This is done by changing the additive constant of 'dMdot-dt,' which was previously set to 0.0 for steady-state, to -14.82, and by changing the additive constant of 'TransientTime' to the problem time at the start of the transient. Over the same period, source and sink pressure decrease linearly to 6 MPa by setting the additive constants of 'dPin-dt' and 'dPout-dt' to -0.2536E+06 and -0.2308E+06, respectively. Calculations are performed for 50 hours, or 180,000 seconds, of problem time.

5.3.2 DLOFC Input

Input for the DLOFC transient is similar to input for the PLOFC transient. The only difference is in the values of the additive constants for 'dPin-dt' and 'dPout-dt.' For this transient, the system is depressurized to 0.1 MPa over 13 seconds, and

so the additive constants for 'dPin-dt' and 'dPout-dt' are set to −0.7162E+06 and −0.6923E+06, respectively. The additive constant for 'dMdot-dt' is the same as the value used for the PLOFC calculations.

5.4 Calculations

MELCOR was run using the steady state input deck until temperatures reached equilibrium. Calculations were performed using the Achenbach correlation in place of the Ergun equation, which is the default correlation for pressure drop in a packed bed. The Achenbach correlation is a modification of the Ergun equation for $\mathrm{Re}/(1-\varepsilon)$ up to 1×10^5 [78]. The Ergun equation is a correlation for experimental data up to a Reynolds number of approximately 2500 [76]. The Achenbach equation incorporates results from experiments carried out at higher Reynolds numbers [78]. For PBMR steady-state operations, values of $\mathrm{Re}/(1-\varepsilon)$ on the order of 10,000 are expected. Thus, the Achenbach correlation is more appropriate for PBMR calculations. It has been implemented by modifying the relevant sensitivity coefficients through user input. Coefficients for the Achenbach correlation can be found in the MELCOR Reference Manual [6].

During initial calculations, it was discovered that heat was not being transferred from the reflector component in ring 7 to the reflector in ring 8. The release version of MELCOR used for this study does not allow ring-to-ring reflector heat transfer. As a result, heat was not being transferred radially outward to the RCCS, and so steady-state results were not valid. Input was adjusted so that COR rings 7 and 8 were removed from the input. The side reflector heat structures were extended to encompass the entire side reflector. The region of the side reflector containing the helium riser tubes was modeled as a new material, called 'POROUS-GRAPH.' This material has the same specific heat capacity as graphite, but its thermal conductivity and density is reduced by 20% to account for the specified porosity in the benchmark.

The inner and outer portions of the side reflector heat structure were modeled as graphite.

Initial calculations also showed that MELCOR was overpredicting fuel temperatures. This is because the correlation used by the COR package to calculate convection heat transfer from the pebble bed is based on flow over an isolated sphere. This correlation does not account for the enhanced heat transfer due to turbulent mixing caused by irregular flow through a packed bed [73]. The packed bed correlation used by MELCOR was modified using sensitivity coefficients. The adjusted convective heat transfer correlation is based on a correlation found in German regulatory standards, which is as follows [79]:

$$\mathrm{Nu} = 1.27\frac{\mathrm{Pr}^{1/3}}{\varepsilon^{1.18}}\mathrm{Re}^{0.36} + 0.033\frac{\mathrm{Pr}^{1/2}}{\varepsilon^{1.07}}\mathrm{Re}^{0.86} \tag{5.3}$$

This correlation is suggested in the benchmark problem definition. However, it could not be implemented directly because the packed bed heat transfer correlation in MELCOR has the following form [6]:

$$\mathrm{Nu} = A + B\mathrm{Re}^{C}\mathrm{Pr}^{D} \tag{5.4}$$

Here, A, B, C, and D are sensitivity coefficients. For high Reynolds number flows, the second term on the right hand side of the equation is much larger than the first term. For gas flow, the Prandtl number is relatively constant over a wide range of temperatures. For this reason, a curve fit of the form

$$\mathrm{Nu} = B\mathrm{Re}^{C} \tag{5.5}$$

was obtained over the range of expected Reynolds numbers using EXCEL®. This curve fit was implemented into MELCOR for steady-state calculations. Relative

errors for this fit for Reynolds numbers expected in this calculation are shown in Table 5.2.

Table 5.2
Error in the heat transfer correlation implemented in MELCOR

Re	Nu (KTA Rules)	Nu (Curve Fit)	Error
1.00E+04	1.75E+02	1.71E+02	2.04%
1.50E+04	2.23E+02	2.23E+02	0.42%
2.00E+04	2.68E+02	2.68E+02	0.12%
2.50E+04	3.09E+02	3.10E+02	0.19%
3.00E+04	3.49E+02	3.49E+02	0.03%
3.50E+04	3.86E+02	3.85E+02	0.27%
4.00E+04	4.23E+02	4.20E+02	0.64%
4.50E+04	4.58E+02	4.54E+02	1.05%
5.00E+04	4.93E+02	4.86E+02	1.48%

After incorporating the above changes, steady-state calculations were performed once again. After one million seconds of problem time, heat structure temperatures were still changing. This is because there is a very large amount of graphite in the reactor. Since the rate of heat transfer to the boundary heat structures is low, the graphite heatup is very slow. At the same time, heat is being transferred by radiation between the side reflector and core barrel, the core barrel and RPV, and the RPV and RCCS. This is a very slow process, which is why thermal equilibrium was not reached after one million seconds. However, temperatures of COR components reach equilibrium after a relatively brief time period. Due to limits on computing time, and due to the fact that the core is at thermal equilibrium – even though boundary heat structures are not – results from these calculations were deemed acceptable for use as initial conditions for transient calculations. Note that heat structure temperatures are approaching an asymptotic value and are changing less than one-hundredth of a degree per hour.

To reduce the size of plot and restart files, and to reduce the time needed to perform future steady-state calculations, the initial heat structure and reflector tem-

peratures specified in the steady state input were set as the final temperatures from the steady state calculations. This input deck was run for ten thousand seconds, which is sufficient for COR components to reach thermal equilibrium. The restart file produced from this calculation was used to initialize the transient calculations.

PLOFC and DLOFC transient calculations were performed using the input described above. A maximum time step of 1 s was used for these calculations. This time step was chosen to prevent errors in the solution of the momentum equation, which were observed for large (> 10 s) time steps. The default packed bed heat transfer correlation was used for transient calculations because of the lower mass flow rates present in the transient calculations.

For transient calculations, conduction and radiation are the primary modes of heat transfer. This differs from steady-state behavior, when convective heat transfer dominates. PLOFC and DLOFC are slow transients, in which decay heat from the fuel is transferred through the pebble bed to the side reflector and out to the RCCS. Natural circulation is expected to develop during the pressurized transient, but not during the depressurized transient. This is because of the increased driving force due to a higher helium density in the pressurized transient.

Results from steady-state and transient calculations are presented in the next section.

5.5 Results

Results from PBMR-400 steady state and transient MELCOR calculations are presented here and compared to results from other codes. Note that all benchmark data presented here were obtained from the benchmark participants in the form of EXCEL® spreadsheets containing final results from the calculations. These spreadsheets were made available for this research activity. Please see Appendix A for a complete listing of all MELCOR parameters plotted in this thesis.

5.5.1 Steady State Results

Steady state results from the PBMR-400 input model with six radial rings are presented here. Figure 5.4 shows the mass flow rate into and out of the reactor. As expected, the mass flow out of the reactor is equal to the specified mass flow of 192.7 kg/s into the reactor. Figure 5.5 shows the inlet and outlet helium velocity. The inlet velocity is constant, as expected, since this value is fixed by boundary conditions. The outlet velocity increases as the outlet temperature increases and reaches a constant value once the helium reaches a steady temperature. The outlet velocity is lower than the inlet velocity because the outlet flow area is approximately three times greater than the inlet flow area.

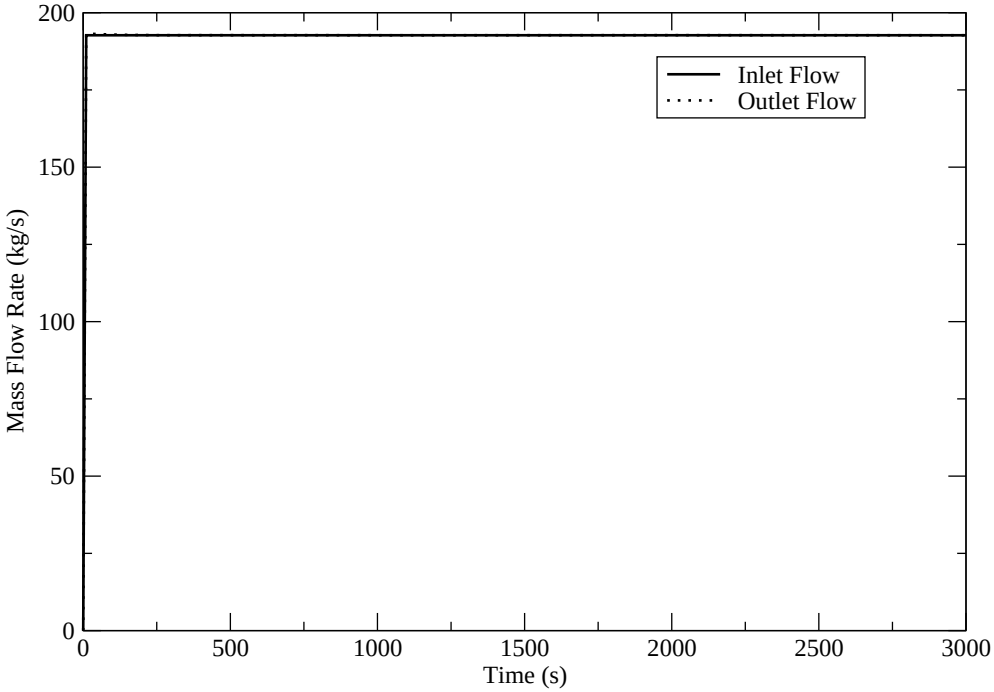

Fig. 5.4. Coolant mass flow into and out of the reactor

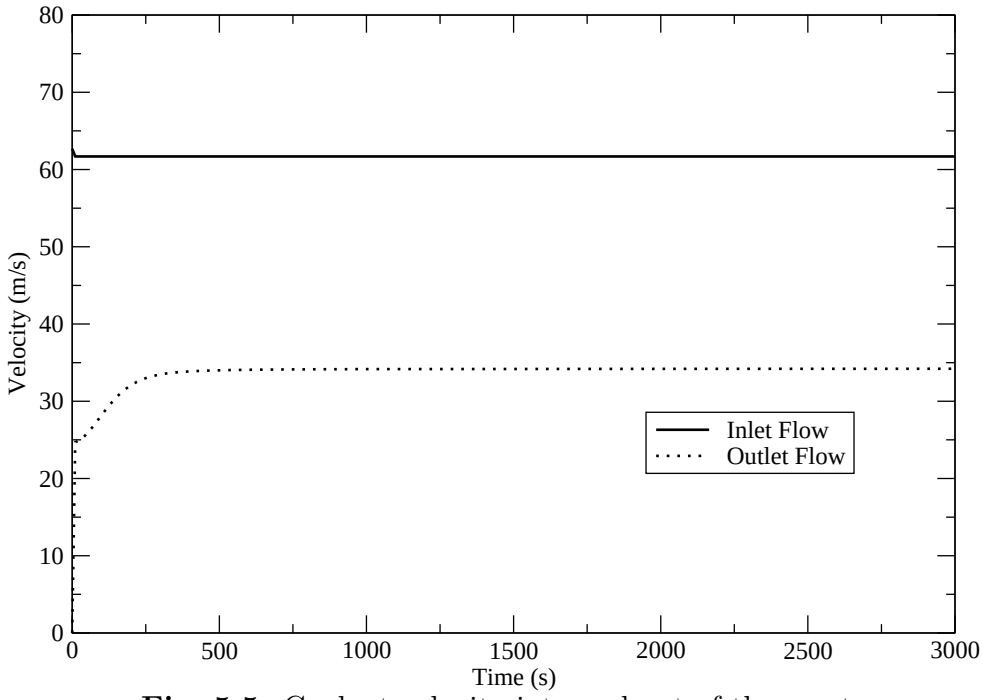

Fig. 5.5. Coolant velocity into and out of the reactor

Core Temperatures

Coolant temperatures in the void region above the core (CVH170) and the outlet plenum (CVH100) are shown in Figure 5.6. The temperature of CVH170 is constant due to the imposed helium inlet temperature. The core temperature rise (i.e. the increase in temperature from CVH170 to CVH100) is shown in Figure 5.7. The calculated core temperature rise increases as the temperature of coolant in the outlet plenum increases. The temperature rise reaches a steady value of 399 °C, which is just below the expected value of 400 °C. The helium outlet temperature calculated by MELCOR compares well with results from the benchmark, as shown in Figure 5.8.

The fact that calculated helium outlet temperatures are slightly less than expected can be attributed to heat losses to the boundary. The rate at which heat is transferred to the HS package is shown in Figure 5.9. Heat losses to the boundary

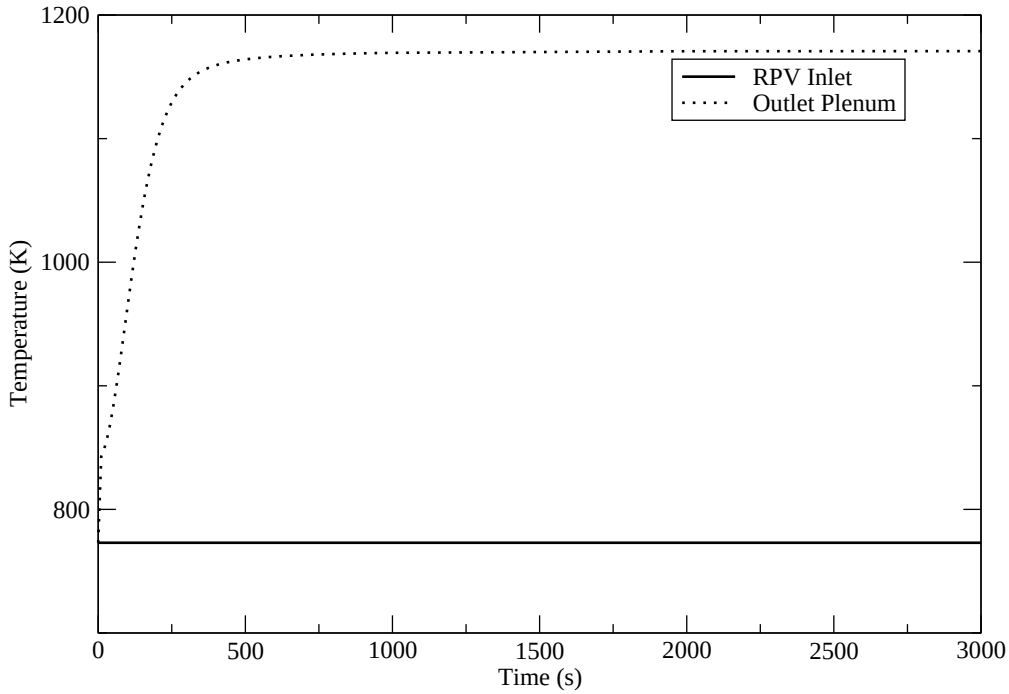

Fig. 5.6. Helium inlet and outlet temperatures

are approximately 700 kW. While this is a small fraction of the total reactor power, it is substantial enough to result in calculated coolant outlet temperatures that are slightly lower than expected.

Figures 5.10-5.14 show axial variations in fuel temperatures in rings 2-6. Note that the fuel temperatures calculated by MELCOR represent the average temperature of the fueled region of the pebble, including the TRISO-coated fuel particles and the graphite matrix surrounding the kernels. In all cases, fuel temperatures increase from an initial value of 773 K to steady-state values within 1000 s of problem time. Radially, temperatures are highest in ring 2 and lowest in ring 5. The temperature profile is due to the imposed radially power profile (Figure 5.3), which peaks in ring 2, adjacent to the central reflector, and reaches a minimum in ring 5. Axially, temperatures are highest near the bottom of the core. This temperature profile differs from that of an LWR, where temperatures are highest at the location of the highest power. This is because the coolant temperature rise from core inlet to outlet

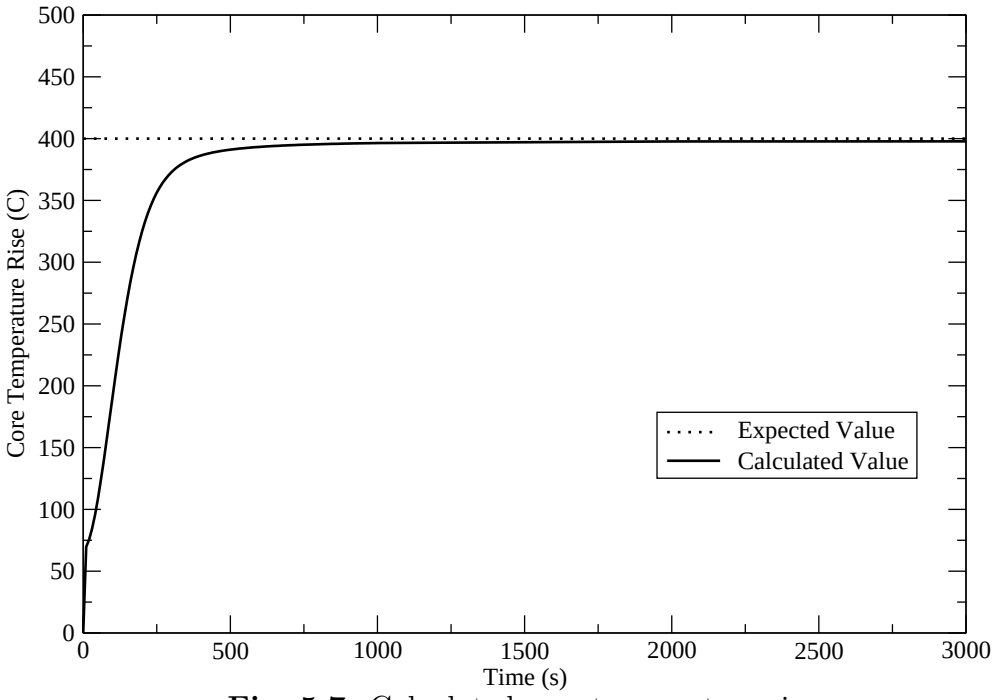

Fig. 5.7. Calculated core temperature rise

(on the order of 20 °C) is low compared with the maximum temperature rise from the coolant to the fuel centerline (on the order of 1000 °C) [80]. In contrast, the temperature rise of the coolant in an HTGR ($\sim$ 400 °C) is significantly higher than the maximum temperature rise from coolant to fuel ($<$ 200 °C) calculated here.

Figure 5.15 compares the radially-averaged axial fuel temperature profile calculated by MELCOR to results from benchmark codes. Each data point represents the average fuel temperature for a given axial level, calculated using a volume-weighted average of fuel temperatures in each radial ring of that axial level. It could be said that, based on the figure, MELCOR results compare well with the benchmark results. However, two comments must be made about this comparison. First, the definition of "fuel" in MELCOR differs from the definition in the benchmark codes. In MELCOR, the entire fueled region of the pebble is considered fuel (FU in MELCOR). In the benchmark codes, "fuel" refers to the UO_2 kernels. The graphite matrix surrounding the TRISO particles, together with the graphite shell surrounding the fueled region,

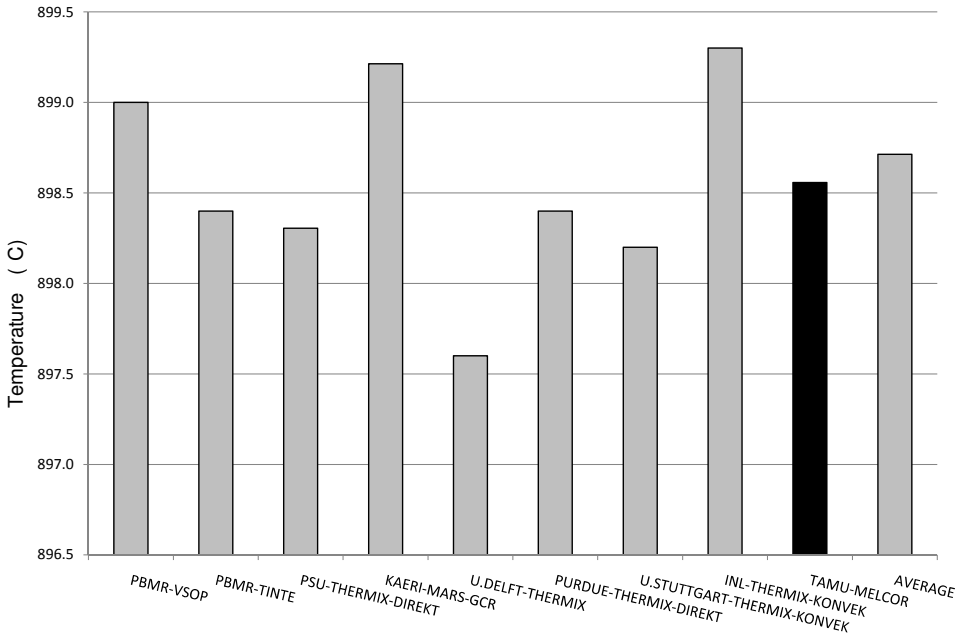

Fig. 5.8. Comparison of calculated steady-state helium outlet temperatures. Results are shown from MELCOR and from the benchmark codes.

is considered the moderator. Figure 5.16 shows the average axial moderator temperatures as calculated by the benchmark codes. MELCOR fuel temperature (TFU) results are presented for comparison.

From Figures 5.15 and 5.16, it is clear that there is a difference of up to about 50 °C between the UO_2 kernel temperature and the moderator temperature. In order to compare MELCOR results to results from the benchmark, average pebble temperatures have been calculated from MELCOR and benchmark results. For MELCOR, the average pebble temperature is calculated using the following formula:

$$T_{avg} = 0.58TFU + 0.42TCL \tag{5.6}$$

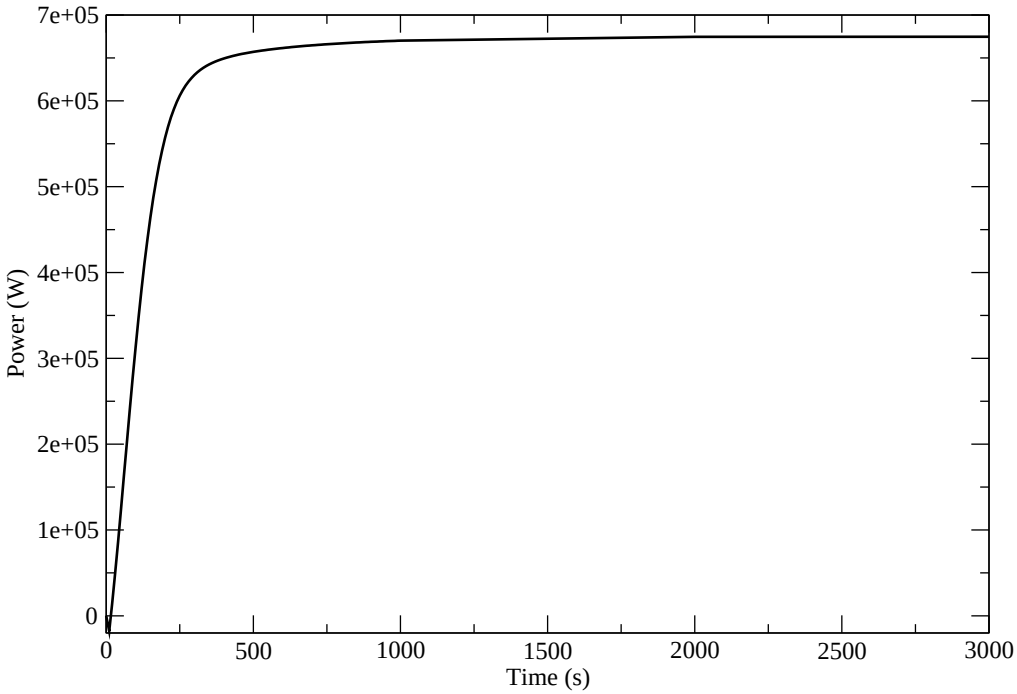

Fig. 5.9. Rate of energy transfer from COR package to HS package

Here, 0.58 and 0.42 are the volume fractions of the fueled and unfueled regions in each pebble. For the benchmark results, the average pebble temperature is as follows:

$$T_{avg} = 0.00868 T_{fuel} + (1 - 0.00868) T_{mod} \tag{5.7}$$

Here, 0.00868 is the volume fraction of UO_2 in each pebble. Results from these calculations are plotted in Figure 5.17. The figure shows that MELCOR results compare well with results from the benchmark codes, once the calculated parameters have been adjusted to match a uniform definition.

As a second comment about the comparison, MELCOR calculations used a convective heat transfer correlation that was modified to fit the form of the equation used by MELCOR. This correlation was used in place of the default correlation, which is inappropriate for this situation for reasons explained in Section 5.4. However, the modified correlation is appropriate only for the specific thermal hydraulic conditions

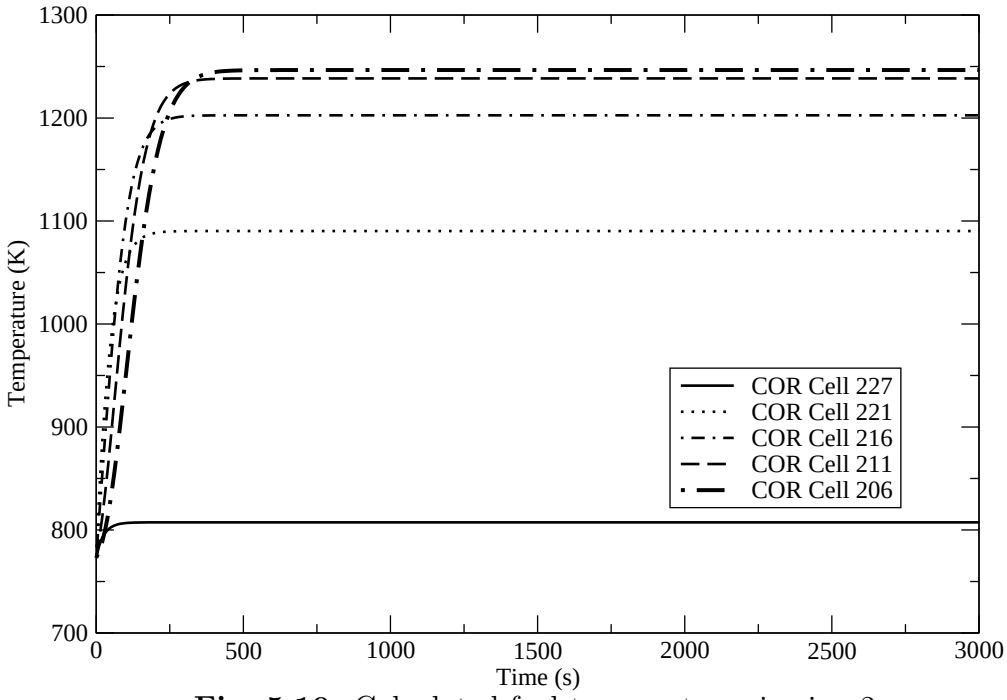

Fig. 5.10. Calculated fuel temperatures in ring 2

found in this problem. A more appropriate convective heat transfer correlation that covers a wider range of conditions should be implemented into MELCOR.

Figures 5.18-5.22 show the axial variation in coolant temperature in rings 2-6. The figures show that temperatures increase with increasing distance from the top of the core. This is to be expected, since the helium is heated along the entire length of the core. Coolant temperatures are highest in ring 2 because the volumetric heat generation rate is highest in ring 2. Note that the coolant exiting the core from ring 2 is at a significantly higher temperature than the reactor outlet temperature. This illustrates the fact that hot jets of coolant may impinge on structures in the lower plenum, such that lower plenum structures may experience temperatures greater than the average core exit temperature. This poses important material qualification concerns that must be addressed in HTGR design.

Figure 5.23 compares radially-averaged coolant temperatures calculated by MELCOR to results from the benchmark. Note that CVH temperatures calculated by

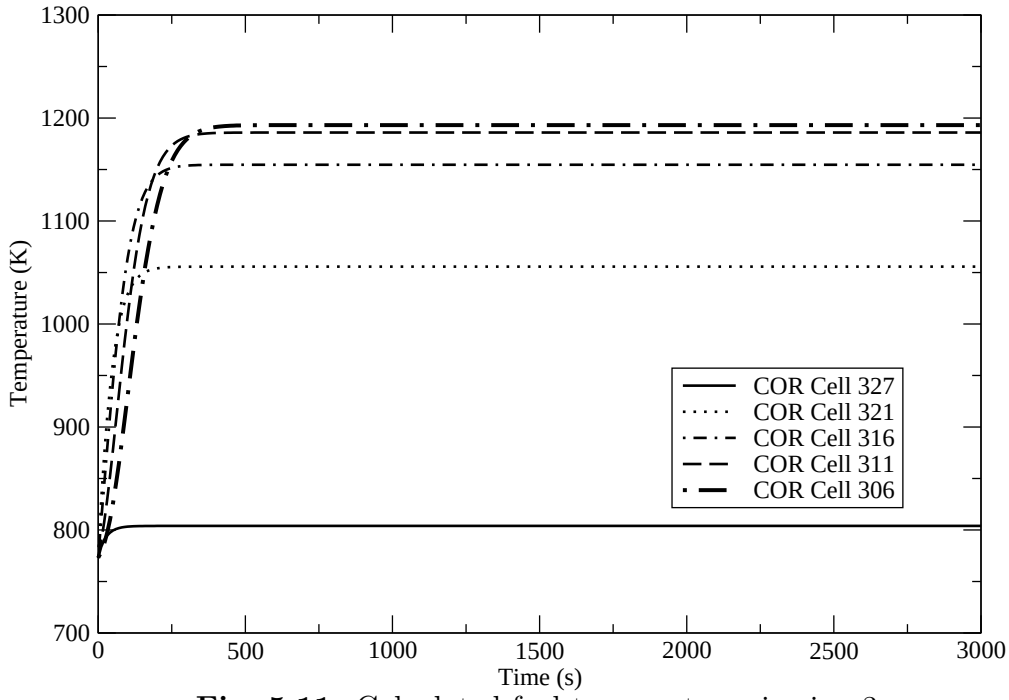

Fig. 5.11. Calculated fuel temperatures in ring 3

MELCOR are not presented along with the benchmark results because there are only 5 CVH volumes in each ring, compared to the 22 volumes per ring used by the benchmark codes. Instead, results from the dT/dz model are presented here. The dT/dz model estimates the local coolant temperature for each COR cell using the average CVH temperature, the flow direction, and the local COR power. The figure shows that coolant temperatures calculated by MELCOR compare well with temperatures reported in the benchmark.

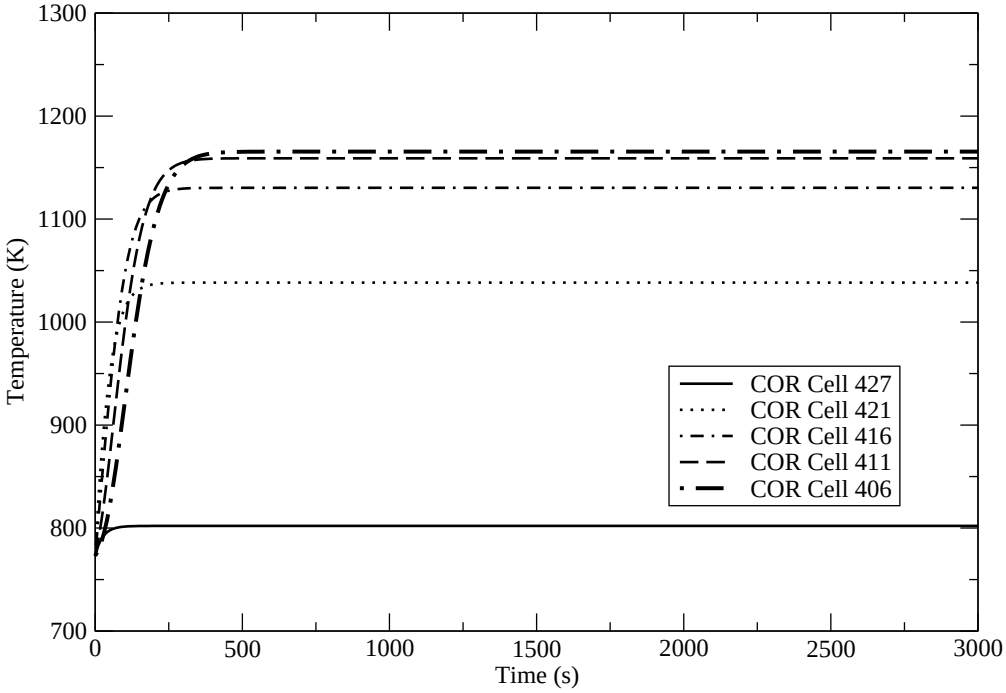

Fig. 5.12. Calculated fuel temperatures in ring 4

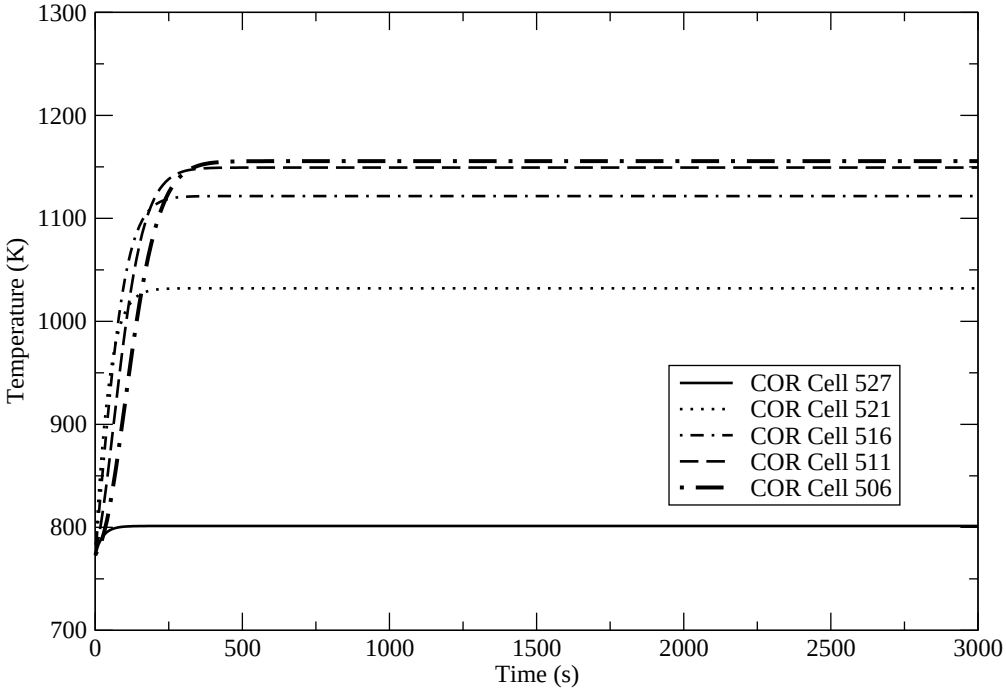

Fig. 5.13. Calculated fuel temperatures in ring 5

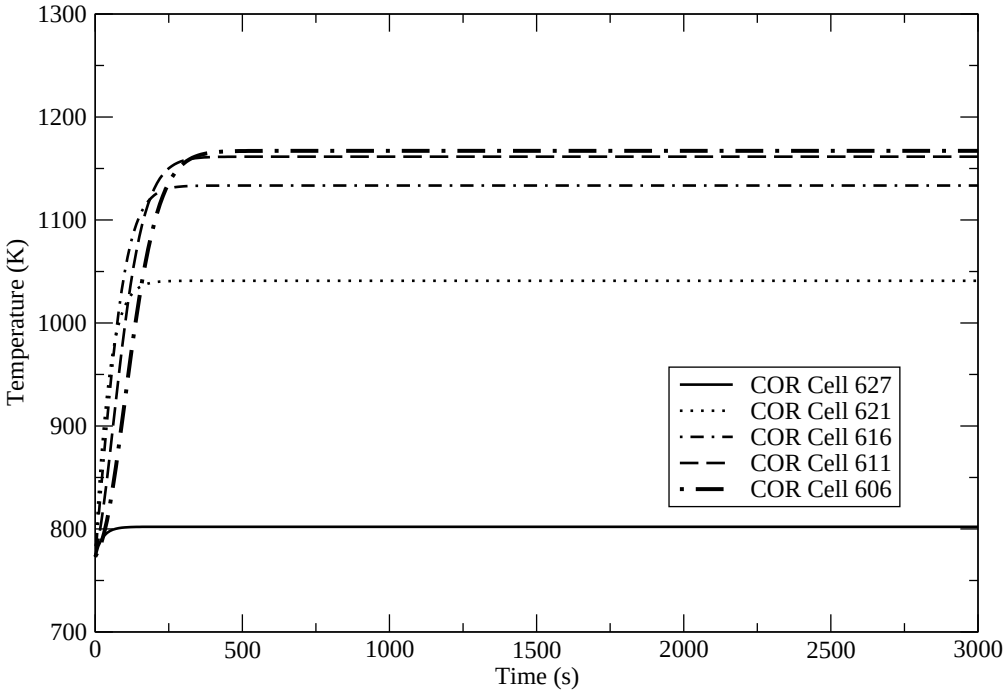

Fig. 5.14. Calculated fuel temperatures in ring 6

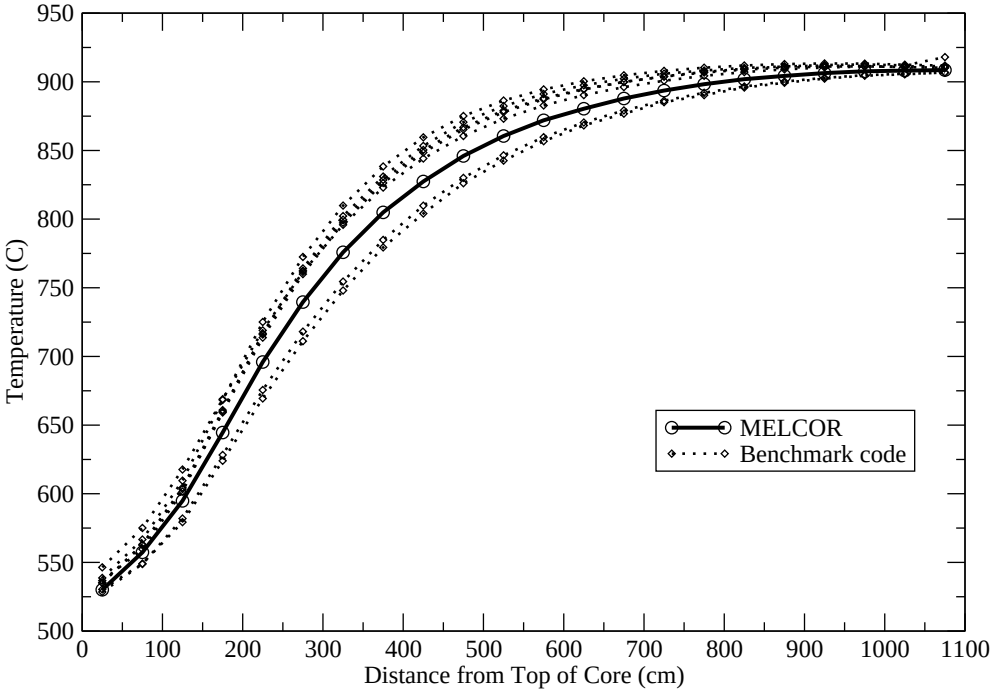

Fig. 5.15. Comparison of calculated average axial fuel temperatures. Results are shown from MELCOR and from the benchmark codes

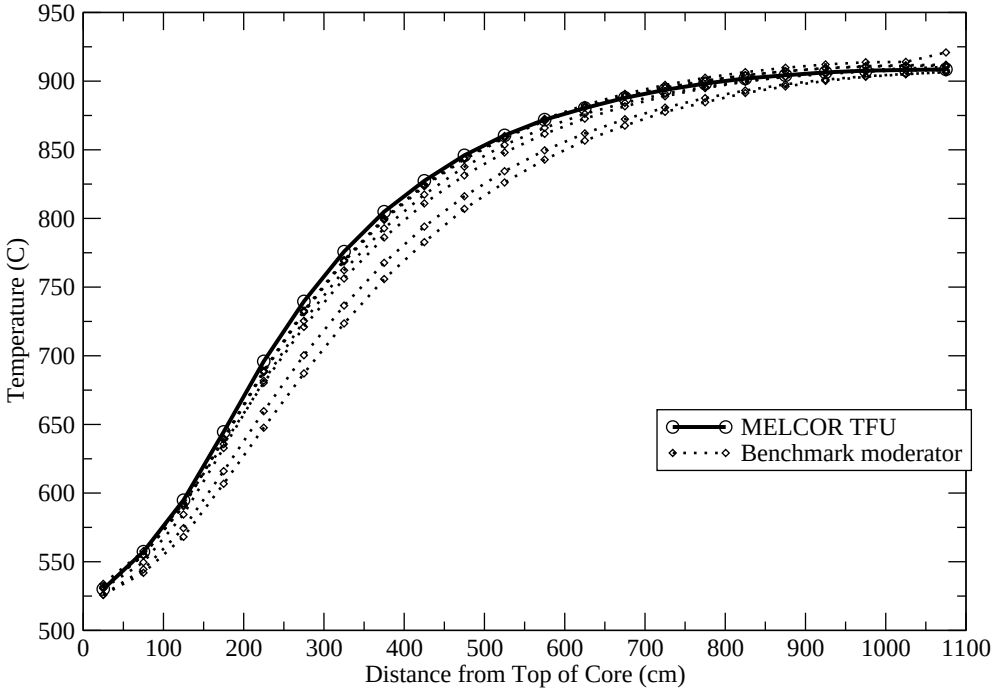

Fig. 5.16. Average axial moderator temperatures calculated by benchmark codes

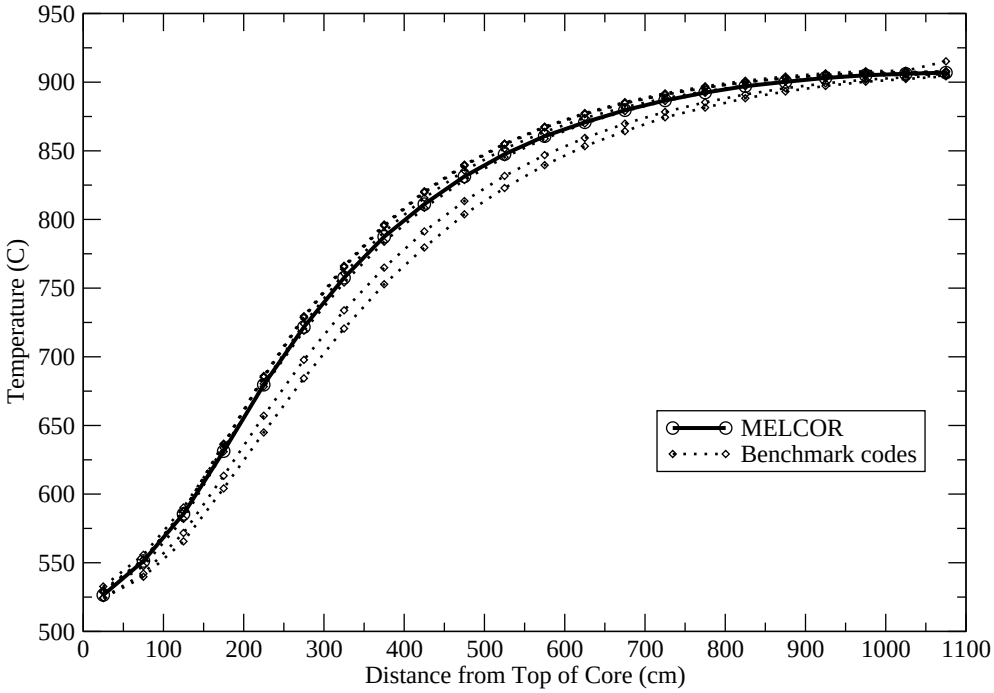

Fig. 5.17. Average pebble temperatures calculated by MELCOR and by benchmark codes

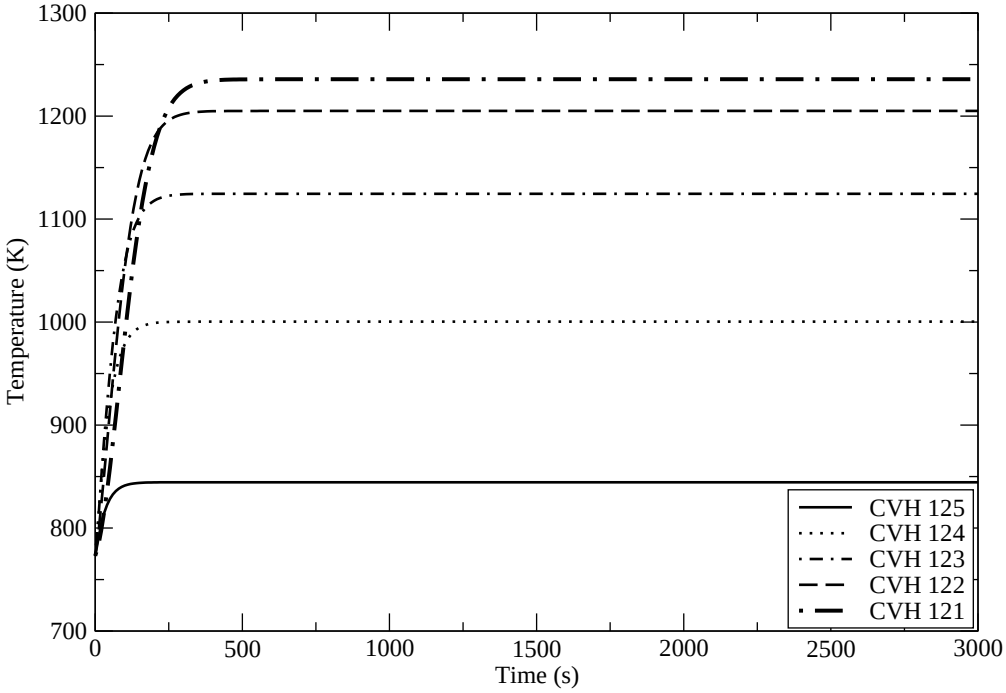

Fig. 5.18. Calculated coolant temperatures in ring 2

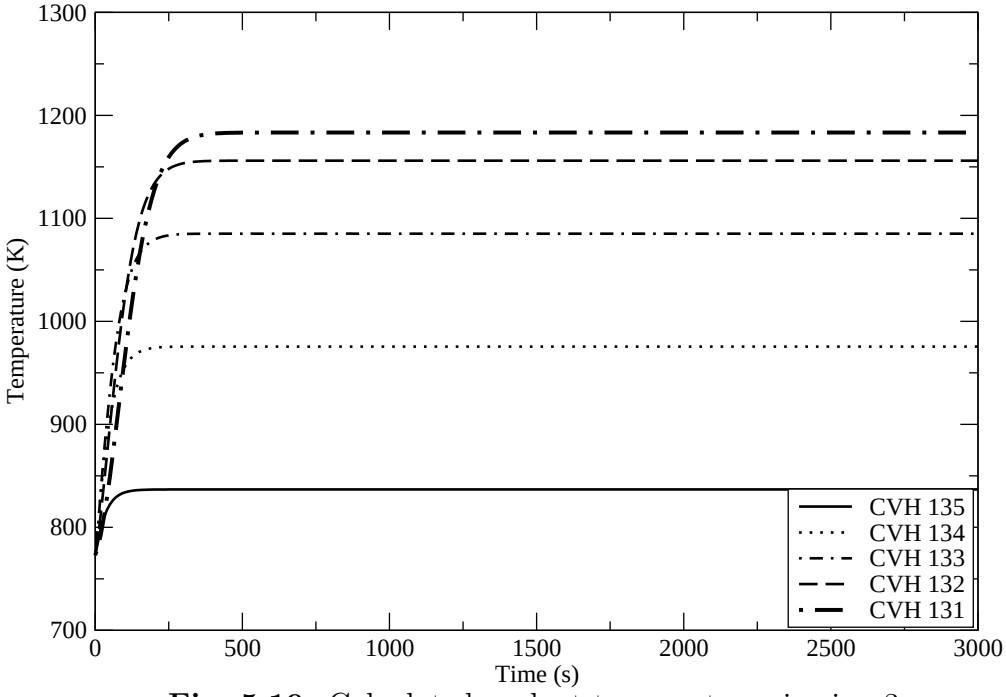

Fig. 5.19. Calculated coolant temperatures in ring 3

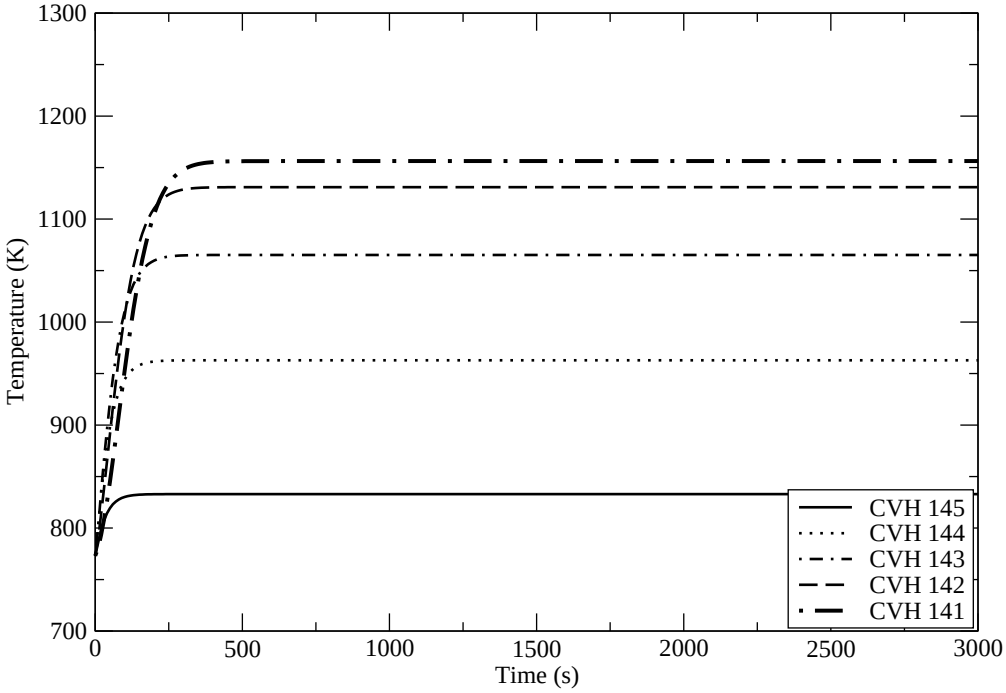

Fig. 5.20. Calculated coolant temperatures in ring 4

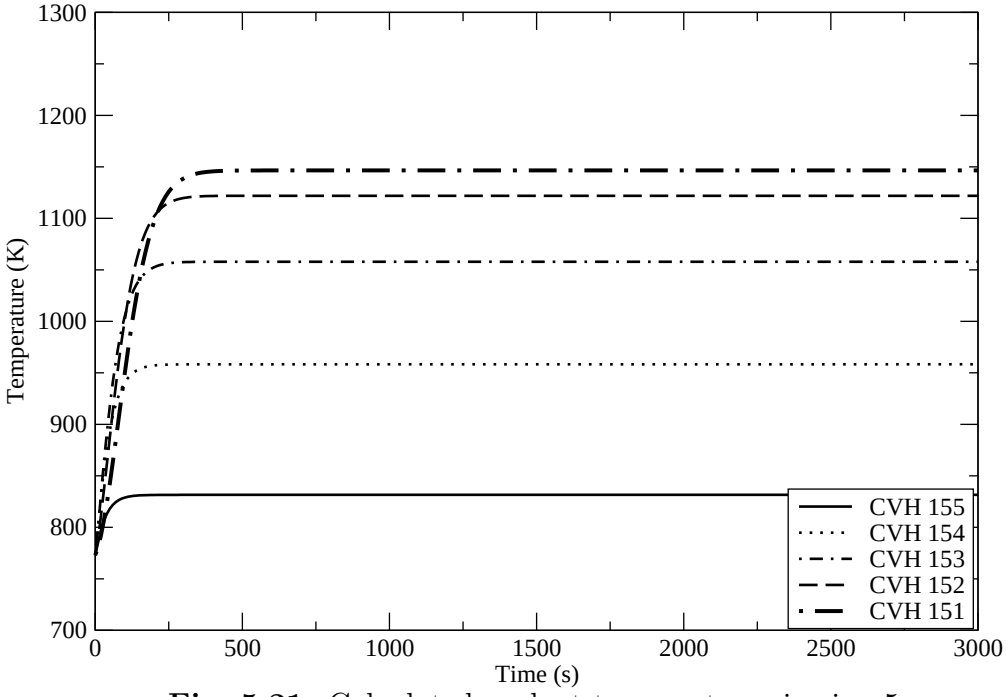

Fig. 5.21. Calculated coolant temperatures in ring 5

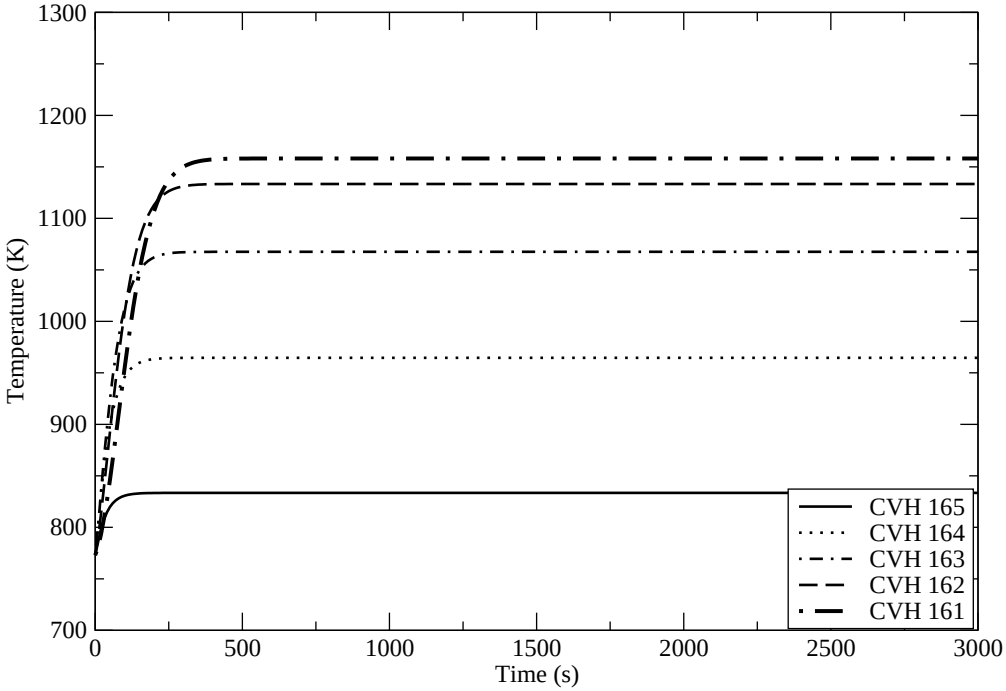

Fig. 5.22. Calculated coolant temperatures in ring 6

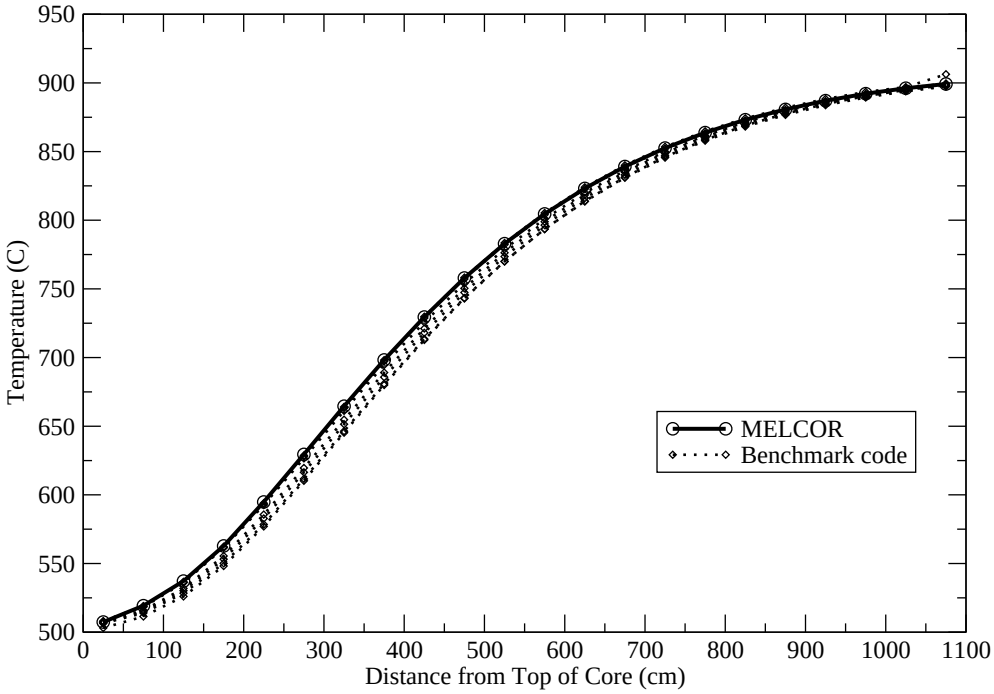

Fig. 5.23. Comparison of calculated average axial coolant temperatures. Results are shown from MELCOR and from the benchmark codes

Core Flow and Pressure Drop

Figures 5.24 and 5.25, respectively, show the pressure drop from the reactor inlet to outlet (CVH181 to CVH210) and from the core inlet to outlet (CVH170 to CVH100). These pressure drops are compared to results from the benchmark codes in Figures 5.26 and 5.27. These figures show that both pressure drops compare well with results from the benchmark codes.

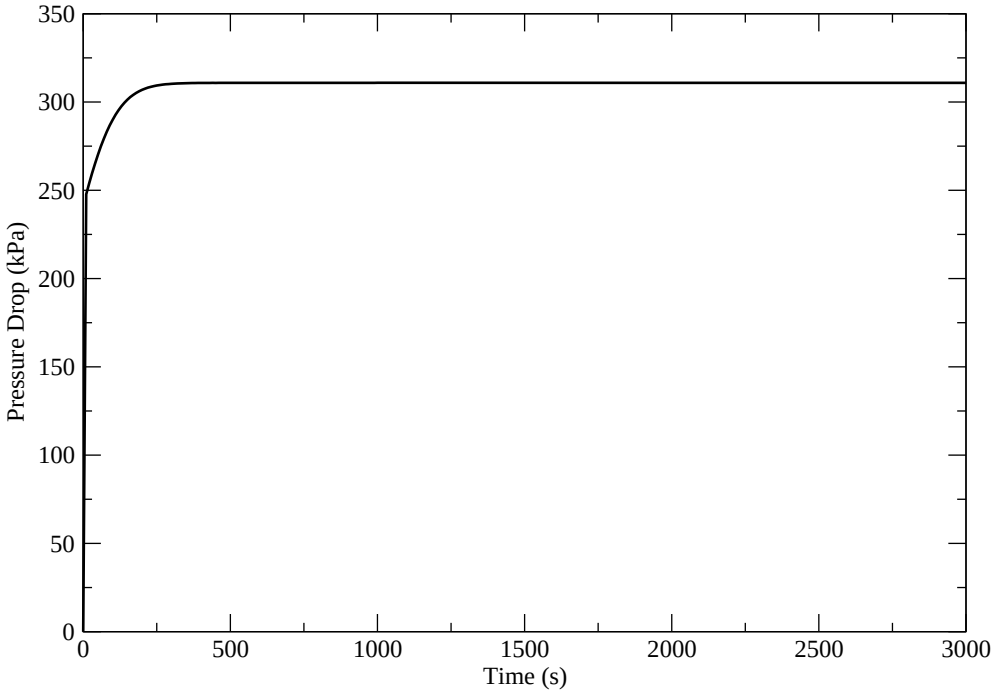

Fig. 5.24. Calculated reactor inlet to outlet pressure drop

In flow through parallel channels, the pressure drop across each channel must be equal [77]. Flow through the PBMR core is analogous to flow through parallel channels in that the pressure drop in each COR ring must be equal to the pressure drop from core inlet to outlet. To meet this requirement, MELCOR adjusts the coolant flow distribution to achieve the same pressure drop from core inlet to outlet for each ring. Radial flow between rings also serves to equalize the pressure drop. Resulting axial mass flux profiles are shown in Figures 5.28-5.32. Radial mass flux

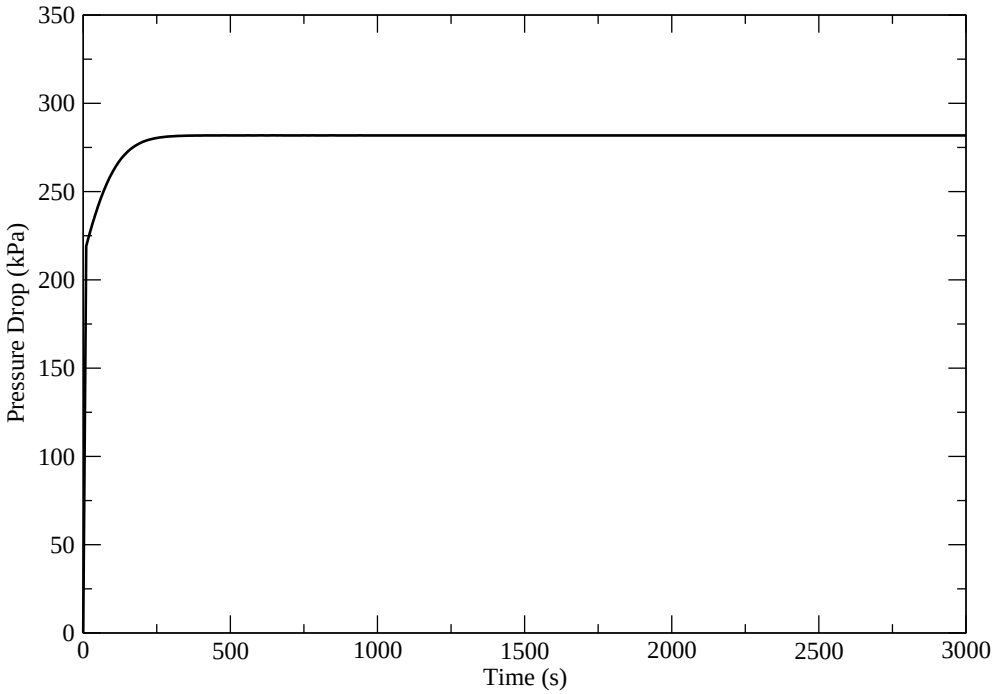

Fig. 5.25. Calculated core inlet to outlet pressure drop

profiles are shown in Figures 5.33-5.37. Fluxes are shown to aid in comparing flow in different radial rings, which have different flow areas. The figures show that the mass flux in rings 2 and 3 decreases slighly with increasing distance from the top of the core. Mass flows outward from rings 2 and 3 to the outer rings of the core. This is because flow resistance increases in rings 2 and 3 due to the increase in gas velocity with temperature. Thus, to equalize the pressure drop across the core, mass flows out of rings 2 and 3 to decrease the frictional pressure losses in rings 2 and 3. Note that the radial mass flux is very small compared to the axial mass flux. This is due to the fact that the axial pressure gradient is much greater than the radial pressure gradient. Low radial mass flow rates were also calculated by the benchmark codes.

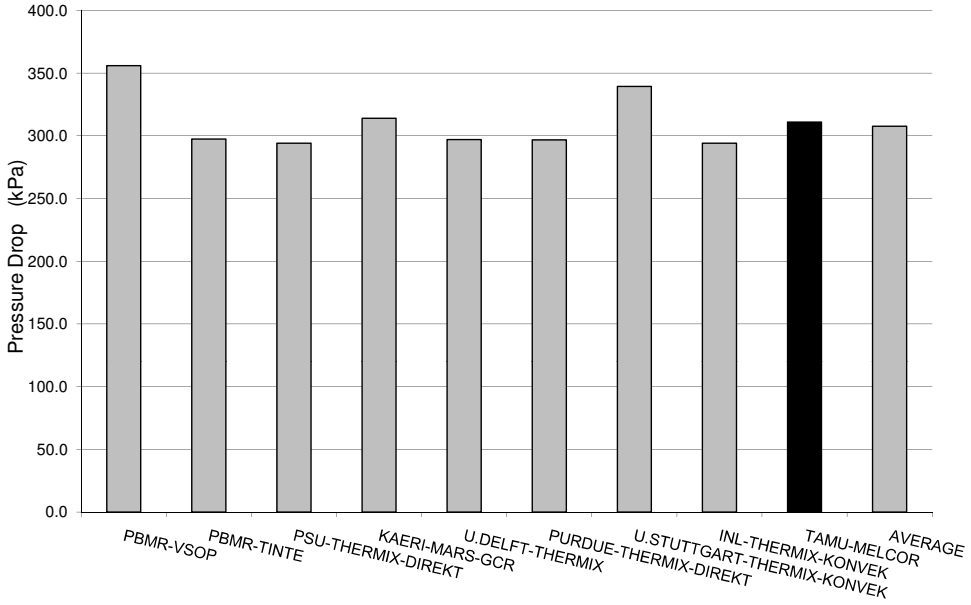

Fig. 5.26. Comparison of reactor inlet-to-outlet pressure drop. Results are shown from MELCOR and from the benchmark codes

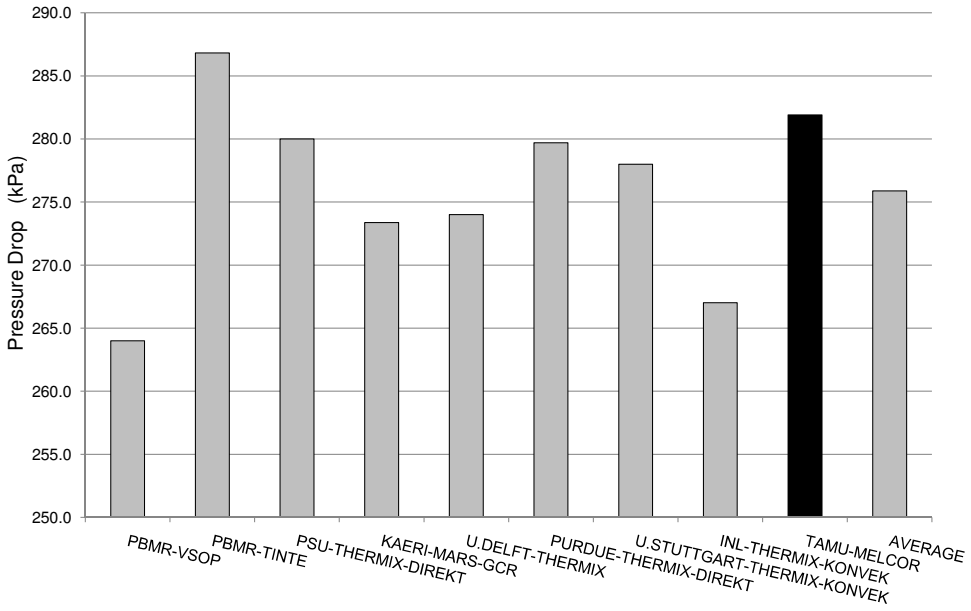

Fig. 5.27. Comparison of core inlet-to-outlet pressure drop. Results are shown from MELCOR and from the benchmark codes

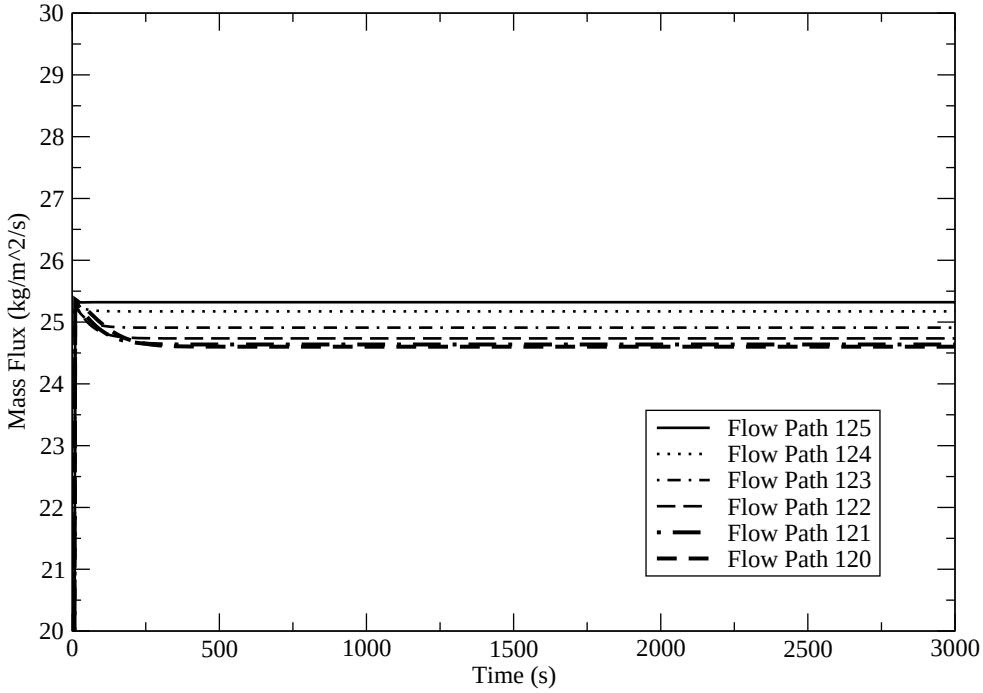

Fig. 5.28. Calculated coolant axial mass fluxes in ring 2

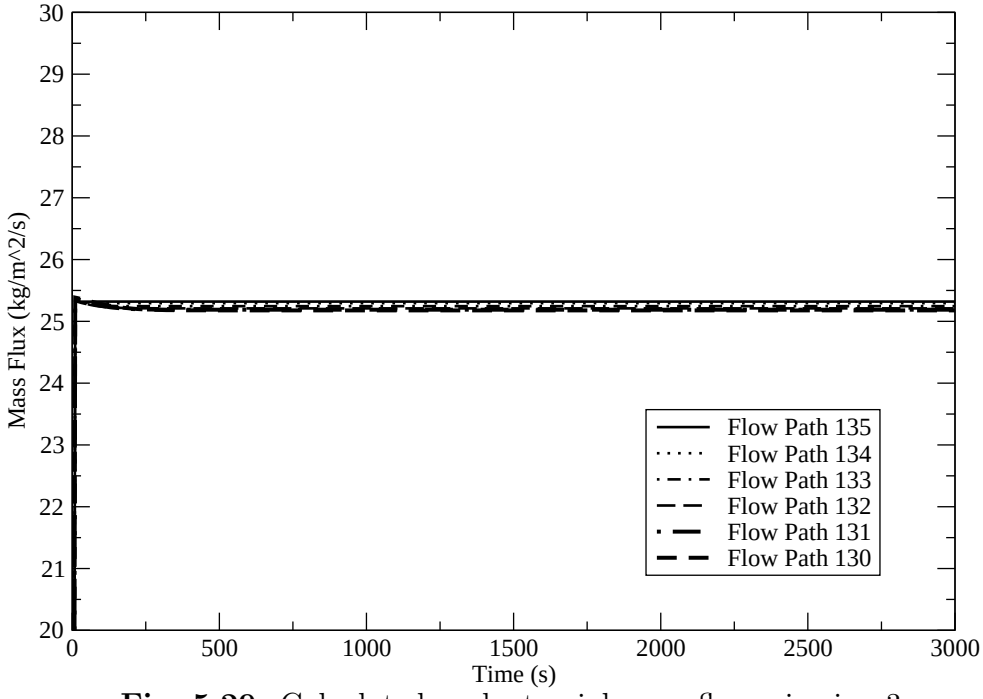

Fig. 5.29. Calculated coolant axial mass fluxes in ring 3

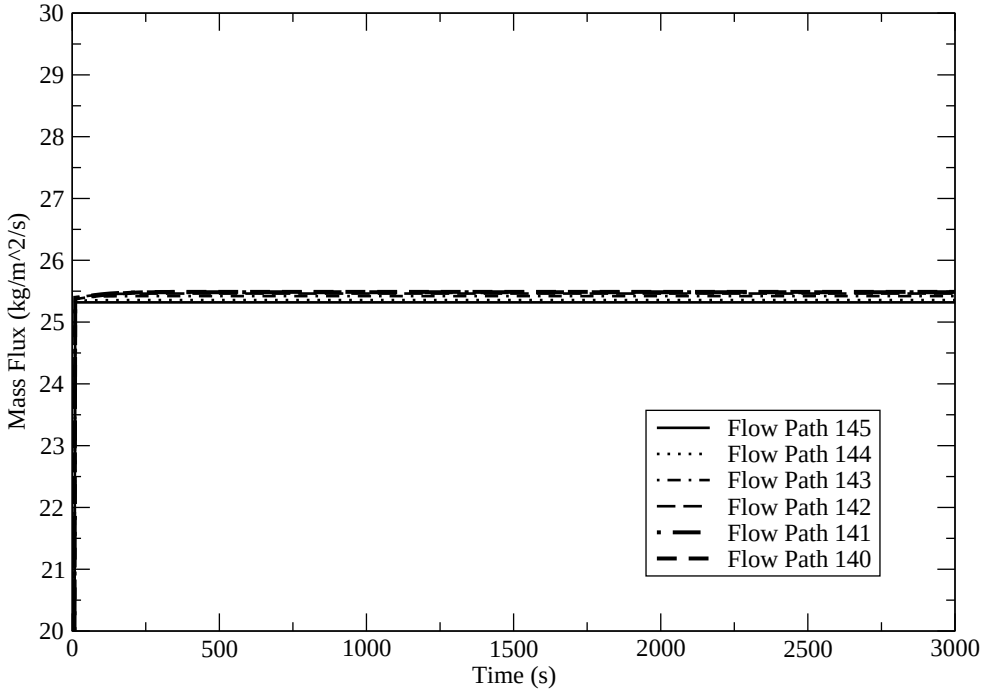

Fig. 5.30. Calculated coolant axial mass fluxes in ring 4

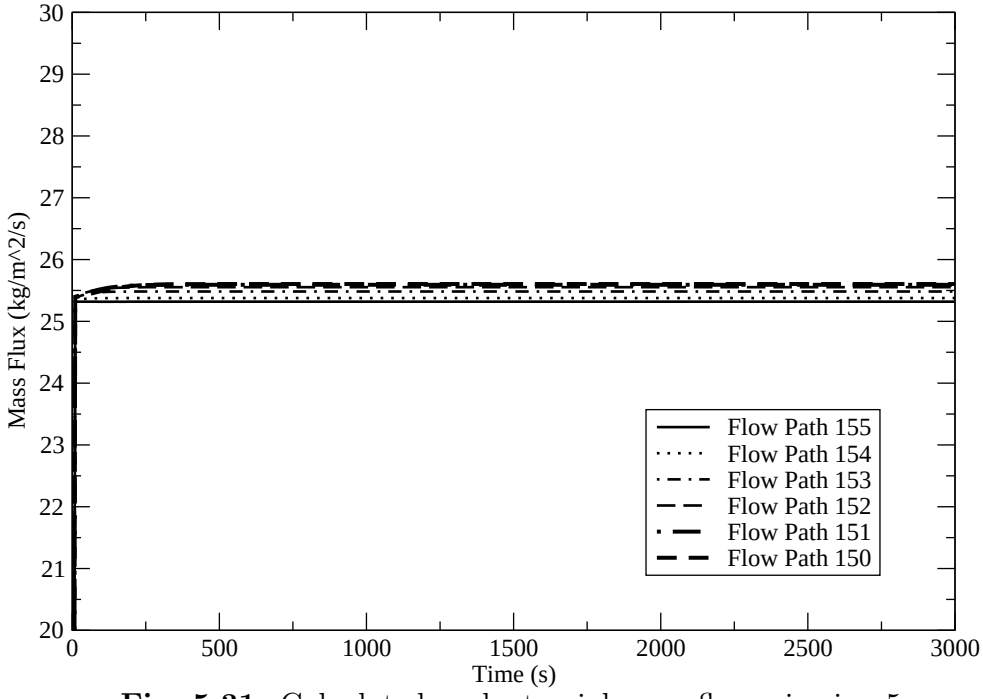

Fig. 5.31. Calculated coolant axial mass fluxes in ring 5

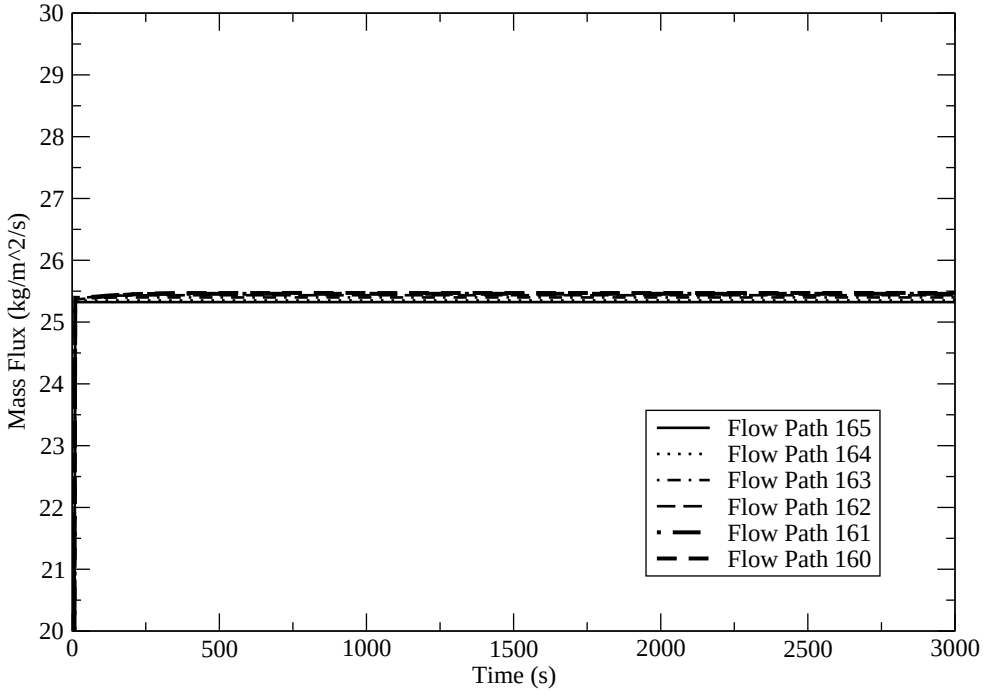

Fig. 5.32. Calculated coolant axial mass fluxes in ring 6

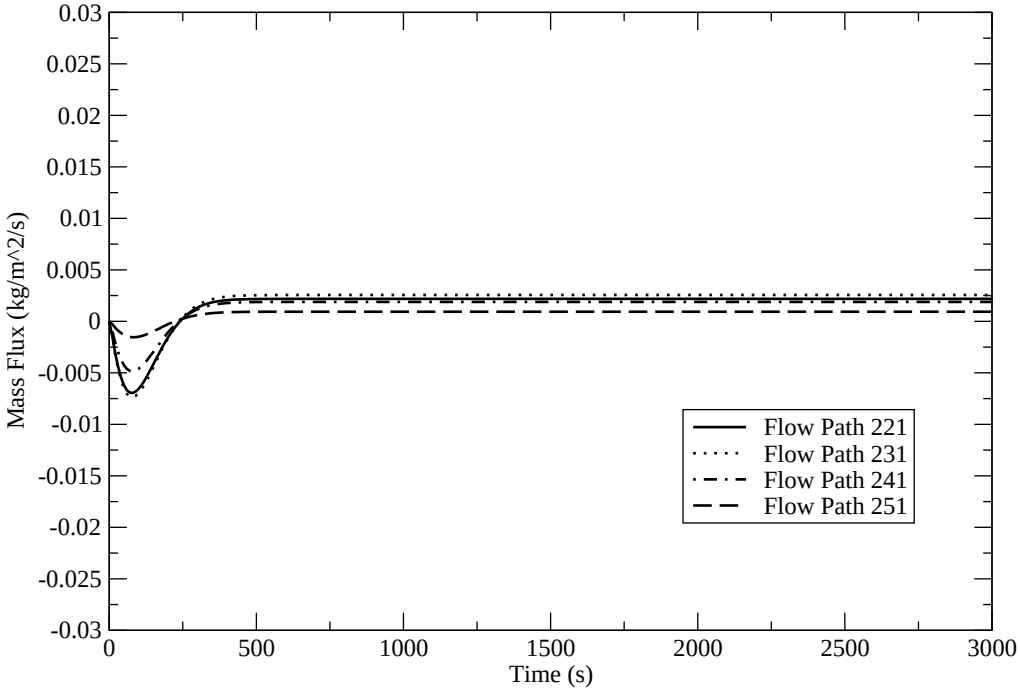

Fig. 5.33. Calculated coolant radial mass fluxes in FL2n1

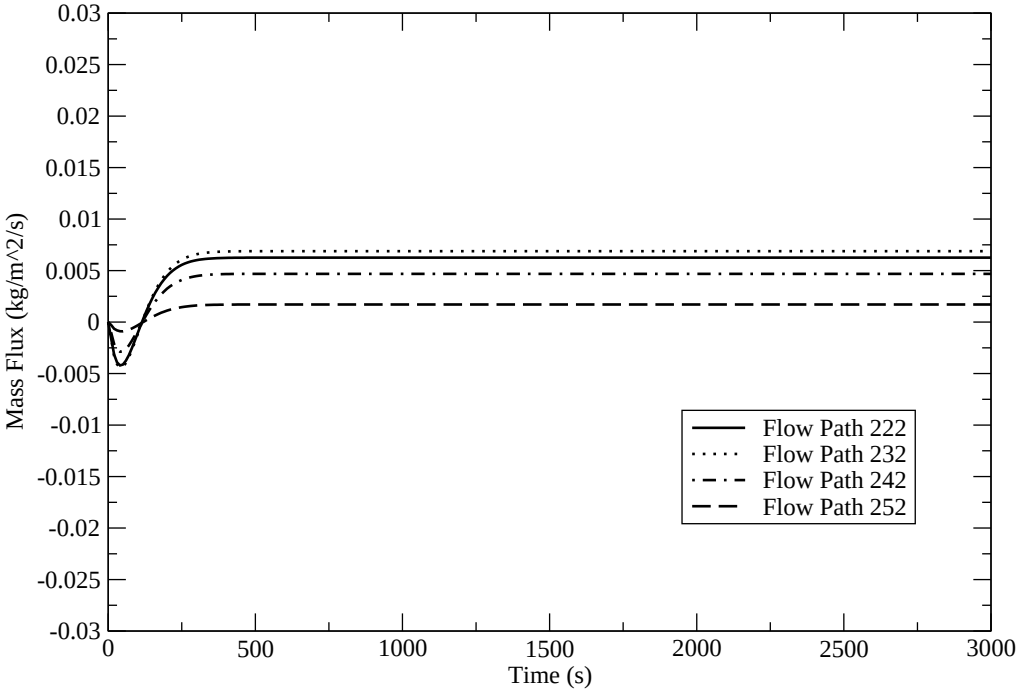

Fig. 5.34. Calculated coolant radial mass fluxes in FL2n2

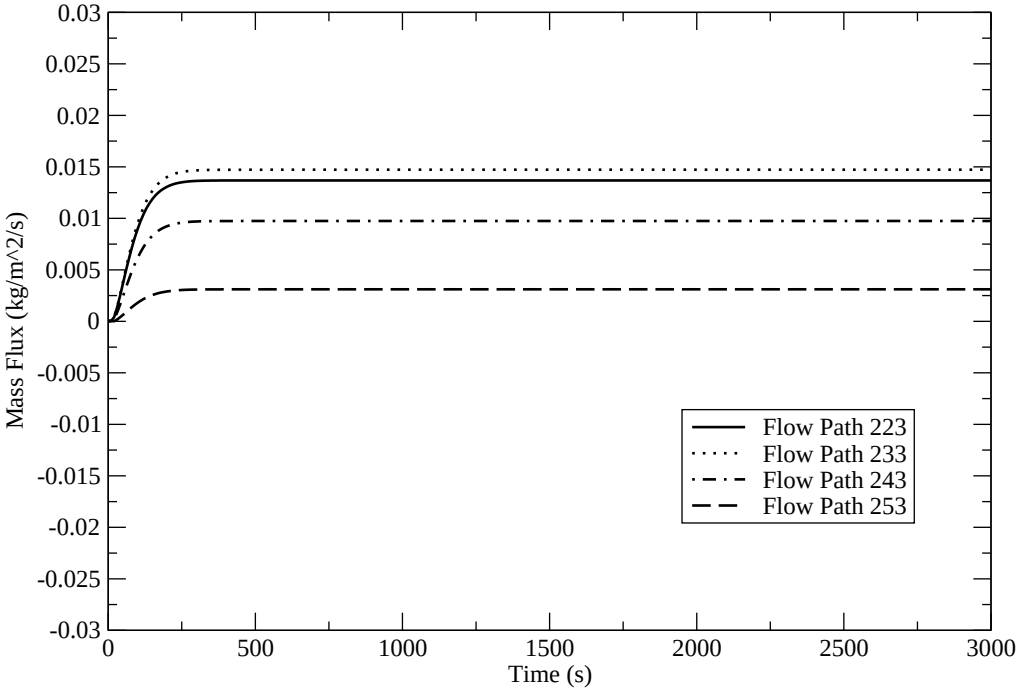

Fig. 5.35. Calculated coolant radial mass fluxes in FL2n3

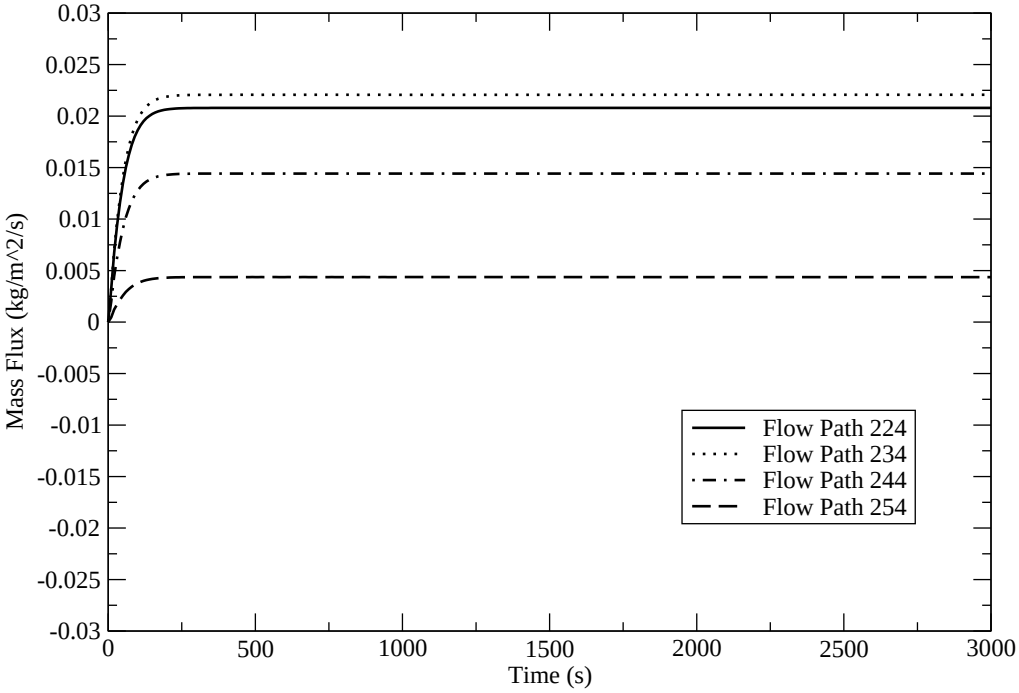

Fig. 5.36. Calculated coolant radial mass fluxes in FL2n4

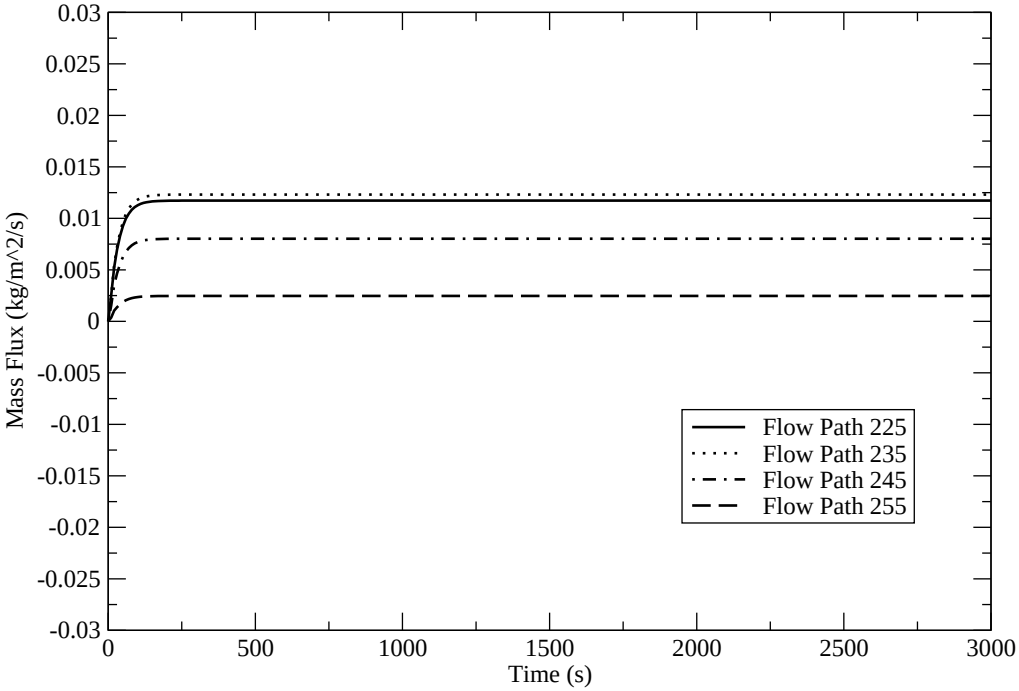

Fig. 5.37. Calculated coolant radial mass fluxes in FL2n5

5.5.2 Pressurized Loss of Forced Cooling Results

MELCOR was run using the PLOFC transient input deck. The calculation was performed for 50 hours per the benchmark specifications.

Figure 5.38 shows that the mass flow into the reactor decreases linearly from 192.7 kg/s to 0 kg/s over the first 13 s of the transient. Figure 5.39 shows that the inlet and outlet pressure decrease linearly to 6 MPa over the same time period. Figure 5.40 shows that the reactor is tripped on a zero mass flow condition, and power switches from constant fission power to decay power. Figure 5.41 compares the decay power profile implemented in MELCOR to the decay power profile in the benchmark. Together, these figures verify that the decay heat profile and control logic for this transient have been implemented correctly.

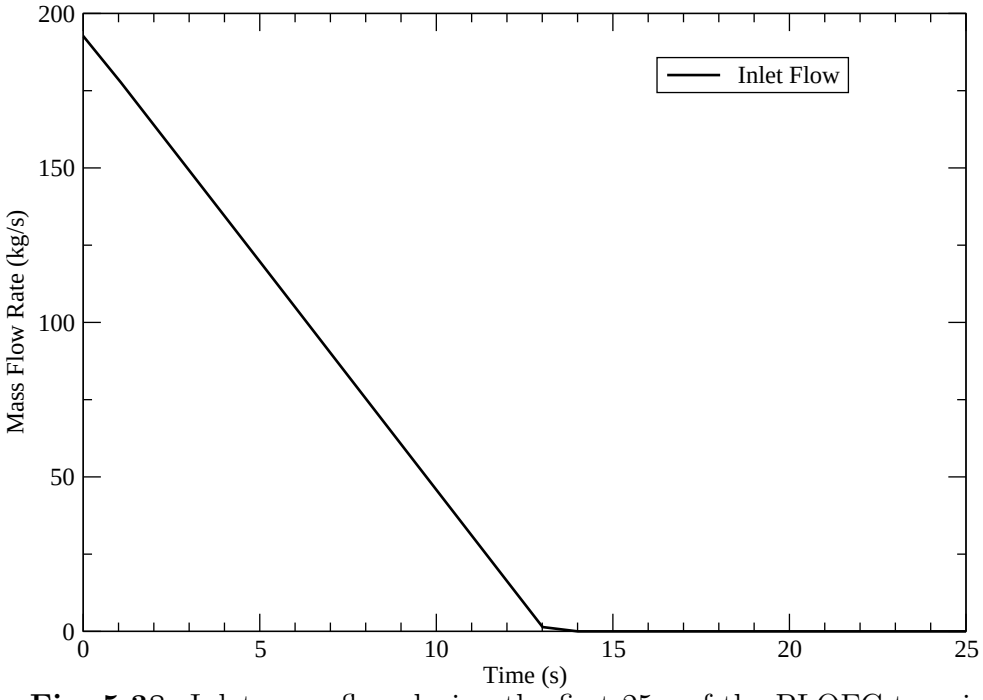

Fig. 5.38. Inlet mass flow during the first 25 s of the PLOFC transient

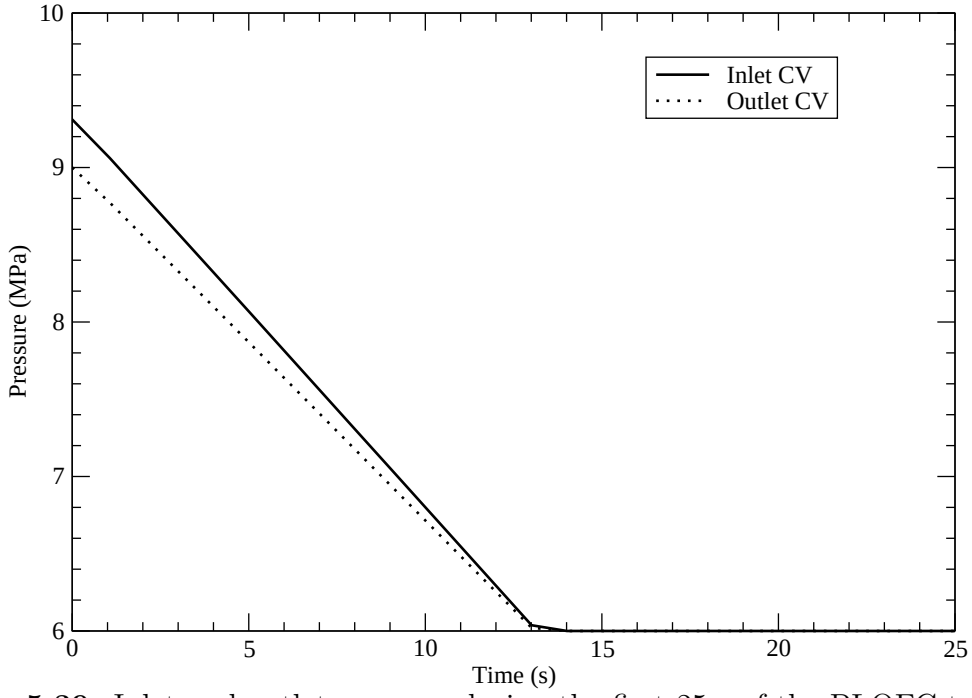

Fig. 5.39. Inlet and outlet pressure during the first 25 s of the PLOFC transient

Core Temperatures

Figure 5.42 shows the fuel temperature behavior in ring 2. Fuel near the top of the core heats up rapidly, reaching a maximum at about 15 h. The rapid heatup is due to the combined effects of high power in the top half of the core and no coolant flow. After reaching a maximum, temperatures gradually decrease. Fuel temperatures near the bottom of the core are approximately constant throughout the transient due to the low power density at the bottom of the core. This general behavior is seen in each core ring.

Figures 5.43-5.47 show snapshots of fuel temperatures at several times during the transient. The figures show that maximum temperatures shift from the bottom of the core to the point at which power is highest, in levels 21 and 22 of ring 2. The radial profile assumes a parabolic shape, which is characteristic of heat conduction in cylinders. This shows that the radial temperature profile is reasonable. However,

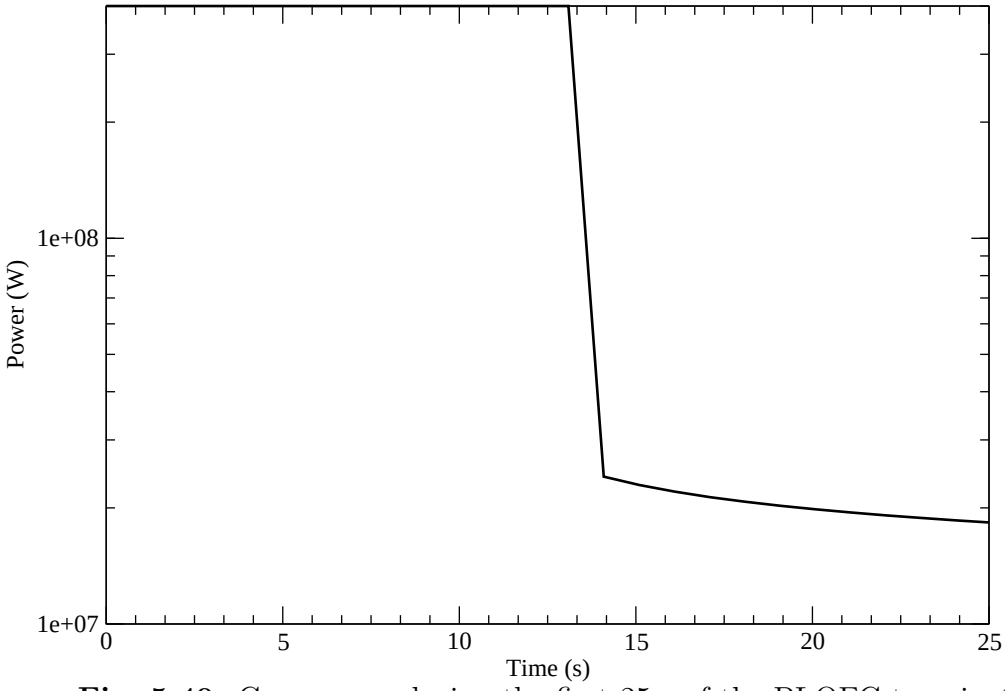

Fig. 5.40. Core power during the first 25 s of the PLOFC transient

the graphs also display step-like axial temperature variations. The step-like increases are prominent at the interfaces between two control volumes. It is clear by looking at the axial power profile in Figure 5.2 that this behavior is not related to the axial power profile, which has a smoother shape.

The most likely explanation for this behavior is that the dT/dz model in MELCOR is incorrectly estimating local coolant temperatures. Initial transient calculations showed more pronounced temperature discontinuities between adjacent axial levels in neighboring control volumes. The large discontinuities were due to the fact that control functions specified that flow was moving downward in each cell. This is correct for steady-state calculations, but during transients, natural circulation flow may develop in the reactor, causing flow to be upward in some rings and downward in others. The code developers at Sandia National Laboratories suggested defining separate control functions to specify the flow direction for each radial ring. This was done by tying the flow direction used for the dT/dz model to the direction of flow

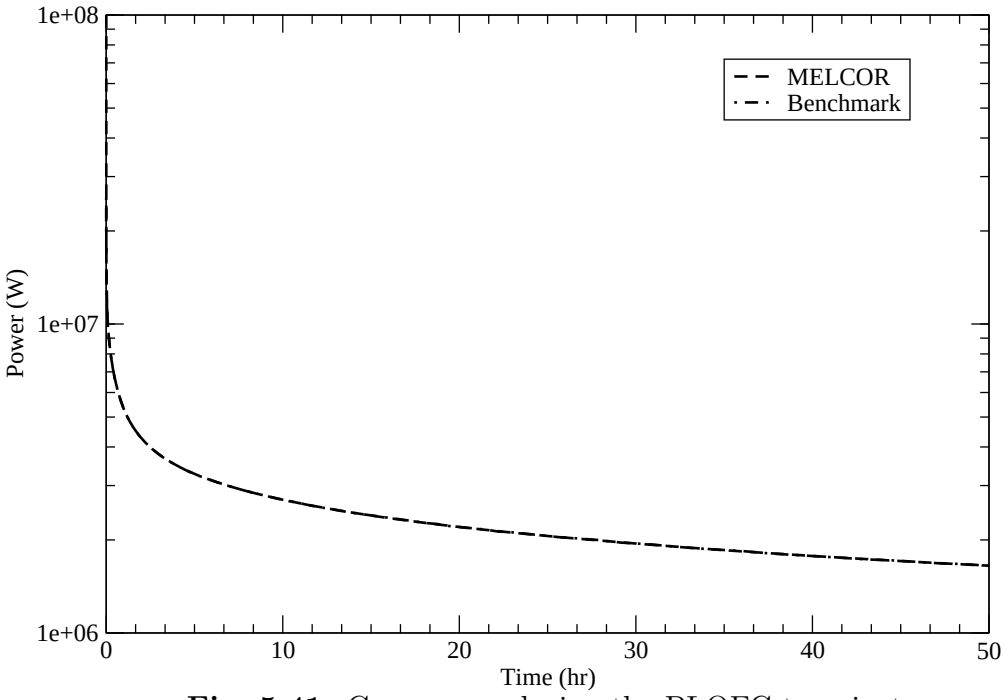

Fig. 5.41. Core power during the PLOFC transient

in the flow paths from CVH170. This alleviated the problem but did not correct it entirely.

Temperatures calculated by MELCOR are higher than those presented in the benchmark, and are in fact above the 1600 °C design limit for TRISO fuel. This can be seen by comparing the MELCOR results shown in Figure 5.48 to results from the benchmark in Figure 5.49. As evidenced by Figure 5.41, the discrepancy in fuel temperatures is not a result of a difference in the decay heat profile. It may be due to a difference between the packed bed natural convection heat transfer correlation used in MELCOR and the correlations used in the benchmark results. Coolant temperature results from the benchmark were unavailable for this activity, so this hypothesis cannot be verified.

Other possible explanations for the higher temperatures calculated by MELCOR are presented in the following sections.

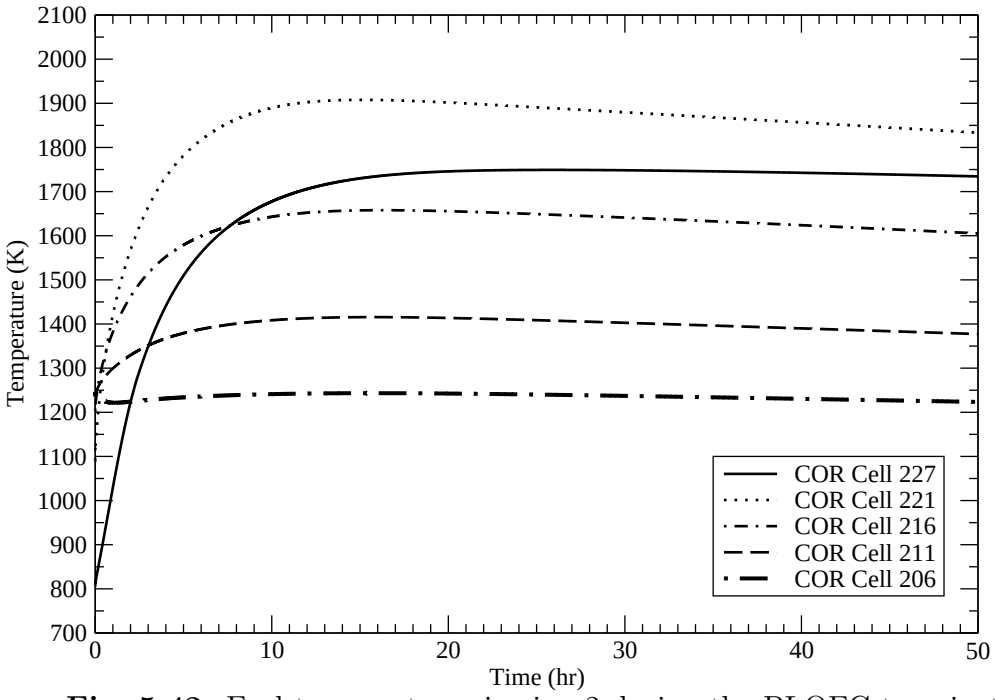

Fig. 5.42. Fuel temperatures in ring 2 during the PLOFC transient

Core Flow

Figures 5.50-5.54 show the coolant axial mass flow in rings 2-6 during the PLOFC transient. Note that flow is plotted in terms of g/s, as opposed to kg/s, due to the low natural circulation flows. The negative flow rates in rings 2-4 indicate that helium is flowing upward through the core. This is expected, since temperatures are higher in rings 2-4 than in rings 5-6. The higher temperatures cause the heat helium to rise through these rings to the void region above the core. This buoyancy force results in the natural circulation flow pattern shown in the figures, where coolant flows upward from the outlet plenum through rings 2-4 to the void above the core, and from this void downward through rings 5-6 back to the outlet plenum. The bulk mass flow rate in either direction is approximately 140 g/s. This compares reasonably well with the benchmark results, where calculated mass flow rates ranged from 10-130 g/s [81].

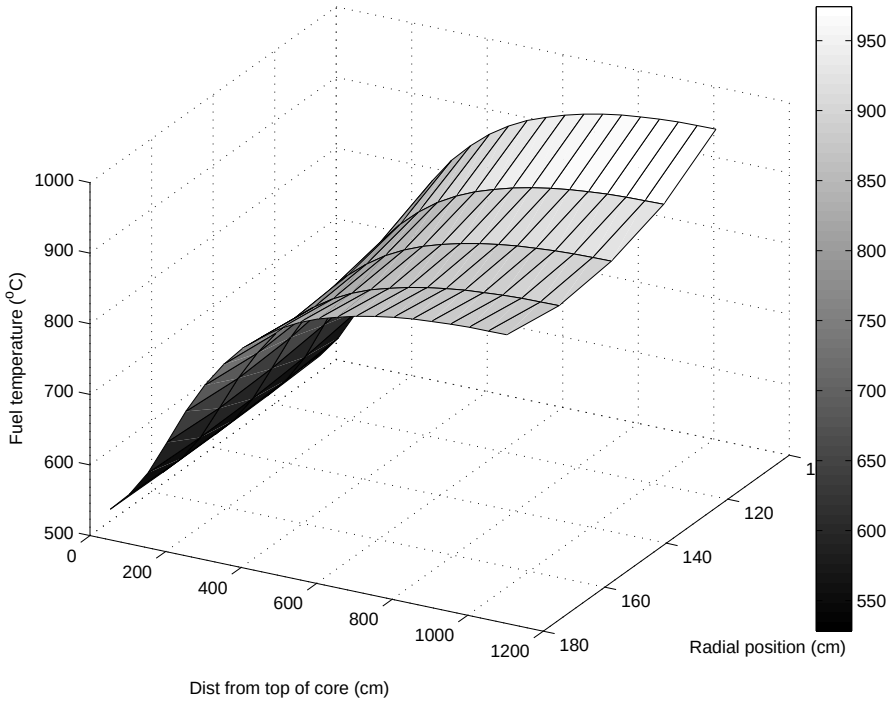

Fig. 5.43. Fuel temperatures at the start of the PLOFC transient

The temperature of helium exiting rings 2-4 is up to 1550 °C. Hot jets from the core impinge on structures in the upper plenum and could potentially melt control rod drive mechanisms. This is significant because it could result in a loss of control rod functionality, which is a major safety concern.

Figures 5.55-5.59 show radial mass flow rates in the core. The figures show that the largest radial flow rates occur at the bottom of the pebble bed core. Coolant primarily flows from ring 2 outward. This result makes sense, since flow resistance is greater in ring 2 due to higher coolant temperatures and, thus, higher velocity. Coolant flows from ring 2 in order to balance the pressure drop across the pebble bed. Note that there is little flow toward the center of the core shown in the graphs. This is because the outlet plenum is modeled as a single control volume. Once flow from rings 5-6 enters the outlet plenum, it is available to flow upward through rings 2-4. The same is true of the void above the core; coolant from rings 2-4 that enters the void is immediately available to flow down through rings 5-6. Radial flow patterns

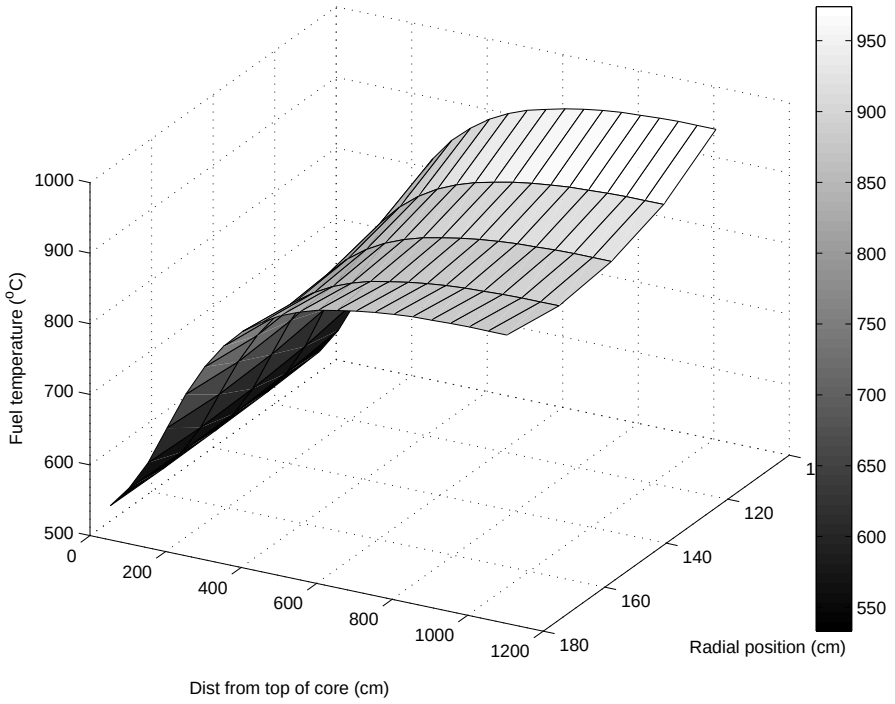

Fig. 5.44. Fuel temperatures at 13 s after start of PLOFC

are not reported in the benchmark documents, and so it is unknown how MELCOR results compare to benchmark results in this respect.

Radiation Heat Transfer to the RCCS

Figure 5.60 shows the total radiation heat removal rate from the RPV. The heat removal rate predicted by MELCOR is significantly lower than the values calculated by the benchmark codes. This would explain why MELCOR fuel temperatures are above the 1600 °C design limit. The reason for this discrepancy must be investigated further.

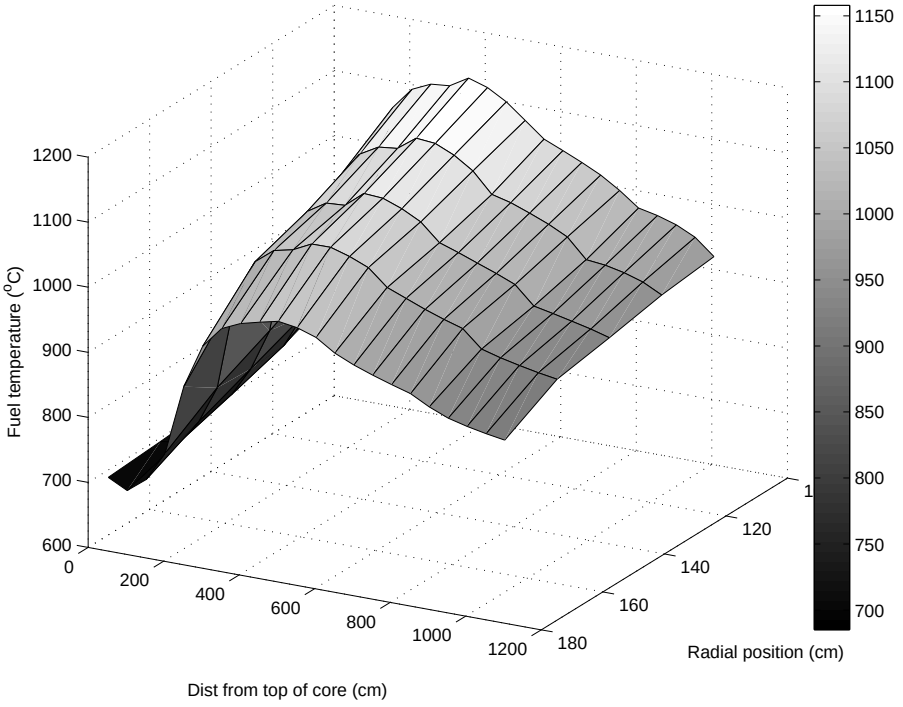

Fig. 5.45. Fuel temperatures at 1 hr after start of PLOFC

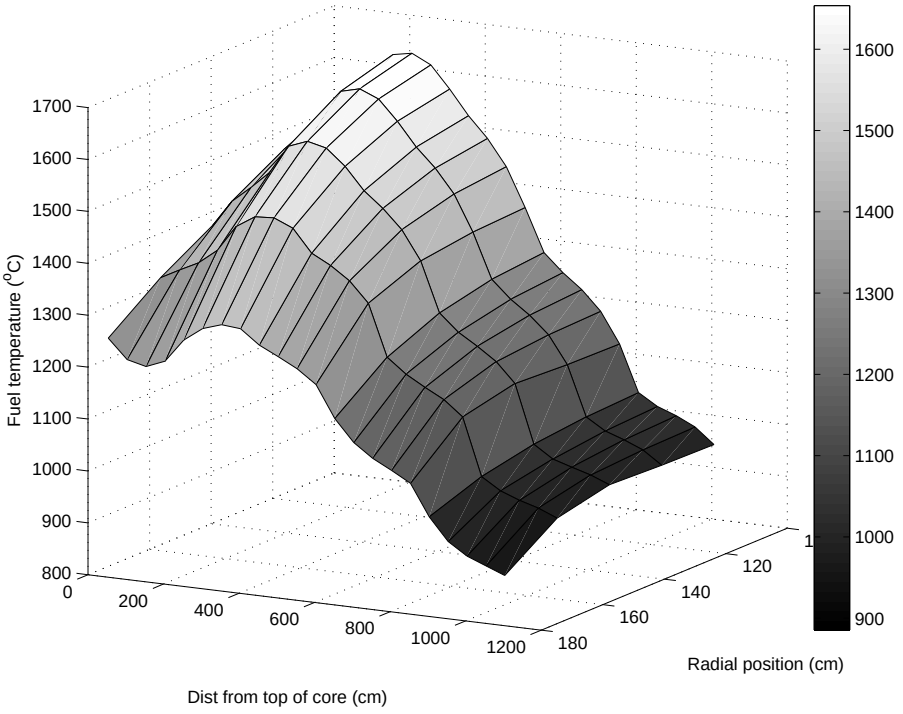

Fig. 5.46. Fuel temperatures at 15 hr after start of PLOFC

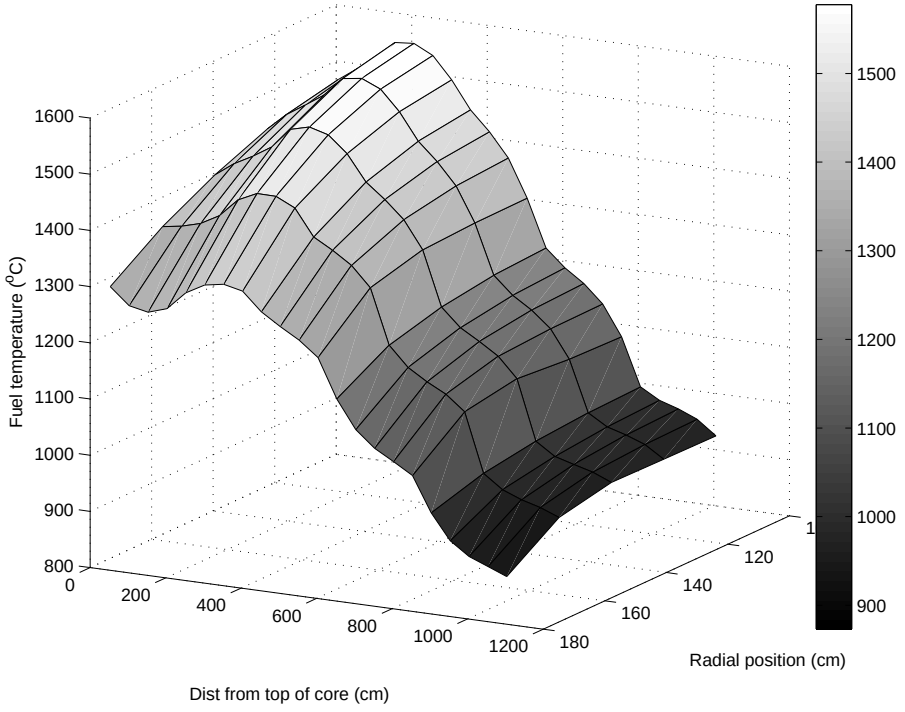

Fig. 5.47. Fuel temperatures at 50 hr after start of PLOFC

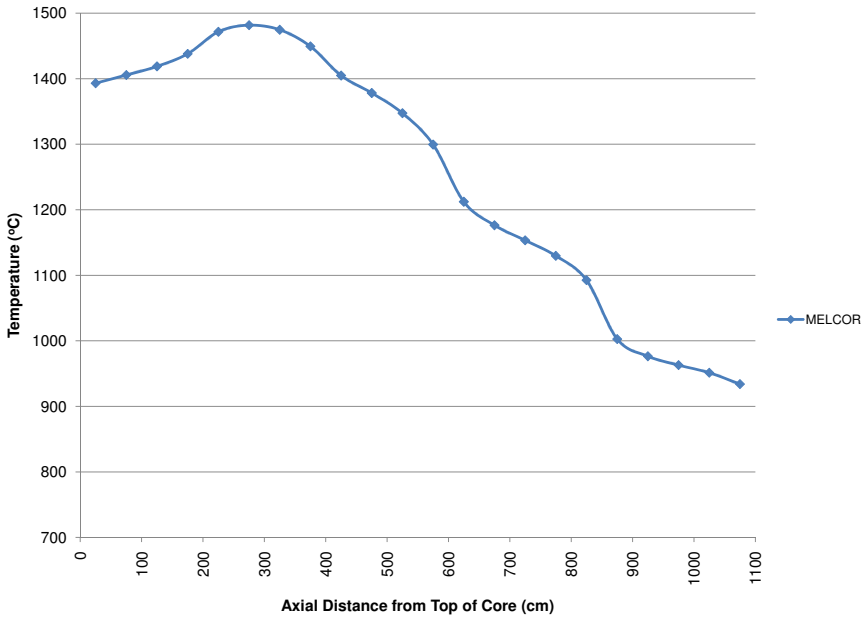

Fig. 5.48. Average axial fuel temperatures at 50 hr after start of PLOFC calculated by MELCOR

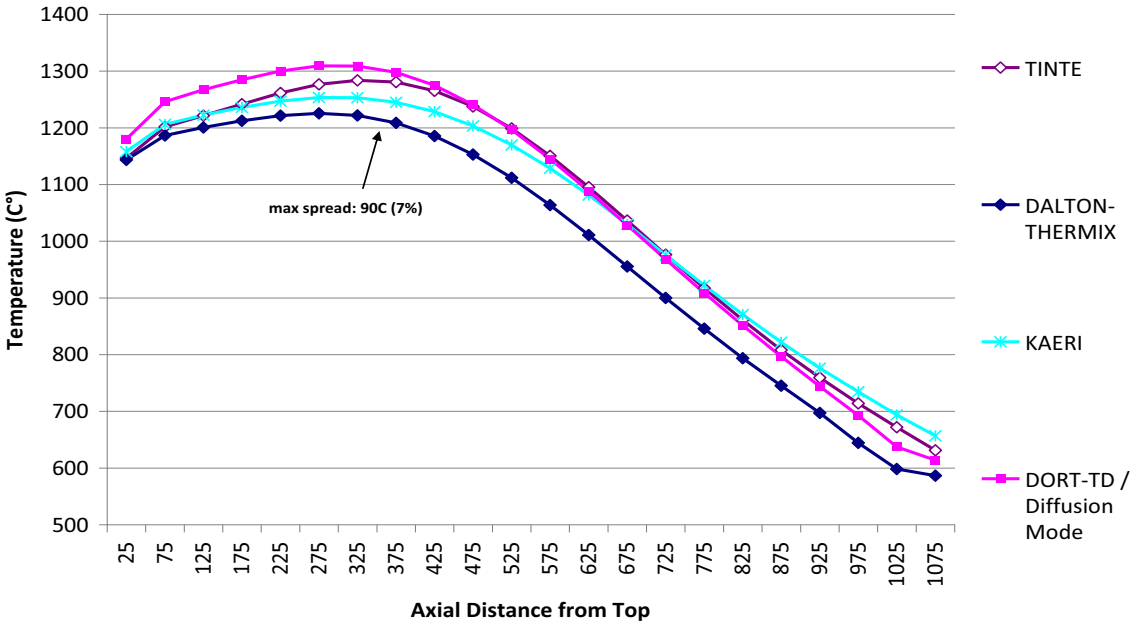

Fig. 5.49. Average axial fuel temperatures at 50 hr after start of PLOFC calculated by the benchmark codes [81]

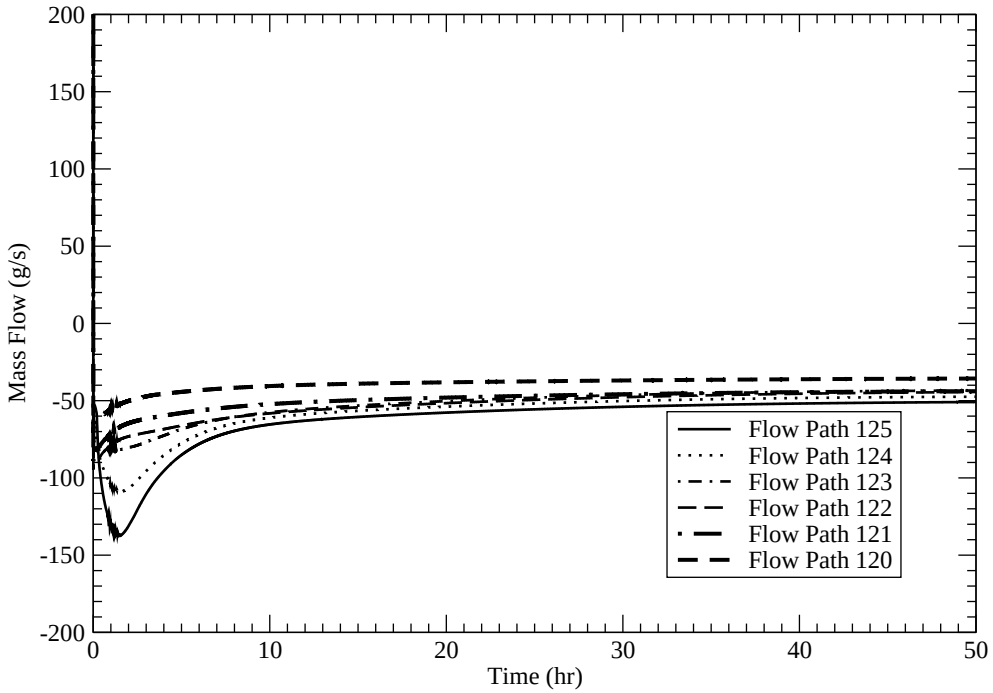

Fig. 5.50. Calculated coolant axial mass flow in ring 2 during PLOFC

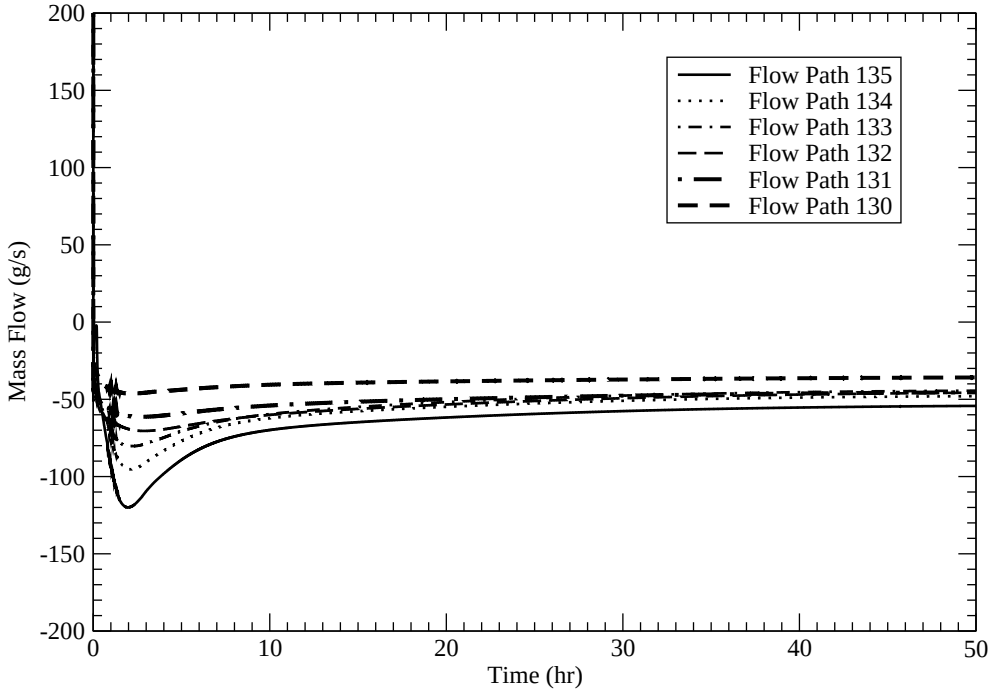

Fig. 5.51. Calculated coolant axial mass flow in ring 3 during PLOFC

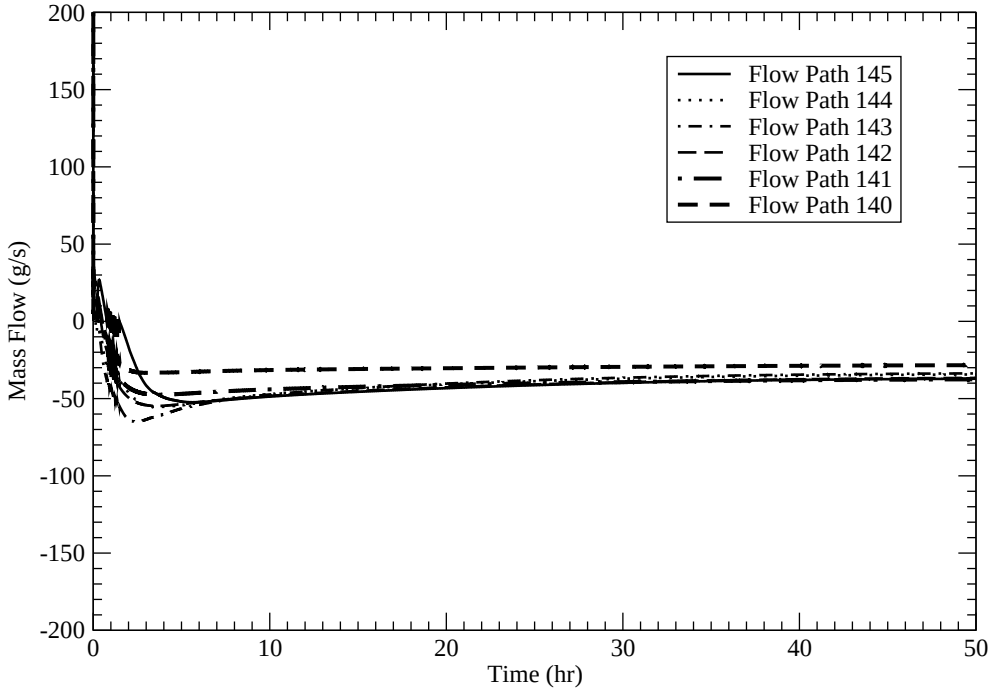

Fig. 5.52. Calculated coolant axial mass flow in ring 4 during PLOFC

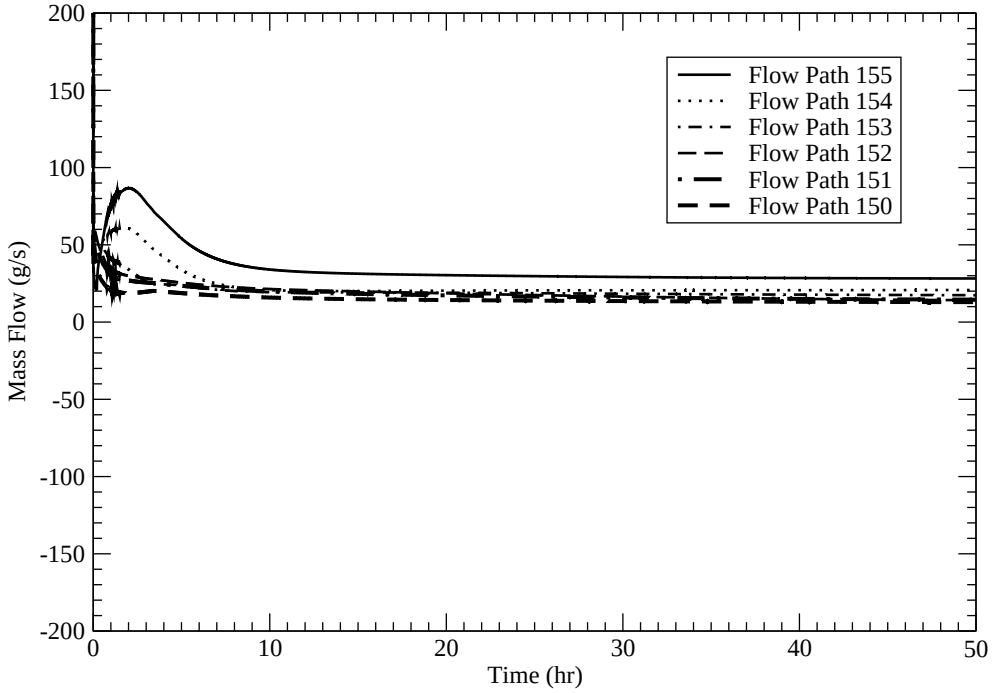

Fig. 5.53. Calculated coolant axial mass flow in ring 5 during PLOFC

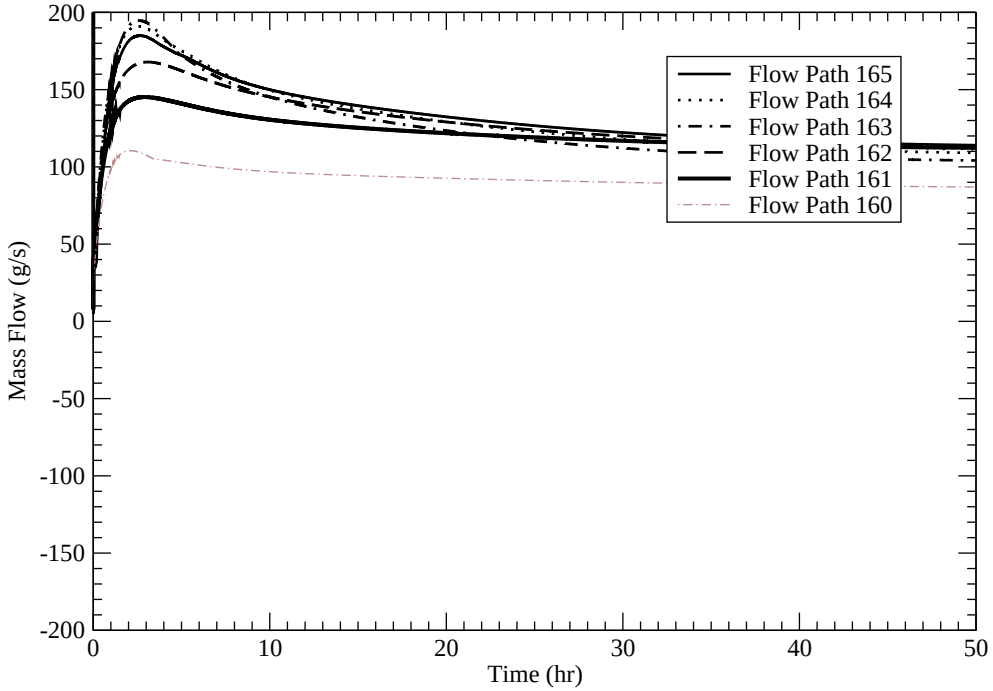

Fig. 5.54. Calculated coolant axial mass flow in ring 6 during PLOFC

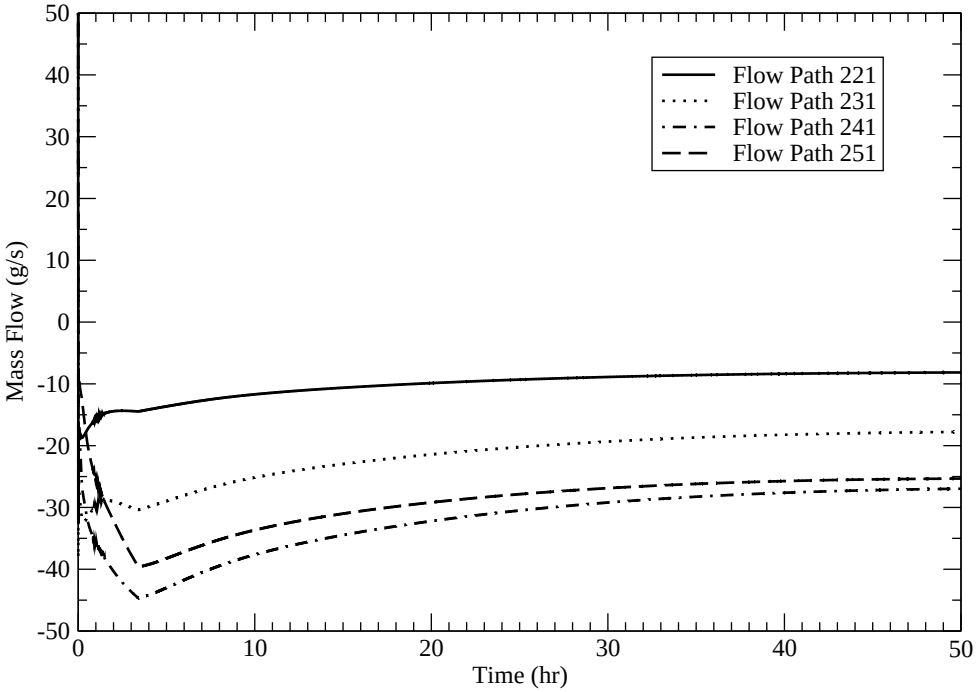

Fig. 5.55. Calculated coolant radial mass flow in FL2n1 during PLOFC

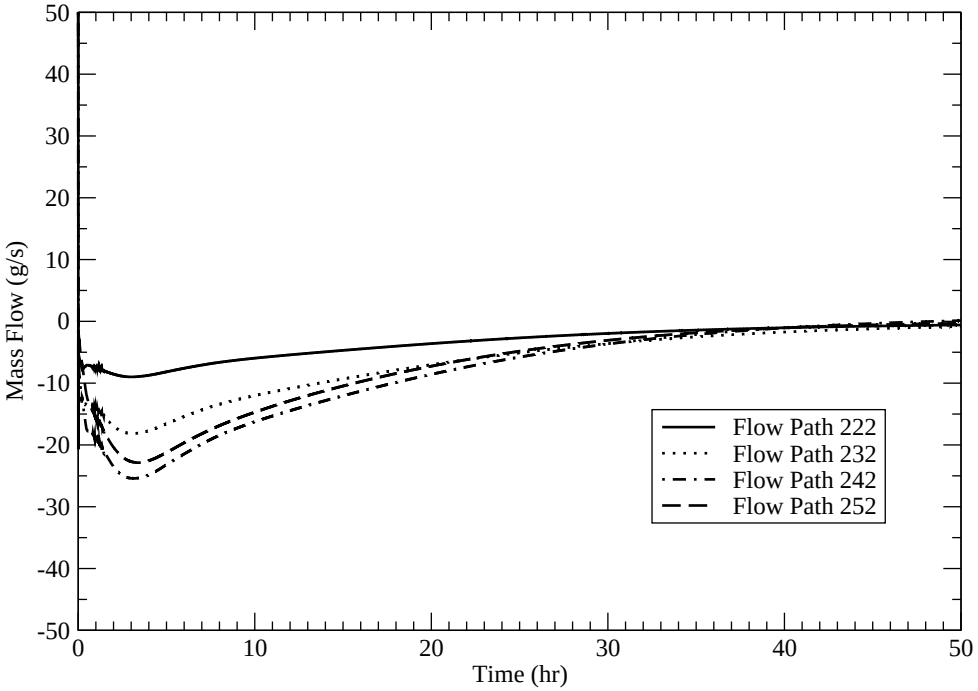

Fig. 5.56. Calculated coolant radial mass flow in FL2n2 during PLOFC

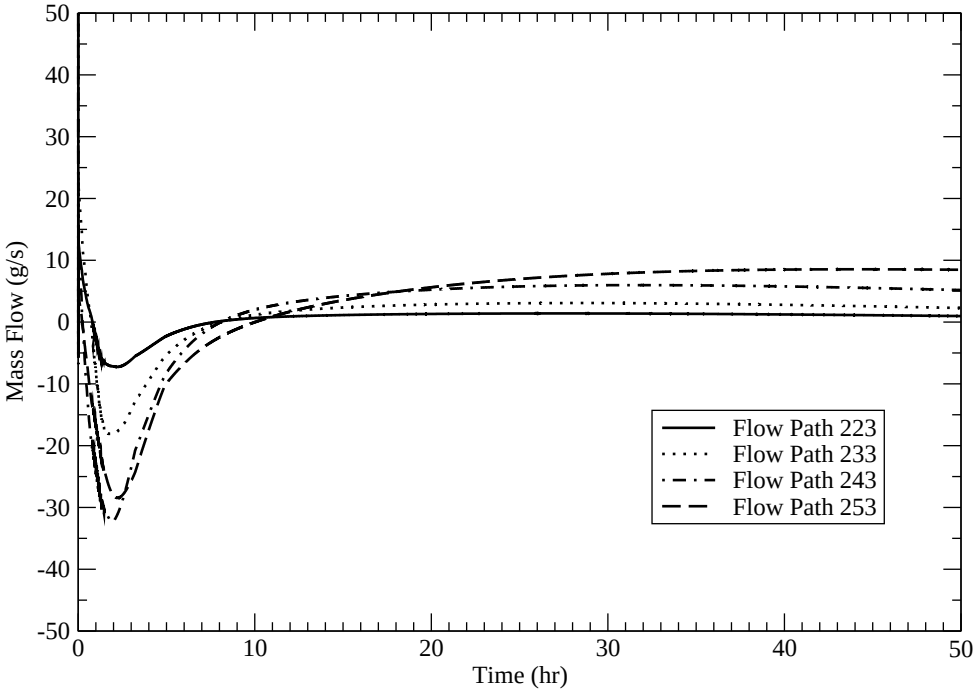

Fig. 5.57. Calculated coolant radial mass flow in FL2n3 during PLOFC

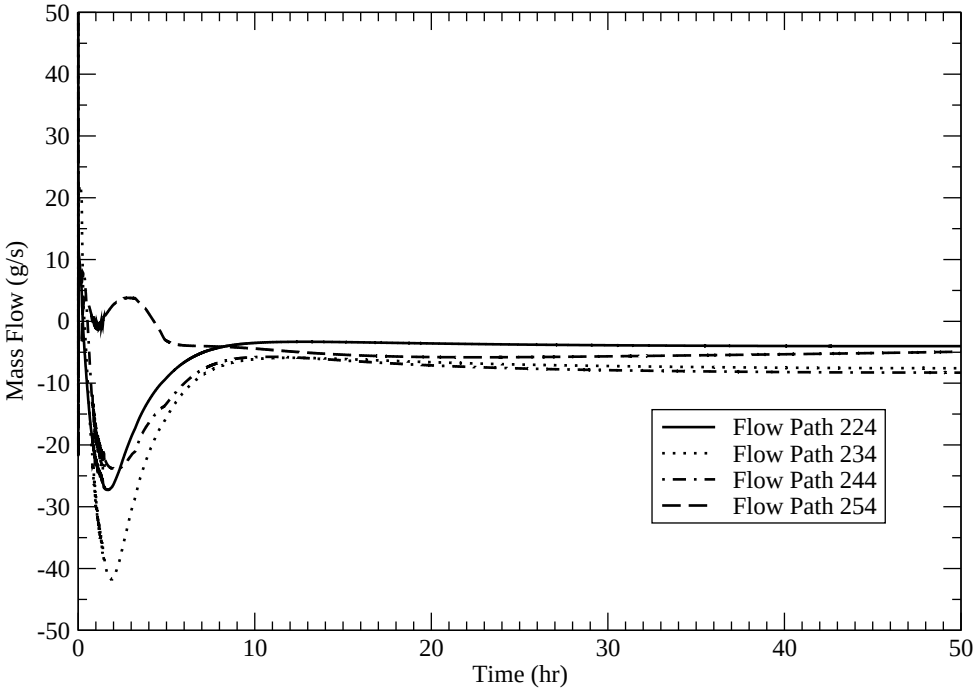

Fig. 5.58. Calculated coolant radial mass flow in FL2n4 during PLOFC

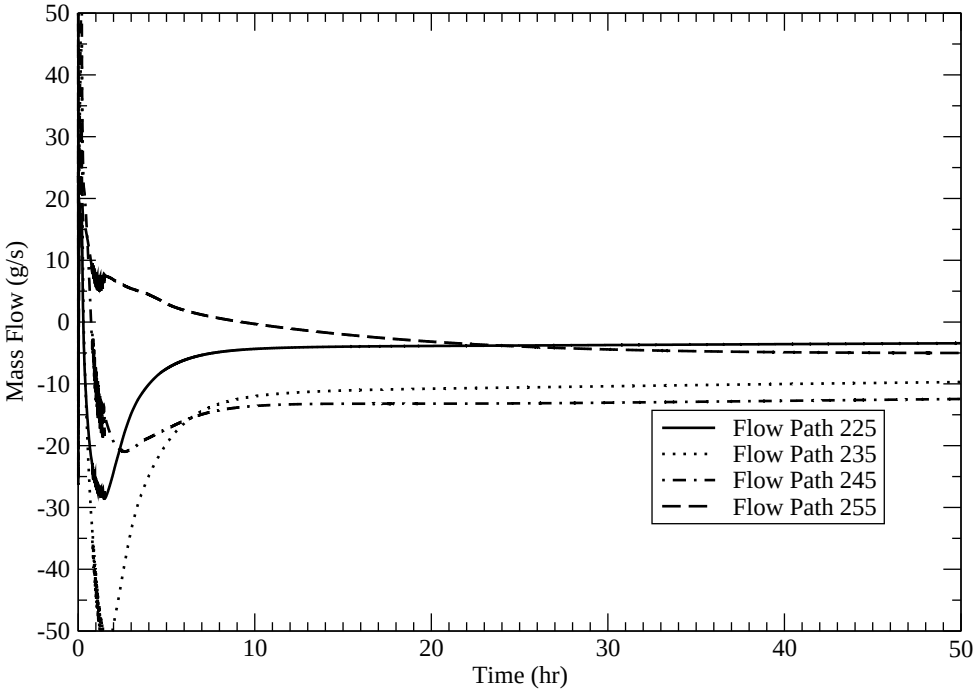

Fig. 5.59. Calculated coolant radial mass flow in FL2n5 during PLOFC

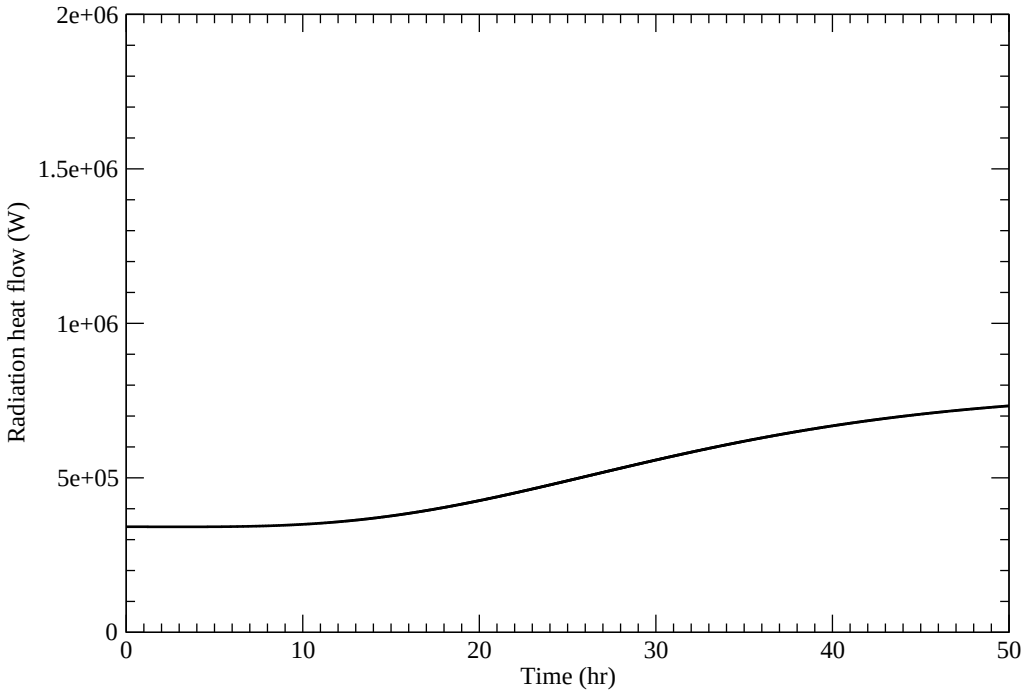

Fig. 5.60. Total radiation heat rate from the RPV during the PLOFC transient

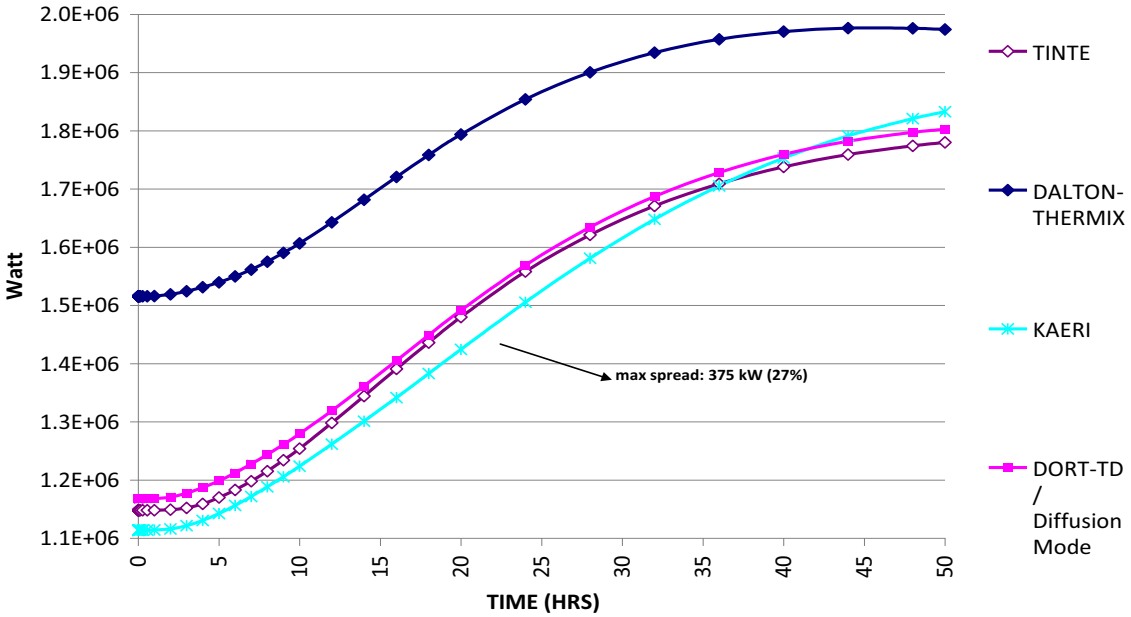

Fig. 5.61. PLOFC RPV radiation heat removal rates calculated by benchmark codes

5.5.3 Depressurized Loss of Forced Cooling Results

MELCOR was run using the DLOFC transient input deck. The calculation was performed for 50 hours per the benchmark specifications.

Figure 5.62 shows that the mass flow into the reactor decreases linearly from 192.7 kg/s to 0 kg/s over the first 13 s of the transient. Figure 5.63 shows that the inlet and outlet pressure decrease linearly to 0.1 MPa over the same time period. Figure 5.64 shows that the reactor is tripped on a zero mass flow condition, and power switches from constant fission power to decay power. Together, these figures verify that the control logic for this transient have been implemented correctly.

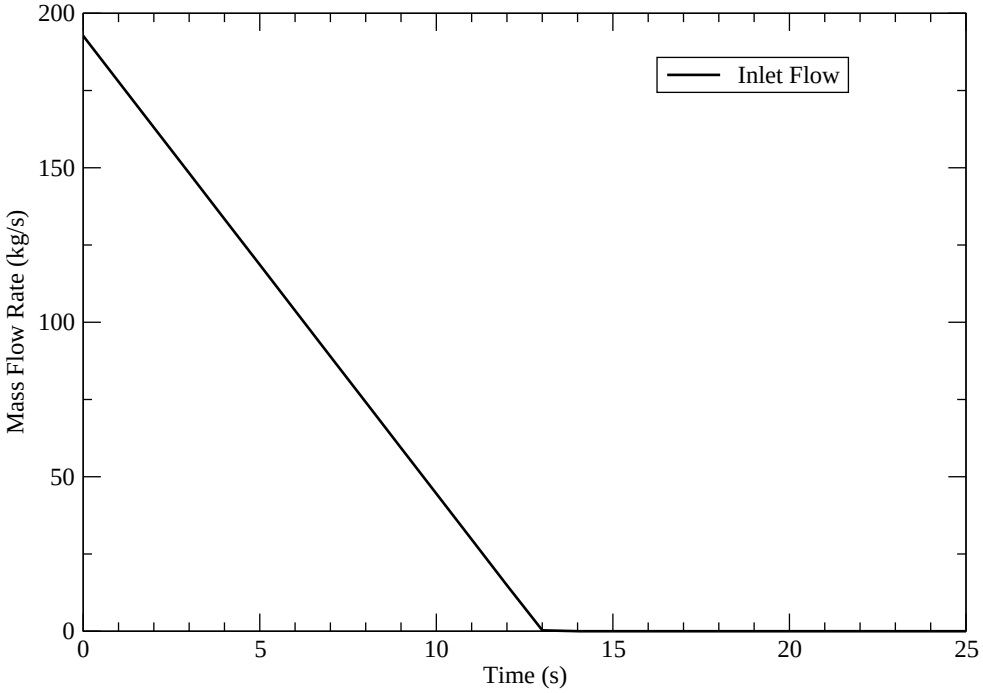

Fig. 5.62. Inlet mass flow during the first 25 s of the DLOFC transient

Figure 5.65 shows the fuel temperature behavior in ring 2. Behavior is similar to that seen in the PLOFC results, though peak DLOFC temperatures are approximately 200 °C higher than PLOFC temperatures. The higher temperatures occur due to the lower mass of coolant in the system and due to a lack of natural circula-

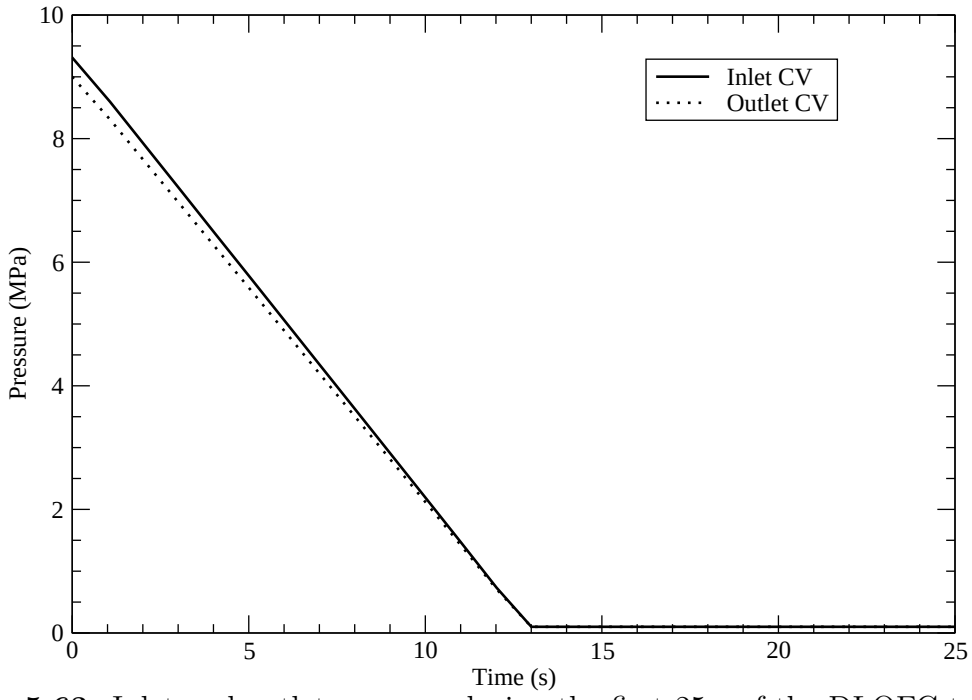

Fig. 5.63. Inlet and outlet pressure during the first 25 s of the DLOFC transient

tion flow. Flow rates predicted for the DLOFC transient are negligible, so thermal streaking is not an issue during depressurized transients.

Again, maximum temperatures predicted by MELCOR are higher than those predicted in the benchmark, which are shown in Figure 5.66. As explained above, this is likely due to the lower heat transfer rate to the core boundary.

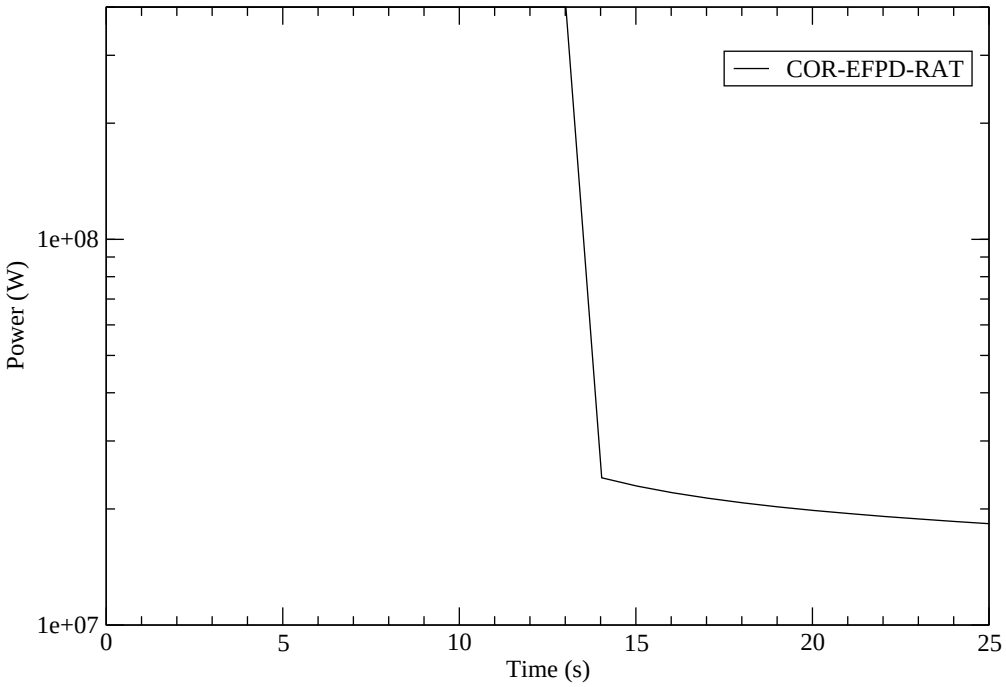

Fig. 5.64. Core power during the first 25 s of the DLOFC transient

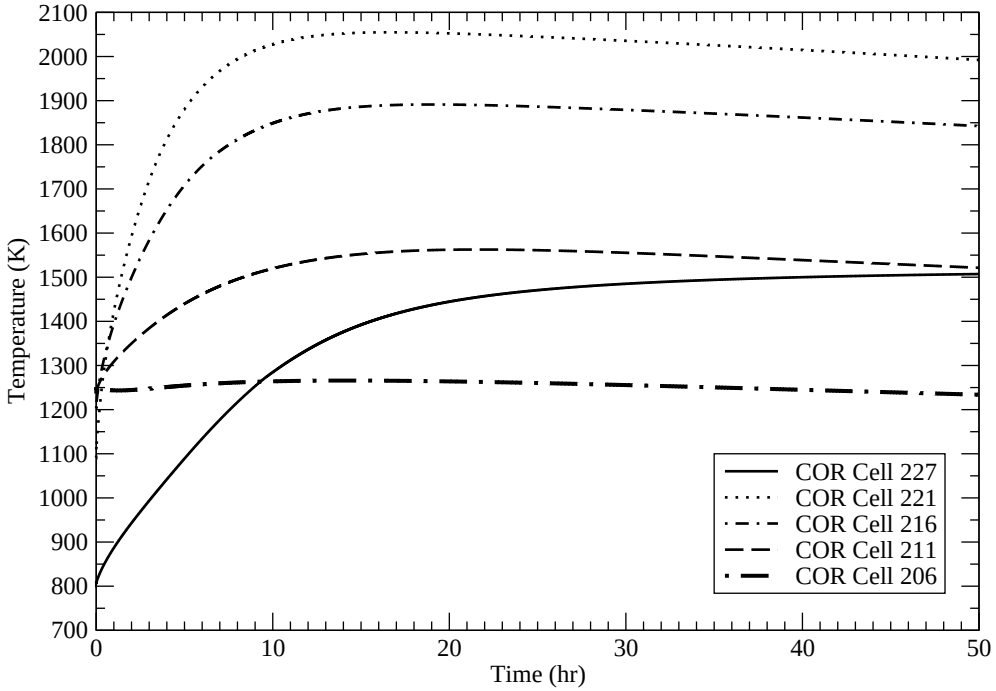

Fig. 5.65. Fuel temperatures in ring 2 during the DLOFC transient

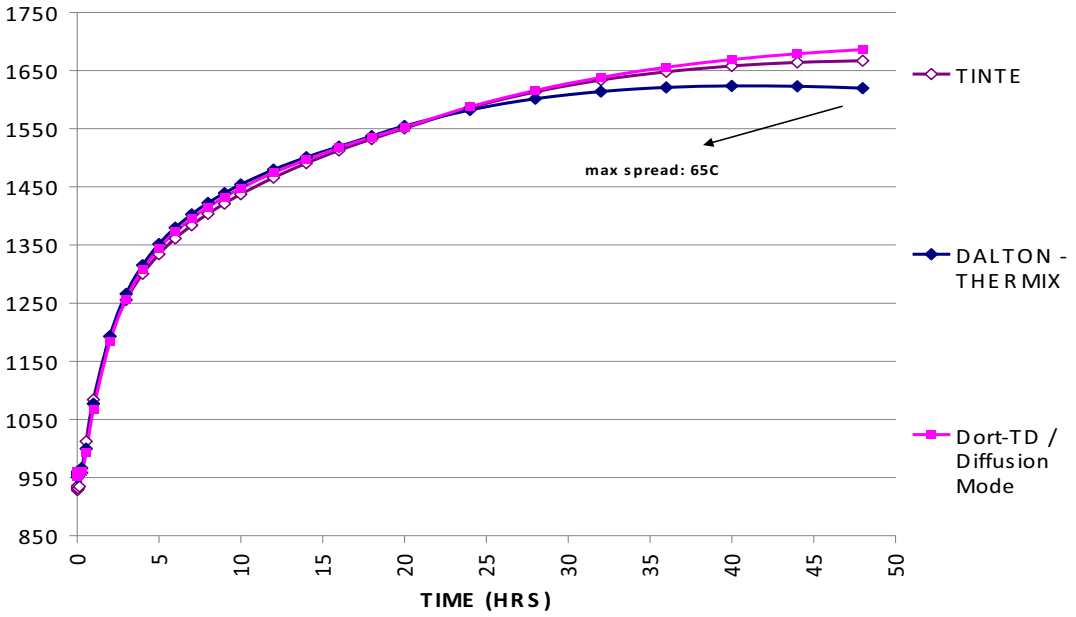

Fig. 5.66. Maximum fuel temperatures during the DLOFC calculated by the benchmark codes [81]

5.6 Summary

A MELCOR 2.1 input deck has been created to model the 400 MW Pebble Bed Modular Reactor. Input is based on the OECD code-to-code benchmark problem definition.

New input techniques have been developed for this study. In particular, proper methods for calculating geometric parameters for fuel, cladding, and reflector components are explained in detail. Also, control logic is included to linearly increase or decrease the coolant inlet mass flow rate, inlet pressure, and outlet pressure, and to trip the reactor on a low-flow condition. This control logic can be used to perform pressurized and depressurized loss of forced cooling transient calculations.

Steady-state calculations were performed with the PBMR-400 deck. Heat structure temperatures slowly reach an asymptotic solution, though core temperatures reach equilibrium after a comparatively short time (approximately 1000 s). Steady-state conditions are used as the initial conditions for PLOFC and DLOFC transient calculations. The transient calculations are set up to assess MELCOR's ability to model core heatup and combined conduction and radiation to the core boundary.

MELCOR's default correlation for forced convection from a packed bed was modified for steady-state calculations. A correlation based on German regulatory rules was fit to the form of the equation in MELCOR. This fit was performed over the range of Reynolds numbers expected during steady-state operations. The fit used here is only valid for this particular circumstance. A more appropriate heat transfer correlation should be implemented into the code for PBR calculations. For transient calculations, sensitivity coefficients controlling the heat transfer correlation were reset to their default values. This is acceptable because the default equation is best suited to low-flow situations.

Steady-state results show that average fuel temperatures reach a maximum of 980 °C in ring 2 near the bottom of the core. This is because the power density is highest in ring 2. The temperature difference between the fuel and coolant (less

than 200 °C) is much lower than the temperature rise for the core inlet to the outlet (400 °C), which is why fuel temperatures are highest near the core exit, rather than at the location of peak power.

Steady-state calculations also show a difference in core coolant exit temperatures from ring 2 to ring 5 of approximately 100 °C. This suggests that hot jets exiting the core could cause thermal stresses in the lower plenum.

Predicted transient temperatures are significantly higher than those calculated for steady-state operations. During the PLOFC transient, peak fuel temperatures are above the 1600 °C limit for TRISO fuel. Temperatures exceed 1800 °C in the DLOFC transient. The high temperatures are likely a result of low heat transfer rates to the core boundary. This issue is still being investigated.

MELCOR results show that natural circulation flow develops in the PLOFC transient. Hot helium exits the top of the core in rings 2-4. This helium could melt control rod drive mechanisms, which is a major safety concern. Natural circulation flow does not develop in the DLOFC transient because the buoyancy difference between the inner and outer core rings is insufficient to initiate flow.

Overall, MELCOR results show good agreement with the benchmark codes. However, it should be noted that temperatures predicted by MELCOR for the transient scenarios are higher than temperatures presented in the benchmark documents.

6. HTTF CALCULATIONS

A MELCOR 2.1 input deck has been created for the High Temperature Test Facility (HTTF), which is currently in the design phase at Oregon State University. This modeling effort can influence the facility layout, particularly the instrumentation plan, by identifying regions of interest in the test facility. Instrumentation can be placed at these locations to obtain test data that correspond to calculated MELCOR parameters. This data will be compared to results from MELCOR calculations as a partial validation of the code for HTGR applications.

This section describes the modeling approach and the code input created for this activity. Preliminary results are presented to demonstrate that the methodology applied to this calculation is appropriate. A method for comparing MELCOR results to future test data from the HTTF is proposed.

6.1 Modeling Approach

The purpose of this activity is to create a MELCOR input deck for the HTTF in order to provide suggestions for the facility instrumentation plan, and to formulate a plan for partially validating MELCOR for HTGR analyses.

Code input is based on preliminary drawings of the facility obtained in July 2009 and personal communications with the facility designers at Oregon State University. The drawings used for this activity represent an earlier version of the HTTF. Notably, the model-to-prototype vessel diameter ratio increased from 1:7.54 [60] to 1:4 [82]. This design change was prompted by difficulties in obtaining a material with a thermal conductivity low enough to achieve the target thermal resistance ratio of 113.7:1 [83]. Updated drawings were not available at the time of this writing; however, basic dimensions for the new design were provided. MELCOR input will be modified once more information about the facility is received.

A number of assumptions were made, especially regarding boundary conditions, due to a lack of design data. These assumptions are noted as they arise in the following sections.

6.2 Facility Design

The HTTF is based on GA's MHTGR, and so it features a prismatic core. (The MHTGR is similar to the GT-MHR, described in Section 2.2.2, and shown in Figures 2.4 and 2.5.) The core has inner and outer equivalent diameters of 14.625 in. and 35 in., is 78 in. high, and features 426 0.625-in. diameter coolant channels and 228 0.5-in. diameter heater rods. Each heater rod is surrounded by 6 coolant channels with a rod-to-channel pitch of 1 in.

The core is bounded by central and side reflectors with outer diameters of 14.625 in. and 58.5 in., respectively, and by top and bottom reflectors 9.8 in. and 17.75 in. high. The core is contained within a 204 in. tall stainless steel 304 vessel with an inner diameter of 64.5 in. and hemispherical top and bottom heads. All of the above dimensions were obtained from the facility designers [82].

Additional dimensions are either assumed or inferred from old drawings of the HTTF. For instance, the HTTF originally featured a 4-in. region immediately below the bottom reflector, containing a steel support plate. Since the length scale of the facility is not affected by recent design changes, it is assumed that the HTTF contains a 4-in. thick steel bottom plate. Below the plate, the earlier drawings show an outlet plenum approximately 26.5 in. high. A 15-in. inner diameter outlet pipe is located in the bottom part of this plenum. An open plenum also extended above the top reflector, the bottom portion of which occupied a cylindrical part of the core barrel, while the top portion of the upper plenum was in a hemispherical cap attached to the core barrel. The total vessel height shown in these drawings is 217 in., with hemispherical caps each having a radius of 21.5 in.

The new vessel is shorter than in the previous design and has larger top and bottom heads. This means that the cylindrical portion of the new vessel is significantly shorter than in the old vessel. For this reason, the cylindrical portion of the upper plenum is assumed to be removed for the MELCOR model. The portion of the outlet plenum above the elevation of the outlet ducts is also assumed to be removed. Both assumptions are consistent with the MHTGR design. The outlet duct is assumed to have an inner diameter of 18 in., which is 1/4 of the inner diameter of the MHTGR cross duct [84].

It is assumed that the vessel wall thickness is 1.31 in., which is 1/4 of the MHTGR vessel wall thickness [84]. The core barrel is assumed to be 1 in. thick, and the gap between the core barrel and the pressure vessel is assumed to be 2 in.. These latter two assumptions are somewhat arbitrary but are nonetheless reasonable when compared to the latest available design drawings. MELCOR input will be updated once more current information is available.

For low-power operation, helium flows into the gap between the core barrel and the vessel from inlet ducts. The coolant flows upward through this gap to the top of the vessel, then downward through penetrations in the core barrel end cap to the upper plenum above the core. Coolant enters flow channels in the top reflector and flows downward through the top reflector, core, and bottom reflector to the outlet plenum, from which the helium flows through outlet ducts and out of the reactor. The design drawings show two inlets and two outlets. It is unknown whether the facility will retain these features.

The HTTF can simulate a number of different break sizes and locations for DLOFC tests. Locations include standpipes that penetrate the top of the vessel, inlet ducts, and outlet ducts. HTTF test plans have not been fully defined, and so a break size and location is assumed for a MELCOR test case.

6.3 Input Description

Input has been created for HTTF low-power, steady-state conditions and for a DLOFC test. This input is described here and in Appendix C.

Figures 6.1 and 6.2 show nodalization diagrams for the COR package and for the CVH-FL packages, respectively. Like the RCCS and PBMR-400 nodalization, the HTTF input model is azimuthally symmetric about the core centerline. Dimensions are presented with the diagrams for clarity.

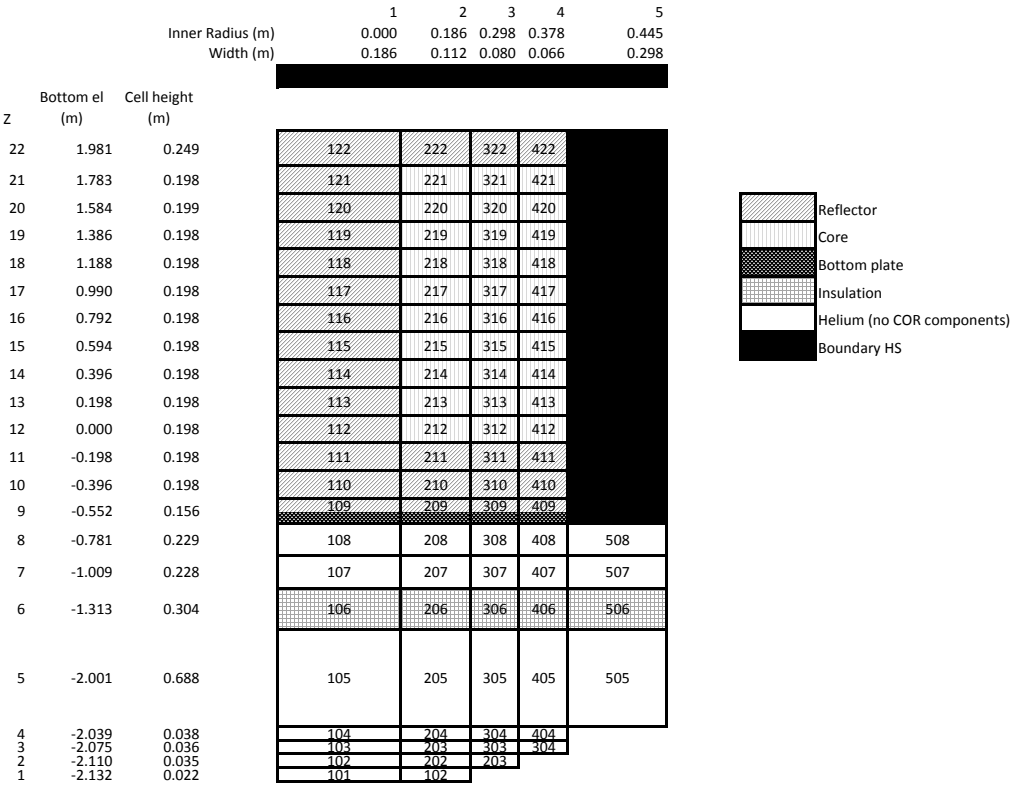

Fig. 6.1. COR nodalization diagram for the HTTF MELCOR input deck

Input for the HTTF is broken up into the following files, each of which performs a specific function: **exec.inp**, **cvh-vessel.inp**, **fl-vessel.inp**, **core.inp**, **hs-**

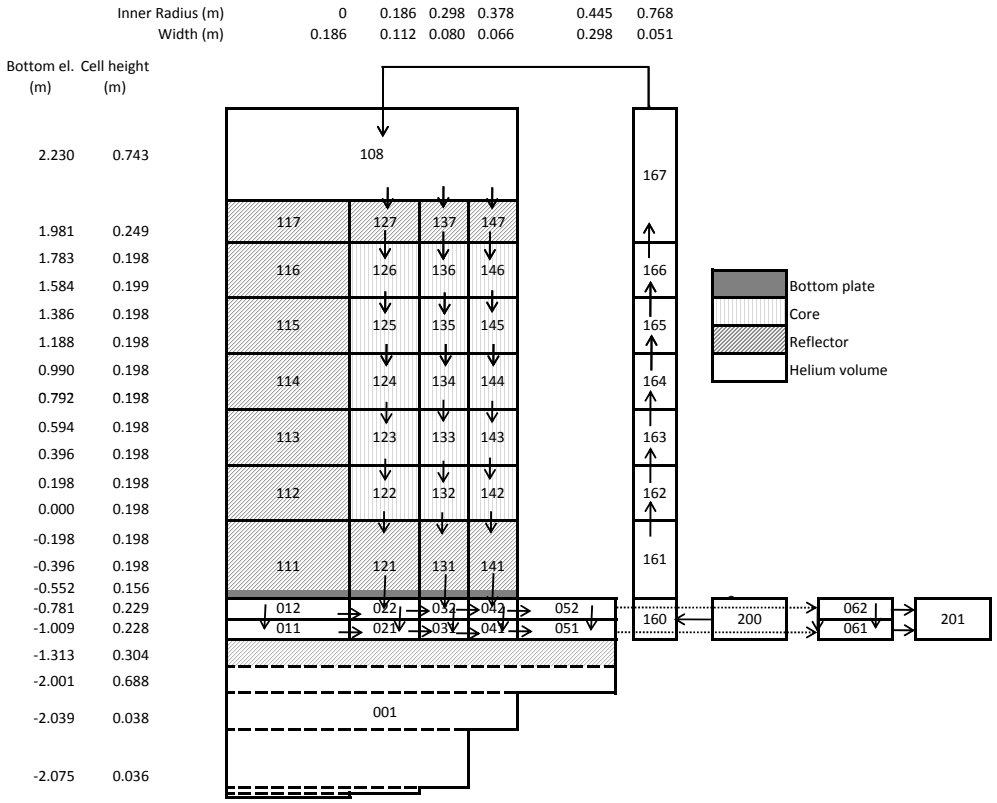

Fig. 6.2. CVH-FL nodalization diagram for the HTTF MELCOR input deck

vessel.inp, **cavity.inp**, **src-sink.inp**, **mp.inp**, **ncg.inp**, and **control-logic.inp**. These files are described in the following sections.

6.3.1 core.inp

The HTTF is modeled as a prismatic reactor (PMR) with nuclear fuel instead of electric heaters. MELCOR can model electric heating elements; however, heaters may only be included in two radial rings. A more detailed nodalization of the core is desired, and so the heaters are modeled as fuel (FU) in MELCOR.

The radius of the fuel was set to the radius of a heater element. However, treatment of the cladding for PMRs is significantly different from the treatment for LWRs and PBRs. For PMRs, the "clad" is the graphite associated with a fuel compact and coolant channel [6]. The clad outer radius can be calculated by first determining the area of graphite associated with a fuel compact and coolant channel using the following formula:

$$A_{graph} = A_{cell} - A_{cool} - A_{fuel} = 6\frac{s^2\sqrt{3}}{4} - 2\frac{\pi D_{cool}^2}{4} - \frac{\pi D_{fuel}^2}{4} \tag{6.1}$$

In the above equation, s is the distance from the center of a coolant channel to the center of a fuel compact, which is equal to 1 in. The area of one coolant channel is multiplied by 2 because there are two coolant channels in a unit cell. Likewise, there are six equilateral triangles in each hexagonal cell. The clad outer radius is equal to

$$R_{clad} = \sqrt{R_{fuel}^2 + A_{graph}/\pi} = 1.04 \text{ in.} = 0.0138 \text{ m} \tag{6.2}$$

This value is declared as the clad outer radius.

For the MELCOR input deck, the facility is divided into 22 axial levels and 5 radial rings. The radius of ring 1 is chosen such that ring 1 contains the central reflector. The dimensions of rings 2-4 are chosen such that the active core is divided into three portions with equal cross-sectional areas. It is assumed that each active core ring contains the same number of heater rods and coolant channels. This assumption is reasonable based on the core details available, namely, that heaters

and coolant channels are arranged in a regular hexagonal lattice. Heater locations form rough concentric circles about the core centerline. Ring 5 in the core package extends outward to the vessel inner wall. Ring 5 is not modeled at elevations above the bottom plate per MELCOR requirements.

Axial level elevations are selected so that the average helium temperature rise across each active core cell is approximately 50 °C. The core is divided into ten axial levels with heights equal to 7.8 in. to meet this requirement. One axial level represents the top reflector. The bottom reflector is divided into three axial levels, the top two of which have heights equal to the height of the active core cells. The lowest level of the bottom reflector also contains the bottom plate. The outlet plenum is divided into two axial levels with equal heights. One level contains the insulation below the outlet plenum. Between the insulation and the bottom head are several other axial levels that contain only helium.

The resulting nodalization is shown in Figure 6.1. Level 9 includes the bottom plate, which marks the division between the active core region and the lower plenum. Cells in levels 9-22 of ring 5 are listed as "NULL" in the input deck, meaning they occupy a region inaccessible to the core package. This space is occupied by core boundary heat structures, which simulate the side reflector and core barrel. Cells that would occupy the space outside of the lower head (such as level 3, ring 5) are also listed as "NULL."

The active core is represented by levels 12-21 of rings 2-4. Part of level 9, along with levels 10-22, of ring 1 model the central reflector. The top reflector is contained in level 22 of rings 2-4. Part of level 9 and levels 10-11 of rings 2-4 represents the bottom reflector. Insulation below the lower plenum is modeled as a supporting structure, made of ZIRC in level 6 of rings 1-5. Material properties for zirconium have been redefined to correspond to a ceramic with the density and heat capacity of graphite and a very low thermal conductivity. Levels 7-8 of rings 1-5 represent the outlet plenum. No core components are modeled in these cells. While there

may be structures in the lower plenum (such as connections for the heater rods), these obstructions have not been defined and are not included in the input. These structures can be accounted for by specifying the flow loss coefficients for flow paths in the lower plenum and by adjusting the volume of CVs in the outlet plenum.

The volume of fuel in each active core cell is calculated by multiplying the area of one heater element by the height of the cell and the number of heaters per ring (equal to one-third of the total number of heaters). The fuel volume is multiplied by the density of UO_2 to get the mass of fuel in each cell. Once heaters have been procured, Material Properties package input will be adjusted to account for the actual heater density.

The volume of "clad" in each cell can be found by subtracting the fuel volume and coolant volume from the total volume in each cell. The coolant volume for each cell is simply the area of one coolant channel times the cell height, times 142 coolant holes per ring. The mass of clad is equal to the volume of clad times the density of graphite. This assumes that the ceramic material used in the core has a density equal to graphite, which is consistent with the designers' plans [60].

To calculate the mass of RF in the top and bottom reflectors and the mass of SS in the bottom plate, it is assumed that the reflectors and the bottom plate have the same number of coolant channels as the active core. This is consistent with earlier design drawings. The volume of RF and SS in each of these cells can be calculated using the same methodology applied for the clad. In the case of the plate, the volume is multiplied by the density of steel to get the mass of SS. The central reflector is assumed to be solid, making the determination of masses self-explanatory. The insulation in level 6 is modeled as a supporting structure with the same density as graphite. The mass of SS in each of these cells can be determined by multiplying the cell volume by the density of graphite.

Channel flow areas for levels 9-22 of rings 2-4 were calculated by multiplying the area of one coolant channel by 142 channels per ring. Bypass flow areas are set to

zero for now, since it is unknown how the core of the HTTF will be assembled. If the HTTF adopts a configuration similar to the MHTGR, then the core will consist of ceramic blocks separated by a measurable gap. Flow through these gaps would be considered bypass flow and will be modeled if the designers decide to use this core layout.

Flow areas for each core cell in the outlet plenum are equal to the total cross sectional area for the cell. Flow areas for cells in the lower plenum (levels 1-6) and in the central reflector (ring 1) are set to zero. Again, input will be adjusted once more information about the facility becomes available.

The central, bottom, and top reflectors are all modeled as cylindrical graphite reflectors in MELCOR. It was noted in Section 5 that the RF component in MELCOR cannot support FU or CL. For this reason, supporting structures must be present in levels 11 and 22 of rings 2-4 so that the core and top reflector do not collapse. These supporting structures are defined as ZIRC, which has been redefined as the ceramic material used for the cladding and reflector. A small mass of supporting structure is included in each of these cells. The same mass is subtracted from the total mass of RF.

All of the reflectors are given negative thicknesses, with magnitude equal to the thickness of the ring they occupy, to signify that the channel side is the outer side. However, since coolant flows through channels in the top and bottom reflectors, the channel side hydraulic diameter for these reflectors is set equal to the diameter of a coolant hole. The channel-side hydraulic diameter for the central reflector is defined as the diameter of ring 1. Bypass-side hydraulic diameters are set to a small value because bypass flow is not modeled as of yet. The bypass hydraulic diameter would be equal to the hydraulic diameter of a ceramic block if such a configuration is adopted for the HTTF.

A uniform axial and radial power profile is assumed for steady-state and transient conditions. These parameters can be easily modified to simulate variable axial and

radial power profiles. All components begin the calculation at 763 K (490 °C), which is the coolant inlet temperature for the vessel.

6.3.2 cvh-vessel.inp and fl-vessel.inp

Control volumes and flow paths simulate the main engineered flow paths described in Section 6.2. Currently, bypass flow is not modeled due to a lack of information about the facility design. Bypass control volumes and flow paths will be added to the input deck in the future.

In the heated portion of the test section and in the top and bottom reflectors, control volumes (CVH121-127, 131-137, 141-147) represent the helium in the coolant channels. In cells containing the central reflector and insulation in the lower plenum, CVs (CVH111-117, the portion of CVH001 in level 6) have negligible volume and are included only to satisfy input requirement. None of the other control volumes contain virtual volume from the COR package. These CVs represent the lower plenum below the insulation, the coolant outlet plenum above the insulation, the upper plenum above the top reflector, and the gap between the core barrel and the vessel.

Each control volume in the active core occupies two COR cells. One CV in each ring (CVH117, 127, 137, 147) contains the coolant volume in the top reflector, while another (CV111, 121, 131, 141) represents the coolant volume in the bottom reflector and support plate. Control volume sizes to speed up calculation run time, which is limited by the Courant limit. The Courant limit prevents all of the material in a CV from flowing out of that CV in a single time step. Thus, increasing control volume size increases the coolant mass in the control volume, which allows for a larger time step. However, due to the steep temperature gradient ($\sim$ 2.6 °C/cm) in the HTTF, control volume size must not significantly affect MELCOR's ability to simulate HTGR thermal hydraulics. As is evident from PBMR400 transient calculations, a large control volume size can result in non-physical temperature behavior in the core due to inaccurate estimations of local coolant temperatures by the dT/dz

model. Four or five COR cells are coupled to each CV in the PBMR400 input deck. By reducing the COR cells per CV to two, non-physical behavior should be significantly reduced. If similar results are observed, then a unique CV will be coupled to each COR cell.

One control volume occupies each COR cell in the outlet plenum (CVH011-012, 021-022, 031-032, 041-042, 051-052). This is done in an attempt to model circulation patterns in the outlet plenum and to simulate stratified flow during air ingress accidents. It is expected that air will occupy the bottom of the plenum, while helium gas will occupy the upper portion of the outlet plenum and everything above it. The HTTF will simulate air ingress, so the MELCOR nodalization scheme has been developed to capture this phenomenon.

In addition, two CVs (CVH061-062) are included to model the top and bottom halves of a portion of the outlet pipe. The length of the pipe is arbitrarily chosen to be 0.25 m. This will be modified in future versions of the input deck. These volumes have been added to model stratified flow in the outlet pipe following a DLOFC.

The upper plenum above the top reflector is modeled as one CV. This is done because mixing in the upper plenum is not a concern, except when natural circulation patterns develop during PLOFC events. Since the primary goal of the HTTF is to simulate DLOFC events, and not PLOFC events, one CV is sufficient for the upper plenum.

Vertical flow paths connect control volumes in the core. Radial flow is not modeled, since all flow passes through vertical channels drilled into the test section. Radial flow would exist in the bypass between blocks in a prismatic reactor, but no bypass flow is considered in this preliminary analysis. Flow paths through the core and top and bottom reflectors have a flow area equal to the total area of coolant channels in one ring. The hydraulic diameter is equal to the diameter of one channel.

Flow paths between the upper plenum and top reflector and between the bottom reflector and outlet plenum each consist of two segments. One segment includes

the portion of the flow path in the reflector. Segment geometry is the same as the geometry of core flow paths. The segment for flow through the upper plenum has flow area and hydraulic diameter equal to the area and diameter of the circle through the upper plenum centroid. This is done to avoid breaking the flow path into many smaller segments with areas and diameters of circles at points along the flow path. Using the area and diameter of the circle through the centroid should be sufficient to capture flow losses in the upper plenum, which should be a fraction of the losses in the coolant channels. Segments for flow into the outlet plenum have a flow area equal to the total ring area, since there are no structures in the outlet plenum. Hydraulic diameter is set equal to the diameter of the outlet plenum, which is enclosed by the core barrel.

Flow paths between control volumes in the barrel-vessel gap have a flow area equal to the cross sectional area of the annulus. The hydraulic diameter is calculated by using the formula

$$D_h = \frac{4A}{P_w} \tag{6.3}$$

where P_w is the total wetted perimeter. This is the standard formula used to calculate hydraulic diameter [77].

6.3.3 hs-vessel.inp

Heat structures are used to model the side reflector, core barrel, and pressure vessel. The side reflector and core barrel at COR levels 9-22 serve as boundary heat structures for the COR package. These are composite heat structures, consisting of the ceramic side reflector and the steel barrel. The barrel portion of the HS is modeled as ALUMINUM. This is done so that thermophysical properties can be modified if the core barrel is made of a different material than the vessel. Currently, ALUMINUM is redefined as STAINLESS-STEEL.

The boundary heat structures have heights and characteristic lengths corresponding to the COR level heights. Both surfaces have convective boundary conditions. The inner surface is coupled to the CVs in COR ring 4. This is appropriate, since some of the coolant channels will be located adjacent to the side reflector inner surface. If there is a gap between core blocks and the side reflector, then the bypass volume used to model this gap will be specified as the control volume at the HS inner surface. The outer surface transfers heat to CVs in the barrel-vessel gap.

The portion of the core barrel along the outlet plenum is modeled as two cylindrical heat structures, one for each COR level in the outlet plenum. These structures have convective boundary conditions and are coupled to CVs in the outlet plenum and in the barrel-vessel gap at the inner and outer surfaces, respectively. The hemispherical end cap for the barrel is modeled as a TOPHALFSPHERE heat structure. The inner surface transfers heat to the upper plenum, while the outer surface transfers heat to the CV in the gap between the barrel end cap and the upper head.

A coarser discretization is used for the vessel. Portions of the vessel at the elevations of the core and top and bottom reflectors have heights corresponding to CVs in the core. A coarser nodalization is chosen because fine detail is not needed for vessel temperatures. The figures of merit for the vessel are peak temperature and radiative and convective heat fluxes. A coarse nodalization should be sufficient to capture vessel heat transfer phenomena. Portions of the vessel above and below the core and outlet plenum elevations have greater heights because temperatures and heat fluxes will be lower in these segments than in the segments around the heated core. Vessel heat structures have convective boundary conditions and are coupled to the gap CVs at the inner surface and cavity CVs at the outer surface. Cavity CVs are described below.

6.3.4 cavity.inp

Details about the cavity (i.e. the air volume between the vessel and the RCCS) and RCCS for the HTTF are currently unavailable, so the distance from the pressure vessel to the RCCS is assumed to be 0.5 m. This is approximately one-quarter of the distance between the RPV and the RCCS for the VGM, so it is a reasonable value for a water-cooled RCCS. However, this assumption is arbitrary and must be changed once the RCCS design is clarified.

It is possible that the HTTF designers will choose to use the RCCS as a boundary condition (perhaps with a constant surface temperature) rather than simulate RCCS behavior. For this reason, the RCCS in the MELCOR input has been modeled as thin (1 cm) heat structures with a constant temperature at the outer surface. RCCS heat structure elevations correspond to the elevations of the vessel heat structures.

The cavity between the vessel and RCCS is broken into control volumes at the same elevations as the vessel and RCCS heat structures. Cavity CVs are filled with air and are not connected by flow paths. The cavity nodalization for the final HTTF MELCOR input deck will likely be similar to the cavity nodalization used for the RCCS studies (Section 4).

6.3.5 src-sink.inp

The vessel inlet and outlet pipes are modeled as property-specified control volumes. This approach is analogous to the techniques used for the PBMR-400 input deck. During steady-state operations, the inlet and outlet CV pressure is set as 800 kPa, which is the maximum pressure of the facility [61]. The inlet temperature is 763 K and the specified outlet temperature is 1273 K. Like in the PBMR400 deck, the specified inlet pressure and outlet temperature have no affect on the calculation. When comparing MELCOR results to future test data, the pressure of CVH160 and

the average temperature of CVH062 and CVH061 should be considered the inlet pressure and outlet temperature.

The coolant velocity from the inlet to CVH160 is set by a control function. The mass flow rate required to produce a mixed outlet temperature of 1273 K for a core power equal to 600 kW was determined using the following formula:

$$\dot{m} = \frac{Q_{core}}{c_p \Delta T} = 0.23 \text{ kg/s} \tag{6.4}$$

This value is used to calculate the coolant inlet velocity. Velocity is equal to the specified mass flow divided by the product of the flow area and the density of CVH160 (the "TO" CV).

Two flow paths lead to the outlet CV, one each for the bottom (CVH061) and top (CVH062) halves of the outlet pipe. The outlet CV contains air, which has no affect on steady-state calculations. However, the outlet CV acts as a source for air ingress during a DLOFC resulting from a complete break of the outlet pipe. This accident scenario has been formulated for a preliminary test case of the MELCOR HTTF input deck and is described in more detail in Section 6.4. As explained in an earlier section, the outlet pipe is divided into two control volumes to simulate stratified helium-air flow during a DLOFC.

6.3.6 control-logic.inp

Control functions have been defined to regulate inlet and outlet CV temperature and pressure and coolant inlet velocity. Coolant inlet velocity is specified by CF 'HeSource.' This is an if-else CF that returns 0.0 if CF 'Trans-Trip' is TRUE and the value of CF 'HeVelocity' if 'Trans-Trip' is FALSE. 'Trans-Trip' is an initially FALSE logical control function that latches TRUE when the time since the start of the transient 'Trans-dt' is greater than 'Trans-Trip-Time.' 'Trans-dt' is the difference between the problem time and a user-specified initial value 'Trans-T0.' 'Trans-dt'

is multiplieed by 0.0 for steady-state calculations, so 'Trans-Trip' is always FALSE. 'Trans-dt' should be multiplied by 1.0 during transient calculations, which can be accomplished by modifying the multiplicative constant for the control function. The values of 'Trans-T0' and 'Trans-Trip-Time' can be adjusted by changing the CF additive constant upon a problem restart. 'HeVelocity' is the steady-state helium velocity calculated using methods described above. The steady-state mass flow is a control function that serves as an argument to 'HeVelocity.' The value of 'SS-Mflow' can be changed in the initial input or upon a calculation restart to modify the steady-state inlet mass flow rate.

Similar logic is used for the inlet and outlet CV temperature and pressure. For each of these parameters, a steady-state and a transient value have been defined. When 'Trans-Trip' is TRUE, control functions return the transient values of the above parameters. Otherwise, steady-state values are returned.

To prevent flow to or from the inlet during an outlet pipe break DLOFC, a valve has been defined in **src-sink.inp** for FL161 connecting CVH160 and CVH161. The valve open fraction is controlled by CF 'InletVlv.' 'InletVlv' is equal to 1.0 (i.e. fully open) when 'Trans-Trip' is FALSE and 0.0 (i.e. fully closed) when 'Trans-Trip' is TRUE.

6.3.7 mp.inp and ncg.inp

The solid materials and non-condensible gases used in this calculation are declared in **mp.inp** and **ncg.inp**. The thermal conductivity of GRAPHITE has been changed from 35.55 W/m K to 1.25 W/m K. This value can be obtained by multiplying the prototype side reflector thermal resistance by 113.7 because the model-to-prototype thermal resistance ratio is 113.7:1 [60], and dividing by 4 because the diameter ratio is 1:4. The thermal resistance ratio applies to the 1:7.54 diameter scale version of the HTTF and does not reflect the current design. However, the thermal conductivity of GRAPHITE can be easily changed by modifying a tabular function. ALUMINUM

and ZIRCALOY are redefined as STAINLESS-STEEL and GRAPHITE, respectively. ZIRCALOY is the material used for insulation in the COR input specifications. This is done because the insulation is modeled as a supporting structure, and supporting structures must be STEEL or ZIRC. ALUMINUM is the core barrel material. This is done so that the core barrel and vessel can be modeled as separate steels with different material properties.

6.3.8 vfhttf.inp

Due to the large uncertainties in core barrel and RCCS dimensions, detailed view factors have not been included for this input deck. Instead, view factors from the core barrel to the vessel and from the vessel to the RCCS are set to 1.0 for pairs of heat structures that are at the same elevation. Once core barrel and RCCS geometry has been clarified, view factors will be calculated using the methodology described in Section 4.2.1.

6.4 Calculations

Two test cases have been performed for the MELCOR HTTF input deck. The first test case is a low-power (600 kW) steady-state calculation with an inlet mass flow rate of 0.23 kg/s. This calculation is run until coolant and cladding temperatures reach a steady state, which occurs by $18,000$ s.

The restart file generated by the steady-state calculation is used for the initial conditions of a depressurized loss of forced cooling transient calculation. The power is set to 300 kW. 'Trans-T0' and 'Trans-Trip-Time' are set to 18,000 and 0, respectively. This causes inlet mass flow rate and inlet and outlet pressure and temperature control functions to return the transient values of these parameters; the inlet mass flow rate is equal to 0.0, inlet and outlet pressures are 100 kPa, and inlet and outlet temperatures are 300 K. Also, the valve in FL161 immediately closes at the start of the transient,

preventing flow from the barrel-vessel gap to the inlet CV. This calculation is run for $10,000$ s, which is sufficient to determine whether or not the transient is progressing as expected.

6.5 Preliminary Results

Preliminary results for the HTTF MELCOR input deck are presented here to demonstrate that calculations proceed as intended. The magnitudes of temperature and flow parameters are less important than the general thermal hydraulic behavior because there are large uncertainties in the HTTF design.

6.5.1 Steady-State Results

Figure 6.3 shows the vessel inlet and outlet mass flow rates. The inlet flow rate is equal to the flow rate calculated using Equation 6.4, which indicates that the inlet boundary condition has been implemented correctly. As expected, the inlet flow equals the outlet flow. Figure 6.4 displays the inlet and outlet pressures. The pressure of CVH160 is used as the inlet pressure, since the pressure of CVH200 (the helium source) has no significance for reasons explained above. The outlet pressure is equal to 800 kW, which indicates that the outlet pressure boundary condition has been implemented properly. However, the inlet-to-outlet pressure drop is very small. This is due in part to the low coolant density and velocity in the HTTF. To preserve flow loss similarity between the model and prototype, orifices will be added to coolant channel inlets to increase the pressure drop. These orifices can be simulated in MELCOR by specifying flow loss coefficients for core flow paths. Regardless, the fact that the inlet-to-outlet pressure drop is positive is a good indication that the input deck is functioning as intended.

Figure 6.5 indicates that the coolant temperature increase from the upper plenum to the outlet plenum is lower than expected by about 10%. However, the expected

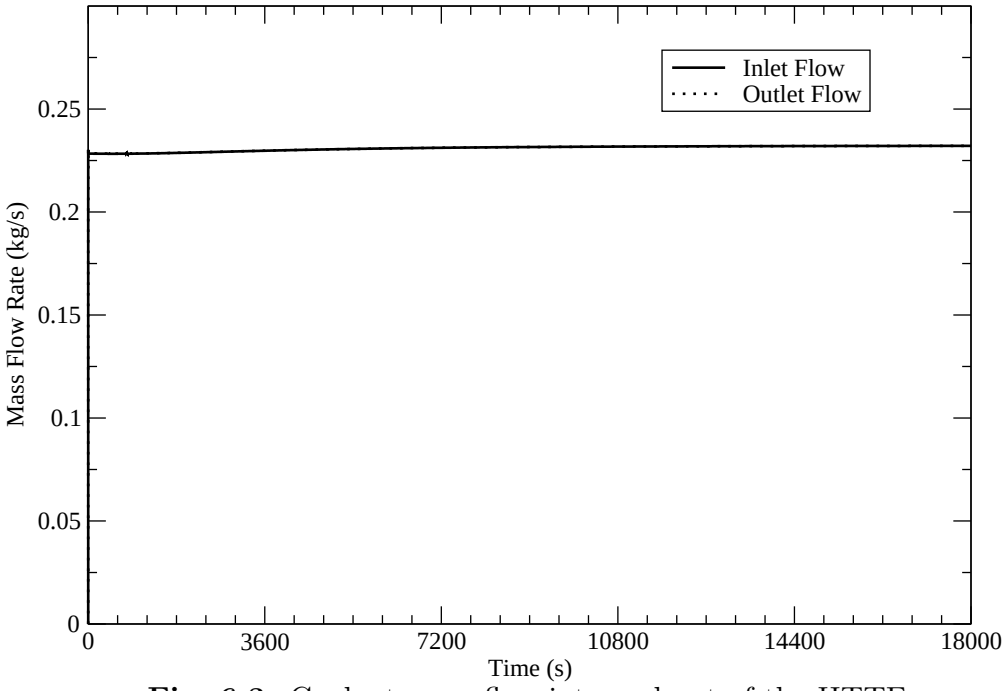

Fig. 6.3. Coolant mass flow into and out of the HTTF

value is based on a simple calculation using Equation 6.4. This equation assumes that the total core power goes toward heating the coolant. It does not account for heat losses to the boundary or to the central reflector. Since the entire system does not reach a steady state, and since the central and side reflectors and other structures are at temperatures below their steady-state values, the heat losses presented here are likely greater than they would be for the HTTF operating at an equilibrium condition. For this reason, temperatures are lower than expected. Still, the calculated thermal behavior of the core is reasonable.

Figures 6.6-6.8 show the coolant temperature distribution in the active core. The axial temperature increase is nearly uniform through the core, which is as expected for the specified uniform power profile. There is little variation in the radial coolant temperature profile. Again, this can be attributed to the constant volumetric heat rate in the core. Also, the side reflector is thick and has a very low thermal conductivity, so it acts like an insulator. This causes the core temperature profile to

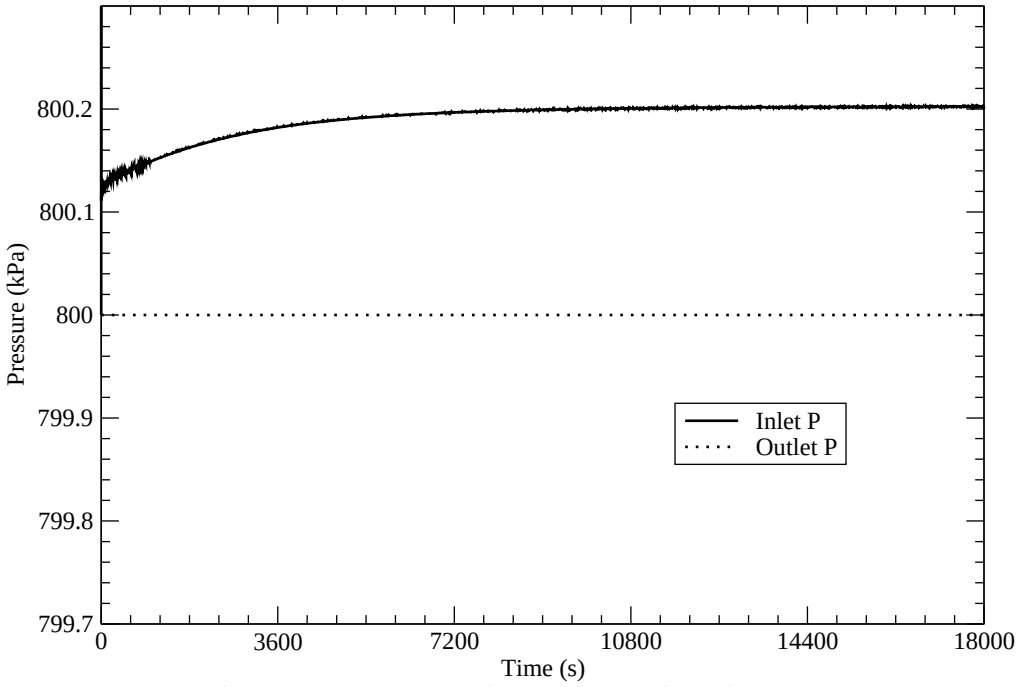

Fig. 6.4. HTTF coolant inlet and outlet pressure

resemble that of a slab with symmetry boundary conditions at either surface. Since the side reflector is not actually an adiabatic boundary, heat is transferred from ring 4 to the reflector. Therefore, temperatures in ring 4 are slightly lower than in rings 2 and 3. In the HTTF, it is unlikely that the thermal conductivity of the ceramic core material will be as low as it is in this model, so there should be a larger radial temperature gradient in the facility. Any changes to the facility design will be reflected in the MELCOR input deck.

As a result of the nearly flat coolant radial temperature profile, the core coolant flow distribution shown in Figure 6.9 is nearly uniform. Flow through the channels in ring 4 is slightly greater due to the lower temperatures in ring 4. This is because there is less flow resistance in ring 4 channels due to slightly lower coolant velocity.

The axial coolant velocity profile in coolant channels in ring 2 is plotted in Figure 6.10. Coolant velocity increases nearly uniformly with increasing temperature along the length of the core.

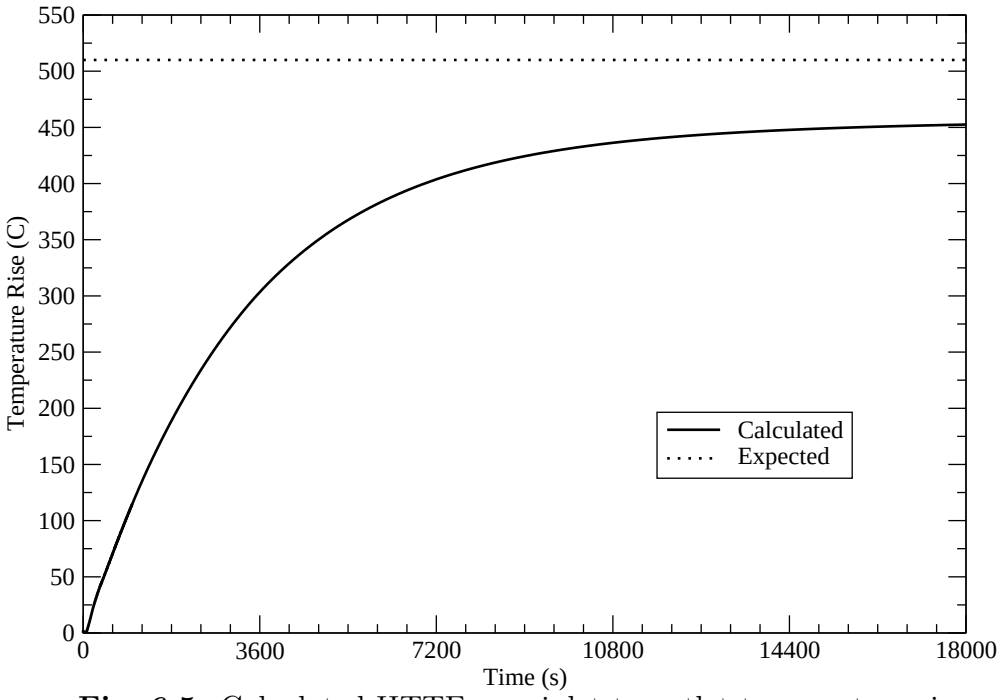

Fig. 6.5. Calculated HTTF core inlet-to-outlet temperature rise

Figures 6.11-6.13 show the ceramic block temperature distribution in the core. Axial and radial block temperature profiles are similar to the coolant temperature distribution. However, ceramic temperatures are significantly higher than coolant temperatures. Note that reported temperatures are average temperatures. Because the "cladding" is thick (1.4 cm, more than the coolant channel radius of 0.8 cm), and because the ceramic has a low thermal conductivity, there is a large temperature gradient across the ceramic block. The temperature of the coolant channel surface is likely much lower than the average temperature reported here.

Overall, calculated thermal hydraulic behavior is reasonable. Thus, steady-state results can be used to initialize transient calculations in order to test the DLOFC input.

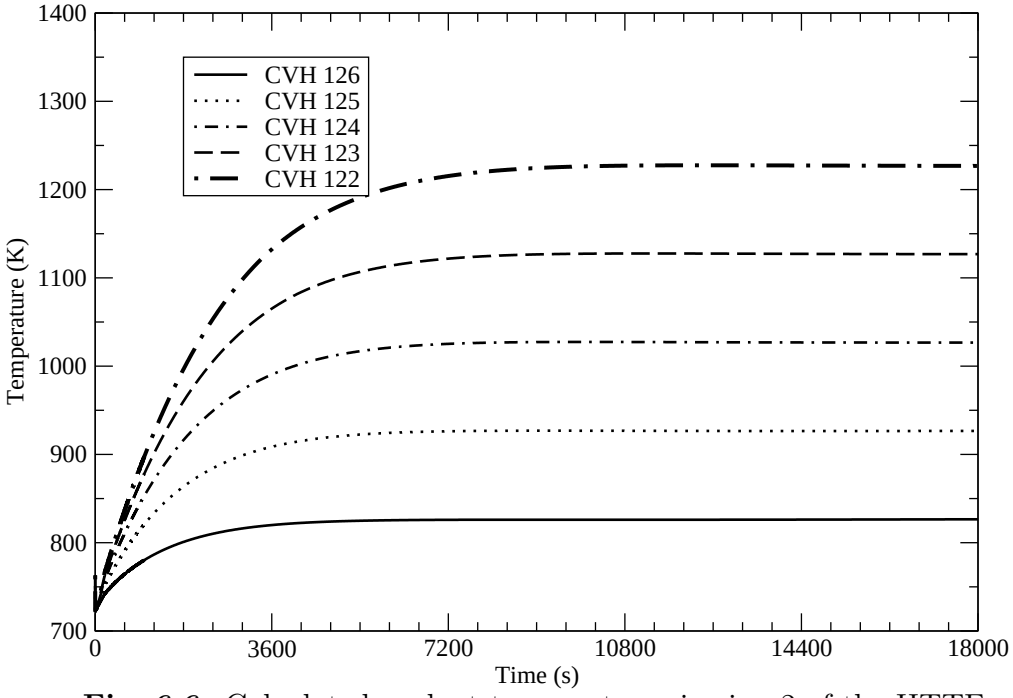

Fig. 6.6. Calculated coolant temperatures in ring 2 of the HTTF

6.5.2 DLOFC Results

Figure 6.14 shows the inlet and outlet pressure throughout the simulation. At 18,000 s plus one time step, inlet and outlet pressure drop instantaneously to 100 kPa. At the same time, a valve near the reactor inlet closes. Together, this simulates a complete break of the outlet pipe. Figures 6.15 and 6.16 display the mass flow rate from the inlet and to the outlet. These figures indicate that there is a very large increase in the mass flow rate through the outlet pipe after the pipe break. This flow rate quickly decreases as the vessel depressurizes. The very rapid depressurization (less than 1 ms) can be attributed to the low coolant inventory in the system. After the depressurization phase, flow through the break is approximately equal to zero.

Figures 6.17-6.19 show the ceramic block temperatures during the accident. As expected, temperatures rise rapidly due to the lack of coolant flow. The temperature rise is linear because the facility power is constant, as is the user-specified heat

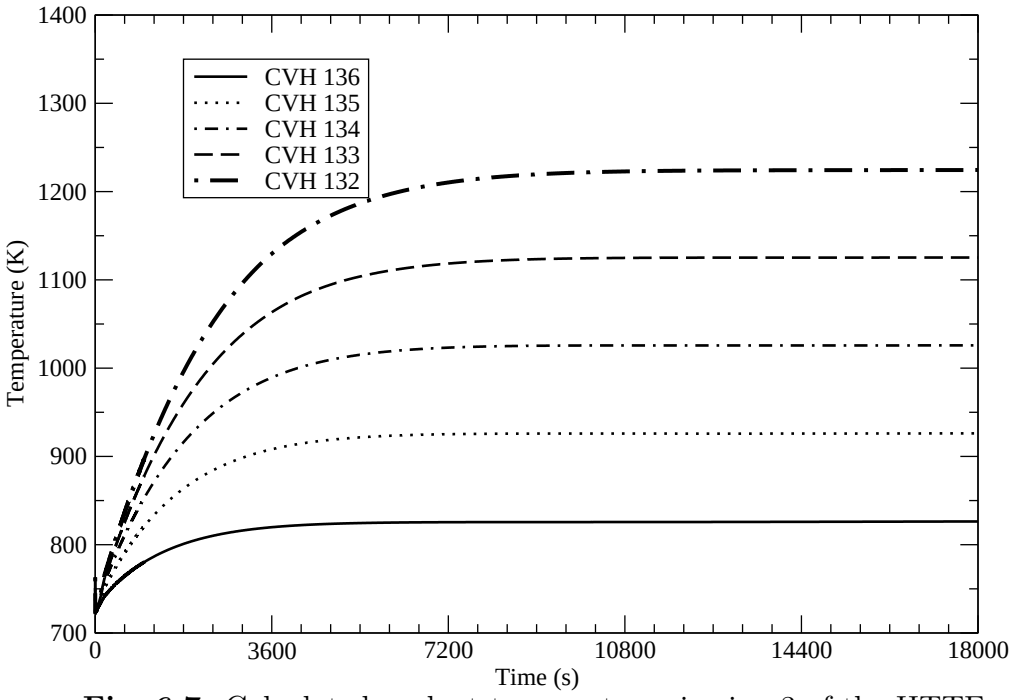

Fig. 6.7. Calculated coolant temperatures in ring 3 of the HTTF

capacity of the clad material. Again, block temperatures in ring 4 are lower than in rings 2 and 3 due to heat transfer to the COR boundary heat structures. Note that HTTF DLOFC tests will more than likely not be run with a constant heater power. Also note that the thermal conductivity of the ceramic material may be higher than the value used here.

The above results indicate that control logic for the DLOFC calculation is functioning properly. Thermal hydraulic behavior during the first few hours of the transient appears reasonable.

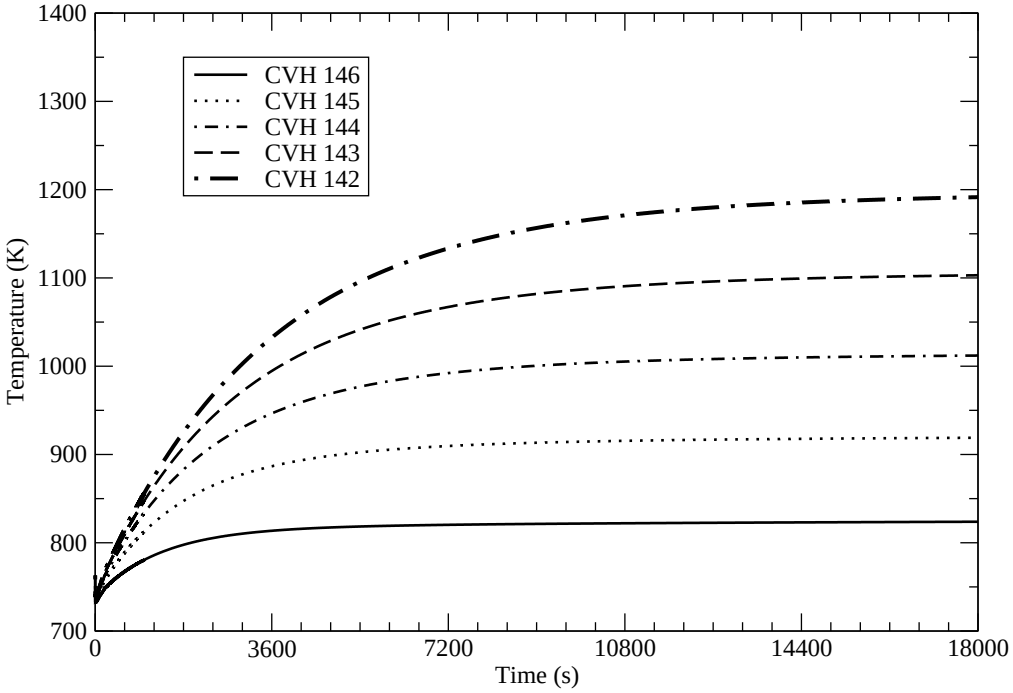

Fig. 6.8. Calculated coolant temperatures in ring 4 of the HTTF

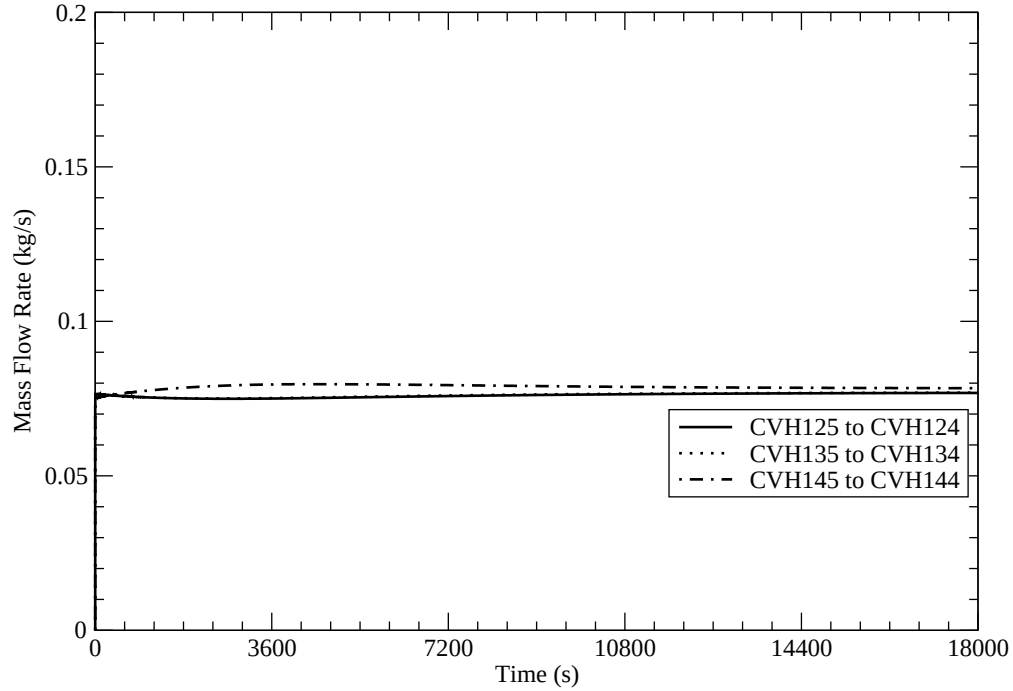

Fig. 6.9. Calculated flow distribution in the HTTF core

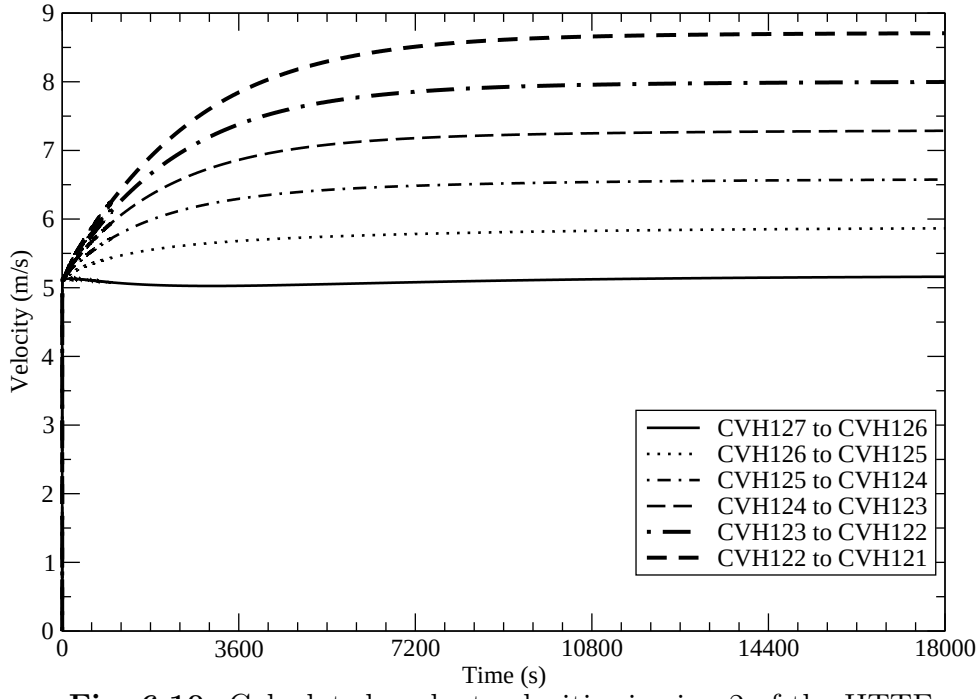

Fig. 6.10. Calculated coolant velocities in ring 2 of the HTTF

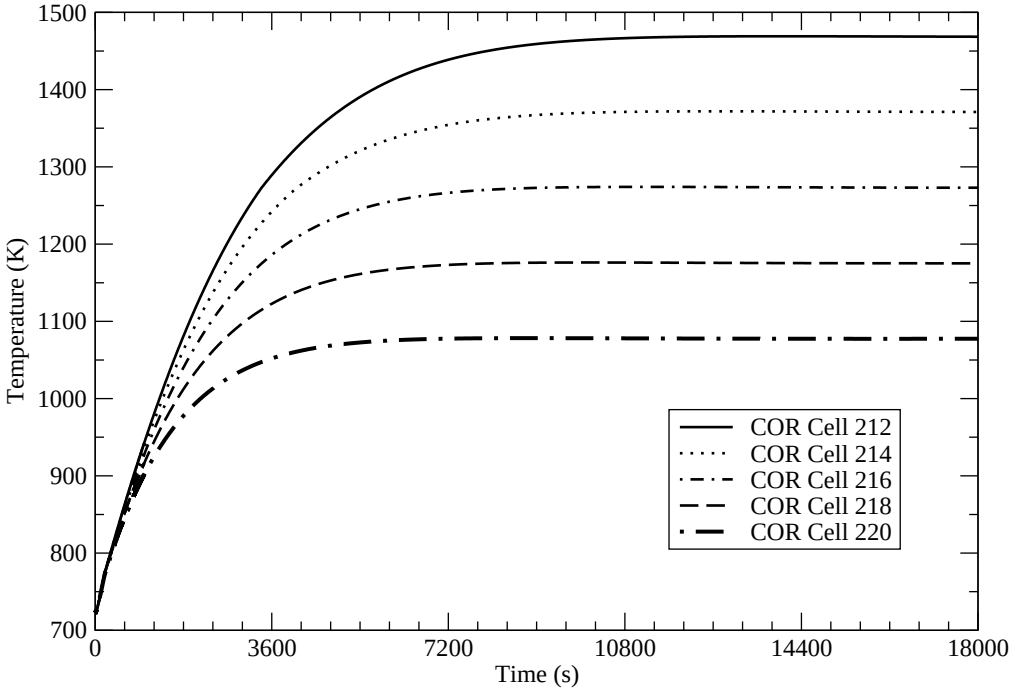

Fig. 6.11. Calculated ceramic temperatures in ring 2 of the HTTF

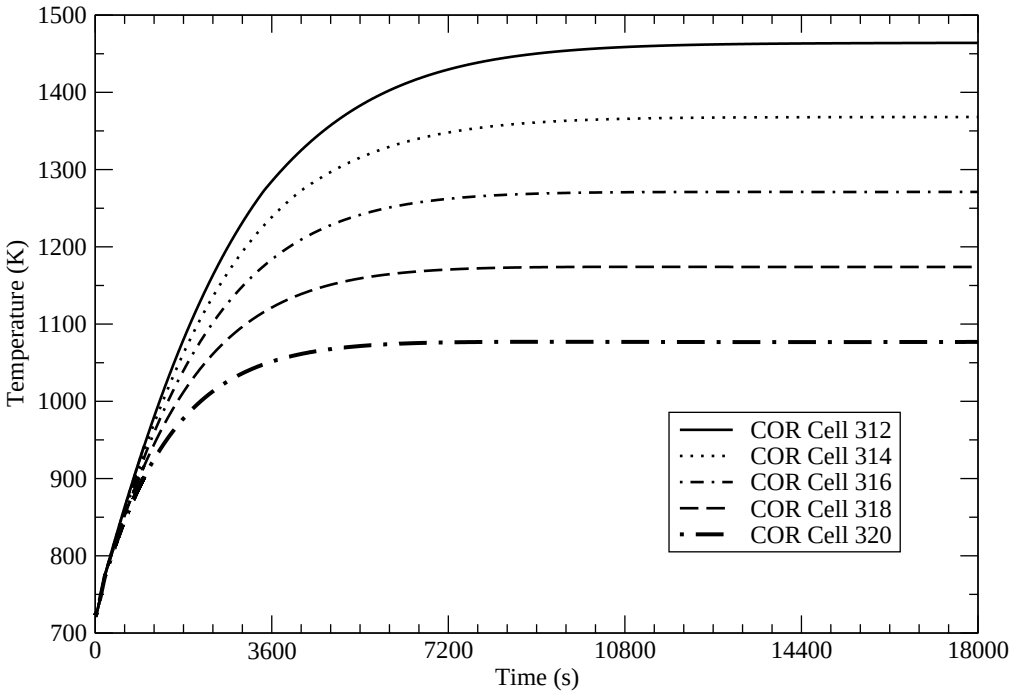

Fig. 6.12. Calculated ceramic temperatures in ring 3 of the HTTF

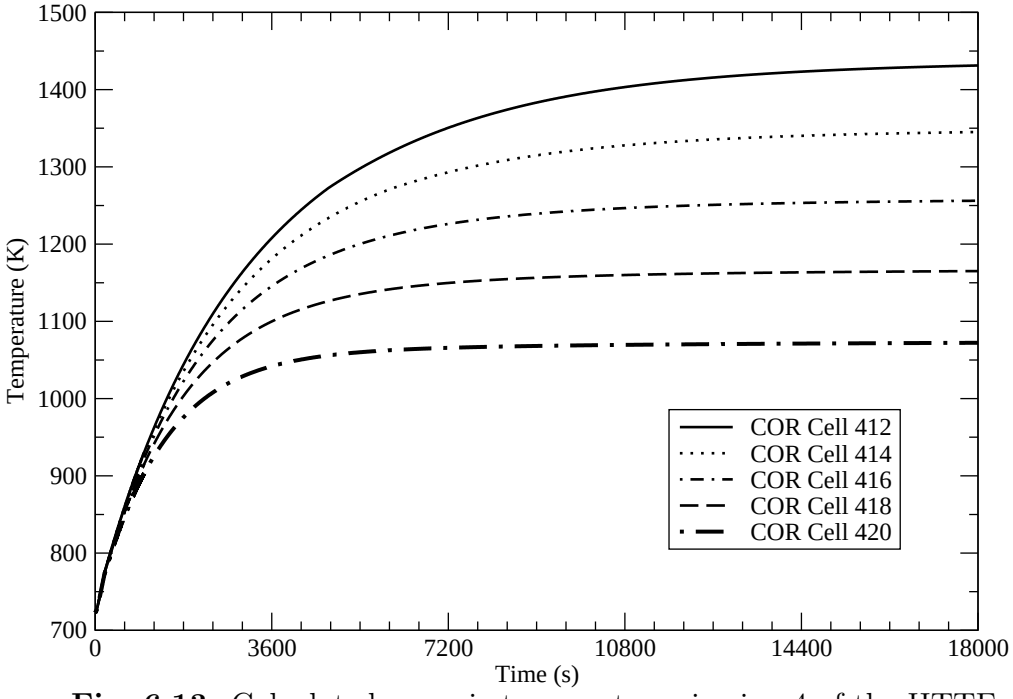

Fig. 6.13. Calculated ceramic temperatures in ring 4 of the HTTF

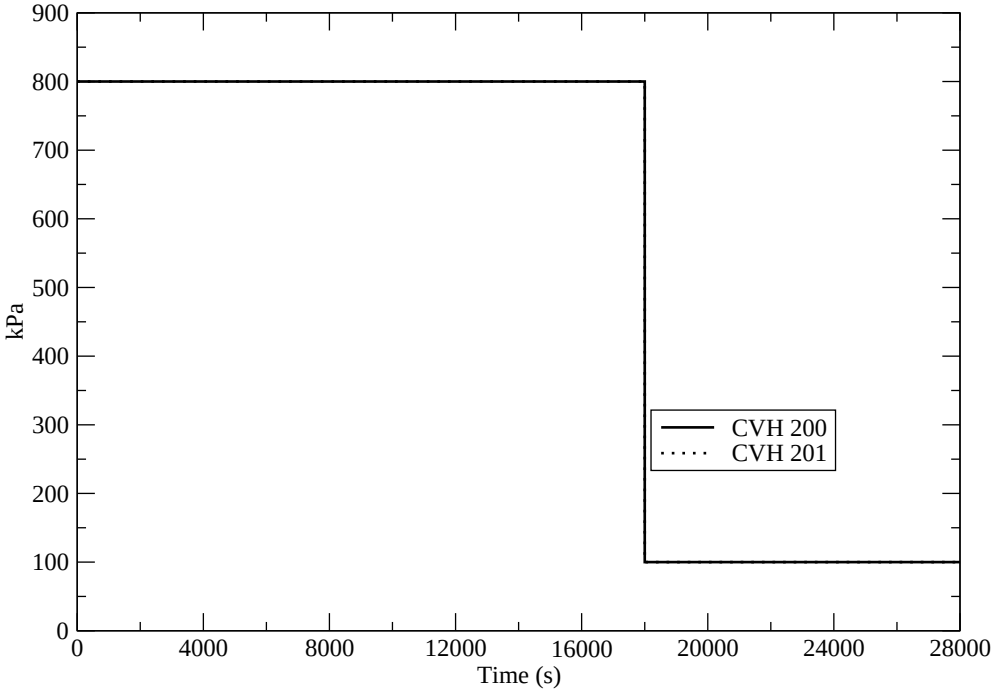

Fig. 6.14. HTTF coolant inlet and outlet pressure for a simulated pipe break at 18,000 s

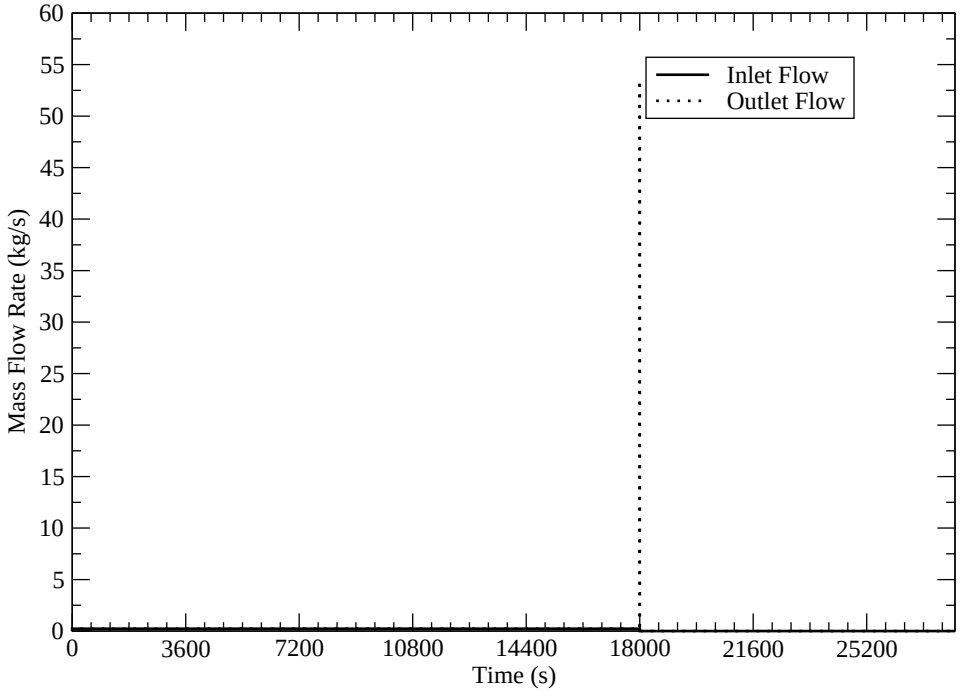

Fig. 6.15. Coolant mass flow into and out of the HTTF for a simulated pipe break at 18,000 s

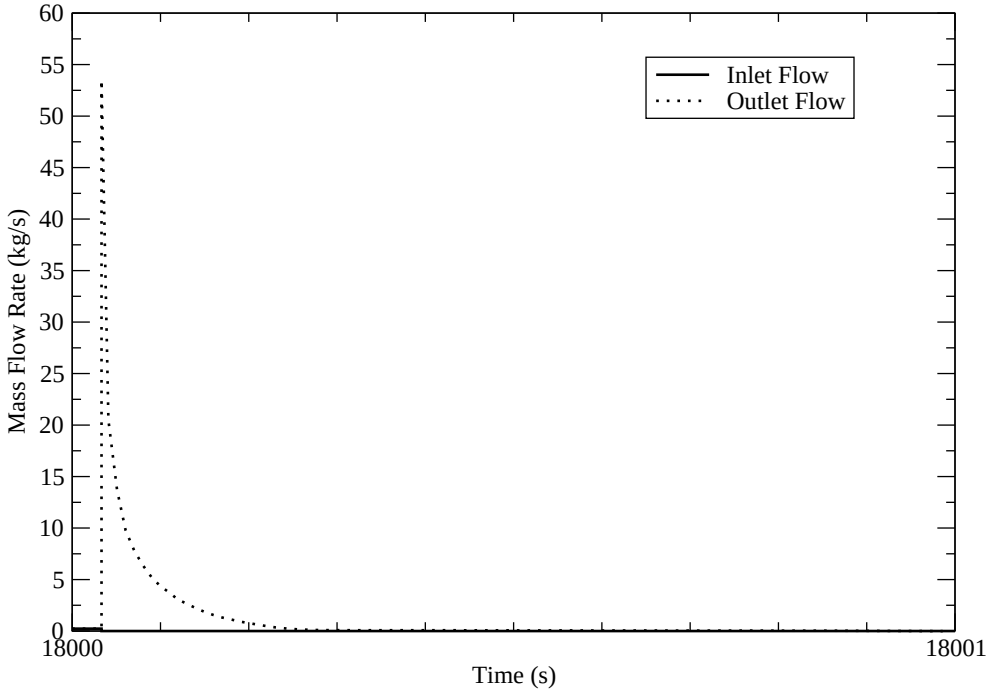

Fig. 6.16. Coolant mass flow into and out of the HTTF after a pipe break

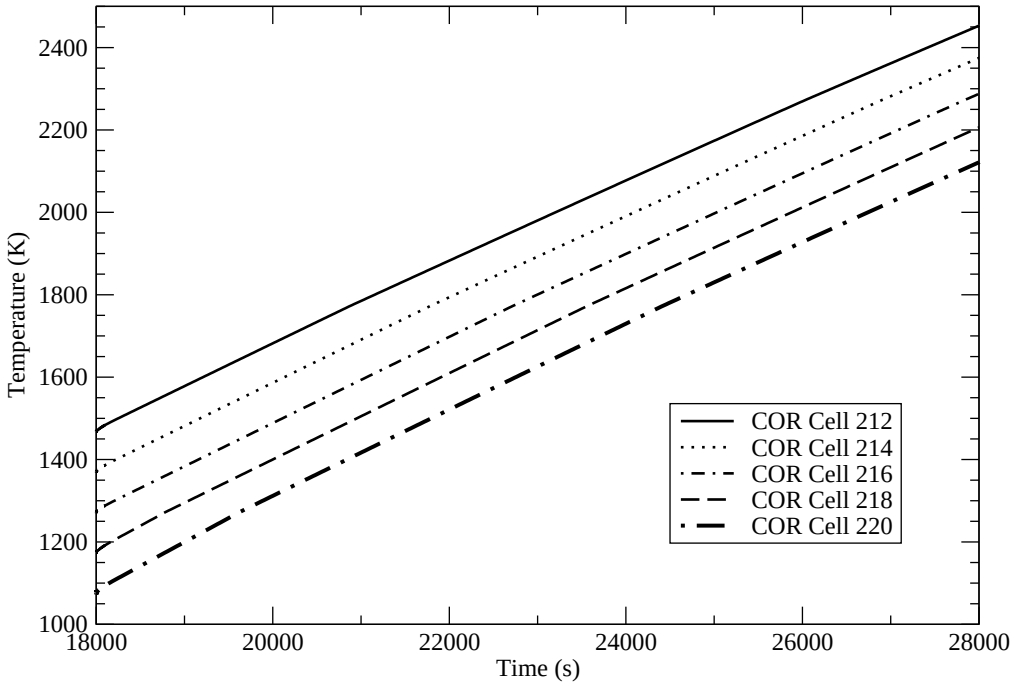

Fig. 6.17. Calculated post-DLOFC ceramic temperatures in HTTF ring 2

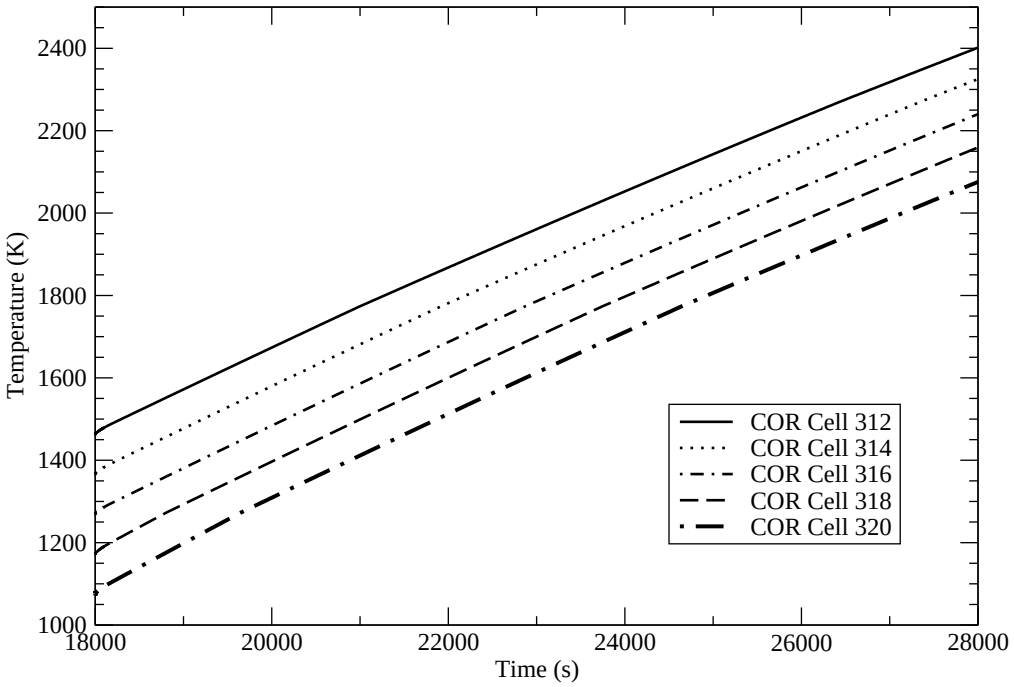

Fig. 6.18. Calculated post-DLOFC ceramic temperatures in HTTF ring 3

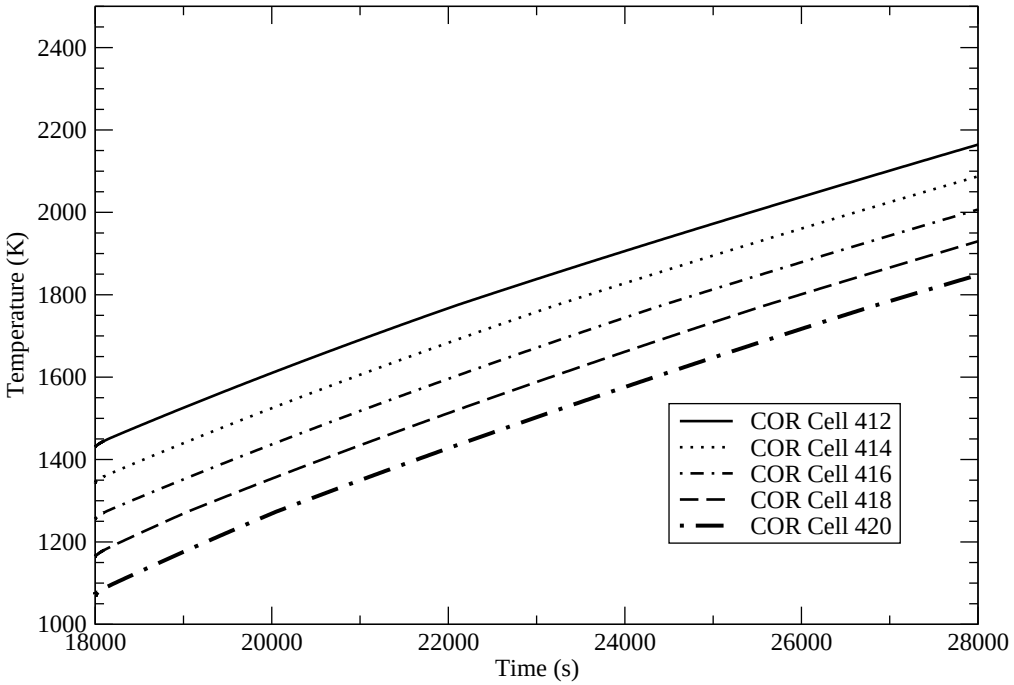

Fig. 6.19. Calculated post-DLOFC ceramic temperatures in HTTF ring 4

6.6 Validating MELCOR using Data from the HTTF

One of the goals of the HTTF is to provide data for validation of computer codes, including MELCOR. It is crucial to identify the data needed to validate MELCOR so that instrumentation can be procured and installed before testing begins at the HTTF.

Instrumentation is needed to measure gas and solid component temperatures, coolant flow rates, and heat fluxes at various axial and radial positions in the system. These locations must be carefully selected so that measured data corresponds to analytical results from MELCOR. Each control volume in MELCOR is at a uniform temperature. For example, the gas in 142 coolant holes between radii 18.6 cm and 29.8 cm and elevations 0.0 cm and 39.6 cm is represented by a single temperature in the MELCOR calculation. In the HTTF, these coolant holes are located around 76 heater rods producing approximately 40 kW in the control volume. Thus, there may be a large temperature difference between points at different axial, radial, and azimuthal locations in a given core CV in MELCOR. This suggests that many thermocouples may be needed to obtain a coolant temperature analogous to the temperature calculated by MELCOR. However, no more than six, and as few as three, thermocouples for each MELCOR CV should be sufficient. Proposed instrumentation arrangements are shown in Figure 6.20. Thermocouples should be placed at axial locations in the middle of the CVs. The measured temperature at the axial midpoint roughly corresponds to the average temperature in a given channel for a uniform axial power profile, which will likely be used for HTTF tests. Measured temperatures can be averaged, and measurement uncertainties can be statistically combined to give a coolant temperature of the form $\mu \pm \sigma$, where μ is the average temperature and σ is the uncertainty for the volume. These values can be compared to MELCOR results. Calculated MELCOR parameters can be said to match experimental results if the parameters fall within the uncertainty ranges of the data points.

Fig. 6.20. Possible thermocouple locations to measure average coolant temperature in a control volume

If these suggestions are followed, 63-126 thermocouples would be needed to obtain coolant temperatures for each control volume in the core and top and bottom reflectors. The same number of thermocouples would likely be needed to measure ceramic temperatures in the core and reflectors. In addition, instrumentation is needed to measure coolant temperatures in the inlet and outlet ducts; barrel and vessel temperature profiles; flow fields in the barrel-vessel gap, core, outlet plenum, and inlet and outlet ducts; pressure drop across the core and the primary test loop; and nitrogen and oxygen concentrations in the bottom reflector and core during an air ingress event. There will be hundreds of data measurement locations for each test run at the facility. An automated method is needed to process experimental data and compare it to results from MELCOR. Such a method can be developed using Python.

Python [85] is a high-level programming language, often compared to Perl, that combines the file-moving and text-processing capabilities of Unix shell scripts and Windows batch files with a large number of built-in functions and modules. These functions and modules provide features like mathematical calculations, file input and

output, and system calls. Python is easier and faster to use than languages like C or C++ and is available on Windows, Mac OS X, and Unix operating systems [86].

HTTF data manipulation, MELCOR data extraction, and HTTF and MELCOR data comparison and plotting can be driven by Python, either directly with built-in functions and modules or indirectly through calls to other software packages. A flow chart for a sample program that performs these tasks is shown in Figure 6.21.

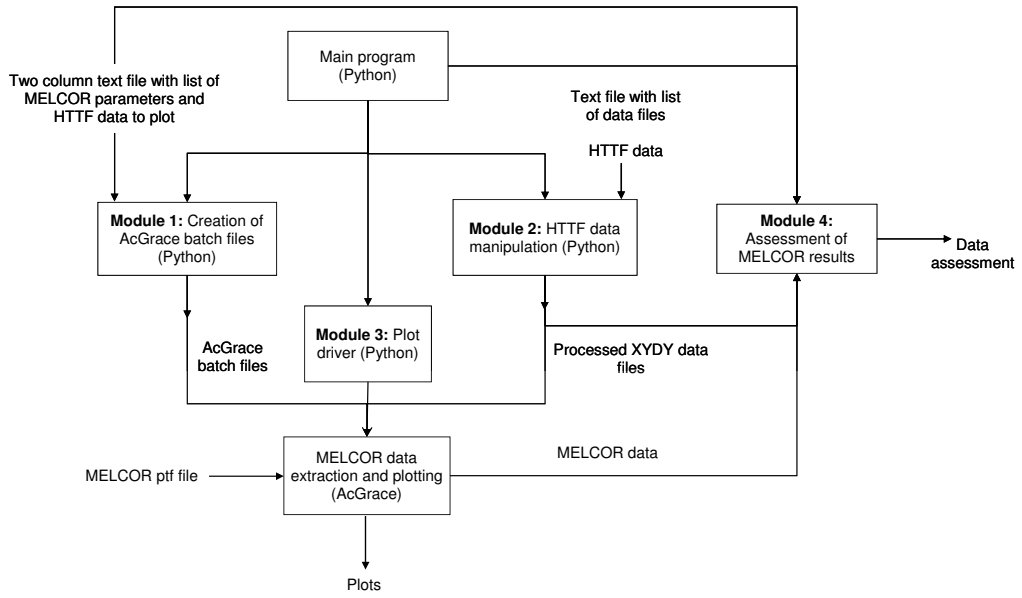

Fig. 6.21. Suggested program flow for HTTF and MELCOR data assessment and plotting

The proposed program is comprised of four Python modules controlled by a main program. Module 1 reads a text file with two columns, the first of which contains the names of MELCOR plot parameters, and the second of which contains the name of the HTTF data file corresponding to the MELCOR parameter in column one. For instance, the first line of the file may be

```
CVH-TVAP_123        T-COOL-123
```

where `T-COOL-123` is the name of a data file with the coolant temperature and associated measurement error as a function of time in the volume corresponding to MELCOR CVH123. The module then creates batch files to plot each pair of MELCOR and HTTF parameters in the text file with AcGrace. The plot appearance (including line styles, symbol styles, axis minimum and maximum values, and labels) can be fully specified in a batch file.

Module 2 reads a text file containing measured HTTF data parameters. Each line specifies the data points to be combined and the method to be used to perform this combination. For instance, the first line may read

```
T-COOL-123-1    T-COOL-123-2    T-COOL-123-3    T-COMBINE
```

where `T-COOL-123-n` is the coolant temperature, measured by thermocouple `n`, in the volume corresponding to MELCOR CVH123, and `T-COMBINE` is a method used to average temperatures and statistically combine their uncertainties. Methods are defined within this second module. The module creates files with processed HTTF data that will be plotted by the batch files created in module 1. Module 2 may also include some means by which to quantify uncertainties in the MELCOR results. However, methods for uncertainty quantification in large-scale simulations must first be developed. This is currently a major research topic at the Department of Energy [87].

Module 3 generates plots by running each batch file created by module 1. This module works by calling AcGrace for each batch file found in the present working directory. AcGrace reads a MELCOR parameter from the PTF file and an HTTF data file created by module 2. The MELCOR parameter, PTF file, and HTTF data file are all specified in each batch file. AcGrace can create plots in .pdf and .ps formats and can export MELCOR data in one of several formats (eg. scientific notation with three significant figures).

Plots generated by module 3 can provide a visual means by which to assess MELCOR results. However, module 4 provides for automated assessment. The

module reads the MELCOR and HTTF parameter text file. For each parameter pair in the file, module 4 determines whether or not MELCOR results lie within the bounds of the processed HTTF data. The module prints the results of this comparison, along with the relative error between the experimental (HTTF) and analytical (MELCOR) results, to a text file.

Python scripts similar to all four of these modules have been written and used to perform much of the analysis presented in this thesis. These scripts could easily be adapted to fit within the above program structure. This Python program can significantly speed up the process of manipulting raw HTTF data and comparing the manipulated data to MELCOR results.

Finally, since the HTTF is a scaled facility, care must be taken when relating results from the HTTF to actual reactor behavior. Guidance on this topic can be found in the HTTF scaling report [60].

6.7 Summary

A MELCOR input deck has been created for the HTTF at Oregon State University. This input is based on preliminary HTTF drawings and communications with researchers at OSU. Since the facility is still in the design phase, a large number of assumptions have been made in order to create a working input model. Assumptions will be addressed once the facility layout has been finalized.

Preliminary results from steady-state and accident calculations indicate that boundary conditions have been implemented correctly. The predicted thermal hydraulic behavior of the facility is reasonable, though further studies must be performed before a more definitive assessment of the calculations is issued. Before this is done, the input deck will be updated to reflect the final HTTF design.

Once the HTTF has been constructed, experimental data will be collected. This data will be compared to results from MELCOR HTTF calculations in order to validate MELCOR. A Python computer program has been proposed to automate

the validation process. The proposed program contains several modules similar to those written to perform the analysis found throughout this thesis.

7. CONCLUSIONS AND RECOMMENDATIONS

MELCOR input decks have been developed for a water-cooled reactor cavity cooling system, the 400 MW Pebble Bed Modular Reactor, and the High Temperature Test Facility. RCCS input development focuses primarily on modeling radiation view factors between the RPV and RCCS. The method developed here can be applied to any situation in which heat is transferred by radiation from the outside of a cylinder to the inside of a larger cylinder. The importance of flow losses on natural circulation flow rates and of the natural convection heat transfer correlation on heat removal rates has also been discussed in relation to the RCCS.

New input techniques that can be used to model HTGRs in MELCOR have been developed for the PBMR400 and the HTTF. These input decks represent the first efforts (beyond code testing at Sandia National Laboratories) to use the new gas-cooled reactor models in the code. Proper code input for HTGR fuel, cladding, and reflectors has been described above.

Lastly, suggestions have been made about instrumentation in the HTTF, and a method that can be used in the MELCOR validation process has been explained.

7.1 Conclusions

A methodology for modeling radiation heat transfer from the reactor pressure vessel to the RCCS in an HTGR has been developed based on an existing view factor relationship. This methodology can easily be applied to any situation in which heat is transferred by radiation between the outer surface of an inner cylinder and the inner surface of an outer cylinder (for example, from the core barrel to the RPV). Calculations performed with the water-cooled RCCS input deck demonstrate that MELCOR can be used to model a water-cooled reactor cavity cooling system, provided that RCCS piping schematics and cavity layout is available. Results show that buoyancy-driven flow develops in the cavity and the RCCS, driven by convection

from the RPV in the former case and by radiative heat transfer from the RPV to the RCCS pipes in the latter case. However, care must be taken when choosing form loss coefficients in the RCCS piping system. Underestimation of form losses leads to overprediction of coolant flow rates and the total RCCS heat removal rate. Nevertheless, input techniques developed here can be adopted for future water-cooled RCCS studies. Such an RCCS input model can be coupled to a full reactor deck to simulate HTGR performance.

A number of input techniques have been developed to model the 400 MW PBMR. New methods for calculating core component geometric parameters – such as fuel, clad, and supporting structure masses and surface areas, and channel flow areas and hydraulic diameters – are explained. Proper input for the new reflector component in MELCOR is described in detail. Also, control logic has been developed and implemented in the PBMR-400 deck to simulate pressurized and depressurized loss of forced cooling accidents. These input techniques can be used in future pebble bed reactor analyses with MELCOR. In general, steady-state and transient results for calculations performed with the MELCOR PBMR-400 deck created here compare well to results from the computer codes used in the benchmark.

Additional input techniques have been developed to model the HTTF. These techniques address the unique modeling challenges presented by prismatic block-type reactors, namely the hexagonal arrangement of fuel compacts and coolant channels in a graphite block. Methods for calculating geometric parameters for the "clad" (i.e. the graphite associated with a fuel compact and coolant channel) are described. Input methods used to model reflectors in the PBMR-400 are applied here to model reflectors in the HTTF.

Preliminary results from MELCOR calculations with the HTTF input deck appear reasonable. However, it is impossible to say conclusively whether or not MELCOR is accurately predicting HTGR behavior. Code comparisons and other analytic studies are useful activities for assessing MELCOR results and for identifying areas

of future research, but a code cannot be validated without experimental data. MELCOR – or any other analysis tool – cannot be used for any studies until it has been validated. Unfortunately, HTGR thermal hydraulic behavior is unavailable, and will remain unavailable until the HTTF commences operation. Once HTTF thermal hydraulic data is collected, a computer program simular to the Python program proposed here should be utilized to speed up the validation process. The proposed program includes modules similar to modules used to perform analyses for this thesis. These modules can be easily modified to perform the functions needed for a partial validation of MELCOR for HTGR analyses.

In the mean time, there are a number of improvements that can be made to MELCOR so that the code is better suited to HTGR analysis by the time the HTTF project enters the testing phase.

7.2 Recommendations

HTGRs differ significantly in terms of design and behavior when compared to the LWRs MELCOR was created to model. The new GCR models implemented in MELCOR 2.1 address many of the unique aspects of HTGRs, notably the prismatic block or pebble bed core geometry and the effects this geometry has on heat transfer and fluid flow in the reactor core; the presence of graphite reflectors; and graphite oxidation. In addition, the most recent code update allows for conduction between reflectors in two adjacent COR rings. This feature is missing from the version of the code used for these analyses, and as a result, rings 7 and 8 in the PBMR input deck were replaced by heat structures. Now, the 8-ring input model described in Section 5.2.1 can be used for future PBMR studies.

These code modifications significantly improve the code as an HTGR analysis tool. Still, several additional enhancements are needed. In particular, the following issues should be addressed:

- The COR reflector component should be able to support fuel and cladding and should be self-supporting. This would allow the user to model bottom and top reflectors as RF, instead of as supporting structures. While this would require the addition of models for graphite structural behavior, it would eliminate the need for complicated input techniques while still allowing reflector oxidation.

- The heat transfer correlation for forced convective flow over a spherical particle should be reevaluated. This correlation is appropriate for low Reynolds number flows, but heat transfer coefficients predicted by this correlation differ significantly from those given by the suggested correlation [79] for convection from a packed bed. Data from heated bed studies are needed to resolve this issue.

At the same time, future work should focus on refining the HTGR modeling techniques developed here. Studies should be performed using the 8-ring PBMR-400 input deck to determine how the reflectors affect code results. The ability of reflectors to conduct heat in both the axial and radial directions could affect peak fuel temperatures during accident calculations by lowering the temperature of the reflectors adjacent to core hot spots.

Finally, the HTTF deck created here must be modified to reflect the final HTTF design, once facility drawings become available. Once this is done, pre-test calculations should be performed to provide input to the facility designers about the instrumentation plan. Post-test calculations will be compared to experimental results in order to validate MELCOR for HTGR applications. Validation will be a difficult task, but the guidance provided in this thesis can provide a starting point for these efforts.

The input techniques described in this thesis can be applied to future HTGR studies with MELCOR. Together, these new input techniques and the suggested code improvements will allow for increasingly best-estimate MELCOR HTGR calcu-

lations, which can be partially validated using the modular Python program proposed in this thesis.

REFERENCES

[1] M.B. Sellman, R.S. Johnson, W.H. Bohlke, Strategic plan for light water reactor research and development, Technical Report, U.S. Department of Energy/Nuclear Power Institute, Feb. 2004.

[2] Gen IV International Forum annual report 2007, Technical Report, Gen IV International Forum, 2007.

[3] Current status and future development of modular high temperature gas cooled reactor technology, Technical Report IAEA-TECDOC-1198, International Atomic Energy Agency, Feb. 2001.

[4] NGNP point design - results of the initial neutronics and thermal-hydraulic assessments during FY 2003, Technical Report, Idaho National Engineering and Environmental Laboratory, Sept. 2003.

[5] MELCOR computer code manuals vol. 1: Primer and users' guide, version 2.1, Technical Report NUREG/CR-6119, Sandia National Laboratories, Sept. 2008.

[6] MELCOR computer code manuals vol. 2: Reference manual, Technical Report NUREG/CR-6119, Sandia National Laboratories, Sept. 2008.

[7] M.F. Young, MELCOR development for HTGR applications, in: Proceedings from the MELCOR Workshop, Bethesda, MD, Sept. 2009, U.S. Nuclear Regulatory Commission, Rockville, MD.

[8] S. Basu, Status of the NRC HTGR R&D activities, in: Proceedings from the Cooperative Severe Accident Research Program, Bethesda, MD, Sept. 2009, U.S. Nuclear Regulatory Commission, Rockville, MD.

[9] Nuclear power plant licensing process, Technical Report NUREG/BR-0298, Rev. 2, U.S. Nuclear Regulatory Commission, Jul. 2009.

[10] Next generation nuclear plant pre-conceptual design report, Technical Report, Idaho National Laboratory, Nov. 2007.

[11] S.J. Ball, S.E. Fisher, Next generation nuclear plant phenomena identification and ranking tables (PIRTs), Technical Report NUREG/CR-6944, U.S. Nuclear Regulatory Commission, Mar. 2008.

[12] K. Hogan, Pebble bed modular reactor analysis with MELCOR, Master's thesis, Purdue University, Aug. 2006.

[13] H. Al-kaabi, Severe accident analysis methods for pebble bed modular reactors, Master's thesis, Purdue University, May 2007.

[14] D. Barbier, F. Bertrand, D. Haubensack, P. Aujollet, N. Alpy, Massive H2 production (I/S cycle) with VHTR heating: Preliminary designs & safety approach for coupling, in: Proceedings from the 3rd Topical Meeting on High Temperature Reactor Technology, Johannesburg, South Africa, Oct. 2006, International Atomic Energy Agency, Vienna, Austria.

[15] C.H. Oh, E.S. Kim, Method and system for the production of hydrogen at reduced VHTR outlet temperatures, in: Proceedings from the 13th International Topical Meeting on Nuclear Reactor Thermal Hydraulics NURETH-13, Kanazawa, Japan, Oct. 2009, American Nuclear Society, La Grange, IL.

[16] J. Lamarsh, A. Baratta, Introduction to Nuclear Engineering, 3rd ed., Prentice Hall, Upper Saddle River, NJ, 2001.

[17] A technology roadmap for Generation IV nuclear energy systems, Technical Report, Gen IV International Forum, Dec. 2002.

[18] R. Versluis, Next Generation Nuclear Plant/Very High Temperature Reactor, in: Proceedings from the NGNP Research and Development FY-09 Technical Review Meeting, Las Vegas, NV, May 2009, U.S. Department of Energy, Washington, DC.

[19] Next generation nuclear plant methods research and development technical program plan, Technical Report INL/EXT-06-11804, Idaho National Laboratory, Sept. 2008.

[20] World list of nuclear power plants, Nuclear News, 51 (3)(2008) 39–63.

[21] H. Fenech, Heat Transfer and Fluid Flow in Nuclear Systems, Pergamon Press Inc., Elmsford, NY, 1981.

[22] D.A. Copinger, D.L. Moses, Fort St. Vrain gas cooled reactor operational experience, Technical Report NUREG/CR-6839, U.S. Nuclear Regulatory Commission, Jan. 2004.

[23] Status of innovative small and medium sized reactor designs 2005, Technical Report IAEA-TECDOC-1485, International Atomic Energy Agency, Mar. 2006.

[24] R.F. Turner, R.D. Burnette, W.J. Scheffel, HTGR fuel performance in the Peach Bottom reactor, Technical Report, Gulf General Atomic, Jul. 1973.

[25] P.J. Venter, M.N. Mitchell, F. Fortier, PBMR reactor design and development, in: Proceedings from the 18th International Conference on Structural Mechanics in Reactor Technology (SMiRT 18), Beijing, China, Aug. 2005, International Association for Structural Mechanics in Reactor Technology.

[26] Fuel performance and fission product behavior in gas cooled reactors, Technical Report IAEA-TECDOC-978, International Atomic Energy Agency, Nov. 1997.

[27] W. Schenk, G. Pott, H. Nabielek, Fuel accident performance testing for small HTRs, Journal of Nuclear Materials, 171 (1)(1990) 19–30.

[28] J.J. Duderstadt, L.J. Hamilton, Nuclear Reactor Analysis, John Wiley & Sons, New York, NY, 1976.

[29] Heat transport and afterheat removal for gas cooled reactors under accident conditions, Technical Report IAEA-TECDOC-1163, International Atomic Energy Agency, 2000.

[30] R.L. Moore, C.H. Oh, B.J. Merrill, D.A. Petti, Studies on air ingress for pebble bed reactors, in: Proceedings of the Conference on High Temperature Reactors, Petten, the Netherlands, Apr. 2002, International Atomic Energy Agency, Vienna, Austria.

[31] R.N. Morris, D.A. Petti, D.A. Powers, B.E. Boyack, TRISO-coated particle fuel phenomena identification and ranking tables (PIRTs) for fission product transport due to manufacturing, operations, and accidents, Technical Report NUREG/CR-6844, U.S. Nuclear Regulatory Commission, Jul. 2004.

[32] P.J. Venter, M.N. Mitchell, Integrated design approach of the pebble bed modular reactor using models, Nuclear Engineering and Design, 237 (12-13)(2007) 1341–1353.

[33] Department of HTTR Project at the Oarai Research Establishment, Design of high temperature engineering test reactor (HTTR), Technical Report JAERI-1332, Japan Atomic Energy Research Institute, Sept. 1994.

[34] Z. Gao, B. Lee, Z. Jiang, Benchmark problem definition and analysis on HTR-10, Technical Report, Institute of Nuclear Energy Technology, Tsinghua University, Nov. 1997.

[35] K. Fleming, PBMR auxiliary systems, in: PBMR Safety and Design Familiarization, Mar. 2006, PBMR (Pty) Ltd.

[36] Bechtel National Inc, 450 MWt reactor cavity cooling system design description, Technical Report DOE-HTGR-90016, Department of Energy, Nov. 1993.

[37] M.T. Farmer, D.J. Kilsdonk, C.P. Tzanos, S. Lomperski, R.W. Aeschlimann, D. Pointer, Topical report: Natural convection shutdown heat removal test facility (NSTF) evaluation for generating additional reactor cavity cooling system (RCCS) data, Technical Report ANL-GenIV-058, Argonne National Laboratory, Sept. 2005.

[38] H. Sato, R. Johnson, R. Schultz, Preliminary studies of coolant by-pass flows in a prismatic very high temperature reactor using computational fluid dynamics, in: Proceedings from the NGNP Research and Development FY-09 Technical Review Meeting, Kanazawa, Japan, Oct. 2009, American Nuclear Society, La Grange, IL.

[39] S. Ball, Sensitivity studies of modular high-temperature gas-cooled reactor postulated accidents, Nuclear Engineering and Design, 236 (5-6)(2006) 454–462.

[40] S. Revankar, K. Vierow, Development of design and simulation model and safety study of large-scale hydrogen production using nuclear power, Technical Report PU/NE 06-14, Sandia National Laboratories/U.S. Department of Energy, Sept. 2006.

[41] H. Haque, W. Feltes, G. Brinkmann, Thermal response of a high temperature reactor during passive cooldown under pressurized and depressurized conditions, in: Proceedings from the 2nd Topical Meeting on High Temperature Reactor Technology, Beijing, China, Sept. 2004, International Atomic Energy Agency, Vienna, Austria.

[42] H.D. Gougar, The application of the PEBBED code suite to the PBMR-400 coupled code benchmark - FY 2006 annual report, Technical Report INL/EXT-06-11842, Idaho National Laboratory, Sept. 2006.

[43] C. Oh, E. Kim, R. Schultz, M. Patterson, D. Petti, Thermal hydraulics of the very high temperature gas cooled reactor, in: Proceedings from the NGNP Research and Development FY-09 Technical Review Meeting, Kanazawa, Japan, Oct. 2009, American Nuclear Society, La Grange, IL.

[44] V. Seker, T.J. Downar, High temperature gas cooled reactor analysis with PARCS/AGREE, in: Proceedings from the NRC-VHTR Program Review Meeting, College Station, TX, Feb. 2009, U.S. Nuclear Regulatory Commission.

[45] E.A. Harvego, S.M.M. Reza, M. Richards, A. Shenoy, An evaluation of reactor cooling and coupled hydrogen production processes using the modular helium reactor, Nuclear Engineering and Design, 236 (14-16)(2006) 1481–1489.

[46] F.G. Cocheme, J. Freixa, Y.A. Hassan, Transient analysis of advanced gas cooled reactor using ATHENA-3D, in: Transactions of the American Nuclear Society, Washington, DC, Nov. 2004, American Nuclear Society, La Grange, IL.

[47] E. Moore, RELAP5-3D model validation and benchmark exercises for advanced gas cooled reactor applications, Master's thesis, Texas A&M University, May 2006.

[48] A. Kadak, T. Zhai, Air ingress benchmarking with computational fluid dynamics analysis, in: Proceedings from the 2nd Topical Meeting on High Temperature Reactor Technology, Beijing, China, Sept. 2004, International Atomic Energy Agency, Vienna, Austria.

[49] J. Simoneau, J. Champigny, B. Mays, L. Lommers, Three-dimensional simulation of the coupled conductive, convective, and radiative heat transfer during decay heat removal in an HTR, Nuclear Engineering and Design, 237 (15-17)(2007) 1923–1937.

[50] G.P. Greyvenstein, H.J. van Antwerpen, A finite volume-based network method for the prediction of heat, mass, and momentum transfer in a pebble bed reactor, in: Proceedings of the Conference on High Temperature Reactors, Petten, the Netherlands, Apr. 2002, International Atomic Energy Agency, Vienna, Austria.

[51] P.G. Rousseau, C.G. du Toit, W.A. Landman, Validation of a transient thermal-fluid systems CFD model for a packed bed high temperature gas-cooled nuclear reactor, in: Proceedings from the 2nd Topical Meeting on High Temperature Reactor Technology, Beijing, China, Sept. 2004, International Atomic Energy Agency, Vienna, Austria.

[52] M.P. van Staden, Analysis of effectiveness of cavity cooling system, in: Proceedings from the 2nd Topical Meeting on High Temperature Reactor Technology, Beijing, China, Sept. 2004, International Atomic Energy Agency, Vienna, Austria.

[53] C. Oh, C. Davis, G.C. Park, RCCS experiments and validation for high temperature gas-cooled reactor, in: Proceedings from the 12th International Topical Meeting on Nuclear Reactor Thermal Hydraulics NURETH-12, Pittsburgh, PA, Oct. 2009, American Nuclear Society, La Grange, IL.

[54] N. Amini, Y.A. Hassan, Proper orthogonal decomposition analysis of jet flows injecting into a rod bundle, in: Transactions of the American Nuclear Society Winter Meeting, Washington, DC, Nov. 2009, American Nuclear Society, La Grange, IL.

[55] Y. Hassan, E.E. Dominguez-Ontiveros, Flow visualization in a pebble bed reactor experiment using PIV and refractive index matching techniques, Nuclear Engineering and Design, 238 (11)(2008) 3080–3085.

[56] H.F. Nieben, The SANA-I-experiments for self-operating removal of afterheat, in: IAEA Research Co-ordination Meeting on Heat Transport and Afterheat Removal for Gas-cooled Reactors under Accident Conditions, Vienna, Austria, Nov. 1993. International Atomic Energy Agency, Vienna, Austria.

[57] R. Schultz, S. Ball, J. King, Catalogue of validation data for gas-cooled reactor operational and accident scenarios, Technical Report INEEL/EXT-04-02294, Idaho National Engineering and Environmental Laboratory, Sept. 2004.

[58] Evaluation of high temperature gas cooled reactor performance: Benchmark analysis related to initial testing of the HTTR and HTR-10, Technical Report IAEA-TECDOC-1382, International Atomic Energy Agency, Nov. 2003.

[59] B.G. Woods, Introduction to HTTF, in: VHTR Cooperative Agreement Program Review Meeting, Ann Arbor, MI, Oct. 2009, U.S. Nuclear Regulatory Commission.

[60] B.G. Woods, R.B. Jackson, B.L. Nelson, Scaling analysis for the very high temperature reactor test facility at oregon state university, Technical Report Draft, Oregon State University, Feb. 2009.

[61] S. Cadell, HTTF design description, in: VHTR Cooperative Agreement Program Review Meeting, Ann Arbor, MI, Oct. 2009, U.S. Nuclear Regulatory Commission.

[62] N. Bixler, Overview and status of MACCS, in: Proceedings from the MELCOR Workshop, Bethesda, MD, Sept. 2009, U.S. Nuclear Regulatory Commission, Rockville, MD.

[63] A. Sharon, J.L. Crocker, R.E. Henry, MAAP-GRAAPH. a nuclear power plant accident simulation tool, in: Proceedings of the SCS Multiconference on Simulators VI, Tampa, FL, Mar. 1989. Society for Computer Simulation International, San Diego, CA.

[64] Idaho National Engineering and Environmental Laboratory, SCDAP/RELAP5-3D code manual, volume 1: Code architecture and interface of thermal hydraulic and core behavior models, Technical Report INEEL/EXT-02-00589, Idaho National Engineering and Environmental Laboratory, 2003.

[65] K. Vierow, Y. Liao, J. Johnson, M. Kenton, R. Gauntt, Severe accident analysis of a PWR station blackout with the MELCOR, MAAP4 and SCDAP/RELAP5 codes, Nuclear Engineering and Design, 234 (1-3)(2004) 129–145.

[66] B.J. Merrill, R.L. Moore, S.T. Polkinghorne, D.A. Petti, Modifications to the MELCOR code for application in fusion accident analyses, Fusion Engineering and Design, 51-52:555–563, 2000.

[67] S.B. Rodriguez, R.O. Gauntt, R. Cole, F. Gelbard, K. McFadden, T. Drennen, B. Martin, Transient analysis of sulfur-iodine cycle experiments and very high temperature reactor simulations using MELCOR-H2, Nuclear Technology, 166 (1)(2009) 76–85.

[68] M. Richards, H. Choi, NGNP parameter fuel and reactor pressure vessel temperature calculations, in: Proceedings from the NGNP Research and Development FY-09 Technical Review Meeting, Kanazawa, Japan, Oct. 2009, American Nuclear Society, La Grange, IL.

[69] A. Woaye-Hune, S. Ehster, Calculation of decay heat removal transient by passive means for a direct cycle modular HTGR, in: Proceedings of the Conference on High Temperature Reactors, Petten, the Netherlands, Apr. 2002, International Atomic Energy Agency, Vienna, Austria.

[70] H.D. Gougar, C.B. Davis, Reactor pressure vessel temperature analysis for prismatic and pebble-bed VHTR designs, Technical Report INL/EXT-06-11057, Idaho National Laboratory, Apr. 2006.

[71] F. Reitsma, K. Ivanov, T. Downar, H. de Haas, S. Sen, G. Strydom, R. Mphahlele, B. Tyobeka, V. Seker, H.D. Gougar, H.C. Lee, PBMR couple neutronics/thermal hydraulics transient benchmark the PBMR-400 core design, Technical Report, Nuclear Energy Agency, Organization for Economic Co-operation and Development, Jun. 2007.

[72] N. Zhen, Prismatic modular reactor analysis, Master's thesis, Texas A&M University, Dec. 2008.

[73] F.R. Incropera, D.P. DeWitt, Fundamentals of Heat and Mass Transfer, John Wiley & Sons, Hoboken, NJ, 6th ed., 2006.

[74] R.L. Reid, J.S. Tennant, Annular ring view factors, AIAA Journal, 11 (10)(1973) 1446–1448.

[75] R. Siegel, J.R. Howell, Thermal Radiation Heat Transfer, Taylor & Francis, New York, NY, 4th ed., 2002.

[76] R.B. Bird, W.E. Stewart, E.N. Lightfoot, Transport Phenomena, John Wiley & Sons, Hoboken, NJ, 2nd ed., 2002.

[77] Y.A. Çengel, J.M. Cimbala, Fluid Mechanics: Fundamentals and Applications, McGraw-Hill, New York, NY, 1st ed., 2006.

[78] E. Achenbach, Heat, flow characteristics of packed beds, Experimental Thermal and Fluid Science, 10:17–27, 1995.

[79] Geschftsstelle des Kerntechnischen Ausschusses, Reactor core design of high-temperature gas-cooled reactors part 2: Heat transfer in spherical fuel elements, Technical Report KTA 3102.2, Nuclear Safety Standards Commission (KTA), Jun. 1983.

[80] N.E. Todreas, M.S. Kazimi, Nuclear Systems I: Thermal Hydraulic Fundamentals, Taylor & Francis, New York, NY, 1989.

[81] F. Reitsma, G. Strydom, OECD 400 MW PBMR benchmark: Transient case 3 comparison results, in: OECD/NEA/NSC PBMR Coupled Neutronics/Thermal Hydraulics Transient Benchmark - 5th Workshop, Interlaken, Switzerland, Sept. 2009. Organisation for Economic Cooperation and Development, Paris, France.

[82] S. Cadell, "Re: HTTF drawings", 3 Feb. 2010, Personal communication.

[83] J. Kelly, V. Seker, Preliminary HTTF pebble bed scoping studies with AGREE, in: VHTR Cooperative Agreement Program Review Meeting, Ann Arbor, MI, Oct. 2009, U.S. Nuclear Regulatory Commission.

[84] Preliminary safety information document for the standard MHTGR, Technical Report HTGR-86-024, U.S. Department of Energy, Sept. 1992.

[85] G. van Rossum, F.L. Drake, Jr., The Python language reference, release 2.6.4, Technical Report, Python Software Foundation, Jan. 2010.

[86] G. van Rossum, F.L. Drake, Jr., Python tutorial, release 2.6.4, Technical Report, Python Software Foundation, Jan. 2010.

[87] Final whitepaper – verification, validation, and uncertainty quantification panel, in: Science Based Nuclear Energy Systems Enabled by Advanced Modeling and Simulation at the Extreme Scale, Crystal City, VA, May 2009. U.S. Department of Energy.

[88] National Institute of Standards and Technology, Thermophysical properties of fluid systems, 1 Feb. 2010, <http://webbook.nist.gov/chemistry/fluid/>.

APPENDIX A
PLOT PARAMETERS

Below is a list of MELCOR parameters plotted in this thesis. Each table entry includes the figure number, the legend string of each data set displayed on the graph, and the corresponding MELCOR variable for each data set. In some cases, the values calculated by MELCOR have been manipulated. These manipulations are noted by footnotes to the table.

Table A.1: MELCOR parameters plotted in each figure

Figure	Legend String	MELCOR Variable
5.4	Inlet Flow	FL-MFLOW_200
	Outlet Flow	FL-MFLOW_210
5.5	Inlet Flow	FL-VELVAP_200
	Outlet Flow	FL-VELVAP_210
5.6	RPV Inlet	CVH-TVAP_170
	Outlet Plenum	CVH-TVAP_100
5.7	Expected Value	y = 400
	Calculated Value	CVH-TVAP_170 [a]
		CVH-TVAP_100
5.8	TAMU-MELCOR	CVH-TVAP_100
	(Benchmark Codes)	— [b]
5.9	—	COR-EBND-RAT
5.10	COR Cell 227	COR-TFU_227
	COR Cell 221	COR-TFU_221
	COR Cell 216	COR-TFU_216
	COR Cell 211	COR-TFU_211

[a] The core temperature rise is equal to CVH-TVAP_100 – CVH-TVAP_170.
[b] Data taken from the PBMR-400 benchmark final distribution [71].

Table A.1 (continued)

Figure	Legend String	MELCOR Variable
	COR Cell 206	COR-TFU_206
5.11	COR Cell 327	COR-TFU_327
	COR Cell 321	COR-TFU_321
	COR Cell 316	COR-TFU_316
	COR Cell 311	COR-TFU_311
	COR Cell 306	COR-TFU_306
5.12	COR Cell 427	COR-TFU_427
	COR Cell 421	COR-TFU_421
	COR Cell 416	COR-TFU_416
	COR Cell 411	COR-TFU_411
	COR Cell 406	COR-TFU_406
5.13	COR Cell 527	COR-TFU_527
	COR Cell 521	COR-TFU_521
	COR Cell 516	COR-TFU_516
	COR Cell 511	COR-TFU_511
	COR Cell 506	COR-TFU_506
5.14	COR Cell 627	COR-TFU_627
	COR Cell 621	COR-TFU_621
	COR Cell 616	COR-TFU_616
	COR Cell 611	COR-TFU_611
	COR Cell 606	COR-TFU_606
5.15	MELCOR	CFVALU_906:927 [c]
	Benchmark Code	— [b]
5.16	MELCOR	CFVALU_906:927 [c]
	Benchmark Code	— [b]

[c]CFs determine the average fuel temperatures for axial levels 6:27.

Table A.1 (continued)

Figure	Legend String	MELCOR Variable
5.17	MELCOR	COR-TFU_RZZ [d]
		COR-TCL_RZZ
	Benchmark Code	— [e]
5.18	CVH 125	CVH-TVAP_125
	CVH 124	CVH-TVAP_124
	CVH 123	CVH-TVAP_123
	CVH 122	CVH-TVAP_122
	CVH 121	CVH-TVAP_121
5.19	CVH 135	CVH-TVAP_135
	CVH 134	CVH-TVAP_134
	CVH 133	CVH-TVAP_133
	CVH 132	CVH-TVAP_132
	CVH 131	CVH-TVAP_131
5.20	CVH 145	CVH-TVAP_145
	CVH 144	CVH-TVAP_144
	CVH 143	CVH-TVAP_143
	CVH 142	CVH-TVAP_142
	CVH 141	CVH-TVAP_141
5.21	CVH 155	CVH-TVAP_155

[d]For each cell RZZ, R=2:6, ZZ=06:27, the average pebble temperature =0.58(TFU)+0.42(TCL). The average pebble temperature for each level ZZ =[1.1589(T2)+1.3405(T3)+1.5221(T4)+1.7037(T5)+1.8853(T6)]/7.6105, where TR is the average pebble temperature in cell RZZ, 1.1589:1.8853 are the areas of rings 2:6, and 7.6105 is the total empty bed flow area. Thus, the plotted parameters are volume-weighted average pebble temperatures for each axial level ZZ.

[e]For each cell RZZ, R=2:6, ZZ=06:27, the average pebble temperature =0.00868(Tfuel)+(1-0.00868)(Tmod). The average pebble temperature for each level ZZ =[1.1589(T2)+1.3405(T3)+1.5221(T4)+1.7037(T5)+1.8853(T6)]/7.6105, where TR is the average pebble temperature in cell RZZ, 1.1589:1.8853 are the areas of rings 2:6, and 7.6105 is the total empty bed flow area. Thus, the plotted parameters are volume-weighted average pebble temperatures for each axial level ZZ.

Table A.1 (continued)

Figure	Legend String	MELCOR Variable
	CVH 154	CVH-TVAP_154
	CVH 153	CVH-TVAP_153
	CVH 152	CVH-TVAP_152
	CVH 151	CVH-TVAP_151
5.22	CVH 165	CVH-TVAP_165
	CVH 164	CVH-TVAP_164
	CVH 163	CVH-TVAP_163
	CVH 162	CVH-TVAP_162
	CVH 161	CVH-TVAP_161
5.23	MELCOR	CFVALU_826:847 [f]
	Benchmark Code	— [b]
5.24	—	CVH-P_181 [g]
		CVH-P_210
5.25	—	CVH-P_170 [h]
		CVH-P_100
5.26	TAMU-MELCOR	CVH-P_181 [g]
		CVH-P_210
	(Benchmark Codes)	— [b]
5.27	TAMU-MELCOR	CVH-P_170 [h]
		CVH-P_100
	(Benchmark Codes)	— [b]
5.28	Flow Path 125	FL-MFLOW_125 [i]
	Flow Path 124	FL-MFLOW_124

[f]CFs determine the average helium temperature for axial levels 6:27.
[g]The reactor inlet-to-outlet pressure drop is equal to CVH-P_181 – CVH-P_210.
[h]The core pressure drop is equal to CVH-P_170 – CVH-P_100.
[i]The plotted parameters are FL-MFLOW_1RZ / AR, where AR is the flow area in ring R. This gives the mass flux.

Table A.1 (continued)

Figure	Legend String	MELCOR Variable
	Flow Path 123	FL-MFLOW_123
	Flow Path 122	FL-MFLOW_122
	Flow Path 121	FL-MFLOW_121
	Flow Path 120	FL-MFLOW_120
5.29	Flow Path 135	FL-MFLOW_135 [i]
	Flow Path 134	FL-MFLOW_134
	Flow Path 133	FL-MFLOW_133
	Flow Path 132	FL-MFLOW_132
	Flow Path 131	FL-MFLOW_131
	Flow Path 130	FL-MFLOW_130
5.30	Flow Path 145	FL-MFLOW_145 [i]
	Flow Path 144	FL-MFLOW_144
	Flow Path 143	FL-MFLOW_143
	Flow Path 142	FL-MFLOW_142
	Flow Path 141	FL-MFLOW_141
	Flow Path 140	FL-MFLOW_140
5.31	Flow Path 155	FL-MFLOW_155 [i]
	Flow Path 154	FL-MFLOW_154
	Flow Path 153	FL-MFLOW_153
	Flow Path 152	FL-MFLOW_152
	Flow Path 151	FL-MFLOW_151
	Flow Path 150	FL-MFLOW_150
5.32	Flow Path 165	FL-MFLOW_165 [i]
	Flow Path 164	FL-MFLOW_164
	Flow Path 163	FL-MFLOW_163
	Flow Path 162	FL-MFLOW_162

Table A.1 (continued)

Figure	Legend String	MELCOR Variable
	Flow Path 161	FL-MFLOW_161
	Flow Path 160	FL-MFLOW_160
5.33	Flow Path 221	FL-MFLOW_221 [j]
	Flow Path 231	FL-MFLOW_231
	Flow Path 241	FL-MFLOW_241
	Flow Path 251	FL-MFLOW_251
5.34	Flow Path 222	FL-MFLOW_222 [j]
	Flow Path 232	FL-MFLOW_232
	Flow Path 242	FL-MFLOW_242
	Flow Path 252	FL-MFLOW_252
5.35	Flow Path 223	FL-MFLOW_223 [j]
	Flow Path 233	FL-MFLOW_233
	Flow Path 243	FL-MFLOW_243
	Flow Path 253	FL-MFLOW_253
5.36	Flow Path 224	FL-MFLOW_224 [j]
	Flow Path 234	FL-MFLOW_234
	Flow Path 244	FL-MFLOW_244
	Flow Path 254	FL-MFLOW_254
5.37	Flow Path 225	FL-MFLOW_225 [j]
	Flow Path 235	FL-MFLOW_235
	Flow Path 245	FL-MFLOW_245
	Flow Path 255	FL-MFLOW_255
5.38	Inlet Flow	FL-MFLOW_200 [k]
5.39	Inlet CV	CVH-P_200 [k]

[j]The plotted parameters are FL-MFLOW_2RZ / A, where A =2πr DZ, r is the radius of ring R, and DZ is the flow path height.
[k]Parameter plotted for the first 25 s of the transient.

Table A.1 (continued)

Figure	Legend String	MELCOR Variable
	Outlet CV	CVH-P_210
5.40	—	COR-EFPD-RAT [k]
5.41	MELCOR	COR-EFPD-RAT
	Benchmark	— [b]
5.42	COR Cell 227	COR-TFU_227
	COR Cell 221	COR-TFU_221
	COR Cell 216	COR-TFU_216
	COR Cell 211	COR-TFU_211
	COR Cell 206	COR-TFU_206
5.43	—	COR-TFU_RZZ [l]
5.44	—	COR-TFU_RZZ [l]
5.45	—	COR-TFU_RZZ [l]
5.46	—	COR-TFU_RZZ [l]
5.47	—	COR-TFU_RZZ [l]
5.48	MELCOR	CFVALU_906:927 [c]
5.50	Flow Path 125	FL-MFLOW_125
	Flow Path 124	FL-MFLOW_124
	Flow Path 123	FL-MFLOW_123
	Flow Path 122	FL-MFLOW_122
	Flow Path 121	FL-MFLOW_121
	Flow Path 120	FL-MFLOW_120
5.51	Flow Path 135	FL-MFLOW_135
	Flow Path 134	FL-MFLOW_134
	Flow Path 133	FL-MFLOW_133

[l]Fuel temperature distribution (i.e. temperature as a function of axial and radial position) in the active core plotted at the specified moment in time.

Table A.1 (continued)

Figure	Legend String	MELCOR Variable
	Flow Path 132	FL-MFLOW_132
	Flow Path 131	FL-MFLOW_131
	Flow Path 130	FL-MFLOW_130
5.52	Flow Path 145	FL-MFLOW_145
	Flow Path 144	FL-MFLOW_144
	Flow Path 143	FL-MFLOW_143
	Flow Path 142	FL-MFLOW_142
	Flow Path 141	FL-MFLOW_141
	Flow Path 140	FL-MFLOW_140
5.53	Flow Path 155	FL-MFLOW_155
	Flow Path 154	FL-MFLOW_154
	Flow Path 153	FL-MFLOW_153
	Flow Path 152	FL-MFLOW_152
	Flow Path 151	FL-MFLOW_151
	Flow Path 150	FL-MFLOW_150
5.54	Flow Path 165	FL-MFLOW_165
	Flow Path 164	FL-MFLOW_164
	Flow Path 163	FL-MFLOW_163
	Flow Path 162	FL-MFLOW_162
	Flow Path 161	FL-MFLOW_161
	Flow Path 160	FL-MFLOW_160
5.55	Flow Path 221	FL-MFLOW_221
	Flow Path 231	FL-MFLOW_231
	Flow Path 241	FL-MFLOW_241
	Flow Path 251	FL-MFLOW_251
5.56	Flow Path 222	FL-MFLOW_222

Table A.1 (continued)

Figure	Legend String	MELCOR Variable
	Flow Path 232	FL-MFLOW_232
	Flow Path 242	FL-MFLOW_242
	Flow Path 252	FL-MFLOW_252
5.57	Flow Path 223	FL-MFLOW_223
	Flow Path 233	FL-MFLOW_233
	Flow Path 243	FL-MFLOW_243
	Flow Path 253	FL-MFLOW_253
5.58	Flow Path 224	FL-MFLOW_224
	Flow Path 234	FL-MFLOW_234
	Flow Path 244	FL-MFLOW_244
	Flow Path 254	FL-MFLOW_254
5.59	Flow Path 225	FL-MFLOW_225
	Flow Path 235	FL-MFLOW_235
	Flow Path 245	FL-MFLOW_245
	Flow Path 255	FL-MFLOW_255
5.60	—	CFVALU_770 [m]
5.62	Inlet Flow	FL-MFLOW_200 [k]
5.63	Inlet CV	CVH-P_200 [k]
	Outlet CV	CVH-P_210
5.64	—	COR-EFPD-RAT [k]
5.65	COR Cell 227	COR-TFU_227
	COR Cell 221	COR-TFU_221
	COR Cell 216	COR-TFU_216
	COR Cell 211	COR-TFU_211

[m] CF determines the total radiation heat removal rate from the RPV by summing HS-RAD-FLUX for each RPV HS, then multiplying the sum by 46.4 (the surface area of each RPV HS).

Table A.1 (continued)

Figure	Legend String	MELCOR Variable
	COR Cell 206	COR-TFU_206
6.3	Inlet Flow	FL-MFLOW_200
	Outlet Flow	FL-MFLOW_201 [n]
		FL-MFLOW_202
6.4	Inlet P	CVH-P_160
	Outlet P	CVH-P_201
6.5	Expected Value	y = 510
	Calculated Value	CVH-TVAP_108 [o]
		CVH-TVAP_62
		CVH-TVAP_61
6.6	CVH 126	CVH-TVAP_126
	CVH 125	CVH-TVAP_125
	CVH 124	CVH-TVAP_124
	CVH 123	CVH-TVAP_123
	CVH 122	CVH-TVAP_122
6.7	CVH 136	CVH-TVAP_136
	CVH 135	CVH-TVAP_135
	CVH 134	CVH-TVAP_134
	CVH 133	CVH-TVAP_133
	CVH 132	CVH-TVAP_132
6.8	CVH 146	CVH-TVAP_146
	CVH 145	CVH-TVAP_145
	CVH 144	CVH-TVAP_144
	CVH 143	CVH-TVAP_143

[n]Outlet flow is the sum of flow in flow paths 201 and 202.
[o]The temperature rise is equal to (CVH-TVAP_62+CVH-TVAP_61)/2 – CVH-TVAP_108.

Table A.1 (continued)

Figure	Legend String	MELCOR Variable
	CVH 142	CVH-TVAP_142
6.9	CVH 125 to CVH 124	FL-MFLOW_124
	CVH 135 to CVH 134	FL-MFLOW_134
	CVH 145 to CVH 144	FL-MFLOW_144
6.10	CVH 127 to CVH126	FL-MFLOW_126
	CVH 126 to CVH125	FL-MFLOW_125
	CVH 125 to CVH124	FL-MFLOW_124
	CVH 124 to CVH123	FL-MFLOW_123
	CVH 123 to CVH122	FL-MFLOW_122
	CVH 122 to CVH121	FL-MFLOW_121
6.11	COR Cell 212	COR-TCL_212
	COR Cell 214	COR-TCL_214
	COR Cell 216	COR-TCL_216
	COR Cell 218	COR-TCL_218
	COR Cell 220	COR-TCL_220
6.12	COR Cell 312	COR-TCL_312
	COR Cell 314	COR-TCL_314
	COR Cell 316	COR-TCL_316
	COR Cell 318	COR-TCL_318
	COR Cell 320	COR-TCL_320
6.13	COR Cell 412	COR-TCL_412
	COR Cell 414	COR-TCL_414
	COR Cell 416	COR-TCL_416
	COR Cell 418	COR-TCL_418
	COR Cell 420	COR-TCL_420
6.14	CVH 200	CVH-P_200

Table A.1 (continued)

Figure	Legend String	MELCOR Variable
	CVH 201	CVH-P_201
6.15	Inlet Flow	FL-MFLOW_200
	Outlet Flow	FL-MFLOW_201 [n]
		FL-MFLOW_202
6.16	Inlet Flow	FL-MFLOW_200
	Outlet Flow	FL-MFLOW_201 [n]
		FL-MFLOW_202
6.17	COR Cell 212	COR-TCL_212
	COR Cell 214	COR-TCL_214
	COR Cell 216	COR-TCL_216
	COR Cell 218	COR-TCL_218
	COR Cell 220	COR-TCL_220
6.18	COR Cell 312	COR-TCL_312
	COR Cell 314	COR-TCL_314
	COR Cell 316	COR-TCL_316
	COR Cell 318	COR-TCL_318
	COR Cell 320	COR-TCL_320
6.19	COR Cell 412	COR-TCL_412
	COR Cell 414	COR-TCL_414
	COR Cell 416	COR-TCL_416
	COR Cell 418	COR-TCL_418
	COR Cell 420	COR-TCL_420

APPENDIX B
PBMR-400 CALCULATION NOTEBOOK

This is the calculation notebook for the PBMR-400 MELCOR input deck with 8 radial rings. Unless otherwise noted, the input is based on reference [71]. MELCOR input requirements are described in reference [5]. The steady-state input deck includes the following files:

pbmr400.inp Most of the input for the PBMR-400

pbmr400-src_sink.inp Coolant source and sink specifications and control logic for transient calculations

decay-heat.inp Decay heat input for transient calculations

viewfactors.inp View factors for heat structures

The files **pbmr400-plofc.inp** and **pbmr400-dlofc.inp** contain input for the pressurized and depressurized loss of forced cooling with SCRAM transient exercises described in the benchmark.

B.1 pbmr400.inp

B.1.1 PBMR Environmental Data

CARD	*WORD*	*VALUE*	*BASIS*
MEG_DIAGFILE	—	'pbmr400g.dia'	Filename for MELGEN diagnostic output
MEL_DIAGFILE	—	'pbmr400.dia'	Filename for MELCOR diagnostic output
MEG_OUTPUTFILE	—	'pbmr400g.out'	Filename for MELGEN listing output
MEL_OUTPUTFILE	—	'pbmr400.out'	Filename for MELCOR listing output

PLOTFILE	—	'pbmr400.ptf'	Filename for binary plot data
MEG_RESTARTFILE	—	'pbmr400.rst'	Filename for binary file used to restart MELCOR calculation
MEL_RESTARTFILE	—	'pbmr400.rst'	Filename for binary file used to restart MELCOR calculation
	CYCLE	CYCLE	Calculation restarted at cycle specified on NREST
	NREST	-1	Calculation restarted at last available restart listing
MESSAGEFILE	—	'pbmr400.mes'	Filename for event message output
STATUSFILE	—	'MELSTT_v2-0'	Filename for MELCOR status file
STOPFILE	—	'MELSTP_v2-0'	Filename for MELCOR stop file
WRITENEWINP	—	'pbmr400.txt'	Filename for echoed input

B.1.2 PBMR MELGEN EXEC Input

CARD	*WORD*	*VALUE*	*BASIS*
EXEC_INPUT	—	—	EXEC package start record
EXEC_TITLE	—	'400-MW PBMR (SS)'	Title of calculation
EXEC_JOBID	—	'pbmr400 -'	Job identifier

B.1.3 PBMR COR Input

CARD	*WORD*	*VALUE*	*BASIS*
COR_RT	IRTYP	PBR	Reactor type PBR (pebble bed reactor) selected
	MCRP	B4C	Control rod poison. Not used in the calculation.
COR_GP	RFUEL	0.025	Radius of the fuel. For PBRs, the fueled region of each pebble is considered the 'fuel'. [a]
	RCLAD	0.030	Radius of the clad. For PBRs, the graphite shell around the fueled region of the pebble is the 'clad'.
	DRGAP	0.0	Gap between the fuel and clad. There is no gap in pebble bed fuel.
	PITCH	0.06	Pebble-to-pebble pitch, taken to be equal to the distance between the centers of two pebbles in contact with one another, which is simply the pebble diameter. This parameter appears to have no effect on the calculation.
COR_VP	RCOR	2.606	Outer radius for the COR package in the active region (i.e. the outer radius of the outermost radial ring)

[a] Unless otherwise noted, dimensions are taken from the benchmark problem definition [71]

RVESS	2.606	Vessel radius used by the lower head models. In reality, the vessel radius would be 3.28; however, since lower head behavior is not of interest to this calculation, and since selecting RVESS > RCOR would complicate input requirements, choosing RVESS = RCOR is acceptable.
ILHTRN	RVESS	Reactor lower head transition type. Has no significance for this calculation.
DZRV	0.18	Thickness of the cylindrical portion of the vessel
DZLH	0.18	Thickness of the lower head inside the transition radius specified by ILHTRN. DZLH and DZRV are equal to the physical vessel thickness defined in the benchmark.
ILHTYP	FLAT	Flat lower head selected. A flat head was chosen to simplify the input, since the lower head is not considered in this analysis.

COR_AVP	HLST	-4.35	Elevation of the bottom plate. Elevations below HLST are treated by the lower head model.
	HCSP	-4.35	Elevation of the core support plate. For this problem, the bottom plate in the benchmark nodalization scheme is taken to be the core support plate and bottom plate.
COR_TP	NTPCOR	NO	Lower head is not expected to fail, so this model is not used
	RNTPCOR	NO	RadioNuclide (RN) package is not active for this calculation
	ICFGAP	NO	Fuel-cladding gap conductance control function not used
	ICFFIS	FISPOWALL	Control function is used to specify the whole-core fission power
	CFNAME	'CORE-POWER'	Name of the CF used to specify whole-core fission power. 'CORE-POWER' returns a constant value of 4E+08 (400 MW) during steady-state calculations and 0 after the reactor trips

COR_SS	IA	Table B.7	Axial level number or range of numbers where a supporting structure is present
	IR	Table B.7	Radial ring number or range of numbers where SS is present
	ISSMOD	Table B.7	Structural model option for SS. Note that all SS used in this calculation are not expected to fail, so parameters chosen for SS are selected to prevent failure.
	ISSFAI	TSFAIL	SS will not fail unless temperature exceeds TSSFAI
	TSSFAI	5000	Failure temperature used for SS. This value ensures that SS will not fail during calculations.
	SSMETAL	Table B.7	Name of structural metal. Must be STEEL or ZIRC. Note that ZIRC has been redefined as GRAPHITE.
COR_UDSS	CSSUDF	RFLCT	Name of a user-defined SS type. This SS type is used to represent graphite reflectors that must be modeled as supporting structures to prevent the pebble bed core from collapsing.

	CSSOPT	INTACT	Together, the options on CSSOPT cards specify that SS type RFLCT can support anything until its temperature exceeds TSSFAI (i.e. until the SS fails)
	CSSOPT	DEBRIS	See above
	CSSOPT	SELF	See above
COR_MS	IEUMOD	0	Default used for this model switch
	IHSDT	0	Default used
	IDTDZ	0	Default used
	ICORCV	1	Consistency between fluid volumes in CVH and in COR not required. Normally, MELCOR reports a fatal error if the combined volume occupied by COR components and by CVH for any COR cell is less than the total volume calculated based on the cell dimensions. This requirement was disabled to prevent MELCOR from reporting errors when CVH volume is slighly ($< 0.1\%$) less than CVH volume required for volume consistency
COR_ZP	NAXL	29	Number of axial levels

	Z	Table B.1	Elevation of lower boundary of axial level
	DZ	Table B.1	Axial level height
	PORDP	Table B.1	Porosity of particulate debris. Porosity is equal to the pebble bed porosity (0.39) for levels corresponding to the pebble bed and the 'porous graphite' porosity (0.2) for all other levels.
	IHSA	Table B.1	Boundary heat structure name
	FZPOW	Table B.1	Relative power density in the axial level
COR_RP	NRAD	8	Number of radial rings
	RINGR	Table B.2	Outer radius of ring
	IHSR	Table B.2	Upper boundary heat structure name

	ICFCHN	'FLDIRr'	CF name used to specify the flow direction in the channel of ring 'r', used in estimating local fluid temperatures with the dT/dz model. Each control function is equal to the negative of the velocity in flow path 1r5 (i.e. the flow path connecting the void above the core CVH170 to the control volumes at the top of the pebble bed CVH1r5). If the control function returns a negative value, flow is downward.
	ICFBYP	'FLDIRr'	CF name used to specify the bypass flow direction. This has no significance since bypass flow is not considered.
	FRPOW	Table B.2	Relative power density in the radial ring
COR_RBV	IA	Table B.3	Axial level number or range of numbers
	IR	Table B.3	Radial ring number or range of numbers
	IREF	0	No reference cells are selected. CVs for each COR cell are specified individually.
	JREF	0	See above

	ICVHC	Table B.3	Channel control volume adjacent to COR cell
	ICVHB	Table B.3	Bypass control volume adjacent to COR cell; no bypass flow is modeled, but the name of a CV is required for this record. The channel CV for a COR cell is also used as the bypass CV. Flow through the 'bypass' is prevented by specifying zero flow areas and hydraulic diameters for the bypass.
COR_KFU	IA	Table B.4	Axial level number
	IR	Table B.4	Radial ring number
	XMFUUO	Table B.4	Mass of UO_2 in the cell fuel component. Calculated by determining the number of pebbles in the cell (equal to the total cell volume times the packing fraction 0.61, divided by the volume of one pebble) and multiplying by the mass of UO_2 per pebble (0.0102 kg).
	XMFUHT	0.0	Mass of electric heating element. No electric heaters are used in the calculation.

	XMFUXM	Table B.4	Mass of extra fuel material (graphite) in the fuel component. Calculated by determining the number of pebbles in the cell and multiplying by the mass of graphite in the fueled region of one pebble (equal to the volume of the fueled region of a pebble minus the volume of UO_2 , times the density of graphite).
	XMFUXO	0.0	Mass of oxide of additional fuel material
COR_KCL	IA	Table B.5	Axial level number
	IR	Table B.5	Radial ring number
	XMCLZR	Table B.5	Mass of graphite in the clad. Calculated by multiplying the number of pebbles in the cell by the mass of graphite in the shell around a pebble (equal to the volume of the shell times the density of graphite).
	XMCLZX	0.0	Mass of oxide in cell
	XMCLIN	0.0	Mass of Inconel associated with clad component
COR_KRF	IA	Table B.6	Axial level number
	IR	Table B.6	Radial ring number

	XMRFGR	Table B.6	Mass of graphite in the reflector
COR_KSS	IA	Table B.7	Axial level number
	IR	Table B.7	Radial ring number
	XMSSSS	Table B.7	Mass of steel supporting structure in the cell. Equal to 0.0, except for cells in the bottom plate. For cells in the bottom plate, equal to the volume of the cell times the density of steel.
	XMSSSX	0.0	Mass of steel oxide supporting structure
	XMSSZR	Table B.7	Mass of zirc (redefined as graphite) supporting structure in the cell. Equal to 0.0, except for cells in levels 5 and 29, where SS are needed to prevent core material relocation. For cells in rings 2-6, level 5, equal to the volume of the cell times the fraction of the cell occupied by graphite (0.8), times the density of graphite. For cells in rings 2-6, level 29, equal to the volume of the cell times the density of graphite.

	XMSSZX	0.0	Mass of zirc oxide supporting structure
COR_KPD	IA	ALL	Axial level range of numbers
	IR	ALL	Radial ring range of numbers
	XMPDjj	0.0	Mass of material jj in particulate debris in the cell. No particulate debris is present at the start of the calculation, so the mass of each material in PD is zero.
COR_CIT	IA	ALL	Axial level range of numbers
	IR	ALL	Radial ring range of numbers
	Tjj	773.0	Initial temperature (K) of component jj. Initial temperature equals the reactor inlet temperature.
COR_EDR	IA	ALL	Axial level range of numbers
	IR	ALL	Radial ring range of numbers
	DHYCL	0.06	Cladding equivalent outside diameter. Equal to the pebble diameter.
	DHYPD	0.06	Particulate debris diameter. No PD is expected in the calculation, so this parameter is not used.
	DHYCNC	—	Ignored for PBR calculations
	DHYCNB	—	Ignored for PBR calculations

	DHYSS	0.07	Supporting structure hydraulic diameter. Equal to the hydraulic diameter for the bottom reflector listed in the benchmark documents. This was done because level 5 (i.e. part of the bottom reflector) is modeled as SS. No flow is expected through the other two supporting structures (levels 1 and 29), so hydraulic diameter for these levels is irrelevant.
	DHYNS	—	Nonsupporting structure hydraulic diameter. No NS used in this calculation.
	DHYPB	0.06	Diameter of PD in bypass. No bypass modeled, and no PD expected, so this parameter is insignificant.
COR_RFD	IA	Table B.8	Axial level number
	IR	Table B.8	Radial ring number
	DHYRFC	Table B.8	Channel hydraulic diameter for RF
	DHYRFB	0.01	Bypass hydraulic diameter for RF. Insignificant because bypass flow area is set to zero on another COR record.
COR_RFG	IA	Table B.8	Axial level number

	IR	Table B.8	Radial ring number
	RADI	Table B.8	Reflector channel side radius. Channel side is taken to be the side closest to the fuel. For example, the channel side for the central reflector is the reflector outer radius, while the channel side for the side reflector is the reflector inner radius.
	THKRF	Table B.8	Reflector thickness. A negative value indicates that the channel side is the outside for a cylindrical reflector or the top for a bottom reflector.
	IGEOMRF	Table B.8	Reflector geometry flag. 0 = flat plate, 1 = cylindrical
COR_BFA	IA	Table B.9	Axial level number
	IR	Table B.9	Radial ring number
	ASCLER	Table B.9	Area of outer radial cell boundary. Equal to $2\pi R\,DZ$, where R is the outer radius of ring IR and DZ is the axial level height of level IA.

	AFLOWC	Table B.9	Channel flow area. For pebble bed cells, the flow area is the empty bed area. The blockage models PBR-A and PBR-R account for flow restrictions in the packed bed. For cells with 'porous graphite,' the flow area is equal to 20% of the cross sectional area in the direction of the flow, which accounts for 20% porosity. For cells where no channel flow is expected (such as in the solid reflectors in rings 1 and 7), the flow area is 0.
	AFLOWB	0.0	Bypass flow area is equal to 0 because bypass flow is not modeled
COR_SA	IA	Table B.10	Axial level number
	IR	Table B.10	Radial ring number
	ASFU	Table B.10	Fuel surface area. Equal to the fuel surface area of one pebble ($4\pi r_f^2$, where $r_f = 0.025$ is the radius of the fueled region of the pebble) times the number of pebbles in the cell at level IA and ring IR.

ASCL	Table B.10	Clad surface area. Equal to the surface area of one pebble ($4\pi r_p^2$, where $r_p = 0.03$ is the pebble outer radius) times the number of pebbles in the cell.
ASCN	0.0	Surface area of the canister component, which is not used for PBR calculations

	ASSS	Table B.10	Supporting structure surface area. For the bottom plate and the top reflector, the surface area is $\pi(r_o^2 - r_i^2)$, where r_o and r_i are the outer and inner radii of ring IR (i.e. the surface area is the SS cross sectional area). For the SS representing the bottom reflector in level 5, the surface area is calculated by assuming that coolant flows through tubes with diameter equal to the SS hydraulic diameter specified on the COR_EDR record. Using the level 5 flow areas on the COR_BFA record, the number of 'tubes' is determined by dividing the total flow area by the area of one tube. The surface area is calculated by multiplying the number of tubes by the surface area of one tube.
	ASNS	0.0	Nonsupporting structures are not used in the calculation
COR_RFA	IA	Table B.11	Axial level number
	IR	Table B.11	Radial ring number

	ASRF	Table B.11	Channel side surface area. Calculated assuming flow through tubes with diameters equal to the diameters specified on record COR_RFD. This methodology is analogous to that used to calculate SS surface areas in level 5.
	ASRFB	0.0	Bypass surface areas are set equal to 0 because bypass flow is not considered
COR_LP	IAXSUP	5	Axial level of the core support plate
	HDBH20	100	Heat transfer coefficient from in-vessel falling debris to pool. Default value. Not used because no fuel failure is expected.
	PPFAIL	2.0E7	Differential pressure between lower plenum and reactor cavity that will fail the lower head. Default value.
	VFALL	0.0	Velocity of falling debris. No fuel damage is expected.
C0R_LH	NLH	7	Number of temperature nodes in the lower head
	NINSLH	0	Number of insulation mesh layers in the lower head

COR_LHD	NLHT	8	Number of lower head segments. This represents the minimum number of segments, since at least one segment must be used for each COR ring.
	NLHTA	8	Number of segments in flat portion of the lower head. The cylindrical portion of the vessel below level 5 is modeled using the HS package, not the COR package, and so there are no lower head segments in the cylindrical portion of the vessel.
	TLH	1173	Initial temperature of lower head segment. Equal to the expected core outlet temperature, in order to simulate an adiabatic boundary condition.
	RADLH	Table B.2	Outer radius of lower head segment. RADLH's for segments 1-8 correspond to the outer radii of rings 1-8 shown in Table B.2.

	ICVCAV	'CV50-CAVITY'	Reactor cavity control volume name. 'CV50-CAVITY' is a small volume at a temperature of 1173 K to simulate an adiabatic lower head condition.
COR_FUM	XFUMAT	GRAPH	Graphite is the extra fuel material
COR_CLM	CLMAT	GRAPH	Graphite is the clad material
COR_RFM	RFMAT	GRAPH	Graphite is the reflector material
COR_SC	NNNN	Table B.12	Four-digit identifier for a COR sensitivity coefficient array
	VALUE	Table B.12	New value for the sensitivity coefficient
	NA	Table B.12	Sensitivity coefficient array index. COR sensitivity coefficients are used to modify the packed bed convective heat transfer coefficient and the lower head heat transfer coefficient.

Table B.1: PBMR axial level input

Level	Z (m)	DZ (m)	PORDP	IHSA	FZPOW
1	-4.35	0.35	0.39	'COR-RAD-BND-A1'	0.0
2	-4.0	1.0	0.20	'COR-RAD-BND-A2'	0.0
3	-3.0	1.0	0.20	'COR-RAD-BND-A3'	0.0

Table B.1 (continued)

Level	Z (m)	DZ (m)	PORDP	IHSA	FZPOW
4	-2.0	1.0	0.20	'COR-RAD-BND-A4'	0.0
5	-1.0	1.0	0.20	'COR-RAD-BND-A5'	0.0
6	0.0	0.5	0.39	'COR-RAD-BND-A6'	0.173
7	0.5	0.5	0.39	'COR-RAD-BND-A7'	0.222
8	1.0	0.5	0.39	'COR-RAD-BND-A8'	0.285
9	1.5	0.5	0.39	'COR-RAD-BND-A9'	0.355
10	2.0	0.5	0.39	'COR-RAD-BND-A10'	0.434
11	2.5	0.5	0.39	'COR-RAD-BND-A11'	0.524
12	3.0	0.5	0.39	'COR-RAD-BND-A12'	0.628
13	3.5	0.5	0.39	'COR-RAD-BND-A13'	0.748
14	4.0	0.5	0.39	'COR-RAD-BND-A14'	0.886
15	4.5	0.5	0.39	'COR-RAD-BND-A15'	1.040
16	5.0	0.5	0.39	'COR-RAD-BND-A16'	1.212
17	5.5	0.5	0.39	'COR-RAD-BND-A17'	1.394
18	6.0	0.5	0.39	'COR-RAD-BND-A18'	1.579
19	6.5	0.5	0.39	'COR-RAD-BND-A19'	1.750
20	7.0	0.5	0.39	'COR-RAD-BND-A20'	1.886
21	7.5	0.5	0.39	'COR-RAD-BND-A21'	1.958
22	8.0	0.5	0.39	'COR-RAD-BND-A22'	1.927
23	8.5	0.5	0.39	'COR-RAD-BND-A23'	1.757
24	9.0	0.5	0.39	'COR-RAD-BND-A24'	1.428
25	9.5	0.5	0.39	'COR-RAD-BND-A25'	0.997
26	10.0	0.5	0.39	'COR-RAD-BND-A26'	0.655
27	10.5	0.5	0.39	'COR-RAD-BND-A27'	0.388
28	11.0	0.5	0.39	'COR-RAD-BND-A28'	0.0
29	11.5	1.5	0.2	'COR-RAD-BND-A29'	0.0

Table B.2
PBMR radial ring input

Level	RINGR (m)	IHSR	ICFCHN	FRPOW
1	1.0	'TOP-PLATE-R1'	NO	0.0
2	1.17	'TOP-PLATE-R2'	'FLDIR2'	1.137
3	1.34	'TOP-PLATE-R3'	'FLDIR3'	1.014
4	1.51	'TOP-PLATE-R4'	'FLDIR4'	0.953
5	1.68	'TOP-PLATE-R5'	'FLDIR5'	0.931
6	1.85	'TOP-PLATE-R6'	'FLDIR6'	0.965
7	2.436	'TOP-PLATE-R7'	NO	0.0
8	2.606	'TOP-PLATE-R8'	NO	0.0

Table B.3: PBMR CVH volumes coupled to each COR cell

IA	IR	ICVHC
1-5	1	'COR-CV110'
6-10	1	'COR-CV111'
11-15	1	'COR-CV112'
16-19	1	'COR-CV113'
20-23	1	'COR-CV114'
24-28	1	'COR-CV115'
1-5	2-6	'CV100-LOWER_PLEN'
6-10	2	'COR-CV121'
11-15	2	'COR-CV122'
16-19	2	'COR-CV123'
20-23	2	'COR-CV124'
24-27	2	'COR-CV125'
6-10	3	'COR-CV131'
11-15	3	'COR-CV132'
16-19	3	'COR-CV133'
20-23	3	'COR-CV134'
24-27	3	'COR-CV135'
6-10	4	'COR-CV141'
11-15	4	'COR-CV142'
16-19	4	'COR-CV143'
20-23	4	'COR-CV144'
24-27	4	'COR-CV145'
6-10	5	'COR-CV151'
11-15	5	'COR-CV152'

Table B.3 (continued)

IA	IR	ICVHC
16-19	5	'COR-CV153'
20-23	5	'COR-CV154'
24-27	5	'COR-CV155'
6-10	6	'COR-CV161'
11-15	6	'COR-CV162'
16-19	6	'COR-CV163'
20-23	6	'COR-CV164'
24-27	6	'COR-CV165'
28	2-8	'CV170-VOID'
1-3	7-8	'COR-CV182'
4-27	7	'COR-CV171'
4-27	8	'CV181-RISER'
29	1	'COR-CV116'
29	2	'COR-CV126'
29	3	'COR-CV136'
29	4	'COR-CV146'
29	5	'COR-CV156'
29	6	'COR-CV166'
29	7	'COR-CV176'
29	8	'COR-CV186'

Table B.4
Mass of materials in the fuel component (PBMR)

IA	IR	Mass of UO_2 (kg)	Mass of GRAPH in FU (kg)
1-5	1-6	0.0	0.0
6-27	1	0.0	0.0
6-27	2	31.911	358.650
6-27	3	36.911	414.844
6-27	4	41.911	471.038
6-27	5	46.911	527.232
6-27	6	51.910	583.426
28	1-6	0.0	0.0
ALL	7-8	0.0	0.0

Table B.5
Mass of graphite in the clad component (PBMR)

IA	IR	Mass of GRAPH in CL (kg)
1-5	1-6	0.0
6-27	1	0.0
6-27	2	265.073
6-27	3	306.606
6-27	4	348.138
6-27	5	389.670
6-27	6	431.202
28	1-6	0.0
ALL	7-8	0.0

Table B.6
Mass of graphite in the reflector component (PBMR)

IA	IR	Mass of GRAPH in RF (kg)
1	1-6	0.
2-5	1	3914.4
6-28	1	1957.2
2	2	2062.9
3-4	2	1650.3
2	3	2386.1
3-4	3	1908.9
2	4	2709.3
3-4	4	2167.5
2	5	3032.6
3-4	5	2426.0
2	6	3355.8
3-4	6	2684.6
6-28	2-6	0.
2-5	7	14044.9
6-27	7	7022.5
28	7	5618.0
29	7	21067.4
2-3	8	4793.2
4-5	8	3834.5
6-28	8	1917.3
29	8	7189.7
29	1	5871.6

Table B.7
PBMR supporting structure parameters

IA	IR	ISSMOD	Mass of STEEL in SS (kg)	Mass of ZIRC in SS (kg)
5	2	RFLCT	0.0	1650.3
5	3	RFLCT	0.0	1908.9
5	4	RFLCT	0.0	2167.5
5	5	RFLCT	0.0	2426.0
5	6	RFLCT	0.0	2684.6
1	1	PLATEG	8577.	0.0
1	2	PLATEG	3164.	0.0
1	3	PLATEG	3660.	0.0
1	4	PLATEG	4155.	0.0
1	5	PLATEG	4651.	0.0
1	6	PLATEG	5147.	0.0
1	7	PLATEG	21541.	0.0
1	8	PLATEG	7351.	0.0
29	2	RFLCT	0.0	3094.4
29	3	RFLCT	0.0	3579.2
29	4	RFLCT	0.0	4064.0
29	5	RFLCT	0.0	4548.8
29	6	RFLCT	0.0	5033.7

Table B.8: PBMR reflector geometry input

IA	IR	IGEOMRF	RADI (m)	THKRF (m)	DHYRFC (m)
ALL	1	CYLIND	1.0	-1.0	1.0
2	2	FLAT	1.00	-1.0	0.01
3	2	FLAT	1.00	-1.0	0.144
4	2	FLAT	1.00	-1.0	0.07
2	3	FLAT	1.17	-1.0	0.01
3	3	FLAT	1.17	-1.0	0.144
4	3	FLAT	1.17	-1.0	0.07
2	4	FLAT	1.34	-1.0	0.01
3	4	FLAT	1.34	-1.0	0.144
4	4	FLAT	1.34	-1.0	0.07
2	5	FLAT	1.51	-1.0	0.01
3	5	FLAT	1.51	-1.0	0.144
4	5	FLAT	1.51	-1.0	0.07
2	6	FLAT	1.68	-1.0	0.01
3	6	FLAT	1.68	-1.0	0.144
4	6	FLAT	1.68	-1.0	0.07
2-4	7	FLAT	1.85	-1.0	0.01
6-28	7	CYLIND	1.85	0.568	1.85
2-3	8	FLAT	2.436	-1.0	0.01
4-27	8	CYLIND	2.436	0.17	0.17
28	7	CYLIND	1.85	0.568	0.335
28	8	CYLIND	2.436	0.17	0.335

Table B.9: PBMR COR cell flow areas

IA	IR	ASCELR (m^2)	AFLOWC (m^2)
1	1	2.199	0.01
2	1	12.566	0.0
3	1	6.283	0.0
4-29	1	3.142	0.0
1	2	2.573	0.0
2-5	2	7.351	0.2318
6-27	2	3.676	0.4520
28	2	3.676	1.1589
29	2	11.027	0.0
1	3	2.947	0.0
2-5	3	8.419	0.2681
6-27	3	4.210	0.5228
28	3	4.210	1.3405
29	3	12.629	0.0
1	4	3.321	0.0
2-5	4	9.488	0.3044
6-27	4	4.744	0.5936
28	4	4.744	1.5221
29	4	14.231	0.0
1	5	3.695	0.0
2-5	5	10.556	0.3407
6-27	5	5.278	0.6644
28	5	5.278	1.7037
29	5	15.834	0.0
1	6	4.068	0.0

Table B.9 (continued)

IA	IR	ASCELR (m^2)	AFLOWC (m^2)
2-5	6	11.624	0.3771
4-27	6	5.812	0.7353
28	6	5.812	1.8853
29	6	17.436	0.0
1	7	5.357	0.0
2-5	7	15.306	0.0
6-27	7	7.653	0.0
28	7	7.653	1.3465
29	7	22.959	0.0
1	8	5.731	0.0
2-3	8	16.374	0.0
4-5	8	16.374	0.5386
6-28	8	8.187	0.5386
29	8	24.561	0.0

Table B.10: PBMR COR component surface areas

IA	IR	ASFU (m^2)	ASCL (m^2)	ASSS (m^2)
1	1	0.0	0.0	6.283
2-29	1	0.0	0.0	0.0
2-4	2-8	0.0	0.0	0.0
1	2	0.0	0.0	2.318
5	2	0.0	0.0	13.245
6-27	2	24.547	35.347	0.0
1	3	0.0	0.0	2.681
5	3	0.0	0.0	15.320

Table B.10 (continued)

IA	IR	ASFU (m^2)	ASCL (m^2)	ASSS (m^2)
6-27	3	28.393	40.886	0.0
1	4	0.0	0.0	3.044
5	4	0.0	0.0	17.395
6-27	4	32.239	46.424	0.0
1	5	0.0	0.0	3.407
5	5	0.0	0.0	19.471
6-27	5	36.085	51.962	0.0
1	6	0.0	0.0	3.771
5	6	0.0	0.0	21.546
6-27	6	39.931	57.501	0.0
1	7	0.0	0.0	15.781
2-29	7-8	0.0	0.0	0.0
1	8	0.0	0.0	5.386
29	2	0.0	0.0	1.159
29	3	0.0	0.0	1.341
29	4	0.0	0.0	1.522
29	5	0.0	0.0	1.704
29	6	0.0	0.0	1.885
28	2-6	0.0	0.0	0.0

Table B.11: PBMR reflector component surface area

IA	IR	ASRF (m^2)
2	1	12.566
3	1	6.283
4-28	1	3.142

Table B.11 (continued)

IA	IR	ASRF (m^2)
2	2-6	0.01
4	2	13.245
4	3	15.320
4	4	17.395
4	5	19.471
4	6	21.546
3	2	3.130
3	3	3.620
3	4	4.111
3	5	4.601
3	6	5.091
29	1	0.01
2-5	7	0.01
6-27	7	5.812
28	7	5.521
2-3	8	0.01
4-5	8	12.672
6-28	8	3.168
29	7-8	0.01

Table B.12: PBMR COR sensitivity coefficient modifications

NNNN NA VALUE Explanation

1231	1	0.0	Coefficient A in the equation Nu = $A + B\mathrm{Re}^C\mathrm{Pr}^D$, which determines the heat transfer coefficient for turbulent flow through a packed bed
1231	2	0.2371	Coefficient B in the above equation. The value was obtained by fitting results for Nu, calculated using the KTA rules correlation, to the form Nu = $B\mathrm{Re}^C$ for the expected range of Re for steady-state calculations.
1231	3	0.6483	Coefficient C in the above equation
1231	4	0.0	Coefficient D in the above equation
1246	1	0.0	Heat transfer coefficient from the vessel head to the reactor cavity. Setting this coefficient equal to 0 simulates an adiabatic boundary condition for the lower head.

B.1.4 PBMR CVH input

CARD	*WORD*	*VALUE*	*BASIS*
CV_ID	CVNAME	Table B.13	Control volume name
	ICVNUM	Table B.13	Control volume sequence number
CV_THR	ICVTHR	NONEQUIL	Nonequilibrium thermodynamics switch, meaning Tpool≠Tatmos (irrelevant for single-phase gas)
	IPFSW	FOG	Fog (liquid water in the atmosphere) allowed (irrelevant for single-phase gas)
	ICVACT	ACTIVE	CVs are active, meaning MELCOR advances their thermodynamic state by solving conservation equations
CV_PAS	ITYPTH	SEPARATE	Separate input for pool and atmosphere
	IPORA	ONLYATM	Only atmosphere is present in each control volume
	VAPORSTATE	SUPERHEATED	Atmosphere is superheated. There is no water vapor in any control volume, so this field is irrelevant.
CV_PTD	PTDID	PVOL	Control volume pressure will be specified

	PVOL	Table B.13	Initial CV pressure in Pa. Equal to 9.0E+06 Pa for all CVs in the reactor and 1.0E+5 Pa for cavity CVs.
CV_AAD	ATMID	TATM	Atmosphere temperature will be specified
	TATM	Table B.13	Initial CV temperature
CV_NCG	NMMAT	1 or 2	Number of NCG materials in CV. Equal to 1 for cells containing helium or 2 for cells containing air (nitrogen and oxygen).
	NCGID	RHUM	Relative humidity specified
	RHUM	0.0	Only noncondensible gases are present in the atmosphere
	NAMGAS	HE or N2 and O2	Noncondensibles present in CV. HE for all CVs in the reactor and N2 and O2 for all CVs in the cavity.
	MLFR	1.0 or 0.8 and 0.2	Mole fraction of gas. 1.0 for HE, 0.8 for N2, and 0.2 for O2.
CV_VAT	ICVVZP	Depends on CV	Number of altitude/volume pairs in the volume altitude table. One pair is present for each axial COR cell elevation in the CV.

CVZ	Table B.14	Altitude. Top and bottom elevations for each CV are present in Table B.14.
CVVOL	Table B.14	Volume at altitude CVZ. Total volume of each CV is present in Table B.14.

Table B.13: Initial thermodynamic conditions for CVs in pbmr400.inp

CVNAME	ICVNUM	Pressure (Pa)	Temperature (K)
CV50-CAVITY	50	1.0E+05	1173
CV100-LOWER_PLEN	100	9.0E+06	773
COR-CV110	110	9.0E+06	773
COR-CV111	111	9.0E+06	773
COR-CV112	112	9.0E+06	773
COR-CV113	113	9.0E+06	773
COR-CV114	114	9.0E+06	773
COR-CV115	115	9.0E+06	773
COR-CV116	116	9.0E+06	773
COR-CV121	121	9.0E+06	773
COR-CV122	122	9.0E+06	773
COR-CV123	123	9.0E+06	773
COR-CV124	124	9.0E+06	773
COR-CV125	125	9.0E+06	773
COR-CV126	126	9.0E+06	773
COR-CV131	131	9.0E+06	773
COR-CV132	132	9.0E+06	773

Table B.13 (continued)

CVNAME	ICVNUM	Pressure (Pa)	Temperature (K)
COR-CV133	133	9.0E+06	773
COR-CV134	134	9.0E+06	773
COR-CV135	135	9.0E+06	773
COR-CV136	136	9.0E+06	773
COR-CV141	141	9.0E+06	773
COR-CV142	142	9.0E+06	773
COR-CV143	143	9.0E+06	773
COR-CV144	144	9.0E+06	773
COR-CV145	145	9.0E+06	773
COR-CV146	146	9.0E+06	773
COR-CV151	151	9.0E+06	773
COR-CV152	152	9.0E+06	773
COR-CV153	153	9.0E+06	773
COR-CV154	154	9.0E+06	773
COR-CV155	155	9.0E+06	773
COR-CV156	156	9.0E+06	773
COR-CV161	161	9.0E+06	773
COR-CV162	162	9.0E+06	773
COR-CV163	163	9.0E+06	773
COR-CV164	164	9.0E+06	773
COR-CV165	165	9.0E+06	773
COR-CV166	166	9.0E+06	773
CV170-VOID	170	9.0E+06	773
COR-CV171	171	9.0E+06	773
COR-CV176	176	9.0E+06	773
CV181-RISER	181	9.0E+06	773

Table B.13 (continued)

CVNAME	ICVNUM	Pressure (Pa)	Temperature (K)
COR-CV182	182	9.0E+06	773
COR-CV186	186	9.0E+06	773
GAP-CV301	301	9.0E+06	773
GAP-CV302	302	9.0E+06	773
GAP-CV303	303	9.0E+06	773
GAP-CV304	304	9.0E+06	773
GAP-CV401	401	9.0E+06	773
GAP-CV402	402	9.0E+06	773
GAP-CV403	403	9.0E+06	773
GAP-CV404	404	9.0E+06	773
CAV-CV501	501	1.0E+05	300
CAV-CV502	502	1.0E+05	300
CAV-CV503	503	1.0E+05	300
CAV-CV504	504	1.0E+05	300

Table B.14: Elevation and volume of CVs in pbmr400.inp

ICVNUM	Bottom El. (m)	Top El. (m)	Volume (m^3)
50	-4.6	-4.3 [a]	10.14 [b]
100	-4.35	0.0	4.566 [c]
110	-4.35	0.0	0.09 [d]

[a]Top and bottom elevations for the cavity are chosen such that the lower head is contained in the cavity; otherwise, they are arbitrary

[b]The volume of the cavity is arbitrary since the heat transfer coefficient from the lower head to the cavity has been set to zero

[c]This is equal to the volume of the "porous" portion of the lower reflector (COR levels 3-5 of rings 2-6) multiplied by its porosity, 0.2

[d]This CV is required by the COR package where no volume would exist. Thus, the volume is arbitrarily low.

Table B.14 (continued)

ICVNUM	Bottom El. (m)	Top El. (m)	Volume (m^3)
111	0.0	2.5	0.05 [d]
112	2.5	5.0	0.05 [d]
113	5.0	7.0	0.04 [d]
114	7.0	9.0	0.04 [d]
115	9.0	11.5	0.05 [d]
116	11.5	13.0	0.03 [d]
121	0.0	2.5	1.130 [e]
122	2.5	5.0	1.130 [e]
123	5.0	7.0	0.904 [e]
124	7.0	9.0	0.904 [e]
125	9.0	11.0	0.904 [e]
126	11.5	13.0	0.03 [d]
131	0.0	2.5	1.307 [e]
132	2.5	5.0	1.307 [e]
133	5.0	7.0	1.046 [e]
134	7.0	9.0	1.046 [e]
135	9.0	11.0	1.046 [e]
136	11.5	13.0	0.03 [d]
141	0.0	2.5	1.484 [e]
142	2.5	5.0	1.484 [e]
143	5.0	7.0	1.187 [e]
144	7.0	9.0	1.187 [e]
145	9.0	11.0	1.187 [e]
146	11.5	13.0	0.03 [d]

[e]This is equal to the empty volume of the COR cells coupled to this CV, times the bed porosity, 0.39

Table B.14 (continued)

ICVNUM	Bottom El. (m)	Top El. (m)	Volume (m^3)
151	0.0	2.5	1.661 [e]
152	2.5	5.0	1.661 [e]
153	5.0	7.0	1.329 [e]
154	7.0	9.0	1.329 [e]
155	9.0	11.0	1.329 [e]
156	11.5	13.0	0.03 [d]
161	0.0	2.5	1.838 [e]
162	2.5	5.0	1.838 [e]
163	5.0	7.0	1.471 [e]
164	7.0	9.0	1.471 [e]
165	9.0	11.0	1.471 [e]
166	11.5	13.0	0.03 [d]
170	11.0	11.5	4.864[f]
171	-2.0	11.0	0.260 [d]
176	11.5	13.0	0.03 [d]
181	-2.0	11.0	7.001[g]
182	-4.35	-2.0	0.05 [d]
186	11.5	13.0	0.03 [d]
301	-4.5	0.0	9.9402
302	0.0	4.5	9.9402
303	4.5	9.0	9.9402
304	9.0	13.5	9.9402
401	-4.5	0.0	14.9059
402	0.0	4.5	14.9059

[f]This is equal to the volume of the void region above the core (level 28 of rings 2-6), plus the volume of level 28 of rings 7-8 multiplied by the graphite porosity 0.2

[g]This is equal to the volume of COR levels 4-27 of ring 8 times the graphite porosity 0.2

Table B.14 (continued)

ICVNUM	Bottom El. (m)	Top El. (m)	Volume (m^3)
403	4.5	9.0	14.9059
404	9.0	13.5	14.9059
501	-4.5	0.0	149.7
502	0.0	4.5	149.7
503	4.5	9.0	149.7
504	9.0	13.5	149.7

B.1.5 MELGEN FL Input

CARD	*WORD*	*VALUE*	*BASIS*
FL_ID	FPNAME	Table B.15	Flow path name
	IFPNUM	Table B.15	Flow path number
FL_FT	KCVFM	Table B.15	Name of the "from" control volume
	KCVTO	Table B.15	Name of the "to" control volume
	ZFM	Table B.16	Altitude of "from" junction
	ZTO	Table B.16	Altitude of "to" junction. For core flow paths, ZTO=ZFM, where ZTO is the altitude of the junction between KCVFM and KCVTO for axial flow and the altitude of the midplane of KCVFM and KCVTO for radial flow.
FL_GEO	FLARA	Table B.17	Fully open flow path area. This is equal to the empty bed flow area for flow paths in the core. For vertical flow in the core, FLARA= $\pi(R_o^2 - R_i^2)$. For horizontal flow in the core, FLARA= $2\Delta H$. R_o and R_i are the inner and outer radii of the radial ring associated with the "from" CV. ΔH is the height of the "from" CV.

FLLEN	Table B.17	Momentum exchange length for the flow path. This value is used to calculate momentum exchange between pool and atmosphere. Since flow is single phase gas, this value has no effect on the calculations. FLLEN is set equal to the sum of the segment lengths for the flow path.
FLOPO	1.0	Fraction of the flow path open, set to unity because all flow paths are fully open
FLHGTF	Table B.16	"From" junction flow path opening height. For a horizontal flow path, this is defined as height of the opening in the flow path. It has no rigorous interpretation for vertical flow paths. This parameter is simply used to determine the range of elevations from which flow may be drawn. The default value, equal to the radius of a circle with area FLARA, is used for all vertical flow paths.
FLHGTT	Table B.16	"To" junction flow path opening height.

FL_JSW	KFLGFL	Table B.16	Flow path orientation. '0' signifies vertical flow, and '3' signifies horizontal flow.
FL_BLK	OPTION	Table B.18	Blockage option. 'PBR-A' and 'PBR-R' are used to model flow through a packed bed. These blockage options adjust the flow path area for pebble bed flow. It also activates the use of pebble bed friction factors in pressure drop calculations.
	ICORCR1 and 2	Table B.18	The limiting core rings associated with the flow path
	ICORCA1 and 2	Table B.18	The limiting core axial levels associated with the flow path
FL_SEG	IPNSG	–	Number of flow path segments. All flow paths except 'FLOW-TO-VOID' have one segment. 'FLOW-TO-VOID' has 2 segments.
	SAREA	Table B.17	Segment flow area. For segments with one flow segment, the value of FLARA is used as input for SAREA
	SLEN	Table B.17	Segment flow length. The flow length is set equal to the distance between the midpoints of the "to" and "from" CVs.

SHYD	Table B.17	Segment hydraulic diameter, equal to $2(R_o - R_i)$ for flow through rings and $2\Delta H$ for radial flow between rings

Table B.15: PBMR Flow path connections

FPNAME	IFPNUM	KCVFM	KCVTO
ARING2-FL120	120	COR-CV121	CV100-LOWER_PLEN
ARING2-FL121	121	COR-CV122	COR-CV121
ARING2-FL122	122	COR-CV123	COR-CV122
ARING2-FL123	123	COR-CV124	COR-CV123
ARING2-FL124	124	COR-CV125	COR-CV124
ARING2-FL125	125	CV170-VOID	COR-CV125
ARING3-FL130	130	COR-CV131	CV100-LOWER_PLEN
ARING3-FL131	131	COR-CV132	COR-CV131
ARING3-FL132	132	COR-CV133	COR-CV132
ARING3-FL133	133	COR-CV134	COR-CV133
ARING3-FL134	134	COR-CV135	COR-CV134
ARING3-FL135	135	CV170-VOID	COR-CV135
ARING4-FL140	140	COR-CV141	CV100-LOWER_PLEN
ARING4-FL141	141	COR-CV142	COR-CV141
ARING4-FL142	142	COR-CV143	COR-CV142
ARING4-FL143	143	COR-CV144	COR-CV143
ARING4-FL144	144	COR-CV145	COR-CV144
ARING4-FL145	145	CV170-VOID	COR-CV145
ARING5-FL150	150	COR-CV151	CV100-LOWER_PLEN
ARING5-FL151	151	COR-CV152	COR-CV151

Table B.15 (continued)

FPNAME	IFPNUM	KCVFM	KCVTO
ARING5-FL152	152	COR-CV153	COR-CV152
ARING5-FL153	153	COR-CV154	COR-CV153
ARING5-FL154	154	COR-CV155	COR-CV154
ARING5-FL155	155	CV170-VOID	COR-CV155
ARING6-FL160	160	COR-CV161	CV100-LOWER_PLEN
ARING6-FL161	161	COR-CV162	COR-CV161
ARING6-FL162	162	COR-CV163	COR-CV162
ARING6-FL163	163	COR-CV164	COR-CV163
ARING6-FL164	164	COR-CV165	COR-CV164
ARING6-FL165	165	CV170-VOID	COR-CV165
FLOW-TO-VOID	170	CV181-RISER	CV170-VOID
RRING23-FL221	221	COR-CV121	COR-CV131
RINGS34-FL231	231	COR-CV131	COR-CV141
RINGS45-FL241	241	COR-CV141	COR-CV151
RINGS56-FL251	251	COR-CV151	COR-CV161
RRING23-FL222	222	COR-CV122	COR-CV132
RINGS34-FL232	232	COR-CV132	COR-CV142
RINGS45-FL242	242	COR-CV142	COR-CV152
RINGS56-FL252	252	COR-CV152	COR-CV162
RRING23-FL223	223	COR-CV123	COR-CV133
RINGS34-FL233	233	COR-CV133	COR-CV143
RINGS45-FL243	243	COR-CV143	COR-CV153
RINGS56-FL253	253	COR-CV153	COR-CV163
RRING23-FL224	224	COR-CV124	COR-CV134
RINGS34-FL234	234	COR-CV134	COR-CV144
RINGS45-FL244	244	COR-CV144	COR-CV154

Table B.15 (continued)

FPNAME	IFPNUM	KCVFM	KCVTO
RINGS56-FL254	254	COR-CV154	COR-CV164
RRING23-FL225	225	COR-CV125	COR-CV135
RINGS34-FL235	235	COR-CV135	COR-CV145
RINGS45-FL245	245	COR-CV145	COR-CV155
RINGS56-FL255	255	COR-CV155	COR-CV165

Table B.16: PBMR flow path junction elevations

IFPNUM	ZFM (m)	ZTO (m)	FLHGTF (m)	FLHGTT (m)	Orientation
120	0.0	0.0	—	— [a]	0 [b]
121	2.5	2.5	DEF	DEF	0
122	5.0	5.0	DEF	DEF	0
123	7.0	7.0	DEF	DEF	0
124	9.0	9.0	DEF	DEF	0
125	11.0	11.0	DEF	DEF	0
130	0.0	0.0	DEF	DEF	0
131	2.5	2.5	DEF	DEF	0
132	5.0	5.0	DEF	DEF	0
133	7.0	7.0	DEF	DEF	0
134	9.0	9.0	DEF	DEF	0
135	11.0	11.0	DEF	DEF	0
140	0.0	0.0	DEF	DEF	0
141	2.5	2.5	DEF	DEF	0
142	5.0	5.0	DEF	DEF	0
143	7.0	7.0	DEF	DEF	0

[a] 'DEF' signifies that the default value is used for this parameter
[b] '0' signifies a normal vertical flow path; '3' signifies a normal horizontal flow path

Table B.16 (continued)

IFPNUM	ZFM (m)	ZTO (m)	FLHGTF (m)	FLHGTT (m)	Orientation
144	9.0	9.0	DEF	DEF	0
145	11.0	11.0	DEF	DEF	0
150	0.0	0.0	DEF	DEF	0
151	2.5	2.5	DEF	DEF	0
152	5.0	5.0	DEF	DEF	0
153	7.0	7.0	DEF	DEF	0
154	9.0	9.0	DEF	DEF	0
155	11.0	11.0	DEF	DEF	0
160	0.0	0.0	DEF	DEF	0
161	2.5	2.5	DEF	DEF	0
162	5.0	5.0	DEF	DEF	0
163	7.0	7.0	DEF	DEF	0
164	9.0	9.0	DEF	DEF	0
165	11.0	11.0	DEF	DEF	0
170	11.0	11.25	0.5	0.5	— [c]
221	1.25	1.25	2.5	2.5	3
231	1.25	1.25	2.5	2.5	3
241	1.25	1.25	2.5	2.5	3
251	1.25	1.25	2.5	2.5	3
222	3.75	3.75	2.5	2.5	3
232	3.75	3.75	2.5	2.5	3
242	3.75	3.75	2.5	2.5	3
252	3.75	3.75	2.5	2.5	3
223	6.0	6.0	2.0	2.0	3
233	6.0	6.0	2.0	2.0	3

[c]The orientation is not specified for this flow path because it has vertical and horizontal segments

Table B.16 (continued)

IFPNUM	ZFM (m)	ZTO (m)	FLHGTF (m)	FLHGTT (m)	Orientation
243	6.0	6.0	2.0	2.0	3
253	6.0	6.0	2.0	2.0	3
224	8.0	8.0	2.0	2.0	3
234	8.0	8.0	2.0	2.0	3
244	8.0	8.0	2.0	2.0	3
254	8.0	8.0	2.0	2.0	3
225	10.0	10.0	2.0	2.0	3
235	10.0	10.0	2.0	2.0	3
245	10.0	10.0	2.0	2.0	3
255	10.0	10.0	2.0	2.0	3

Table B.17: PBMR flow path geometry

IFPNUM	FLARA (m^2)	SLEN (m)	SHYD (m)
120	1.1589	3.25	0.34
121	1.1589	2.5	0.34
122	1.1589	2.25	0.34
123	1.1589	2.0	0.34
124	1.1589	2.0	0.34
125	1.1589	1.25	0.34
130	1.3405	3.25	0.34
131	1.3405	2.5	0.34
132	1.3405	2.25	0.34
133	1.3405	2.0	0.34
134	1.3405	2.0	0.34
135	1.3405	1.25	0.34

Table B.17 (continued)

IFPNUM	FLARA (m^2)	SLEN (m)	SHYD (m)
140	1.5221	3.25	0.34
141	1.5221	2.5	0.34
142	1.5221	2.25	0.34
143	1.5221	2.0	0.34
144	1.5221	2.0	0.34
145	1.5221	1.25	0.34
150	1.7037	3.25	0.34
151	1.7037	2.5	0.34
152	1.7037	2.25	0.34
153	1.7037	2.0	0.34
154	1.7037	2.0	0.34
155	1.7037	1.25	0.34
160	1.8853	3.25	0.34
161	1.8853	2.5	0.34
162	1.8853	2.25	0.34
163	1.8853	2.0	0.34
164	1.8853	2.0	0.34
165	1.8853	1.25	0.34
170	0.5386 [a]	13.75 [b]	0.17 / 0.077 [c]
221	18.3783	0.17	5.0
231	21.0487	0.17	5.0
241	23.7190	0.17	5.0
251	26.3894	0.17	5.0

[a]This flow path has two segments, each of which has an area of 0.5386 m. The first segment represents flow through the helium risers. The second segment represents flow through the porous graphite reflector in rings 7 and 8 of level 28.
[b]Segment lengths for this flow path are 13.0 m and 0.75 m.
[c]The two hydraulic diameters are for the first and second segment, respectively.

Table B.17 (continued)

IFPNUM	FLARA (m^2)	SLEN (m)	SHYD (m)
222	18.3783	0.17	5.0
232	21.0487	0.17	5.0
242	23.7190	0.17	5.0
252	26.3894	0.17	5.0
223	14.7027	0.17	4.0
233	16.8389	0.17	4.0
243	18.9752	0.17	4.0
253	21.1115	0.17	4.0
224	14.7027	0.17	4.0
234	16.8389	0.17	4.0
244	18.9752	0.17	4.0
254	21.1115	0.17	4.0
225	14.7027	0.17	4.0
235	16.8389	0.17	4.0
245	18.9752	0.17	4.0
255	21.1115	0.17	4.0

Table B.18: PBMR flow path blockage model options

IFPNUM	Blockage option	ICORCR1	ICORCR2	ICORCA1	ICORCA2
120	PBR-A	2	2	6	8
121	PBR-A	2	2	9	13
122	PBR-A	2	2	14	17
123	PBR-A	2	2	18	21
124	PBR-A	2	2	22	25
125	PBR-A	2	2	26	27

Table B.18 (continued)

IFPNUM	Blockage option	ICORCR1	ICORCR2	ICORCA1	ICORCA2
130	PBR-A	3	3	6	8
131	PBR-A	3	3	9	13
132	PBR-A	3	3	14	17
133	PBR-A	3	3	18	21
134	PBR-A	3	3	22	25
135	PBR-A	3	3	26	27
140	PBR-A	4	4	6	8
141	PBR-A	4	4	9	13
142	PBR-A	4	4	14	17
143	PBR-A	4	4	18	21
144	PBR-A	4	4	22	25
145	PBR-A	4	4	26	27
150	PBR-A	5	5	6	8
151	PBR-A	5	5	9	13
152	PBR-A	5	5	14	17
153	PBR-A	5	5	18	21
154	PBR-A	5	5	22	25
155	PBR-A	5	5	26	27
160	PBR-A	6	6	6	8
161	PBR-A	6	6	9	13
162	PBR-A	6	6	14	17
163	PBR-A	6	6	18	21
164	PBR-A	6	6	22	25
165	PBR-A	6	6	26	27
170	N/A	N/A	N/A	N/A	N/A
221	PBR-R	2	3	6	10

Table B.18 (continued)

IFPNUM	Blockage option	ICORCR1	ICORCR2	ICORCA1	ICORCA2
231	PBR-R	3	4	6	10
241	PBR-R	4	5	6	10
251	PBR-R	5	6	6	10
222	PBR-R	2	3	11	15
232	PBR-R	3	4	11	15
242	PBR-R	4	5	11	15
252	PBR-R	5	6	11	15
223	PBR-R	2	3	16	19
233	PBR-R	3	4	16	19
243	PBR-R	4	5	16	19
253	PBR-R	5	6	16	19
224	PBR-R	2	3	20	23
234	PBR-R	3	4	20	23
244	PBR-R	4	5	20	23
254	PBR-R	5	6	20	23
225	PBR-R	2	3	24	27
235	PBR-R	3	4	24	27
245	PBR-R	4	5	24	27
255	PBR-R	5	6	24	27

B.1.6 PBMR Top Boundary HS Input

CARD	*WORD*	*VALUE*	*BASIS*
HS_ID	HSNAME	Table B.19	Heat structure name
	IHSNUM	Table B.19	Heat structure number
HS_GD	IGEOM	RECTANGULAR	Heat structure has rectangular geometry.

	ISS	SS	Steady-state initialization of heat structure temperatures is performed by MELGEN
HS_EOD	HSALT	Table B.19	Elevation of the lowest point on the heat structure
	ALPHA	0	Heat structure orientation, defined as the cosine of the acute angle between a vertical line and a heat structure surface. '0' indicates a horizontal surface with left-hand side on the bottom.
HS_SRC	ISRC	NO	No internal power source is used for the heat structures in this input.
HS_ND	NP	2	Number of temperature nodes. Each heat structure has two nodes, one at each surface.
	XI	0.0 / 0.35	Location of temperature nodes. Node locations are at the lower and upper boundary surfaces.
	TEMPIN	—	Initial temperature of the node. Since steady-state initialization is chosen, this value is ignored.
	MATNAM	STAINLESS-STEEL-304	Heat structure material. Properties of STAINLESS-STEEL-304 have been revised per the benchmark specifications.

HS_LB	IBCL	CalcCoefHS	The left surface has a convective boundary condition. The HS package calculates the convective heat transfer coefficient.
	IBVL	—	The boundary volume associated with the left surface is COR-CV1r6, where 'r' is the radial ring. These CVs have negligible volume and are not connected by flow paths, so heat transfer from this surface is negligible.
	MTEVAL	NO	Mass transfer is not evaluated. Since there is no water in the system, there is no mass transfer because there is no evaporation or condensation.
HS_LBP	IFLOWL	EXT	Flow over the surface is external. Since there is not actually flow over the surface, this parameter is irrelevant.
	CPFPL	0.0	The minimum value of the pool fraction for which heat transfer to the pool is calculated is set to 0.0. Since there is no pool, this parameter is irrelevant.

	CPFAL	0.0	The maximum value of the pool fraction for which heat transfer to the atmosphere is calculated is set to zero. Since there is no pool and since the heat transferred to the atmosphere is negligible in this situation, this parameter is irrelevant.
HS_LBS	ASURFL	Table B.19	Left boundary surface area, equal to $\pi(R_o^2 - R_i^2)$, where R_o and R_i are the outer and inner radii of the radial ring for which this HS serves as the boundary.
	CLNL	Table B.19	Characteristic length of the left boundary surface, equal to $2(R_o - R_i)$.
	BNDZL	Table B.19	Axial length of the left boundary surface, defined as the dimension of the surface in a direction perpendicular to the direction of energy flow within the heat structure. For this situation, CLNL=BNDZL.
HS_RB	IBCR	Symmetry	An adiabatic boundary condition is applied to the right surface per the benchmark specifications.
	IBVR	NO	No boundary volume can be selected for a surface with a 'Symmetry' boundary condition.
	MTEVAR	NO	No mass transfer is evaluated.

HS_RBP	IFLOWR	EXT	This field is required by MELGEN but has no impact for an adiabatic boundary.
	CPFPR	0.0	See above.
	CPFAR	0.0	See above.
HS_FT	IFTNUM	OFF	Liquid film-tracking is turned off.

Table B.19: PBMR upper boundary HS Input

HSNAME	IHSNUM	HSALT (m)	ASURFL (m^2)	BNDZL (m)
TOP-PLATE-R1	10000	3.1416	2.0	2.0
TOP-PLATE-R2	20000	1.1589	0.34	0.34
TOP-PLATE-R3	30000	1.3405	0.34	0.34
TOP-PLATE-R4	40000	1.5521	0.34	0.34
TOP-PLATE-R5	50000	1.7037	0.34	0.34
TOP-PLATE-R6	60000	1.8853	0.34	0.34
TOP-PLATE-R7	70000	7.8904	1.172	1.172
TOP-PLATE-R8	80000	2.6928	0.34	0.34

B.1.7 PBMR Side Reflector HS Input

CARD	*WORD*	*VALUE*	*BASIS*
HS_ID	HSNAME	Table B.20	Heat structure name
	IHSNUM	Table B.20	Heat structure number
HS_GD	IGEOM	CYLINDRICAL	Heat structure has cylindrical geometry.
	ISS	SS	Steady-state initialization of heat structure temperatures is performed by MELGEN

HS_EOD	HSALT	Table B.20	Elevation of the lowest point on the heat structure
	ALPHA	1	Heat structure orientation. '1' indicates a vertical surface.
HS_SRC	ISRC	NO	No internal power source is used for the heat structures in this input.
HS_ND	NP	2	Number of temperature nodes. Each heat structure has two nodes, one at each surface.
	XI	2.606 / 2.75	Location of temperature nodes. Node locations are at the inner and outer boundary surfaces. The axis of the cylinder corresponds to the core centerline
	TEMPIN	—	Initial temperature of the node. Since steady-state initialization is chosen, this value is ignored.
	MATNAM	GRAPHITE	Heat structure material. Properties of GRAPHITE have been revised per the benchmark specifications.
HS_LB	IBCL	CalcCoefHS	The left surface has a convective boundary condition. The HS package calculates the convective heat transfer coefficient.
	IBVL	Table B.20	The boundary volume associated with the left surface.
	MTEVAL	NO	Mass transfer is not evaluated.
HS_LBP	IFLOWL	EXT	Flow over the surface is external.

	CPFPL	0.5	The minimum value of the pool fraction for which heat transfer to the pool is calculated is set to 0.5. Since there is no pool, this parameter is irrelevant.
	CPFAL	0.5	The maximum value of the pool fraction for which heat transfer to the atmosphere is calculated is set to 0.5. This value ensures that heat transfer to the atmosphere is always allowed since the pool fraction will always be less than 0.5.
HS_LBS	ASURFL	—	Left boundary surface area. This parameter is ignored for cylindrical heat structures. MELGEN calculates the boundary surface area from the axial length and inner node location.
	CLNL	Table B.20	Characteristic length of the left boundary surface, equal to the axial length of the heat structure.
	BNDZL	Table B.20	Axial length of the left boundary surface. For this situation, CLNL=BNDZL.
HS_RB	IBCR	CalcCoefHS	The right surface has a convective boundary condition. The HS package calculates the convective heat transfer coefficient.

	IBVR	Table B.20	Right surface boundary volume. The gap between the side reflector and core barrel forms the boundary for these heat structures.
	MTEVAR	NO	No mass transfer is evaluated.
HS_RBP	IFLOWR	EXT	External flow is selected.
	CPFPR	0.0	See above.
	CPFAR	0.0	See above.
HS_RBS	ASURFR	—	Right boundary surface area. Ignored for cylindrical heat structures.
	CLNR	Table B.20	Characteristic length of the right surface. For this situation, CLNR=CLNL.
	BNDZR	Table B.20	Axial length of the right surface. For this situation, BNDZR=BNDZL.
HS_FT	IFTNUM	OFF	Liquid film-tracking is turned off.

Table B.20: PBMR side reflector HS input

HSNAME	IHSNUM	HSALT (m)	IBVL	IBVR	BNDZL
COR-RAD-BND-A1	70001	-4.35	182	301	0.35
COR-RAD-BND-A2	70002	-4.0	182	301	1.0
COR-RAD-BND-A3	70003	-3.0	182	301	1.0
COR-RAD-BND-A4	70004	-2.0	181	301	1.0
COR-RAD-BND-A5	70005	-1.0	181	301	1.0
COR-RAD-BND-A6	70006	0.0	181	302	0.5
COR-RAD-BND-A7	70007	0.5	181	302	0.5
COR-RAD-BND-A8	70008	1.0	181	302	0.5

Table B.20 (continued)

HSNAME	IHSNUM	HSALT (m)	IBVL	IBVR	BNDZL
COR-RAD-BND-A9	70009	1.5	181	302	0.5
COR-RAD-BND-A10	70010	2.0	181	302	0.5
COR-RAD-BND-A11	70011	2.5	181	302	0.5
COR-RAD-BND-A12	70012	3.0	181	302	0.5
COR-RAD-BND-A13	70013	3.5	181	302	0.5
COR-RAD-BND-A14	70014	4.0	181	302	0.5
COR-RAD-BND-A15	70015	4.5	181	303	0.5
COR-RAD-BND-A16	70016	5.0	181	303	0.5
COR-RAD-BND-A17	70017	5.5	181	303	0.5
COR-RAD-BND-A18	70018	6.0	181	303	0.5
COR-RAD-BND-A19	70019	6.5	181	303	0.5
COR-RAD-BND-A20	70020	7.0	181	303	0.5
COR-RAD-BND-A21	70021	7.5	181	303	0.5
COR-RAD-BND-A22	70022	8.0	181	303	0.5
COR-RAD-BND-A23	70023	8.5	181	303	0.5
COR-RAD-BND-A24	70024	9.0	181	304	0.5
COR-RAD-BND-A25	70025	9.5	181	304	0.5
COR-RAD-BND-A26	70026	10.0	181	304	0.5
COR-RAD-BND-A27	70027	10.5	181	304	0.5
COR-RAD-BND-A28	70028	11.0	170	304	0.5
COR-RAD-BND-A29	70029	11.5	186	304	1.5

B.1.8 PBMR Core Barrel HS Input

CARD	*WORD*	*VALUE*	*BASIS*
HS_ID	HSNAME	Table B.21	Heat structure name
	IHSNUM	Table B.21	Heat structure number

HS_GD	IGEOM	CYLINDRICAL	Heat structure has cylindrical geometry.
	ISS	SS	Steady-state initialization of heat structure temperatures is performed by MELGEN
HS_EOD	HSALT	Table B.21	Elevation of the lowest point on the heat structure
	ALPHA	1	Heat structure orientation. '1' indicates a vertical surface.
HS_SRC	ISRC	NO	No internal power source is used for the heat structures in this input.
HS_ND	NP	2	Number of temperature nodes. Each heat structure has two nodes, one at each surface.
	XI	2.875 / 2.925	Location of temperature nodes. Node locations are at the inner and outer boundary surfaces. The axis of the cylinder corresponds to the core centerline.
	TEMPIN	—	Initial temperature of the node. Since steady-state initialization is chosen, this value is ignored.
	MATNAM	STAINLESS-STEEL-304	Heat structure material. Properties have been revised per the benchmark specifications.

HS_LB	IBCL	CalcCoefHS	The left surface has a convective boundary condition. The HS package calculates the convective heat transfer coefficient.
	IBVL	Table B.20	The boundary volume associated with the left surface. The gap between the side reflector and core barrel forms the boundary for these heat structures.
	MTEVAL	NO	Mass transfer is not evaluated.
HS_LBP	IFLOWL	EXT	Flow over the surface is external.
	CPFPL	0.0	The minimum value of the pool fraction for which heat transfer to the pool is calculated is set to 0.0.
	CPFAL	0.0	The maximum value of the pool fraction for which heat transfer to the atmosphere is calculated is set to 0.0.
HS_LBS	ASURFL	—	Left boundary surface area. This parameter is ignored for cylindrical heat structures.
	CLNL	Table B.21	Characteristic length of the left boundary surface, equal to the axial length of the heat structure.
	BNDZL	Table B.21	Axial length of the left boundary surface. For this situation, CLNL=BNDZL.

Table B.21
PBMR core barrel HS input

HSNAME	IHSNUM	HSALT (m)	IBVL	IBVR	BNDZL
CORE-BARREL-1	80001	-4.5	301	401	4.5
CORE-BARREL-2	80002	0.0	302	402	4.5
CORE-BARREL-3	80003	4.5	303	403	4.5
CORE-BARREL-4	80004	9.0	304	404	4.5

HS_RB	IBCR	CalcCoefHS	The right surface has a convective boundary condition. The HS package calculates the convective heat transfer coefficient.
	IBVR	Table B.21	Right surface boundary volume. The gap between the core barrel and RPV forms the boundary for these heat structures.
	MTEVAR	NO	No mass transfer is evaluated.
HS_RBP	IFLOWR	EXT	External flow is selected.
	CPFPR	0.0	See above.
	CPFAR	0.0	See above.
HS_RBS	ASURFR	—	Right boundary surface area. Ignored for cylindrical heat structures.
	CLNR	Table B.21	Characteristic length of the right surface. For this situation, CLNR=CLNL.
	BNDZR	Table B.21	Axial length of the right surface. For this situation, BNDZR=BNDZL.
HS_FT	IFTNUM	OFF	Liquid film-tracking is turned off.

B.1.9 PBMR RPV HS Input

CARD	*WORD*	*VALUE*	*BASIS*
HS_ID	HSNAME	Table B.22	Heat structure name
	IHSNUM	Table B.22	Heat structure number
HS_GD	IGEOM	CYLINDRICAL	Heat structure has cylindrical geometry.
	ISS	SS	Steady-state initialization of heat structure temperatures is performed by MELGEN
HS_EOD	HSALT	Table B.22	Elevation of the lowest point on the heat structure
	ALPHA	1	Heat structure orientation. '1' indicates a vertical surface.
HS_SRC	ISRC	NO	No internal power source is used for the heat structures in this input.
HS_ND	NP	2	Number of temperature nodes. Each heat structure has two nodes, one at each surface.
	XI	3.1 / 3.28	Location of temperature nodes. Node locations are at the inner and outer boundary surfaces. The axis of the cylinder corresponds to the core centerline.
	TEMPIN	—	Initial temperature of the node. Since steady-state initialization is chosen, this value is ignored.

	MATNAM	ALUMINUM	Heat structure material. Material has been redefined as steel per the benchmark specifications.
HS_LB	IBCL	CalcCoefHS	The left surface has a convective boundary condition. The HS package calculates the convective heat transfer coefficient.
	IBVL	Table B.22	The boundary volume associated with the left surface. The gap between the core barrel and RPV forms the boundary for these heat structures.
	MTEVAL	NO	Mass transfer is not evaluated.
HS_LBP	IFLOWL	EXT	Flow over the surface is external.
	CPFPL	0.0	The minimum value of the pool fraction for which heat transfer to the pool is calculated is set to 0.0.
	CPFAL	0.0	The maximum value of the pool fraction for which heat transfer to the atmosphere is calculated is set to 0.0.
HS_LBS	ASURFL	—	Left boundary surface area. This parameter is ignored for cylindrical heat structures.
	CLNL	Table B.22	Characteristic length of the left boundary surface, equal to the axial length of the heat structure.

	BNDZL	Table B.22	Axial length of the left boundary surface. For this situation, CLNL=BNDZL.
HS_RB	IBCR	CalcCoefHS	The right surface has a convective boundary condition. The HS package calculates the convective heat transfer coefficient.
	IBVR	Table B.22	Right surface boundary volume. The gap between the RPV and RCCS forms the boundary for these heat structures.
	MTEVAR	NO	No mass transfer is evaluated.
HS_RBP	IFLOWR	EXT	External flow is selected.
	CPFPR	0.0	See above.
	CPFAR	0.0	See above.
HS_RBS	ASURFR	—	Right boundary surface area. Ignored for cylindrical heat structures.
	CLNR	Table B.22	Characteristic length of the right surface. For this situation, CLNR=CLNL.
	BNDZR	Table B.22	Axial length of the right surface. For this situation, BNDZR=BNDZL.
HS_FT	IFTNUM	OFF	Liquid film-tracking is turned off.

B.1.10 PBMR RCCS HS Input

CARD	*WORD*	*VALUE*	*BASIS*
HS_ID	HSNAME	Table B.23	Heat structure name
	IHSNUM	Table B.23	Heat structure number

HS_GD	IGEOM	CYLINDRICAL	Heat structure has cylindrical geometry.
	ISS	SS	Steady-state initialization of heat structure temperatures is performed by MELGEN
HS_EOD	HSALT	Table B.23	Elevation of the lowest point on the heat structure
	ALPHA	1	Heat structure orientation. '1' indicates a vertical surface.
HS_SRC	ISRC	NO	No internal power source is used for the heat structures in this input.
HS_ND	NP	2	Number of temperature nodes. Each heat structure has two nodes, one at each surface.
	XI	4.62 / 4.63	Location of temperature nodes. Node locations are at the inner and outer boundary surfaces. The axis of the cylinder corresponds to the core centerline.
	TEMPIN	—	Initial temperature of the node. Since steady-state initialization is chosen, this value is ignored.
	MATNAM	STAINLESS-STEEL-304	Heat structure material. Properties have been redefined per the benchmark specifications.

HS_LB	IBCL	CalcCoefHS	The left surface has a convective boundary condition. The HS package calculates the convective heat transfer coefficient.
	IBVL	Table B.22	The boundary volume associated with the left surface. The gap between the RPV and RCCS forms the boundary for these heat structures.
	MTEVAL	NO	Mass transfer is not evaluated.
HS_LBP	IFLOWL	EXT	Flow over the surface is external.
	CPFPL	0.0	The minimum value of the pool fraction for which heat transfer to the pool is calculated is set to 0.0.
	CPFAL	0.0	The maximum value of the pool fraction for which heat transfer to the atmosphere is calculated is set to 0.0.
HS_LBS	ASURFL	—	Left boundary surface area. This parameter is ignored for cylindrical heat structures.
	CLNL	Table B.23	Characteristic length of the left boundary surface, equal to the axial length of the heat structure.
	BNDZL	Table B.23	Axial length of the left boundary surface. For this situation, CLNL=BNDZL.

HS_RB	IBCR	TempTimeTF	The right surface has a fixed temperature boundary condition specified by a tabular function.
	NAMECFTF	RADIAL_BC	Tabular function used to specify the temperature of the outer boundary of the RCCS heat structures. This tabular function sets the temperature as 293 K.
	IBVR	NO	No boundary volume is allowed for a fixed temperature boundary.
	MTEVAR	NO	No mass transfer is evaluated.
HS_RBP	IFLOWR	EXT	External flow is selected.
	CPFPR	0.0	See above.
	CPFAR	0.0	See above.
HS_FT	IFTNUM	OFF	Liquid film-tracking is turned off.

Table B.22
PBMR RPV HS input

HSNAME	IHSNUM	HSALT (m)	IBVL	IBVR	BNDZL
RPV-1	90001	-4.5	401	501	4.5
RPV-2	90002	0.0	402	502	4.5
RPV-3	90003	4.5	403	503	4.5
RPV-4	90004	9.0	404	504	4.5

Table B.23
PBMR RCCS HS input

HSNAME	IHSNUM	HSALT (m)	IBVL	BNDZL
RCCS-1	91001	-4.5	501	4.5
RCCS-2	91002	0.0	502	4.5
RCCS-3	91003	4.5	503	4.5
RCCS-4	91004	9.0	504	4.5

B.1.11 MELGEN NCG Input

CARD	*WORD*	*VALUE*	*BASIS*
NCG_ID	MNAME	'HE'	Helium gas is used in this calculation
NCG_PRP	CV0	3130	Constant value for helium specific heat at constant volume. Equal to the specific heat at constant pressure listed in the benchmark (5195 J/kgK) [71] divided by the specific heat ratio for helium (1.66) [88].
NCG_PRP	MNAME	'H2'	Hydrogen gas. Not used in this calculation, but must still be specified.
NCG_PRP	MNAME	'CO'	Carbon monoxide. Must be listed whenever GRAPHITE is present.
NCG_PRP	MNAME	'02'	Oxygen. Present in reactor cavity CVs.
NCG_PRP	MNAME	'C02'	Carbon dioxide. Must be listed whenver GRAPHITE is present.
NCG_PRP	MNAME	'CH4'	Methane. Must be specified by is not used.
NCG_PRP	MNAME	'N2'	Nitrogen. Present in the reactor cavity CVs.

B.1.12 MELGEN MP Input

CARD	*WORD*	*VALUE*	*BASIS*
MP_ID	MATNAM	'GRAPHITE'	Graphite used in this calculation

MP_PRTF	CPS	'CPS-GRAPH'	Tabular function (TF) used to define graphite specific heat. TF values listed in Table B.24. From the benchmark document [71].
	THC	'THC-GRAPH'	TF specifying graphite thermal conductivity. See Table B.24. From [71].
	RHO	'RHO-GRAPH'	TF specifying graphite density. See Table B.24. From [71].
MP_PRC	RHOM	1780	Constant value for graphite density [71]
MP_ID	MATNAM	'STAINLESS-STEEL-304'	Steel used to represent the core barrel. Properties are redefined to match those given in the benchmark document [71].
MP_PRTF	CPS	'CPS-SS316'	Tabular function (TF) used to define core barrel specific heat. TF values listed in Table B.24. From [71].
	THC	'THC-SS316'	TF specifying core barrel thermal conductivity. See Table B.24. From [71].
	RHO	'RHO-STEEL'	TF specifying core barrel density. See Table B.24. From [71].
MP_PRC	RHOM	7800	Constant value for core barrel density [71]

MP_ID	MATNAM	'ZIRCALOY'	Zircaloy redefined as graphite. Used for supporting structures in the lower reflector because GRAPH cannot be chosen as SS material.
MP_PRTF	CPS	'CPS-GRAPH'	Tabular function (TF) used to define graphite specific heat. TF values listed in Table B.24. From [71].
	THC	'THC-GRAPH'	TF specifying graphite thermal conductivity. See Table B.24. From [71].
	RHO	'RHO-GRAPH'	TF specifying graphite density. See Table B.24. From [71].
	ENH	'ENH-GRAPH'	TF specifying graphite enthalpy. Equal to the product of the specific heat and the difference between the temperature in the table and the reference temperature. See Table B.24.
MP_PRC	RHOM	1780	Constant value for graphite density [71]
MP_ID	MATNAM	'ALUMINUM'	Steel used to represent the RPV. Properties are redefined to match those given in the benchmark document [71].

MP_PRTF	CPS	'CPS-SA508'	Tabular function (TF) used to define RPV specific heat. TF values listed in Table B.24. From [71].
	THC	'THC-SA508'	TF specifying RPV thermal conductivity. See Table B.24. From [71].
	RHO	'RHO-STEEL'	TF specifying RPV density. See Table B.24. From [71].
	ENH	'ENH-STEEL'	TF specifying RPV enthalpy. Equal to the product of the specific heat and the difference between the temperature in the table and the reference temperature. See Table B.24.
MP_PRC	RHOM	7800	Constant value for RPV density [71]
	TMLT	1700	Melting temperature for stainless steel [6]
MP_ID	MATNAM	'URANIUM-DIOXIDE'	UO_2 used as fuel material
MP_PRC	RHOM	10400	Constant UO_2 density specified in the benchmark definition [71]
MP_ID	MATNAM	'ZIRCONIUM-OXIDE '	Must be listed per COR package requirements but is not used
MP_ID	MATNAM	'STAINLESS-STEEL '	Material listed as STEEL in COR package. Used to model SS.

MP_ID	MATNAM	'STAINLESS-STEEL-OXIDE '	Must be declared when STAINLESS-STEEL is present
MP_ID	MATNAM	'ALUMINUM-OXIDE '	Must be declared when ALUMINUM is present
MP_ID	MATNAM	'CARBON-STEEL '	Material used to model the lower head
MP_ID	MATNAM	'BORON-CARBIDE '	Must be listed per COR package requirements but is not used

Table B.24: Material properties defined for PBMR-400 calculations

Material	Property	Value	Units
GRAPHITE	Specific heat	1697	J/kgK
	Thermal conductivity	26.0	W/mK
	Density	1780	kg/m^3
SS-304 [a]	Specific heat	540	J/kgK
	Thermal conductivity	17	W/mK
	Density	7800	kg/m^3
ALUMINUM [b]	Specific heat	525	J/kgK
	Thermal conductivity	38	W/mK
	Density	7800	kg/m^3
URANIUM-DIOXIDE	Density	10400	kg/m^3

[a] Redefined as SS-316, the core barrel material
[b] Redefined as SA-508, the RPV material

B.2 pbmr400-src_sink.inp

B.2.1 CVH-FL Source/Sink Input

CARD	*WORD*	*VALUE*	*BASIS*
CV_ID	CVNAME	'SRC-CV200'	Helium source CV name
	ICVNUM	200	Source CV number
CV_THR	ICVTHR	NONEQUIL	Tpool ≠ Tatmos
	IPFSW	FOG	Default
	ICVACT	PROP-SPECIFIED	CV thermodynamic properties are specified as a function of time
CV_PAS	ITYPTH	SEPARATE	Separate pool and atmosphere input
	IPORA	ONLYATM	Only atmosphere is present
	VAPORSTATE	SUPERHEATED	Helium is superheated
CV_VAT	CVZ	-2.0 / -1.5	Altitudes in the altitude/volume table
	CVVOL	0.0 / 1.0	Volume at altitude CVZ. Total volume is irrelevant, since the state of the volume is PROP-SPECIFIED.
CV_PTD	PVOL	'SourcePressure'	Name of CF specifying source pressure
CV_AAD	TATM	'SourceTemp'	CF specifying source temperature

CV_NCG	RHUM	'Src-Sink_RHUM'	CF specifying source relative humidity. 'Src-Sink_RHUM' returns 0.0 throughout the calculations.
	NAMGAS	'HE'	CV contains helium
	CFNAME	'Src-Sink_HeFrac'	Mole fraction of helium in the source CV. CF returns 1.0 throughout the calculations.
CV_ID	CVNAME	'SINK-CV210'	Helium sink CV name
	ICVNUM	210	Sink CV number
CV_THR	ICVTHR	NONEQUIL	Tpool $\neq$ Tatmos
	IPFSW	FOG	Default
	ICVACT	PROP-SPECIFIED	CV thermodynamic properties are specified as a function of time
CV_PAS	ITYPTH	SEPARATE	Separate pool and atmosphere input
	IPORA	ONLYATM	Only atmosphere is present
	VAPORSTATE	SUPERHEATED	Helium is superheated
CV_VAT	CVZ	-3.0 / -2.5	Altitudes in the altitude/volume table
	CVVOL	0.0 / 1.0	Volume at altitude CVZ. Total volume is irrelevant, since the state of the volume is PROP-SPECIFIED.
CV_PTD	PVOL	'SinkPressure'	Name of CF specifying sink pressure

CV_AAD	TATM	'SinkTemp'	CF specifying sink temperature
CV_NCG	RHUM	'Src-Sink_RHUM'	CF specifying source relative humidity. 'Src-Sink_RHUM' returns 0.0 throughout the calculations.
	NAMGAS	'HE'	CV contains helium
	CFNAME	'Src-Sink_HeFrac'	Mole fraction of helium in the sink CV. CF returns 1.0 throughout the calculations.
FL_ID	FPNAME	'HeSource'	Source flow path name
	IFPNUM	200	Source flow path number
FL_FT	KCVFM	'SRC-CV200'	'FROM' CV name
	KCVTO	'CV181-RISER'	'TO' CV name
	ZFM	-1.75	'FROM' junction altitude
	ZTO	-1.75	'TO' junction altitude
FL_GEO	FLARA	0.5386	Flow area. Equal to the total helium riser flow area.
	FLLEN	1.0	Flow path length. Flow path length is arbitrary and has little impact on the calculation, since the reactor inlet pressure is considered to be the pressure in CV181.
	FLOPO	1.0	Flow path is fully open
FL_SEG	SAREA	0.5386	Segment flow area. Since there is only one segment, SAREA=FLARA.

	SLEN	1.0	Segment length, equal to FLLEN
	SHYD	0.07	Segment hydraulic diameter, equal to the diameter of the riser tubes
FL_VTM	FLNAME	'HeSource'	Name of flow path that will be time-dependent
	NFUN	'HeSource'	Name of CF used to define the flow velocity as a function of time
FL_ID	FPNAME	'HeSink'	Sink flow path name
	IFPNUM	210	Sink flow path number
FL_FT	KCVFM	'CV100-LOWER_PLENUM'	'FROM' CV name
	KCVTO	'SINK-CV210'	'TO' CV name
	ZFM	-2.75	'FROM' junction altitude
	ZTO	-2.75	'TO' junction altitude
FL_GEO	FLARA	1.522	Flow area. This value is insignificant, since the outlet pressure is considered to be the pressure in CV100.
	FLLEN	0.51	Flow path length. This value is arbitrary for the reason cited above.
	FLOPO	1.0	Flow path is fully open
FL_SEG	SAREA	1.522	Segment flow area. Since there is only one segment, SAREA=FLARA.

SLEN	0.51	Segment length, equal to FLLEN
SHYD	0.144	Segment hydraulic diameter, equal to the lower plenum hydraulic diameter

B.2.2 Source/Sink Control Logic

CARD	*WORD*	*VALUE*	*BASIS*
CF_ID	CFNAME	'TransientTime'	CF defines the time at the start of a transient
	ICFNUM	001	CF number
	CFTYPE	EQUALS	CF has EQUALS type
CF_SAI	CFSCAL	0.0	CF returns CFSCAL * Function Value + CFADCN. Function value is multiplied by 0.0.
	CFADCN	0.0	0.0 is added to function value. To change 'TransientTime' on a calculation restart, simply change the value of CFSCAL. This will set the CF as a constant equal to CFSCAL, until CFSCAL is modified upon a calculation restart.
	CFVALR	0.0	Initial value for the CF

CF_ARG	NCFARG	1	One argument is required for an EQUALS CF
	CHARG	EXEC-TIME	CF variable argument. The variable used is arbitrary, since it is multiplied by zero. This is done to create a constant CF.
	ARSCAL	0.0	Function value is equal to ARSCAL * Variable + ARADCN. EXEC-TIME is multiplied by zero to create a constant CF.
	ARADCN	0.0	Because the variable is multiplied by zero, and because this quantity is added to zero, the CF will return whatever value is input for CFADCN
CF_ID	CFNAME	'TransientDT'	CF returns the time elapsed since the start of the transient (defined by 'TransientTime')
	ICFNUM	002	CF number
	CFTYPE	ADD	CF has type ADD

CF_SAI	CFSCAL	0.0	Function value is multiplied by zero for steady-state calculations to ensure that the thermodynamic state of the inlet and outlet is constant. For transient calculations, CFSCAL should be changed to 1.0 in the MELCOR input deck.
	CFADCN	0.0	—
	CFVALR	0.0	CF is initially 0.0
CF_ARG	NCFARG	2	Two arguments are added together for this CF type
	CHARG	EXEC-TIME	The first argument is the problem time
	ARSCAL	1.0	—
	ARADCN	0.0	—
	CHARG	CF-VALU('TransientTime')	The second argument is the value chosen as the transient start time
	ARSCAL	-1.0	'TransientTime' is multiplied by -1.0 so that 'TransientTime' is subtracted from EXEC-TIME

	ARADCN	0.0	—
CF_ID	CFNAME	‘dMdot-dt’	CF defines the time rate of change of the mass flow rate. This CF, in conjunction with CFs described below, allows the user to linearly increase or decrease the mass flow rate.
	ICFNUM	003	CF number
	CFTYPE	EQUALS	CF has EQUALS type
CF_SAI	CFSCAL	0.0	—
	CFADCN	0.0	No change in mass flow rate is specified for steady-state calculations. This value is changed upon problem restart for transient calculations during which the mass flow rate decreases.
	CFVALR	0.0	Initial value for the CF
CF_ARG	NCFARG	1	One argument is required for an EQUALS CF
	CHARG	EXEC-TIME	Arbitrary variable
	ARSCAL	0.0	—
	ARADCN	0.0	CF returns value of CFADCN

CF_ID	CFNAME	'FlowLoss'	CF calculates the total change in flow since the start of the transient
	ICFNUM	004	CF number
	CFTYPE	MULTIPLY	CF has type MULTIPLY
CF_SAI	CFSCAL	0.0	Function value is multiplied by zero for steady-state calculations. For transient calculations, CFSCAL should be changed to 1.0 in the MELCOR input deck.
	CFADCN	0.0	—
	CFVALR	0.0	CF is initially 0.0
CF_ARG	NCFARG	2	Two arguments are multiplied together for this CF type
	CHARG	CF-VALU('TransientDT')	The first argument is the time elapsed since the start of the transient
	ARSCAL	1.0	—
	ARADCN	0.0	—

	CHARG	CF-VALU(‘dMdot-dt’)	The second argument is the rate of change of the mass flow rate. Multiplying by the first argument gives the total change in mass flow rate (in kg/s) since the start of the transient.
	ARSCAL	1.0	—
	ARADCN	0.0	—
CF_ID	CFNAME	‘dPin-dt’	CF defines the time rate of change of the source pressure. This CF, in conjunction with CFs described below, allows the user to linearly increase or decrease the coolant inlet pressure.
	ICFNUM	005	CF number
	CFTYPE	EQUALS	CF has EQUALS type
CF_SAI	CFSCAL	0.0	—
	CFADCN	0.0	No change in inlet pressure is specified for steady-state calculations. This value is changed upon problem restart for transient calculations.
	CFVALR	0.0	Initial value for the CF

CF_ARG	NCFARG	1	One argument is required for an EQUALS CF
	CHARG	EXEC-TIME	Arbitrary variable
	ARSCAL	0.0	—
	ARADCN	0.0	CF returns value of CFADCN
CF_ID	CFNAME	'PinLoss'	CF calculates the total change in inlet pressure since the start of the transient
	ICFNUM	006	CF number
	CFTYPE	MULTIPLY	CF has type MULTIPLY
CF_SAI	CFSCAL	0.0	Function value is multiplied by zero for steady-state calculations. For transient calculations, CFSCAL should be changed to 1.0 in the MELCOR input deck.
	CFADCN	0.0	—
	CFVALR	0.0	CF is initially 0.0
CF_ARG	NCFARG	2	Two arguments are multiplied together for this CF type
	CHARG	CF-VALU('TransientDT')	The first argument is the time elapsed since the start of the transient

	ARSCAL	1.0	—
	ARADCN	0.0	—
	CHARG	CF-VALU(‘dPin-dt’)	The second argument is the rate of change of the inlet pressure. Multiplying by the first argument gives the total change in inlet pressure (in Pa) since the start of the transient.
	ARSCAL	1.0	—
	ARADCN	0.0	—
CF_ID	CFNAME	‘dPout-dt’	CF defines the time rate of change of the sink pressure. This CF, in conjunction with CFs described below, allows the user to linearly increase or decrease the coolant outlet pressure.
	ICFNUM	007	CF number
	CFTYPE	EQUALS	CF has EQUALS type
CF_SAI	CFSCAL	0.0	—

	CFADCN	0.0	No change in outlet pressure is specified for steady-state calculations. This value is changed upon problem restart for transient calculations.
	CFVALR	0.0	Initial value for the CF
CF_ARG	NCFARG	1	One argument is required for an EQUALS CF
	CHARG	EXEC-TIME	Arbitrary variable
	ARSCAL	0.0	—
	ARADCN	0.0	CF returns value of CFADCN
CF_ID	CFNAME	'PoutLoss'	CF calculates the total change in outlet pressure since the start of the transient
	ICFNUM	008	CF number
	CFTYPE	MULTIPLY	CF has type MULTIPLY
CF_SAI	CFSCAL	0.0	Function value is multiplied by zero for steady-state calculations. For transient calculations, CFSCAL should be changed to 1.0 in the MELCOR input deck.
	CFADCN	0.0	—

	CFVALR	0.0	CF is initially 0.0
CF_ARG	NCFARG	2	Two arguments are multiplied together for this CF type
	CHARG	CF-VALU('TransientDT')	The first argument is the time elapsed since the start of the transient
	ARSCAL	1.0	—
	ARADCN	0.0	—
	CHARG	CF-VALU('dPout-dt')	The second argument is the rate of change of the outlet pressure. Multiplying by the first argument gives the total change in outlet pressure (in Pa) since the start of the transient.
	ARSCAL	1.0	—
	ARADCN	0.0	—
CF_ID	CFNAME	'Pmin'	CF defines the minimum allowable inlet or outlet pressure. This CF is used to set the long-term (constant) inlet and outlet pressure.
	ICFNUM	009	CF number
	CFTYPE	EQUALS	CF has type EQUALS
CF_SAI	CFSCAL	0.0	—

	CFADCN	0.0	This CF has no effect on steady-state calculations
	CFVALR	0.0	—
CF_ARG	NCFARG	1	One argument is required for an EQUALS CF
	CHARG	EXEC-TIME	Arbitrary variable
	ARSCAL	0.0	—
	ARADCN	0.0	CF returns value of CFADCN
CF_ID	CFNAME	'SS_MFlow'	CF is used to define the steady-state mass flow rate
	ICFNUM	050	CF number
	CFTYPE	EQUALS	CF has type EQUALS
CF_SAI	CFSCAL	1.0	—
	CFADCN	0.0	—
	CFVALR	192.7	Initial CF value. Equal to the steady-state mass flow rate.
CF_ARG	NCFARG	1	One argument
	CHARG	EXEC-TIME	Arbitrary variable
	ARSCAL	0.0	—
	ARADCN	192.7	Function value is equal to 192.7

CF_ID	CFNAME	‘MFlow’	CF returns sum of the steady-state mass flow rate and the total change in flow since the start of the transient (‘FlowLoss’)
	ICFNUM	051	CF number
	CFTYPE	ADD	CF has type ADD
CF_SAI	CFSCAL	1.0	—
	CFADCN	0.0	—
	CFVALR	192.7	CF is initially 192.7, equal to the steady-state flow rate
CF_ARG	NCFARG	2	Two arguments are added together for this CF type
	CHARG	CF-VALU(‘SS_MFlow’)	The first argument is the steady-state mass flow rate
	ARSCAL	1.0	—
	ARADCN	0.0	—

	CHARG	CF-VALU('FlowLoss')	The second argument is the change in flow rate since the start of the transient. This value is negative for decreasing flow. The sum of these two arguments gives the mass flow rate for the next time step.
	ARSCAL	1.0	—
	ARADCN	0.0	—
CF_ID	CFNAME	'CF_HeSource'	CF calculates the coolant inlet velocity corresponding to the flow rate 'MFlow'
	ICFNUM	052	CF number
	CFTYPE	DIVIDE	CF has type DIVIDE. This CF type divides the second argument by the first argument.
CF_SAI	CFSCAL	1.0	—
	CFADCN	0.0	—
	CFVALR	62.696	Steady-state coolant inlet velocity
CF_ARG	NCFARG	2	Two arguments are divided for this CF type
	CHARG	CVH-RHO(SRC-CV200,HE)	The first argument is the coolant inlet density

	ARSCAL	0.5386	The density is multiplied by the flow area ($v = \dot{m}/(\rho A)$)
	ARADCN	0.0	—
	CHARG	CF-VALU('MFlow')	The second argument is the mass flow rate 'MFlow'
	ARSCAL	1.0	—
	ARADCN	0.0	—
CF_ID	CFNAME	'SourceCheck'	CF determines whether the value of the mass flow rate 'MFlow' is positive. If the flow is not positive, the control function latches FALSE.
	ICFNUM	053	CF number
	CFTYPE	L-GT	CF has logical-greater than type. TRUE is returned when ARG1>ARG2.
CF_LIV	LCFVAL	TRUE	CF is initially TRUE
CF_CLS	CLASS	LATCH	CF is classified as LATCH, meaning the CF will change state only once, retaining its new value from that point onward

CF_ARG	NCFARG	2	Two arguments are required for an L-GT CF
	CHARG	CF-VALU(‘MFlow’)	The first argument is the mass flow rate ‘MFlow’
	ARSCAL	1.0	—
	ARADCN	0.0	—
	CHARG	EXEC-TIME	Arbitrary variable
	ARSCAL	0.0	Variable is multiplied by zero, so that the CF checks whether or not ‘MFlow’ is positive
	ARADCN	0.0	—
CF_ID	CFNAME	‘HeSource’	CF returns the coolant inlet velocity to the FL package
	ICFNUM	054	CF number
	CFTYPE	L-A-IFTE	CF has type logical-if-then-else. This CF type returns ARG2 if ARG1 is TRUE and returns ARG3 if ARG1 is FALSE.
CF_SAI	CFSCAL	1.0	—
	CFADCN	0.0	—
	CFVALR	62.696	Steady-state coolant inlet velocity
CF_ARG	NCFARG	3	Three arguments are divided for this CF type

	CHARG	CF-VALU(‘SourceCheck’)	CF returns ARG2 if ‘SourceCheck’ is TRUE and ARG3 if ‘SourceCheck’ is FALSE
	CHARG	CF-VALU(’CF_HeSource’)	CF returns the inlet velocity calculated by ‘CF_HeSource’ if the flow is positive
	ARSCAL	1.0	—
	ARADCN	0.0	—
	CHARG	EXEC-TIME	CF returns 0.0 for the inlet velocity if the flow calculated by ‘MFlow’ is not positive
	ARSCAL	0.0	—
	ARADCN	0.0	—
CF_ID	CFNAME	’SS_Pin’	CF is used to define the steady-state inlet pressure
	ICFNUM	301	CF number
	CFTYPE	EQUALS	CF has type EQUALS
CF_SAI	CFSCAL	1.0	—
	CFADCN	0.0	—
	CFVALR	9.311E6	Initial CF value. Approximately equal to the steady-state inlet pressure calculated by MELCOR.

CF_ARG	NCFARG	1	One argument
	CHARG	EXEC-TIME	Arbitrary variable
	ARSCAL	0.0	—
	ARADCN	9.311E6	Function value is equal to 9.311E6
CF_ID	CFNAME	‘Pin’	CF returns sum of the steady-state inlet pressure and the total change in inlet pressure since the start of the transient (‘PinLoss’)
	ICFNUM	302	CF number
	CFTYPE	ADD	CF has type ADD
CF_SAI	CFSCAL	1.0	—
	CFADCN	0.0	—
	CFVALR	9.311E6	—
CF_ARG	NCFARG	2	Two arguments are added together for this CF type
	CHARG	CF-VALU(‘SS_Pin’)	The first argument is the steady-state inlet pressure
	ARSCAL	1.0	—
	ARADCN	0.0	—

	CHARG	CF-VALU('PinLoss')	The second argument is the change in inlet pressure since the start of the transient. This value is negative for decreasing pressure. The sum of these two arguments gives the inlet pressure for the next time step.
	ARSCAL	1.0	—
	ARADCN	0.0	—
CF_ID	CFNAME	'PinCheck'	CF determines whether the value of the inlet pressure 'MFlow' is greater than the specified minimum inlet pressure 'Pmin'
	ICFNUM	303	CF number
	CFTYPE	L-GT	CF has logical-greater than type. TRUE is returned when ARG1R>ARG2.
CF_LIV	LCFVAL	TRUE	CF is initially TRUE
CF_CLS	CLASS	LATCH	CF is classified as LATCH
CF_ARG	NCFARG	2	Two arguments are required for an L-GT CF

	CHARG	CF-VALU(‘Pin’)	The first argument is the inlet pressure ‘Pin’
	ARSCAL	1.0	—
	ARADCN	0.0	—
	CHARG	CF-VALU(‘Pmin’)	The second argument is the minimum pressure ‘Pmin’
	ARSCAL	1.0	—
	ARADCN	0.0	—
CF_ID	CFNAME	‘SourcePressure’	CF returns the coolant inlet pressure to the CVH package
	ICFNUM	304	CF number
	CFTYPE	L-A-IFTE	CF has type logical-if-then-else
CF_SAI	CFSCAL	1.0	—
	CFADCN	0.0	—
	CFVALR	9.311E6	Steady-state coolant inlet pressure
CF_ARG	NCFARG	3	Three arguments are required for this CF type
	CHARG	CF-VALU(‘PinCheck’)	CF returns ARG2 if ‘PinCheck’ is TRUE and ARG3 if ‘PinCheck’ is FALSE

	CHARG	CF-VALU('Pin')	CF returns the inlet pressure calculated by 'Pin' if the value is greater than 'Pmin'
	ARSCAL	1.0	—
	ARADCN	0.0	—
	CHARG	CF-VALU('Pmin')	CF returns the value of 'Pmin' for the inlet pressure
	ARSCAL	1.0	—
CF_ID	CFNAME	'SS_Pout'	CF is used to define the steady-state outlet pressure
	ICFNUM	311	CF number
	CFTYPE	EQUALS	CF has type EQUALS
CF_SAI	CFSCAL	1.0	—
	CFADCN	0.0	—
	CFVALR	9.0E6	Initial CF value
CF_ARG	NCFARG	1	One argument
	CHARG	EXEC-TIME	Arbitrary variable
	ARSCAL	0.0	—
	ARADCN	9.0E6	Function value is equal to 9.0E6

CF_ID	CFNAME	'Pout'	CF returns sum of the steady-state outlet pressure and the total change in outlet pressure since the start of the transient ('PoutLoss')
	ICFNUM	312	CF number
	CFTYPE	ADD	CF has type ADD
CF_SAI	CFSCAL	1.0	—
	CFADCN	0.0	—
	CFVALR	9.0E6	—
CF_ARG	NCFARG	2	Two arguments are added together for this CF type
	CHARG	CF-VALU('SS_Pout')	The first argument is the steady-state outlet pressure
	ARSCAL	1.0	—
	ARADCN	0.0	—
	CHARG	CF-VALU('PoutLoss')	The second argument is the change in outlet pressure since the start of the transient. This value is negative for decreasing pressure. The sum of these two arguments gives the outlet pressure for the next time step.

	ARSCAL	1.0	—
	ARADCN	0.0	—
CF_ID	CFNAME	‘PoutCheck’	CF determines whether the value of the outlet pressure ‘MFlow’ is greater than the specified minimum outlet pressure ‘Pmin’
	ICFNUM	313	CF number
	CFTYPE	L-GT	CF has logical-greater than type. TRUE is returned when ARG1>ARG2.
CF_LIV	LCFVAL	TRUE	CF is initially TRUE
CF_CLS	CLASS	LATCH	CF is classified as LATCH
CF_ARG	NCFARG	2	Two arguments are required for an L-GT CF
	CHARG	CF-VALU(‘Pout’)	The first argument is the outlet pressure ‘Pout’
	ARSCAL	1.0	—
	ARADCN	0.0	—
	CHARG	CF-VALU(‘Pmin’)	The second argument is the minimum pressure ‘Pmin’
	ARSCAL	1.0	—
	ARADCN	0.0	—

CF_ID	CFNAME	'SinkPressure'	CF returns the coolant outlet pressure to the CVH package
	ICFNUM	314	CF number
	CFTYPE	L-A-IFTE	CF has type logical-if-then-else
CF_SAI	CFSCAL	1.0	—
	CFADCN	0.0	—
	CFVALR	9.0E6	Steady-state coolant outlet pressure
CF_ARG	NCFARG	3	Three arguments are required for this CF type
	CHARG	CF-VALU('PoutCheck')	CF returns ARG2 if 'PoutCheck' is TRUE and ARG3 if 'PoutCheck' is FALSE
	CHARG	CF-VALU('Pout')	CF returns the outlet pressure calculated by 'Pout' if the value is greater than 'Pmin'
	ARSCAL	1.0	—
	ARADCN	0.0	—
	CHARG	CF-VALU('Pmin')	CF returns the value of 'Pmin' for the outlet pressure
	ARSCAL	1.0	—
	ARADCN	0.0	—

CF_ID	CFNAME	'SourceTemp'	CF returns the coolant inlet temperature to the CVH package. During steady-state calculations, inlet temperature is constant at 773 K. For transients, inlet temperature equals the temperature in CV181. This is done to simulate an adiabatic boundary at the reactor inlet.
	ICFNUM	320	CF number
	CFTYPE	L-A-IFTE	CF has type logical-if-then-else
CF_SAI	CFSCAL	1.0	—
	CFADCN	0.0	—
	CFVALR	773	Steady-state coolant inlet temperature
CF_ARG	NCFARG	3	Three arguments are required for this CF type
	CHARG	CF-VALU('SourceCheck')	CF returns ARG2 if 'SourceCheck' is TRUE (i.e. if mass flow rate ¿ 0) and ARG3 if 'SourceCheck' is FALSE
	CHARG	EXEC-TIME	Arbitrary variable
	ARSCAL	0.0	—

	ARADCN	773.0	Steady-state inlet temperature
	CHARG	CVH-TVAP(‘CV181-RISER’)	CF returns temperature of CV181 for the inlet temperature
	ARSCAL	1.0	—
	ARADCN	0.0	—
CF_ID	CFNAME	‘SinkTemp’	CF returns the coolant outlet temperature to the CVH package. The sink temperature is equal to the temperature of the outlet plenum nearest the reactor outlet (COR level 3, ring 6).
	ICFNUM	321	CF number
	CFTYPE	EQUALS	CF has type EQUALS
CF_SAI	CFSCAL	1.0	—
	CFADCN	0.0	—
	CFVALR	773.0	Initial temperature of the outlet plenum
CF_ARG	NCFARG	1	One argument is required for this CF type
	CHARG	COR-CellTemp(3,6,SVC)	CF returns the local coolant temperature in COR cell 603 as the sink temperature
	ARSCAL	1.0	—

	ARADCN	0.0	—
CF_ID	CFNAME	‘Src-Sink_RHUM’	CF defines the relative humidity of the inlet and outlet. Relative humidity for both CVs is 0.0.
	ICFNUM	322	CF number
	CFTYPE	EQUALS	CF has EQUALS type
CF_SAI	CFSCAL	0.0	—
	CFADCN	0.0	—
	CFVALR	0.0	Initial value for the CF
CF_ARG	NCFARG	1	One argument is required for an EQUALS CF
	CHARG	EXEC-TIME	Arbitrary variable
	ARSCAL	0.0	—
	ARADCN	0.0	—
CF_ID	CFNAME	‘Src-Sink_HeFrac’	CF defines the mole fraction of helium in the inlet and outlet. ¡ole fraction for both CVs is 1.0.
	ICFNUM	323	CF number
	CFTYPE	EQUALS	CF has EQUALS type
CF_SAI	CFSCAL	0.0	—
	CFADCN	1.0	—
	CFVALR	1.0	Initial value for the CF
CF_ARG	NCFARG	1	One argument is required for an EQUALS CF
	CHARG	EXEC-TIME	Arbitrary variable
	ARSCAL	0.0	—

ARADCN 0.0 —

B.3 decay-heat.inp

B.3.1 DCH Package Input

CARD	*WORD*	*VALUE*	*BASIS*
DCH_RCT	REACTP	PWR	Reactor type. PBR is not an option for this record. Reactor type is insignificant, since the default power is overridden and the RadioNuclide package is not active.
DCH_SHT	ISHTCF	'TRIP-SIGNAL'	Logical valued control function used to determine reactor shutdown time. When this CF changes state from FALSE to TRUE, fission power (controlled by CF 'CORE-POWER') is turned off and decay power is activated. 'TRIP-SIGNAL' becomes true when the inlet mass flow rate equals 0.0.
DCH_OPW	OPRPOW	400.E6	Reactor operating power
DCH_DPW	TFCFNAME	'DECAY-PWR'	TF defining decay power as a function of time. TF values are shown in Table B.25.
DCH_CL	RDCNAM	XE / CS / BA	User input radionuclide class names

FLAGCLS	DEFAULT	Default values are used for all RN classes. Since RN package is inactive, this has no impact on the calculation.

Table B.25: Decay Heat Curve

Time after trip (s)	Fraction of full power
0.00E+00	0.000E+00 [a] [b]
1.00E-06	6.426E-02
2.50E-01	6.298E-02
5.00E-01	6.193E-02
7.50E-01	6.097E-02
1.00E+00	6.008E-02
1.25E+00	5.928E-02
1.50E+00	5.854E-02
1.75E+00	5.785E-02
2.00E+00	5.720E-02
2.50E+00	5.603E-02
3.00E+00	5.500E-02
3.50E+00	5.407E-02
4.00E+00	5.324E-02
4.50E+00	5.249E-02
5.00E+00	5.180E-02
5.50E+00	5.116E-02
6.00E+00	5.057E-02
6.50E+00	5.003E-02

[a] From [71]

[b] Values are multiplied by 400.E6 to give the full core decay power

Table B.25 (continued)

Time after trip (s)	Fraction of full power
7.00E+00	4.952E-02
7.50E+00	4.904E-02
8.00E+00	4.860E-02
8.50E+00	4.817E-02
9.00E+00	4.777E-02
9.50E+00	4.740E-02
1.00E+01	4.704E-02
1.10E+01	4.636E-02
1.20E+01	4.574E-02
1.30E+01	4.518E-02
1.40E+01	4.465E-02
1.50E+01	4.417E-02
1.60E+01	4.371E-02
1.70E+01	4.329E-02
1.80E+01	4.289E-02
1.90E+01	4.251E-02
2.00E+01	4.216E-02
2.25E+01	4.135E-02
2.50E+01	4.062E-02
2.75E+01	3.997E-02
3.00E+01	3.938E-02
3.50E+01	3.833E-02
4.00E+01	3.742E-02
4.50E+01	3.663E-02
5.00E+01	3.592E-02
5.50E+01	3.527E-02

Table B.25 (continued)

Time after trip (s)	Fraction of full power
6.00E+01	3.469E-02
6.50E+01	3.416E-02
7.00E+01	3.367E-02
7.50E+01	3.321E-02
8.00E+01	3.279E-02
8.50E+01	3.240E-02
9.00E+01	3.203E-02
9.50E+01	3.169E-02
1.00E+02	3.137E-02
1.10E+02	3.078E-02
1.20E+02	3.026E-02
1.30E+02	2.979E-02
1.40E+02	2.936E-02
1.50E+02	2.897E-02
1.60E+02	2.860E-02
1.70E+02	2.827E-02
1.80E+02	2.795E-02
1.90E+02	2.766E-02
2.00E+02	2.739E-02
2.25E+02	2.677E-02
2.50E+02	2.624E-02
2.75E+02	2.576E-02
3.00E+02	2.533E-02
3.50E+02	2.458E-02
4.00E+02	2.394E-02
4.50E+02	2.338E-02

Table B.25 (continued)

Time after trip (s)	Fraction of full power
5.00E+02	2.287E-02
5.50E+02	2.241E-02
6.00E+02	2.199E-02
6.50E+02	2.160E-02
7.00E+02	2.123E-02
7.50E+02	2.089E-02
8.00E+02	2.057E-02
8.50E+02	2.027E-02
9.00E+02	1.998E-02
9.50E+02	1.971E-02
1.00E+03	1.945E-02
1.10E+03	1.897E-02
1.20E+03	1.854E-02
1.30E+03	1.814E-02
1.40E+03	1.777E-02
1.50E+03	1.742E-02
1.60E+03	1.710E-02
1.70E+03	1.680E-02
1.80E+03	1.651E-02
1.90E+03	1.624E-02
2.00E+03	1.599E-02
2.25E+03	1.541E-02
2.50E+03	1.491E-02
2.75E+03	1.446E-02
3.00E+03	1.406E-02
3.25E+03	1.370E-02

Table B.25 (continued)

Time after trip (s)	Fraction of full power
3.50E+03	1.337E-02
3.75E+03	1.308E-02
4.00E+03	1.281E-02
4.25E+03	1.256E-02
4.50E+03	1.234E-02
4.75E+03	1.212E-02
5.00E+03	1.193E-02
5.25E+03	1.175E-02
5.50E+03	1.158E-02
5.75E+03	1.142E-02
6.00E+03	1.127E-02
6.50E+03	1.099E-02
7.00E+03	1.075E-02
7.50E+03	1.053E-02
8.00E+03	1.032E-02
8.50E+03	1.014E-02
9.00E+03	9.968E-03
9.50E+03	9.810E-03
1.00E+04	9.664E-03
1.05E+04	9.528E-03
1.10E+04	9.401E-03
1.15E+04	9.282E-03
1.20E+04	9.169E-03
1.25E+04	9.063E-03
1.30E+04	8.962E-03
1.30E+04	8.962E-03

Table B.25 (continued)

Time after trip (s)	Fraction of full power
1.35E+04	8.867E-03
1.40E+04	8.776E-03
1.40E+04	8.776E-03
1.45E+04	8.690E-03
1.50E+04	8.607E-03
1.50E+04	8.607E-03
1.55E+04	8.529E-03
1.60E+04	8.453E-03
1.60E+04	8.453E-03
1.65E+04	8.381E-03
1.70E+04	8.311E-03
1.70E+04	8.311E-03
1.75E+04	8.245E-03
1.80E+04	8.180E-03
1.80E+04	8.180E-03
1.85E+04	8.119E-03
1.90E+04	8.059E-03
1.95E+04	8.001E-03
2.00E+04	7.945E-03
2.25E+04	7.692E-03
2.50E+04	7.471E-03
2.75E+04	7.277E-03
3.00E+04	7.103E-03
3.00E+04	7.103E-03
3.25E+04	6.946E-03
3.50E+04	6.802E-03

Table B.25 (continued)

Time after trip (s)	Fraction of full power
3.75E+04	6.670E-03
4.00E+04	6.548E-03
4.00E+04	6.548E-03
4.25E+04	6.434E-03
4.50E+04	6.329E-03
4.75E+04	6.230E-03
5.00E+04	6.137E-03
5.00E+04	6.137E-03
5.25E+04	6.050E-03
5.50E+04	5.967E-03
5.75E+04	5.889E-03
6.00E+04	5.816E-03
6.25E+04	5.746E-03
6.50E+04	5.679E-03
6.75E+04	5.615E-03
7.00E+04	5.555E-03
7.25E+04	5.497E-03
7.50E+04	5.441E-03
7.75E+04	5.388E-03
8.00E+04	5.337E-03
8.25E+04	5.288E-03
8.50E+04	5.240E-03
8.75E+04	5.195E-03
9.00E+04	5.151E-03
9.25E+04	5.108E-03
9.50E+04	5.067E-03

Table B.25 (continued)

Time after trip (s)	Fraction of full power
1.00E+05	4.989E-03
1.05E+05	4.912E-03
1.10E+05	4.840E-03
1.15E+05	4.772E-03
1.20E+05	4.708E-03
1.25E+05	4.646E-03
1.30E+05	4.588E-03
1.35E+05	4.533E-03
1.40E+05	4.480E-03
1.45E+05	4.429E-03
1.50E+05	4.381E-03
1.55E+05	4.335E-03
1.60E+05	4.290E-03
1.65E+05	4.247E-03
1.70E+05	4.206E-03
1.75E+05	4.166E-03
1.80E+05	4.127E-03
1.85E+05	4.090E-03
1.90E+05	4.054E-03
1.95E+05	4.019E-03
2.00E+05	3.985E-03
2.05E+05	3.953E-03
2.10E+05	3.921E-03
2.15E+05	3.890E-03
2.20E+05	3.860E-03
2.25E+05	3.830E-03

Table B.25 (continued)

Time after trip (s)	Fraction of full power
2.30E+05	3.802E-03
2.35E+05	3.774E-03
2.40E+05	3.747E-03
2.45E+05	3.721E-03
2.50E+05	3.695E-03
2.55E+05	3.670E-03
2.60E+05	3.645E-03
2.65E+05	3.621E-03
2.70E+05	3.597E-03
2.75E+05	3.574E-03
2.80E+05	3.552E-03
2.85E+05	3.530E-03
2.90E+05	3.508E-03
2.95E+05	3.487E-03
3.00E+05	3.466E-03
3.05E+05	3.446E-03
3.10E+05	3.426E-03
3.15E+05	3.406E-03
3.20E+05	3.387E-03
3.25E+05	3.368E-03
3.30E+05	3.349E-03
3.35E+05	3.331E-03
3.40E+05	3.313E-03
3.45E+05	3.295E-03
3.50E+05	3.277E-03
3.55E+05	3.260E-03

Table B.25 (continued)

Time after trip (s)	Fraction of full power
3.60E+05	3.244E-03
3.65E+05	3.227E-03

B.3.2 Decay Heat Control Logic

CARD	*WORD*	*VALUE*	*BASIS*
CF_ID	CFNAME	'TRIP-SIGNAL'	CF signals reactor trip to the DCH package
	ICFNUM	352	CF number
	CFTYPE	L-NOT	CF has logical-not equal type. TRUE is returned when CF 'SourceCheck' is FALSE (i.e. mass flow is greater than 0).
CF_LIV	LCFVAL	FALSE	CF is initially FALSE
CF_CLS	CLASS	LATCH	CF is classified as LATCH, meaning the CF will change state only once, retaining its new value from that point onward
CF_ARG	NCFARG	1	One argument is required for an L-NOT CF
	CHARG	CF-VALU('SourceCheck')	CF variable argument. 'SourceCheck' is a logical CF that returns TRUE when the inlet mass flow rate is 0.

B.4 viewfactors.inp

B.4.1 Input for Structure to Structure Radiation Heat Transfer

CARD	*WORD*	*VALUE*	*BASIS*
HS_RD	NUMPAIR	144	Number of heat structure pairs for radiation heat transfer calculations
	IHSRD1	Table B.26	Name of the first heat structure in the pair.
	LRBND1	RIGHT	Heat is transferred from the right side of IHSRD1.
	IHSRD2	Table B.26	Name of the second heat structure in the pair.
	LRBND2	LEFT	Heat is transferred from the left side of IHSRD1.
	VIEW	Table B.26	View factor from the right side of IHSRD1 to the left side of IHSRD2. View factors are determined using the methodology found in Section 4.2.1.
	ICFRD1	Emis	Name of a control function used to define the emissivity of IHSRD1. 'Emis' has a constant value of 0.8 per the benchmark specifications.
	ICFRD2	Emis	Name of a control function used to define the emissivity of IHSRD2.

Table B.26: View factors for structure to structure radiation heat transfer (PBMR)

IHSRD1	IHSRD2	VIEW
COR-RAD-BND-A1	CORE-BARREL-1	9.136E-01
COR-RAD-BND-A1	CORE-BARREL-2	0.000E+00
COR-RAD-BND-A1	CORE-BARREL-3	0.000E+00
COR-RAD-BND-A1	CORE-BARREL-4	0.000E+00
COR-RAD-BND-A2	CORE-BARREL-1	9.722E-01
COR-RAD-BND-A2	CORE-BARREL-2	0.000E+00
COR-RAD-BND-A2	CORE-BARREL-3	0.000E+00
COR-RAD-BND-A2	CORE-BARREL-4	0.000E+00
COR-RAD-BND-A3	CORE-BARREL-1	9.994E-01
COR-RAD-BND-A3	CORE-BARREL-2	9.636E-05
COR-RAD-BND-A3	CORE-BARREL-3	0.000E+00
COR-RAD-BND-A3	CORE-BARREL-4	0.000E+00
COR-RAD-BND-A4	CORE-BARREL-1	9.992E-01
COR-RAD-BND-A4	CORE-BARREL-2	6.942E-04
COR-RAD-BND-A4	CORE-BARREL-3	0.000E+00
COR-RAD-BND-A4	CORE-BARREL-4	0.000E+00
COR-RAD-BND-A5	CORE-BARREL-1	9.452E-01
COR-RAD-BND-A5	CORE-BARREL-2	5.472E-02
COR-RAD-BND-A5	CORE-BARREL-3	0.000E+00
COR-RAD-BND-A5	CORE-BARREL-4	0.000E+00
COR-RAD-BND-A6	CORE-BARREL-1	1.048E-01
COR-RAD-BND-A6	CORE-BARREL-2	8.952E-01
COR-RAD-BND-A6	CORE-BARREL-3	2.568E-05
COR-RAD-BND-A6	CORE-BARREL-4	2.376E-06

Table B.26 (continued)

IHSRD1	IHSRD2	VIEW
COR-RAD-BND-A7	CORE-BARREL-1	4.716E-03
COR-RAD-BND-A7	CORE-BARREL-2	9.952E-01
COR-RAD-BND-A7	CORE-BARREL-3	3.820E-05
COR-RAD-BND-A7	CORE-BARREL-4	2.902E-06
COR-RAD-BND-A8	CORE-BARREL-1	1.077E-03
COR-RAD-BND-A8	CORE-BARREL-2	9.988E-01
COR-RAD-BND-A8	CORE-BARREL-3	5.986E-05
COR-RAD-BND-A8	CORE-BARREL-4	3.585E-06
COR-RAD-BND-A9	CORE-BARREL-1	3.971E-04
COR-RAD-BND-A9	CORE-BARREL-2	9.995E-01
COR-RAD-BND-A9	CORE-BARREL-3	1.005E-04
COR-RAD-BND-A9	CORE-BARREL-4	4.485E-06
COR-RAD-BND-A10	CORE-BARREL-1	1.859E-04
COR-RAD-BND-A10	CORE-BARREL-2	9.996E-01
COR-RAD-BND-A10	CORE-BARREL-3	1.859E-04
COR-RAD-BND-A10	CORE-BARREL-4	5.693E-06
COR-RAD-BND-A11	CORE-BARREL-1	1.005E-04
COR-RAD-BND-A11	CORE-BARREL-2	9.995E-01
COR-RAD-BND-A11	CORE-BARREL-3	3.971E-04
COR-RAD-BND-A11	CORE-BARREL-4	7.347E-06
COR-RAD-BND-A12	CORE-BARREL-1	5.986E-05
COR-RAD-BND-A12	CORE-BARREL-2	9.988E-01
COR-RAD-BND-A12	CORE-BARREL-3	1.077E-03
COR-RAD-BND-A12	CORE-BARREL-4	9.665E-06
COR-RAD-BND-A13	CORE-BARREL-1	3.820E-05
COR-RAD-BND-A13	CORE-BARREL-2	9.952E-01

Table B.26 (continued)

IHSRD1	IHSRD2	VIEW
COR-RAD-BND-A13	CORE-BARREL-3	4.716E-03
COR-RAD-BND-A13	CORE-BARREL-4	1.301E-05
COR-RAD-BND-A14	CORE-BARREL-1	2.568E-05
COR-RAD-BND-A14	CORE-BARREL-2	8.952E-01
COR-RAD-BND-A14	CORE-BARREL-3	1.048E-01
COR-RAD-BND-A14	CORE-BARREL-4	1.798E-05
COR-RAD-BND-A15	CORE-BARREL-1	1.798E-05
COR-RAD-BND-A15	CORE-BARREL-2	1.048E-01
COR-RAD-BND-A15	CORE-BARREL-3	8.952E-01
COR-RAD-BND-A15	CORE-BARREL-4	2.568E-05
COR-RAD-BND-A16	CORE-BARREL-1	1.301E-05
COR-RAD-BND-A16	CORE-BARREL-2	4.716E-03
COR-RAD-BND-A16	CORE-BARREL-3	9.952E-01
COR-RAD-BND-A16	CORE-BARREL-4	3.820E-05
COR-RAD-BND-A17	CORE-BARREL-1	9.665E-06
COR-RAD-BND-A17	CORE-BARREL-2	1.077E-03
COR-RAD-BND-A17	CORE-BARREL-3	9.988E-01
COR-RAD-BND-A17	CORE-BARREL-4	5.986E-05
COR-RAD-BND-A18	CORE-BARREL-1	7.347E-06
COR-RAD-BND-A18	CORE-BARREL-2	3.971E-04
COR-RAD-BND-A18	CORE-BARREL-3	9.995E-01
COR-RAD-BND-A18	CORE-BARREL-4	1.005E-04
COR-RAD-BND-A19	CORE-BARREL-1	5.693E-06
COR-RAD-BND-A19	CORE-BARREL-2	1.859E-04
COR-RAD-BND-A19	CORE-BARREL-3	9.996E-01
COR-RAD-BND-A19	CORE-BARREL-4	1.859E-04

Table B.26 (continued)

IHSRD1	IHSRD2	VIEW
COR-RAD-BND-A20	CORE-BARREL-1	4.485E-06
COR-RAD-BND-A20	CORE-BARREL-2	1.005E-04
COR-RAD-BND-A20	CORE-BARREL-3	9.995E-01
COR-RAD-BND-A20	CORE-BARREL-4	3.971E-04
COR-RAD-BND-A21	CORE-BARREL-1	3.585E-06
COR-RAD-BND-A21	CORE-BARREL-2	5.986E-05
COR-RAD-BND-A21	CORE-BARREL-3	9.988E-01
COR-RAD-BND-A21	CORE-BARREL-4	1.077E-03
COR-RAD-BND-A22	CORE-BARREL-1	2.902E-06
COR-RAD-BND-A22	CORE-BARREL-2	3.820E-05
COR-RAD-BND-A22	CORE-BARREL-3	9.952E-01
COR-RAD-BND-A22	CORE-BARREL-4	4.716E-03
COR-RAD-BND-A23	CORE-BARREL-1	2.376E-06
COR-RAD-BND-A23	CORE-BARREL-2	2.568E-05
COR-RAD-BND-A23	CORE-BARREL-3	8.952E-01
COR-RAD-BND-A23	CORE-BARREL-4	1.048E-01
COR-RAD-BND-A24	CORE-BARREL-1	1.965E-06
COR-RAD-BND-A24	CORE-BARREL-2	1.798E-05
COR-RAD-BND-A24	CORE-BARREL-3	1.048E-01
COR-RAD-BND-A24	CORE-BARREL-4	8.952E-01
COR-RAD-BND-A25	CORE-BARREL-1	1.639E-06
COR-RAD-BND-A25	CORE-BARREL-2	1.301E-05
COR-RAD-BND-A25	CORE-BARREL-3	4.716E-03
COR-RAD-BND-A25	CORE-BARREL-4	9.952E-01
COR-RAD-BND-A26	CORE-BARREL-1	1.380E-06
COR-RAD-BND-A26	CORE-BARREL-2	2.797E-05

Table B.26 (continued)

IHSRD1	IHSRD2	VIEW
COR-RAD-BND-A26	CORE-BARREL-3	2.818E-03
COR-RAD-BND-A26	CORE-BARREL-4	9.988E-01
COR-RAD-BND-A27	CORE-BARREL-1	1.169E-06
COR-RAD-BND-A27	CORE-BARREL-2	7.347E-06
COR-RAD-BND-A27	CORE-BARREL-3	3.971E-04
COR-RAD-BND-A27	CORE-BARREL-4	9.995E-01
COR-RAD-BND-A28	CORE-BARREL-1	9.982E-07
COR-RAD-BND-A28	CORE-BARREL-2	5.693E-06
COR-RAD-BND-A28	CORE-BARREL-3	1.859E-04
COR-RAD-BND-A28	CORE-BARREL-4	9.996E-01
CORE-BARREL-1	RPV-1	9.658E-01
CORE-BARREL-1	RPV-2	1.706E-02
CORE-BARREL-1	RPV-3	1.784E-05
CORE-BARREL-1	RPV-4	2.656E-06
CORE-BARREL-2	RPV-1	1.706E-02
CORE-BARREL-2	RPV-2	9.658E-01
CORE-BARREL-2	RPV-3	1.706E-02
CORE-BARREL-2	RPV-4	1.784E-05
CORE-BARREL-3	RPV-1	1.784E-05
CORE-BARREL-3	RPV-2	1.706E-02
CORE-BARREL-3	RPV-3	9.658E-01
CORE-BARREL-3	RPV-4	1.706E-02
CORE-BARREL-4	RPV-1	2.656E-06
CORE-BARREL-4	RPV-2	1.784E-05
CORE-BARREL-4	RPV-3	1.706E-02
CORE-BARREL-4	RPV-4	9.658E-01

Table B.26 (continued)

IHSRD1	IHSRD2	VIEW
RPV-1	RCCS-1	7.812E-01
RPV-1	RCCS-2	1.056E-01
RPV-1	RCCS-3	2.996E-03
RPV-1	RCCS-4	4.888E-04
RPV-2	RCCS-1	1.056E-01
RPV-2	RCCS-2	7.812E-01
RPV-2	RCCS-3	1.056E-01
RPV-2	RCCS-4	2.996E-03
RPV-3	RCCS-1	2.996E-03
RPV-3	RCCS-2	1.056E-01
RPV-3	RCCS-3	7.812E-01
RPV-3	RCCS-4	1.056E-01
RPV-4	RCCS-1	4.888E-04
RPV-4	RCCS-2	2.996E-03
RPV-4	RCCS-3	1.056E-01
RPV-4	RCCS-4	7.812E-01

B.5 pbmr400-plofc.inp

B.5.1 PBMR PLOFC COR Input

CARD	*WORD*	*VALUE*	*BASIS*
COR_SC	NNNN	Table B.27	Four-digit identifier for a COR sensitivity coefficient array
	VALUE	Table B.27	New value for the sensitivity coefficient

NA	Table B.27	Sensitivity coefficient array index. COR sensitivity coefficients are used to restore the default coefficient values for the packed bed convective heat transfer correlation.

Table B.27: COR sensitivity coefficient modifications for PBMR transients

NNNN	NA	VALUE	Explanation
1231	1	2.0	Coefficient A in the equation Nu $= A + B\mathrm{Re}^{C}\mathrm{Pr}^{D}$, which determines the heat transfer coefficient for turbulent flow through a packed bed
1231	2	0.6	Coefficient B in the above equation
1231	3	0.5	Coefficient C in the above equation
1231	4	0.333	Coefficient D in the above equation
1246	1	0.0	Heat transfer coefficient from the vessel head to the reactor cavity. Setting this coefficient equal to 0 simulates an adiabatic boundary condition for the lower head.

B.5.2 PBMR PLOFC CF Input

CARD	*WORD*	*VALUE*	*BASIS*
CF_ID	CFNAME	'TransientTime'	CF defines the time at the start of a transient
	ICFNUM	001	CF number
	CFTYPE	EQUALS	CF has EQUALS type

CF_SAI	CFSCAL	0.0	—
	CFADCN	10000.0	The transient starts at 10,000 s. To get the initial conditions for the PLOFC and DLOFC transients, steady-state calculations were performed until the reactor reached thermal equilibrium. Since this took a very long time (on the order of one million seconds of problem time), heat structure and reflector steady-state temperatures were input as the initial values in the steady-state input deck. Steady-state calculations were then performed for 10,000 s, and the results of these calculations were used to initialize the transients.
	CFVALR	10000.0	Initial value for the CF
CF_ID	CFNAME	'TransientDT'	CF determines the time since the start of the transient
	ICFNUM	002	CF number
	CFTYPE	EQUALS	CF has EQUALS type
CF_SAI	CFSCAL	1.0	By changing this value for 0.0 to 1.0, the control logic needed to simulate changes in mass flow rate and inlet and outlet pressure and to trip the reactor is activated.
	CFADCN	0.0	—
	CFVALR	0.0	Initial value for the CF

CF_ID	CFNAME	‘dMdot-dt’	CF defines the time rate of change of the mass flow rate
	ICFNUM	003	CF number
	CFTYPE	EQUALS	CF has EQUALS type
CF_SAI	CFSCAL	0.0	—
	CFADCN	-14.82	This change in mass flow rate corresponds to a decrease in inlet flow from 192 kg/s to 0.0 over 13 s
	CFVALR	0.0	Initial value for the CF
CF_ID	CFNAME	‘dPin-dt’	CF defines the time rate of change of the source pressure
	ICFNUM	005	CF number
	CFTYPE	EQUALS	CF has EQUALS type
CF_SAI	CFSCAL	0.0	—
	CFADCN	-0.2536+06	This value corresponds to a decrease in inlet pressure from its steady-state value to Pmin over 13 s
	CFVALR	0.0	Initial value for the CF
CF_ID	CFNAME	‘dPout-dt’	CF defines the time rate of change of the sink pressure
	ICFNUM	007	CF number
	CFTYPE	EQUALS	CF has EQUALS type
CF_SAI	CFSCAL	0.0	—
	CFADCN	-0.2308+06	This value corresponds to a decrease in outlet pressure from its steady-state value to Pmin over 13 s
	CFVALR	0.0	Initial value for the CF

CF_ID	CFNAME	'Pmin'	CF defines the minimum allowable inlet or outlet pressure. This CF is used to set the long-term (constant) inlet and outlet pressure.
	ICFNUM	009	CF number
	CFTYPE	EQUALS	CF has type EQUALS
CF_SAI	CFSCAL	0.0	—
	CFADCN	6.0E+06	This is the inlet and outlet pressure for PLOFC calculations
	CFVALR	0.0	—

B.6 pbmr400-dlofc.inp

B.6.1 PBMR DLOFC COR Input

CARD	*WORD*	*VALUE*	*BASIS*
COR_SC	NNNN	Table B.27	Four-digit identifier for a COR sensitivity coefficient array
	VALUE	Table B.27	New value for the sensitivity coefficient
	NA	Table B.27	Sensitivity coefficient array index; COR sensitivity coefficients are used to restore the default coefficient values for the packed bed convective heat transfer correlation

B.6.2 PBMR DLOFC CF Input

CARD	*WORD*	*VALUE*	*BASIS*

CF_ID	CFNAME	'TransientTime'	CF defines the time at the start of a transient
	ICFNUM	001	CF number
	CFTYPE	EQUALS	CF has EQUALS type
CF_SAI	CFSCAL	0.0	—
	CFADCN	10000.0	The transient starts at 10,000 s. See explanation in the PLOFC input description.
	CFVALR	10000.0	Initial value for the CF
CF_ID	CFNAME	'TransientDT'	CF determines the time since the start of the transient
	ICFNUM	002	CF number
	CFTYPE	EQUALS	CF has EQUALS type
CF_SAI	CFSCAL	1.0	By changing this value for 0.0 to 1.0, the control logic needed to simulate changes in mass flow rate and inlet and outlet pressure and to trip the reactor is activated.
	CFADCN	0.0	—
	CFVALR	0.0	Initial value for the CF
CF_ID	CFNAME	'dMdot-dt'	CF defines the time rate of change of the mass flow rate
	ICFNUM	003	CF number
	CFTYPE	EQUALS	CF has EQUALS type
CF_SAI	CFSCAL	0.0	—
	CFADCN	-14.82	This change in mass flow rate corresponds to a decrease in inlet flow from 192 kg/s to 0.0 over 13 s

	CFVALR	0.0	Initial value for the CF
CF_ID	CFNAME	‘dPin-dt’	CF defines the time rate of change of the source pressure
	ICFNUM	005	CF number
	CFTYPE	EQUALS	CF has EQUALS type
CF_SAI	CFSCAL	0.0	—
	CFADCN	-0.7162E+06	This value corresponds to a decrease in inlet pressure from its steady-state value to Pmin over 13 s
	CFVALR	0.0	Initial value for the CF
CF_ID	CFNAME	‘dPout-dt’	CF defines the time rate of change of the sink pressure
	ICFNUM	007	CF number
	CFTYPE	EQUALS	CF has EQUALS type
CF_SAI	CFSCAL	0.0	—
	CFADCN	-0.6923+06	This value corresponds to a decrease in outlet pressure from its steady-state value to Pmin over 13 s
	CFVALR	0.0	Initial value for the CF
CF_ID	CFNAME	‘Pmin’	CF defines the minimum allowable inlet or outlet pressure. This CF is used to set the long-term (constant) inlet and outlet pressure.
	ICFNUM	009	CF number
	CFTYPE	EQUALS	CF has type EQUALS
CF_SAI	CFSCAL	0.0	—
	CFADCN	0.1E+06	This is the inlet and outlet pressure for DLOFC calculations

CFVALR	0.0	—

APPENDIX C
HTTF CALCULATION NOTEBOOK

This is the calculation notebook for the HTTF MELCOR input deck. Design data used in this modeling effort can be found in references [59–61, 82]. MELCOR input requirements are described in reference [5]. The steady-state input deck includes the following files:

exec.inp EXEC package input

core.inp COR input

cvh-vessel.inp CVH input for control volumes within the HTTF pressure vessel, including those in the core, upper and lower plena, and barrel-vessel gap

fl-vessel.inp FL input for flow paths connecting the CVs within the HTTF vessel

hs-vessel.inp HS input for the side reflector, core barrel, and RPV

src-sink.inp CVH and FL input for the source and sink CVs and flow paths connecting the source and sink to the vessel CVs

cavity.inp CVH input for control volumes between the vessel and RCCS and HS input for the RCCS

vfhttf.inp Structure-to-structure radiation view factors

ncg.inp NCG input

mp.inp Material properties input

control-logic.inp CF input for HTTF control logic

The file **dlofc.inp** contains input to simulate a complete break of the outlet pipe.

C.1 exec.inp

C.1.1 Environmental Data for HTTF Steady-State Calculations

CARD	*WORD*	*VALUE*	*BASIS*

MEG_DIAGFILE	—	'httfg.dia'	Filename for MELGEN diagnostic output
MEL_DIAGFILE	—	'httf.dia'	Filename for MELCOR diagnostic output
MEG_OUTPUTFILE	—	'httfg.out'	Filename for MELGEN listing output
MEL_OUTPUTFILE	—	'httf.out'	Filename for MELCOR listing output
PLOTFILE	—	'httf.ptf'	Filename for binary plot data
MEG_RESTARTFILE	—	'httf.rst'	Filename for binary file used to restart MELCOR calculation
MEL_RESTARTFILE	—	'httf.rst'	Filename for binary file used to restart MELCOR calculation
	CYCLE	CYCLE	Calculation restarted at cycle specified on NREST
	NREST	-1	Calculation restarted at last available restart listing
MESSAGEFILE	—	'httf.mes'	Filename for event message output
STATUSFILE	—	'MELSTT_v2-0'	Filename for MELCOR status file
STOPFILE	—	'MELSTP_v2-0'	Filename for MELCOR stop file
WRITENEWINP	—	'httf.txt'	Filename for echoed input

C.1.2 HTTF MELGEN EXEC Input

CARD	*WORD*	*VALUE*	*BASIS*
EXEC_INPUT	—	—	EXEC package start record
EXEC_TITLE	—	'HTTF'	Title of calculation
EXEC_JOBID	—	'httf -'	Job identifier

C.1.3 HTTF MELCOR EXEC Input

CARD	*WORD*	*VALUE*	*BASIS*
EXEC_TITLE	—	'HTTF'	Title of calculation
EXEC_JOBID	—	'httf -'	Job identifier
EXEC_TEND	TEND	1.8E+04	End of calculation time
EXEC_TIME	NTMINV	2	Dimension of timestep table. For the first 1000 s, the plot, edit, and restart intervals are shorter because the thermodynamic state of the HTTF is changing at a much more rapid rate than later in the calculation.
	N	1	The first set of timestep input
	TIME	0.0	The time this data set goes into effect
	DTMAX	0.5	Arbitrary. The actual timestep will be less due to the Courant limit.

DTMIN	1.0E-05	Arbitrary, but should be no more than 1.0E-02, since the maximum timestep due to the Courant limit is $\sim$ 4.0E-02.
DTEDIT	500.	MELCOR prints an edit to OUTPUTFILE every 500 seconds
DTPLOT	1.0	Plot frequency
DTREST	1000.	Restart frequency
DCREST	1.0E+10	Default value. This ensures that restart generation is not a function of CPU time.
N	2	The second set of timestep input
TIME	1000.0	The time this data set goes into effect
DTMAX	2.0	Arbitrary. The actual timestep will be less due to the Courant limit.
DTMIN	1.0E-05	Arbitrary, but should be no more than 1.0E-02, since the maximum timestep due to the Courant limit is $\sim$ 4.0E-02
DTEDIT	2000.	Edit frequency
DTPLOT	10.0	Plot frequency
DTREST	5000.	Restart frequency

	DCREST	1.0E+10	Default value. This ensures that restart generation is not a function of CPU time.
EXEC_CPULEFT	CPULEFT	0.30E+02	Minimum number of CPU seconds left at the end of the calculation
EXEC_CPULIM	CPULIM	0.1E+06	Maximum number of CPU seconds allowed for this execution
EXEC_CYMESF	NCYEDD	100	Number of cycles between messages written to the terminal
	NCYEDP	10000	Number of cycles between messages written to OUTPUTFILE

C.2 core.inp

CARD	*WORD*	*VALUE*	*BASIS*
COR_RT	IRTYP	PMR	Reactor type PMR (prismatic reactor) selected
	MCRP	B4C	Control rod poison. Not used in the calculation.
COR_GP	RFUEL	6.35E-03	Radius of the fuel. From [82].
	RCLAD	2.02E-02	Radius of the clad. For PMRs, the graphite associated with a fuel hole and coolant channel is the 'clad'. Calculated by transforming the hexagonal unit cell to a cylindrical cell. Dimensions obtained from [82].

	DRGAP	0.0	Gap between the fuel and clad. There is no gap in prismatic fuel
	PITCH	4.40E-02	Rod-to-rod pitch. Equal to the distance from the center of a fuel hole to the center of a coolant hole (0.0254 cm, [82]) times $\sqrt{3}$ (i.e. $2\cos 30^{o}$).
COR_VP	RCOR	0.445	Outer radius for the COR package in the active region (i.e. the outer radius of the outermost radial ring). Equal to the outer core radius [82].
	RVESS	0.819	Radius of the inside of the vessel cylinder. From [82].
	ILHTRN	RVESS	Reactor lower head transition type. Has no significance for this calculation.
	DZRV	0.33	Thickness of the cylindrical portion of the vessel. This value is 1/4 of the vessel thickness for the MHTGR [84].
	DZLH	0.33	Thickness of the lower head inside the transition radius specified by ILHTRN. See above.
	ILHTYP	HEMISPHERE	HTTF has a hemispherical lower head

COR_AVP	HLST	-0.552	Elevation of the bottom plate. The bottom plate is assumed to be a 4-in.-thick steel plate immediately below the bottom reflector, similar to that shown in available drawings of the facility.
	HCSP	-0.552	Elevation of the core support plate. See above.
COR_TP	NTPCOR	NO	Lower head is not expected to fail, so this model is not used
	RNTPCOR	NO	RadioNuclide (RN) package is not active for this calculation
	ICFGAP	NO	Fuel-cladding gap conductance control function not used
	ICFFIS	FISPOWALL	Control function is used to specify the whole-core fission power
	CFNAME	'CORE-POWER'	Name of the CF used to specify whole-core fission power. 'CORE-POWER' returns a constant value of 600E+03 (600 kW) during steady-state calculations. The value can be changed upon a calculation restart to simulate decay power.

COR_SS	IA	Table C.7	Axial level number or range of numbers where a supporting structure is present
	IR	Table C.7	Radial ring number or range of numbers where SS is present
	ISSMOD	PLATEG	Structural model option for SS. Note that all SS used in this calculation are not expected to fail, so parameters chosen for SS are selected to prevent failure.
	ISSFAI	TSFAIL	SS will not fail unless temperature exceeds TSSFAI
	TSSFAI	5000	Failure temperature used for SS. This value ensures that SS will not fail during calculations.
	SSMETAL	Table C.7	Name of structural metal. Must be STEEL or ZIRC. Note that ZIRC has been redefined as GRAPHITE (i.e. the ceramic material used for the HTTF core).
COR_MS	IEUMOD	0	Default used for this model switch
	IHSDT	0	Default used
	IDTDZ	0	Default used

	ICORCV	1	Consistency between fluid volumes in CVH and in COR not required. Normally, MELCOR reports a fatal error if the combined volume occupied by COR components and by CVH for any COR cell is less than the total volume calculated based on the cell dimensions. This requirement was disabled to prevent MELCOR from reporting errors when CVH volume is slighly ($< 0.1\%$) less than CVH volume required for volume consistency.
COR_BCP	ICBCD	CL	Component that conducts to boundary heat structures
	MATBCD	HE	Helium specified as gap material for conduction to boundary heat structures
	DXBCD	0.0001	Arbitrary value used for the gap thickness, since HTTF geometry has not be fully specified by the designers

	CDFBCD	0.06	Boundary conduction thermal diffusion constant. $= \sqrt{\pi/(\rho c_p k)_{HE}}$ [6], with properties evaluated at HTTF average temperature (750 °C) and pressure (800 kPa).
COR_ZP	NAXL	22	Number of axial levels
	Z	Table C.1	Elevation of lower boundary of axial level
	DZ	Table C.1	Axial level height
	PORDP	0.0	Porosity of particulate debris. No PD expected in the HTTF.
	IHSA	Table C.1	Boundary heat structure name
	FZPOW	Table C.1	Relative power density in the axial level
COR_RP	NRAD	5	Number of radial rings. Note that there are only 4 rings in the active core.
	RINGR	Table C.2	Outer radius of ring
	ASCELA	Table C.2	Cross-sectional area of ring
	IHSR	'CB-23'	Upper boundary heat structure name. HS represents the cylindrical core barrel end cap, shown in available design drawings.

	ICFCHN	'FLDIRr'	CF name used to specify the flow direction in the channel of ring 'r', used in estimating local fluid temperatures with the dT/dz model. Each control function is equal to the negative of the velocity in flow path 1r6.
	ICFBYP	NO	No CF is used to specify the bypass flow direction because bypass flow is not considered
	FRPOW	Table C.2	Relative power density in the radial ring
COR_RBV	IA	Table C.3	Axial level number or range of numbers
	IR	Table C.3	Radial ring number or range of numbers
	IREF	0 or NULL	No reference cells are selected. CVs for each COR cell are specified individually. NULL indicates that the cell occupies volume inaccessible to the COR package (such as outside of the lower head or between RCOR and RVESS above the elevation of the bottom plate).
	JREF	0	See above

	ICVHC	Table C.3	Channel control volume adjacent to COR cell. CVs are not specified for NULL cells.
	ICVHB	Table C.3	Bypass control volume adjacent to COR cell. No bypass flow is modeled, but the name of a CV is required for this record. The channel CV for a COR cell is also used as the bypass CV. Flow through the 'bypass' is prevented by specifying zero flow areas and hydraulic diameters for the bypass.
COR_KFU	IA	Table C.4	Axial level number
	IR	Table C.4	Radial ring number
	XMFUUO	Table C.4	Mass of UO_2 in the cell fuel component. Calculated by multiplying the total volume of fuel per cell (equal to cell height times 1/3 of the total cross sectional area of fuel, since the active core rings are assumed to have equal flow areas and an equal number of fuel holes) by the density of UO_2 .

	XMFUHT	0.0	Mass of electric heating element. The electrical heaters used in the HTTF are modeled as FU due to limitations with the electrical heater capabilities in the code.
	XMFUXM	0.0	Mass of extra fuel material in the fuel component. Currently, heaters are modeled as UO_2 . The properties of UO_2 can be modified once a heater material has been selected.
	XMFUXO	0.0	Mass of oxide of additional fuel material
COR_KCL	IA	Table C.5	Axial level number
	IR	Table C.5	Radial ring number
	XMCLZR	Table C.5	Mass of graphite in the clad. Calculated by subtracting the volume of fuel and the volume of coolant per cell from the total cell volume, and multiplying by the clad density.
	XMCLZX	0.0	Mass of oxide in cell
	XMCLIN	0.0	Mass of Inconel associated with clad component
COR_KRF	IA	Table C.6	Axial level number
	IR	Table C.6	Radial ring number

	XMRFGR	Table C.6	Mass of GRAPHITE in the reflector
COR_KSS	IA	Table C.7	Axial level number
	IR	Table C.7	Radial ring number
	XMSSSS	Table C.7	Mass of steel supporting structure in the cell. Equal to 0.0, except for cells in the bottom plate. For cell 109, equal to the volume of the cell times the density of steel. For cells 209, 309, and 409, equal to the difference between the volume of the cell and the volume of coolant in the cell (the lower plate is assumed to have the same number of coolant channels as the core, which is consistent with available HTTF drawings), times the density of steel.
	XMSSSX	0.0	Mass of steel oxide supporting structure

	XMSSZR	Table C.7	Mass of zirc (redefined as GRAPHITE) supporting structure in the cell. Equal to 0.0, except for cells in level 6 (insulation), for which XMSSZR is equal to the volume of the cell times the density of graphite. Also, a small fraction of the mass of the reflector in rings 2-4 of levels 11 and 22 is input as SS instead of RF, since RF cannot support FU or CL and is not self-supporting.
	XMSSZX	0.0	Mass of zirc oxide supporting structure
COR_KPD	IA	ALL	Axial level range of numbers
	IR	ALL	Radial ring range of numbers
	XMPDjj	0.0	Mass of material jj in particulate debris in the cell. No particulate debris is present at the start of the calculation, so the mass of each material in PD is zero.
COR_CIT	IA	ALL	Axial level range of numbers
	IR	ALL	Radial ring range of numbers

	Tjj	763.0	Initial temperature (K) of component jj. Initial temperature equals the reactor inlet temperature.
COR_EDR	IA	ALL	Axial level range of numbers
	IR	ALL	Radial ring range of numbers
	DHYCL	0.0404	Cladding equivalent outside diameter. Clad diameter determined by transforming hexagonal unit cell to cylindrical geometry.
	DHYPD	0.0159	Particulate debris diameter. No PD is expected in the calculation, so this parameter is irrelevant.
	DHYCNC	—	Ignored for PMR calculations
	DHYCNB	—	Ignored for PMR calculations
	DHYSS	0.0159	Supporting structure hydraulic diameterj. Equal to the diameter of a coolant channel [82].
	DHYNS	—	Nonsupporting structure hydraulic diameter. No NS used in this calculation.
	DHYPB	0.0159	Diameter of PD in bypass. No bypass modeled, and no PD expected, so this parameter is insignificant.
COR_RFD	IA	Table C.8	Axial level number

	IR	Table C.8	Radial ring number
	DHYRFC	Table C.8	Channel hydraulic diameter for RF
	DHYRFB	0.0001	Bypass hydraulic diameter for RF. Insignificant because bypass flow area is set to zero on another COR record.
COR_RFG	IA	Table C.8	Axial level number
	IR	Table C.8	Radial ring number
	RADI	Table C.8	Reflector channel side radius. Channel side is taken to be the side closest to the fuel. For example, the channel side for the central reflector is the reflector outer radius, while the channel side for the side reflector is the reflector inner radius.
	THKRF	Table C.8	Reflector thickness. A negative value indicates that the channel side is the outside for a cylindrical reflector or the top for a bottom reflector.
	IGEOMRF	1	Reflector geometry flag. 1 = cylindrical.
COR_BFA	IA	Table C.9	Axial level number
	IR	Table C.9	Radial ring number

	ASCLER	Table C.9	Area of outer radial cell boundary. Equal to $2\pi R\,DZ$, where R is the outer radius of ring IR and DZ is the axial level height of level IA.
	AFLOWC	Table C.9	Channel flow area. For cells in the HTTF core, equal to the total coolant flow area times 1/3 (because rings 2-4 are assumed to have the same number of coolant channels, and because there is no flow through ring 1).
	AFLOWB	0.0	Bypass flow area is equal to 0 because bypass flow is not modeled
COR_SA	IA	Table C.10	Axial level number
	IR	Table C.10	Radial ring number
	ASFU	Table C.10	Fuel surface area. Equal to the surface area of compacts in one fuel hole ($2\pi r_f DZ$, where $r_f = 0.00635$ is the fuel hole radius and DZ is the cell height) times the number of fuel holes per cell (76).

	ASCL	Table C.10	Clad surface area. Equal to the surface area of one coolant channel ($2\pi r_c DZ$, where r_c = 0.00794 is the coolant channel radius and DZ is the cell height) times the number of coolant channels per cell (142).
	ASCN	0.0	Surface area of the canister component, which is not used for PBR calculations
	ASSS	Table C.10	Supporting structure surface area. For the bottom plate, the surface area is $\pi(r_o^2 - r_i^2) - 76\pi r_c^2 + 76\pi r_c DZ$ (the surface area of the bottom of the plate, minus the area occupied by coolant channels, plus the surface area of the inside of the coolant channels), where r_o and r_i are the outer and inner radii of ring IR, r_c is the radius of one coolant channel, and DZ is the height of the cell. For the SS representing the insulation, the surface area is $\pi(r_o^2 - r_i^2)$.
	ASNS	0.0	Nonsupporting structures are not used in the calculation
COR_RFA	IA	Table C.11	Axial level number

	IR	Table C.11	Radial ring number
	ASRF	Table C.11	Channel side surface area. Equal to the surface area of one coolant channel times the number of coolant channels in the reflector.
	ASRFB	0.0	Bypass surface areas are set equal to 0 because bypass flow is not considered
COR_LP	IAXSUP	9	Axial level of the core support plate
	HDBH20	100	Heat transfer coefficient from in-vessel falling debris to pool. Default value. Not used because no fuel failure is expected,
	PPFAIL	2.0E7	Differential pressure between lower plenum and reactor cavity that will fail the lower head. Default value.
	VFALL	1.0	Velocity of falling debris. No fuel damage is expected.
C0R_LH	NLH	3	Number of temperature nodes in the lower head
	NINSLH	0	Number of insulation mesh layers in the lower head
COR_LHD	NLHT	11	Number of lower head segments

NLHTA	8	Number of segments in hemispherical portion of the lower head
TLH	763	Initial temperature of lower head segment. Equal to the vessel coolant inlet temperature.
RADLH	Table C.2	Outer radius of lower head segment. Lower head segment radii are chosen to fulfill COR package input requirements.
ICVCAV	'CV301-CAVITY'	Reactor cavity control volume name

Table C.1
HTTF axial level input

Level	Z (m)	DZ (m)	IHSA	FZPOW
1	-2.132	0.022	NO	0.0
2	-2.110	0.035	NO	0.0
3	-2.075	0.036	NO	0.0
4	-2.039	0.038	NO	0.0
5	-2.001	0.688	NO	0.0
6	-1.313	0.304	NO	0.0
7	-1.009	0.228	NO	0.0
8	-0.781	0.229	NO	0.0
9	-0.552	0.156	'SR_CB-09'	0.0
10	-0.396	0.198	'SR_CB-10'	0.0
11	-0.198	0.198	'SR_CB-11'	0.0
12	0.000	0.198	'SR_CB-12'	0.1
13	0.198	0.198	'SR_CB-13'	0.1
14	0.396	0.198	'SR_CB-14'	0.1
15	0.594	0.198	'SR_CB-15'	0.1
16	0.792	0.198	'SR_CB-16'	0.1
17	0.990	0.198	'SR_CB-17'	0.1
18	1.188	0.198	'SR_CB-18'	0.1
19	1.386	0.198	'SR_CB-19'	0.1
20	1.584	0.199	'SR_CB-20'	0.1
21	1.783	0.198	'SR_CB-21'	0.1
22	1.981	0.249	'SR_CB-22'	0.0

Table C.2
HTTF radial ring input

Level	RINGR (m)	IHSR	ICFCHN	FRPOW
1	0.186	0.108	NO	0.00
2	0.298	0.171	'FLDIR2'	0.33
3	0.378	0.171	'FLDIR3'	0.33
4	0.445	0.171	'FLDIR4'	0.33
5	0.819	1.487	NO	0.00

Table C.3: HTTF CVH volumes coupled to each COR cell

IA	IR	ICVHC
1	1-2	'CV001-LP'
2	1-3	'CV001-LP'
3	1-4	'CV001-LP'
4	1-4	'CV001-LP'
5	1-5	'CV001-LP'
6	1-5	'CV001-LP'
1	3-5	NULL
2	4-5	NULL
3	5	NULL
4	5	NULL
7	1	'CV011-LP'
8	1	'CV012-LP'
7	2	'CV021-LP'
8	2	'CV022-LP'
7	3	'CV031-LP'
8	3	'CV032-LP'
7	4	'CV041-LP'
8	4	'CV042-LP'
9-11	1	'CV111-CR'
12-13	1	'CV112-CR'
14-15	1	'CV113-CR'
16-17	1	'CV114-CR'
18-19	1	'CV115-CR'
20-21	1	'CV116-CR'

Table C.3 (continued)

IA	IR	ICVHC
22	1	'CV117-CR'
9-11	2	'CV121-Core'
12-13	2	'CV122-Core'
14-15	2	'CV123-Core'
16-17	2	'CV124-Core'
18-19	2	'CV125-Core'
20-21	2	'CV126-Core'
22	2	'CV127-Core'
9-11	3	'CV131-Core'
12-13	3	'CV132-Core'
14-15	3	'CV133-Core'
16-17	3	'CV134-Core'
18-19	3	'CV135-Core'
20-21	3	'CV136-Core'
22	3	'CV137-Core'
9-11	4	'CV141-Core'
12-13	4	'CV142-Core'
14-15	4	'CV143-Core'
16-17	4	'CV144-Core'
18-19	4	'CV145-Core'
20-21	4	'CV146-Core'
22	4	'CV147-Core'
7	5	'CV051-LP'
8	5	'CV052-LP'
9-22	5	NULL

Table C.4
Mass of materials in the fuel component (HTTF)

IA	IR	Mass of UO_2 (kg)
1-22	1	0.000
1-11	2-4	0.000
12-21	2-4	20.892
22	2-4	0.000

Table C.5
Mass of graphite in the clad component (HTTF)

IA	IR	Mass of GRAPH in CL (kg)
1-22	1	0.000
1-11	2-4	0.000
12-21	2-4	45.573
22	2-4	0.000

Table C.6
Mass of graphite in the reflector component (HTTF)

IA	IR	Mass of GRAPH in RF (kg)
1-8	1-4	0.000
9	1	10.200
10-21	1	37.124
22	1	46.672
9	2-4	12.521
10	2-4	45.573
11	2-4	44.573
22	2-4	56.293

Table C.7
HTTF supporting structure parameters

IA	IR	Mass of STEEL in SS (kg)	Mass of ZIRC in SS (kg)
9	1	87.320	0.000
9	2-4	137.595	0.000
11	2-4	0.000	1.000
22	2-4	0.000	1.000
6	1	0.000	56.999
6	2-4	0.000	89.816
6	5	0.000	782.208

Table C.8
HTTF reflector geometry input

IA	IR	RADI (m)	THKRF (m)	DHYRFC (m)
9-22	1	1.86E-01	-1.86E-01	.3715
9-11	2	2.98E-01	-1.12E-01	.0159
9-12	3	3.78E-01	-8.04E-02	.0159
9-13	4	4.45E-01	-6.61E-02	.0159

Table C.9: HTTF COR cell flow areas

IA	IR	ASCELR (m^2)	AFLOWC (m^2)
1	1	2.57E-02	1.00E-03
2	1	4.08E-02	1.00E-03
3	1	4.20E-02	1.00E-03
4	1	4.43E-02	1.00E-03
5	1	8.03E-01	1.00E-03
6	1	3.55E-01	1.00E-03
7-8	1	2.66E-01	1.08E-01
9	1	1.82E-01	1.00E-03
10-21	1	2.31E-01	1.00E-03
22	1	2.90E-01	1.00E-03
1	2	4.12E-02	1.00E-03
2	2	6.56E-02	1.00E-03
3	2	6.74E-02	1.00E-03
4	2	7.12E-02	1.00E-03
5	2	1.29E+00	1.00E-03
6	2	5.69E-01	1.00E-03
7-8	2	4.27E-01	1.71E-01
9	2	2.92E-01	2.81E-02
10-21	2	3.71E-01	2.81E-02
22	2	4.66E-01	2.81E-02
1	3	5.23E-02	1.00E-03
2	3	8.32E-02	1.00E-03
3	3	8.56E-02	1.00E-03
4	3	9.04E-02	1.00E-03
5	3	1.64E+00	1.00E-03

Table C.9 (continued)

IA	IR	ASCELR (m^2)	AFLOWC (m^2)
6	3	7.23E-01	1.00E-03
7-8	3	5.42E-01	1.71E-01
9	3	3.71E-01	2.81E-02
10-21	3	4.71E-01	2.81E-02
22	3	5.92E-01	2.81E-02
1	4	6.14E-02	1.00E-03
2	4	9.78E-02	1.00E-03
3	4	1.01E-01	1.00E-03
4	4	1.06E-01	1.00E-03
5	4	1.92E+00	1.00E-03
6	4	8.49E-01	1.00E-03
7-8	4	6.37E-01	1.71E-01
9	4	4.36E-01	2.81E-02
10-21	4	5.53E-01	2.81E-02
22	4	6.95E-01	2.81E-02
1	5	1.13E-01	1.00E-03
2	5	1.80E-01	1.00E-03
3	5	1.85E-01	1.00E-03
4	5	1.96E-01	1.00E-03
5	5	3.54E+00	1.00E-03
6	5	1.56E+00	1.00E-03
7-8	5	1.17E+00	1.49E+00

Table C.10
HTTF COR component surface areas

IA	IR	ASFU (m^2)	ASCL (m^2)	ASSS (m^2)
1-5	1-4	0.0	0.0	0.0
6	1	0.0	0.0	1.08E-01
6	2-4	0.0	0.0	1.71E-01
7-8	1-4	0.0	0.0	0.0
9	1	0.0	0.0	1.08E-01
9	2-4	0.0	0.0	1.59E-01
10-22	1	0.0	0.0	0.0
10	2-4	0.0	0.0	0.0
11	2-4	0.0	0.0	1.56E-01
12-21	2-4	6.00E-01	1.40E+00	0.0
22	2-4	0.0	0.0	1.56E-01
1	5	0.0	0.0	0.0
2	5	0.0	0.0	0.0
3	5	0.0	0.0	0.0
4	5	0.0	0.0	0.0
5	5	0.0	0.0	0.0
6	5	0.0	0.0	1.49E+00
7-8	5	0.0	0.0	0.0

Table C.11
HTTF reflector component surface area

IA	IR	ASRF
9	1	1.82E-01
10-21	1	2.31E-01
22	1	2.90E-01
9	2-4	3.85E-01
10-11	2-4	1.40E+00
22	2-4	1.76E+00

C.3 cvh-vessel.inp

CARD	*WORD*	*VALUE*	*BASIS*
CV_ID	CVNAME	Table C.12	Control volume name
	ICVNUM	Table C.12	Control volume sequence number
CV_THR	ICVTHR	NONEQUIL	Nonequilibrium thermodynamics switch, meaning Tpool≠Tatmos (irrelevant for single-phase gas)
	IPFSW	FOG	Fog (liquid water in the atmosphere) allowed (irrelevant for single-phase gas)
	ICVACT	ACTIVE	CVs are active, meaning MELCOR advances their thermodynamic state by solving conservation equations
CV_PAS	ITYPTH	SEPARATE	Separate input for pool and atmosphere
	IPORA	ONLYATM	Only atmosphere is present in each control volume
	VAPORSTATE	SUPERHEATED	Atmosphere is superheated. There is no water vapor in any control volume, so this field is irrelevant.
CV_PTD	PTDID	PVOL	Control volume pressure will be specified

	PVOL	8.00E+05	Initial CV pressure in Pa. Equal to 8.0E+05 Pa for all CVs within the vessel.
CV_AAD	ATMID	TATM	Atmosphere temperature will be specified
	TATM	763.0	Initial CV temperature
CV_NCG	NMMAT	1	Number of NCG materials in CV (initially, only helium is present within the vessel)
	NCGID	RHUM	Relative humidity specified
	RHUM	0.0	Only noncondensible gases are present in the atmosphere
	NAMGAS	HE	Noncondensible present in CV
	MLFR	1.0	Mole fraction of NAMGAS
CV_VAT	ICVVZP	Depends on CV	Number of altitude/volume pairs in the volume altitude table. One pair is present for each axial COR cell elevation in the CV.
	CVZ	Table C.12	Altitude. Top and bottom elevations for each CV are present in Table C.12.
	CVVOL	Table C.12	Volume at altitude CVZ. Total volume of each CV is present in Table C.12.

Table C.12: Elevation and volume of CVs within the HTTF vessel

CVNAME	ICVNUM	Bottom El. (m)	Top El. (m)	Volume (m^3)
001	'CV001-LP'	-2.132	-1.009	1.15E+00
011	'CV011-LP'	-1.009	-0.781	2.47E-02
012	'CV012-LP'	-0.781	-0.552	2.48E-02
021	'CV021-LP'	-1.009	-0.781	3.89E-02
022	'CV022-LP'	-0.781	-0.552	3.91E-02
031	'CV031-LP'	-1.009	-0.781	3.89E-02
032	'CV032-LP'	-0.781	-0.552	3.91E-02
041	'CV041-LP'	-1.009	-0.781	3.89E-02
042	'CV042-LP'	-0.781	-0.552	3.91E-02
051	'CV051-LP'	-1.009	-0.781	2.54E-01
052	'CV052-LP'	-0.781	-0.552	2.55E-01
061	'CV061-Outlet'	-1.009	-0.781	2.04E-02
062	'CV062-Outlet'	-0.781	-0.552	2.06E-02
108	'CV108-UP'	2.230	2.973	8.59E-01
111	'CV111-CR'	-0.552	0.000	1.00E-09
112	'CV112-CR'	0.000	0.396	1.00E-09
113	'CV113-CR'	0.396	0.792	1.00E-09
114	'CV114-CR'	0.792	1.188	1.00E-09
115	'CV115-CR'	1.188	1.584	1.00E-09
116	'CV116-CR'	1.584	1.981	1.00E-09
117	'CV117-CR'	1.981	2.230	1.00E-09
121	'CV121-Core'	-0.552	0.000	1.55E-02
122	'CV122-Core'	0.000	0.396	1.11E-02
123	'CV123-Core'	0.396	0.792	1.11E-02

Table C.12 (continued)

CVNAME	ICVNUM	Bottom El. (m)	Top El. (m)	Volume (m^3)
124	'CV124-Core'	0.792	1.188	1.11E-02
125	'CV125-Core'	1.188	1.584	1.11E-02
126	'CV126-Core'	1.584	1.981	1.12E-02
127	'CV127-Core'	1.981	2.230	7.00E-03
131	'CV131-Core'	-0.552	0.000	1.55E-02
132	'CV132-Core'	0.000	0.396	1.11E-02
133	'CV133-Core'	0.396	0.792	1.11E-02
134	'CV134-Core'	0.792	1.188	1.11E-02
135	'CV135-Core'	1.188	1.584	1.11E-02
136	'CV136-Core'	1.584	1.981	1.12E-02
137	'CV137-Core'	1.981	2.230	7.00E-03
141	'CV141-Core'	-0.552	0.000	1.55E-02
142	'CV142-Core'	0.000	0.396	1.11E-02
143	'CV143-Core'	0.396	0.792	1.11E-02
144	'CV144-Core'	0.792	1.188	1.11E-02
145	'CV145-Core'	1.188	1.584	1.11E-02
146	'CV146-Core'	1.584	1.981	1.12E-02
147	'CV147-Core'	1.981	2.230	7.00E-03
160	'CV160-Gap'	-1.009	-0.552	1.16E-01[a]
161	'CV161-Gap'	-0.552	0.000	1.40E-01
162	'CV162-Gap'	0.000	0.396	1.00E-01
163	'CV163-Gap'	0.396	0.792	1.00E-01
164	'CV164-Gap'	0.792	1.188	1.00E-01
165	'CV165-Gap'	1.188	1.584	1.00E-01

[a]CV160-167 represent the gap between the core barrel and the vessel. The gap is assumed to be 0.0508 m (2 in.), which is reasonable when compared to available HTTF drawings.

Table C.12 (continued)

CVNAME	ICVNUM	Bottom El. (m)	Top El. (m)	Volume (m^3)
166	'CV166-Gap'	1.584	2.230	1.64E-01
167	'CV167-Gap'	2.230	3.049	2.01E-01

C.4 fl-vessel.inp

CARD	*WORD*	*VALUE*	*BASIS*
FL_ID	FPNAME	Table C.13	Flow path name
	IFPNUM	Table C.13	Flow path number
FL_FT	KCVFM	Table C.13	Name of the "from" control volume
	KCVTO	Table C.13	Name of the "to" control volume
	ZFM	Table C.14	Altitude of "from" junction
	ZTO	Table C.14	Altitude of "to" junction. For core flow paths, ZTO=ZFM, where ZTO is the altitude of the junction between KCVFM and KCVTO for axial flow and the altitude of the midplane of KCVFM and KCVTO for radial flow.

FL_GEO	FLARA	Table C.15	Fully open flow path area. This is equal to the empty bed flow area for flow paths in the core. For vertical flow in the core, FLARA= $\pi(R_o^2 - R_i^2)$. For horizontal flow in the core, FLARA= $2\Delta H$. R_o and R_i are the inner and outer radii of the radial ring associated with the "from" CV. ΔH is the height of the "from" CV.
	FLLEN	Table C.15	Momentum exchange length for the flow path. This value is used to calculate momentum exchange between pool and atmosphere. Since flow is single phase gas, this value has no effect on the calculations. FLLEN is set equal to the sum of the segment lengths for the flow path.
	FLOPO	1.0	Fraction of the flow path open, set to unity because all flow paths are fully open

	FLHGTF	Table C.14	"From" junction flow path opening height. For a horizontal flow path, this is defined as height of the opening in the flow path. It has no rigorous interpretation for vertical flow paths. This parameter is simply used to determine the range of elevations from which flow may be drawn. One quarter of the flow path length is used for FLHGTF and FLHGTT.
	FLHGTT	Table C.14	"To" junction flow path opening height.
FL_JSW	KFLGFL	Table C.14	Flow path orientation. '0' signifies vertical flow, and '3' signifies horizontal flow.

FL_SEG	IPNSG	—	Number of flow path segments. Flow paths from the upper plenum to the top reflector ('TopRlctr-FL1r7', where r is ring 2, 3, or 4) and from the bottom reflector to the outlet plenum ('BotRlctr-FL141') have two segments, one of which represents the coolant channels in the reflector. The other represents flow in the upper or outlet plenum. All other flow paths have one segment
	SAREA	Table C.15	Segment flow area. For segments with one flow segment, the value of FLARA is used as input for SAREA
	SLEN	Table C.15	Segment flow length. The flow length is set equal to the distance between the midpoints of the "to" and "from" CVs.

SHYD	Table C.15	Segment hydraulic diameter. For flow in the lower plenum, the hydraulic diameter is equal to the barrel diameter. For flow in the upper plenum, the hydraulic diameter is equal to the diameter of the circle whose center is the upper plenum centroid. For radial flow in the lower plenum, the hydraulic diameter is twice the plenum height.

Table C.13: HTTF flow path connections

FPNAME	IFPNUM	KCVFM	KCVTO
'LowPlen-FL011'	011	'CV012-LP'	'CV011-LP'
'LowPlen-FL021'	021	'CV022-LP'	'CV021-LP'
'LowPlen-FL022'	022	'CV121-Core'	'CV022-LP'
'LowPlen-FL031'	031	'CV032-LP'	'CV031-LP'
'LowPlen-FL032'	032	'CV131-Core'	'CV032-LP'
'LowPlen-FL041'	041	'CV042-LP'	'CV041-LP'
'LowPlen-FL042'	042	'CV141-Core'	'CV042-LP'
'LowPlen-FL051'	051	'CV052-LP'	'CV051-LP'
'Outlet-FL061'	061	'CV062-Outlet'	'CV061-Outlet'
'UP-FL108'	108	'CV167-Gap'	'CV108-UP'
'BotRlctr-FL121'	121	'CV122-Core'	'CV121-Core'
'Core-FL122'	122	'CV123-Core'	'CV122-Core'
'Core-FL123'	123	'CV124-Core'	'CV123-Core'

Table C.13 (continued)

FPNAME	IFPNUM	KCVFM	KCVTO
'Core-FL124'	124	'CV125-Core'	'CV124-Core'
'Core-FL125'	125	'CV126-Core'	'CV125-Core'
'Core-FL126'	126	'CV127-Core'	'CV126-Core'
'TopRlctr-FL127'	127	'CV108-UP'	'CV127-Core'
'BotRlctr-FL131'	131	'CV132-Core'	'CV131-Core'
'Core-FL132'	132	'CV133-Core'	'CV132-Core'
'Core-FL133'	133	'CV134-Core'	'CV133-Core'
'Core-FL134'	134	'CV135-Core'	'CV134-Core'
'Core-FL135'	135	'CV136-Core'	'CV135-Core'
'Core-FL136'	136	'CV137-Core'	'CV136-Core'
'TopRlctr-FL137'	137	'CV108-UP'	'CV137-Core'
'BotRlctr-FL141'	141	'CV142-Core'	'CV141-Core'
'Core-FL142'	142	'CV143-Core'	'CV142-Core'
'Core-FL143'	143	'CV144-Core'	'CV143-Core'
'Core-FL144'	144	'CV145-Core'	'CV144-Core'
'Core-FL145'	145	'CV146-Core'	'CV145-Core'
'Core-FL146'	146	'CV147-Core'	'CV146-Core'
'TopRlctr-FL147'	147	'CV108-UP'	'CV147-Core'
'Gap-FL161'	161	'CV160-Gap'	'CV161-Gap'
'Gap-FL162'	162	'CV161-Gap'	'CV162-Gap'
'Gap-FL163'	163	'CV162-Gap'	'CV163-Gap'
'Gap-FL164'	164	'CV163-Gap'	'CV164-Gap'
'Gap-FL165'	165	'CV164-Gap'	'CV165-Gap'
'Gap-FL166'	166	'CV165-Gap'	'CV166-Gap'
'Gap-FL167'	167	'CV166-Gap'	'CV167-Gap'
'LowPlen-221'	221	'CV011-LP'	'CV021-LP'

Table C.13 (continued)

FPNAME	IFPNUM	KCVFM	KCVTO
'LowPlen-222'	222	'CV012-LP'	'CV022-LP'
'LowPlen-231'	231	'CV021-LP'	'CV031-LP'
'LowPlen-232'	232	'CV022-LP'	'CV032-LP'
'LowPlen-241'	241	'CV031-LP'	'CV041-LP'
'LowPlen-242'	242	'CV032-LP'	'CV042-LP'
'LowPlen-251'	251	'CV041-LP'	'CV051-LP'
'LowPlen-252'	252	'CV042-LP'	'CV052-LP'
'LowPlen-261'	261	'CV051-LP'	'CV061-Outlet'
'LowPlen-262'	262	'CV052-LP'	'CV062-Outlet'

Table C.14: HTTF flow path junction elevations

IFPNUM	ZFM (m)	ZTO (m)	FLHGTF (m)	FLHGTT (m)	Orientation
011	-0.781	-0.781	0.057	0.057	0[a]
021	-0.781	-0.781	0.057	0.057	0
022	-0.552	-0.552	0.098	0.098	0
031	-0.781	-0.781	0.057	0.057	0
032	-0.552	-0.552	0.098	0.098	0
041	-0.781	-0.781	0.057	0.057	0
042	-0.552	-0.552	0.098	0.098	0
051	-0.781	-0.781	0.057	0.057	0
061	-0.781	-0.781	0.057	0.057	0
108	2.998	2.973	0.129	0.129	0
121	0.000	0.000	0.119	0.119	0
122	0.396	0.396	0.099	0.099	0

[a] '0' signifies a normal vertical flow path; '3' signifies a normal horizontal flow path

Table C.14 (continued)

IFPNUM	ZFM (m)	ZTO (m)	FLHGTF (m)	FLHGTT (m)	Orientation
123	0.792	0.792	0.099	0.099	0
124	1.188	1.188	0.099	0.099	0
125	1.584	1.584	0.099	0.099	0
126	1.981	1.981	0.081	0.081	0
127	2.230	2.230	0.101	0.101	0
131	0.000	0.000	0.119	0.119	0
132	0.396	0.396	0.099	0.099	0
133	0.792	0.792	0.099	0.099	0
134	1.188	1.188	0.099	0.099	0
135	1.584	1.584	0.099	0.099	0
136	1.981	1.981	0.081	0.081	0
137	2.230	2.230	0.101	0.101	0
141	0.000	0.000	0.119	0.119	0
142	0.396	0.396	0.099	0.099	0
143	0.792	0.792	0.099	0.099	0
144	1.188	1.188	0.099	0.099	0
145	1.584	1.584	0.099	0.099	0
146	1.981	1.981	0.081	0.081	0
147	2.230	2.230	0.101	0.101	0
161	-0.552	-0.552	0.126	0.126	0
162	0.000	0.000	0.119	0.119	0
163	0.396	0.396	0.099	0.099	0
164	0.792	0.792	0.099	0.099	0
165	1.188	1.188	0.099	0.099	0
166	1.584	1.584	0.130	0.130	0
167	2.230	2.230	0.392	0.392	0

Table C.14 (continued)

IFPNUM	ZFM (m)	ZTO (m)	FLHGTF (m)	FLHGTT (m)	Orientation
221	-0.895	-0.895	0.228	0.228	3
222	-0.667	-0.667	0.229	0.229	3
231	-0.895	-0.895	0.228	0.228	3
232	-0.667	-0.667	0.229	0.229	3
241	-0.895	-0.895	0.228	0.228	3
242	-0.667	-0.667	0.229	0.229	3
251	-0.895	-0.895	0.228	0.228	3
252	-0.667	-0.667	0.229	0.229	3
261	-0.895	-0.895	0.228	0.228	3
262	-0.667	-0.667	0.229	0.229	3

Table C.15: HTTF flow path geometry

IFPNUM	FLARA (m^2)	SLEN (m)	SHYD (m)
011	1.084E-01	2.285E-01	1.486E+00
021	1.708E-01	2.285E-01	1.486E+00
022 [a]	2.811E-02	2.760E-01	1.588E-02
	1.708E-01	1.145E-01	1.486E+00
031	1.708E-01	2.285E-01	1.486E+00
032 [a]	2.811E-02	2.760E-01	1.588E-02
	1.708E-01	1.145E-01	1.486E+00
041	1.708E-01	2.285E-01	1.486E+00
042 [a]	2.811E-02	2.760E-01	1.588E-02
	1.708E-01	1.145E-01	1.486E+00
051	1.113E+00	2.285E-01	1.486E+00

[a]This flow path has two segments. The first segment represents flow through the upper plenum. The second segment represents flow through channels in the top reflector.

Table C.15 (continued)

IFPNUM	FLARA (m^2)	SLEN (m)	SHYD (m)
061	5.715E-02	2.285E-01	4.572E-01
108	1.057E+00	5.151E-01	1.160E+00
121	2.811E-02	4.740E-01	1.588E-02
122	2.811E-02	3.960E-01	1.588E-02
123	2.811E-02	3.960E-01	1.588E-02
124	2.811E-02	3.960E-01	1.588E-02
125	2.811E-02	3.965E-01	1.588E-02
126	2.811E-02	3.230E-01	1.588E-02
127 [b]	1.057E+00	2.786E-01	1.160E+00
	2.811E-02	1.245E-01	1.588E-02
131	2.811E-02	4.740E-01	1.588E-02
132	2.811E-02	3.960E-01	1.588E-02
133	2.811E-02	3.960E-01	1.588E-02
134	2.811E-02	3.960E-01	1.588E-02
135	2.811E-02	3.965E-01	1.588E-02
136	2.811E-02	3.230E-01	1.588E-02
137 [b]	1.057E+00	2.786E-01	1.160E+00
	2.811E-02	1.245E-01	1.588E-02
141	2.811E-02	4.740E-01	1.588E-02
142	2.811E-02	3.960E-01	1.588E-02
143	2.811E-02	3.960E-01	1.588E-02
144	2.811E-02	3.960E-01	1.588E-02
145	2.811E-02	3.965E-01	1.588E-02
146	2.811E-02	3.230E-01	1.588E-02

[b]This flow path has two segments. The first segment represents flow through channels in the bottom reflector. The second segment represents flow through the outlet plenum.

Table C.15 (continued)

IFPNUM	FLARA (m^2)	SLEN (m)	SHYD (m)
147 [b]	1.057E+00	2.786E-01	1.160E+00
	2.811E-02	1.245E-01	1.588E-02
161	2.534E-01	5.045E-01	1.016E-01
162	2.534E-01	4.740E-01	1.016E-01
163	2.534E-01	3.960E-01	1.016E-01
164	2.534E-01	3.960E-01	1.016E-01
165	2.534E-01	3.960E-01	1.016E-01
166	2.534E-01	5.210E-01	1.016E-01
167	2.534E-01	1.570E+00	1.016E-01
221	2.661E-01	1.490E-01	4.560E-01
222	2.672E-01	1.490E-01	4.580E-01
231	4.270E-01	9.635E-02	4.560E-01
232	4.289E-01	9.635E-02	4.580E-01
241	5.421E-01	7.320E-02	4.560E-01
242	5.445E-01	7.320E-02	4.580E-01
251	6.368E-01	1.823E-01	4.560E-01
252	6.396E-01	1.823E-01	4.580E-01
261	1.064E+00	8.437E-01	4.560E-01
262	1.069E+00	8.437E-01	4.580E-01

C.5 hs-vessel.inp

C.5.1 HTTF Top Boundary HS Input

CARD *WORD* *VALUE* *BASIS*

HS_ID	HSNAME	'CB-23'	Heat structure name. HS represents hemispherical end cap at the top of the core barrel.
	IHSNUM	52300	Heat structure number
HS_GD	IGEOM	TOPHALFSPHERE	Heat structure has hemispherical geometry.
	ISS	SS	Steady-state initialization of heat structure temperatures is performed by MELGEN
HS_EOD	HSALT	2.230	Elevation of the lowest point on the heat structure
	ALPHA	1.0	Has no meaning for hemispherical geometry
HS_SRC	ISRC	NO	No internal power source is used for the heat structures in this input.
HS_ND	NP	2	Number of temperature nodes. Each heat structure has two nodes, one at each surface.
	XI	0.743 / 0.768	Location of temperature nodes. Node locations are at the inner and outer boundary surfaces.
	TEMPIN	—	Initial temperature of the node. Since steady-state initialization is chosen, this value is ignored.
	MATNAM	ALUMINUM	Heat structure material. ALUMINUM has been redefined as STAINLESS-STEEL for this calculation.

HS_LB	IBCL	CalcCoefHS	The left surface has a convective boundary condition. The HS package calculates the convective heat transfer coefficient.
	IBVL	'CV108-UP'	The boundary volume associated with the left surface is CV108, which represents the upper plenum
	MTEVAL	NO	Mass transfer is not evaluated. Since there is no water in the system, there is no mass transfer because there is no evaporation or condensation.
HS_LBP	IFLOWL	INT	Flow over the surface is classified as internal
	CPFPL	0.5	The minimum value of the pool fraction for which heat transfer to the pool is calculated is set to 0.5. Since there is no pool, this parameter is irrelevant.
	CPFAL	0.5	The maximum value of the pool fraction for which heat transfer to the atmosphere is calculated is set to 0.5. This ensures that heat transfer to the atmosphere will always be considered for this problem.
HS_LBS	ASURFL	3.468	Left boundary surface area, equal to $2\pi R_i^2$, where R_i is the inner radius of the HS

	CLNL	0.743	Characteristic length of the left boundary surface, equal to the HS radius
	BNDZL	0.743	Axial length of the left boundary surface, defined as the dimension of the surface in a direction perpendicular to the direction of energy flow within the heat structure. For this situation, CLNL=BNDZL.
HS_RB	IBCR	CalcCoefHS	The right surface has a convective boundary condition
	IBVR	'CV167-Gap'	The boundary volume for this HS is CV167, which represents the helium in the gap between the barrel end cap and the vessel upper head
	MTEVAR	NO	No mass transfer is evaluated.
HS_RBP	IFLOWR	EXT	Flow is external
	CPFPR	0.5	Critical pool fraction. See above.
	CPFAR	0.5	Critical pool fraction for atmosphere. See above.
HS_RBS	ASURFL	3.709	Left boundary surface area, equal to $2\pi R_i^2$, where R_i is the inner radius of the HS
	CLNR	0.768	Characteristic length of the right boundary surface, equal to the HS outer radius

	BNDZR	0.768	Axial length of the right boundary surface, defined as the dimension of the surface in a direction perpendicular to the direction of energy flow within the heat structure. For this situation, CLNR=BNDZR.
HS_FT	IFTNUM	OFF	Liquid film-tracking is turned off.

C.5.2 HTTF Side Reflector and Core Barrel HS Input

CARD	*WORD*	*VALUE*	*BASIS*
HS_ID	HSNAME	Table C.16	Heat structure name
	IHSNUM	Table C.16	Heat structure number
HS_GD	IGEOM	CYLINDRICAL	Heat structure has cylindrical geometry.
	ISS	SS	Steady-state initialization of heat structure temperatures is performed by MELGEN
HS_EOD	HSALT	Table C.16	Elevation of the lowest point on the heat structure
	ALPHA	1	Heat structure orientation. '1' indicates a vertical surface.
HS_SRC	ISRC	NO	No internal power source is used for the heat structures in this input.

HS_ND	NP	4	Number of temperature nodes. Node locations are as follows: side reflector inner surface, side reflector midpoint, side reflector outer surface (which is also the core barrel inner surface), core barrel outer surface. HS 50700 and 50800 only have 2 nodes, which are at the core barrel inner and outer surfaces. 50700 and 50800 represent the portion of the core barrel around the coolant outlet plenum. The barrel thickness was determined by subtracting the assumed barrel-vessel gap thickness from the difference between the vessel inner radius and the side reflector outer radius, both of which are known parameters [82].
	XI	0.445 / 0.594 / 0.743 / 0.768	Location of temperature nodes. For HS 50700 and 50800, the two node locations are 0.743 and 0.768.
	TEMPIN	—	Initial temperature of the node. Since steady-state initialization is chosen, this value is ignored.

	MATNAM	GRAPHITE / ALUMINUM	Heat structure materials. GRAPHITE is used for the first two meshes (between nodes 1 and 3), while ALUMINUM is used for the last mesh (between nodes 3 and 4). GRAPHITE and ALUMINUM properties have been modified (Section C.10).
HS_LB	IBCL	CalcCoefHS	The left surface has a convective boundary condition. The HS package calculates the convective heat transfer coefficient.
	IBVL	Table C.16	The boundary volume associated with the left surface
	MTEVAL	NO	Mass transfer is not evaluated.
HS_LBP	IFLOWL	INT	Flow over the surface is internal.
	CPFPL	0.5	The minimum value of the pool fraction for which heat transfer to the pool is calculated is set to 0.5. Since there is no pool, this parameter is irrelevant.
	CPFAL	0.5	The maximum value of the pool fraction for which heat transfer to the atmosphere is calculated is set to 0.5. This value ensures that heat transfer to the atmosphere is always allowed since the pool fraction will always be less than 0.5.

HS_LBS	ASURFL	—	Left boundary surface area. This parameter is ignored for cylindrical heat structures. MELGEN calculates the boundary surface area using the axial length and inner node location.
	CLNL	Table C.16	Characteristic length of the left boundary surface, equal to the axial length of the heat structure.
	BNDZL	Table C.16	Axial length of the left boundary surface. For this situation, CLNL=BNDZL.
HS_RB	IBCR	CalcCoefHS	The right surface has a convective boundary condition. The HS package calculates the convective heat transfer coefficient.
	IBVR	Table C.16	Right surface boundary volume. The gap between the barrel and vessel forms the boundary for these heat structures.
	MTEVAR	NO	No mass transfer is evaluated.
HS_RBP	IFLOWR	EXT	External flow is selected.
	CPFPR	0.5	Critical pool fraction. See above.
	CPFAR	0.5	Critical pool fraction for atmosphere. See above.
HS_RBS	ASURFR	—	Right boundary surface area. Ignored for cylindrical heat structures.

	CLNR	Table C.16	Characteristic length of the right surface. For this situation, CLNR=CLNL.
	BNDZR	Table C.16	Axial length of the right surface. For this situation, BNDZR=BNDZL.
HS_FT	IFTNUM	OFF	Liquid film-tracking is turned off.

Table C.16: HTTF side reflector and core barrel HS input

HSNAME	IHSNUM	HSALT (m)	IBVL	IBVR	BNDZL
'CB-07'	50700	-1.009E+00	051	160	0.228
'CB-08'	50800	-7.810E-01	052	160	0.229
'SR_CB-09'	50900	-5.520E-01	141	161	0.156
'SR_CB-10'	51000	-3.960E-01	141	161	0.198
'SR_CB-11'	51100	-1.980E-01	141	161	0.198
'SR_CB-12'	51200	0.000E+00	142	162	0.198
'SR_CB-13'	51300	1.980E-01	142	162	0.198
'SR_CB-14'	51400	3.960E-01	143	163	0.198
'SR_CB-15'	51500	5.940E-01	143	163	0.198
'SR_CB-16'	51600	7.920E-01	144	164	0.198
'SR_CB-17'	51700	9.900E-01	144	164	0.198
'SR_CB-18'	51800	1.188E+00	145	165	0.198
'SR_CB-19'	51900	1.386E+00	145	165	0.198
'SR_CB-20'	52000	1.584E+00	146	166	0.199
'SR_CB-21'	52100	1.783E+00	146	166	0.198
'SR_CB-22'	52200	1.981E+00	147	166	0.249

C.5.3 HTTF RPV HS Input

CARD	*WORD*	*VALUE*	*BASIS*
HS_ID	HSNAME	Table C.17	Heat structure name
	IHSNUM	Table C.17	Heat structure number
HS_GD	IGEOM	CYLINDRICAL	Heat structure has cylindrical geometry.
	ISS	SS	Steady-state initialization of heat structure temperatures is performed by MELGEN
HS_EOD	HSALT	Table C.17	Elevation of the lowest point on the heat structure
	ALPHA	1	Heat structure orientation. '1' indicates a vertical surface.
HS_SRC	ISRC	NO	No internal power source is used for the heat structures in this input.
HS_ND	NP	2	Number of temperature nodes. Each heat structure has two nodes, one at each surface.
	XI	0.819 / 0.852	Location of temperature nodes. Node locations are at the inner and outer boundary surfaces. The vessel thickness is assumed to be 1/4 of the MHTGR vessel thickness [84] because the HTTF is a 1/4 length scale facility. The inner vessel radius is known [82].

	TEMPIN	—	Initial temperature of the node. Since steady-state initialization is chosen, this value is ignored.
	MATNAM	STAINLESS-STEEL-304	Heat structure material. The vessel material is unknown, so it has been assumed that the vessel is made of SS304. Properties of SS304 can be modified once the HTTF vessel has been procured.
HS_LB	IBCL	CalcCoefHS	The left surface has a convective boundary condition. The HS package calculates the convective heat transfer coefficient.
	IBVL	Table C.17	The boundary volume associated with the left surface. The gap between the core barrel and RPV forms the boundary for these heat structures.
	MTEVAL	NO	Mass transfer is not evaluated.
HS_LBP	IFLOWL	INT	Flow over the surface is internal.
	CPFPL	0.5	The minimum value of the pool fraction for which heat transfer to the pool is calculated is set to 0.5. Since there is no pool, this parameter is irrelevant.

	CPFAL	0.5	The maximum value of the pool fraction for which heat transfer to the atmosphere is calculated is set to 0.5. This value ensures that heat transfer to the atmosphere is always allowed since the pool fraction will always be less than 0.5.
HS_LBS	ASURFL	—	Left boundary surface area. This parameter is ignored for cylindrical heat structures.
	CLNL	Table C.17	Characteristic length of the left boundary surface, equal to the axial length of the heat structure.
	BNDZL	Table C.17	Axial length of the left boundary surface. For this situation, CLNL=BNDZL.
HS_RB	IBCR	CalcCoefHS	The right surface has a convective boundary condition. The HS package calculates the convective heat transfer coefficient.
	IBVR	Table C.17	Right surface boundary volume. The cavity between the RPV and RCCS forms the boundary for these heat structures.
	MTEVAR	NO	No mass transfer is evaluated.
HS_RBP	IFLOWR	EXT	External flow is selected.
	CPFPR	0.5	Critical pool fraction. See above.

	CPFAR	0.5	Critical pool fraction for atmosphere. See above.
HS_RBS	ASURFR	—	Right boundary surface area. Ignored for cylindrical heat structures.
	CLNR	Table C.17	Characteristic length of the right surface. For this situation, CLNR=CLNL.
	BNDZR	Table C.17	Axial length of the right surface. For this situation, BNDZR=BNDZL.
HS_FT	IFTNUM	OFF	Liquid film-tracking is turned off.

Table C.17
HTTF RPV HS input

HSNAME	IHSNUM	HSALT (m)	IBVL	IBVR	BNDZL
'RPV-00'	60000	-1.009	160	301	0.457
'RPV-01'	60100	-0.552	161	301	0.552
'RPV-02'	60200	0.000	162	302	0.396
'RPV-03'	60300	0.396	163	303	0.396
'RPV-04'	60400	0.792	164	304	0.396
'RPV-05'	60500	1.188	165	305	0.396
'RPV-06'	60600	1.584	166	306	0.646

C.5.4 HTTF Vessel Upper Head HS Input

CARD	*WORD*	*VALUE*	*BASIS*
HS_ID	HSNAME	'RPV-07'	Heat structure name. HS represents hemispherical upper head of the HTTF vessel
	IHSNUM	60700	Heat structure number
HS_GD	IGEOM	TOPHALFSPHERE	Heat structure has hemispherical geometry.
	ISS	SS	Steady-state initialization of heat structure temperatures is performed by MELGEN
HS_EOD	HSALT	2.230	Elevation of the lowest point on the heat structure
	ALPHA	1.0	Has no meaning for hemispherical geometry
HS_SRC	ISRC	NO	No internal power source is used for the heat structures in this input.
HS_ND	NP	2	Number of temperature nodes. Each heat structure has two nodes, one at each surface.
	XI	0.819 / 0.852	Location of temperature nodes. Node locations are at the inner and outer boundary surfaces.
	TEMPIN	—	Initial temperature of the node. Since steady-state initialization is chosen, this value is ignored.

	MATNAM	STAINLESS-STEEL-304	Heat structure material.
HS_LB	IBCL	CalcCoefHS	The left surface has a convective boundary condition. The HS package calculates the convective heat transfer coefficient.
	IBVL	'CV167-Gap'	The boundary volume for this surface is CV167, which represents the helium in the gap between the barrel end cap and the vessel upper head
	MTEVAL	NO	Mass transfer is not evaluated. Since there is no water in the system, there is no mass transfer because there is no evaporation or condensation.
HS_LBP	IFLOWL	INT	Flow over the surface is classified as internal
	CPFPL	0.5	The minimum value of the pool fraction for which heat transfer to the pool is calculated is set to 0.5. Since there is no pool, this parameter is irrelevant.
	CPFAL	0.5	The maximum value of the pool fraction for which heat transfer to the atmosphere is calculated is set to 0.5. This ensures that heat transfer to the atmosphere will always be considered for this problem.

HS_LBS	ASURFL	4.216	Left boundary surface area, equal to $2\pi R_i^2$, where R_i is the inner radius of the HS
	CLNL	0.819	Characteristic length of the left boundary surface, equal to the HS inner radius
	BNDZL	0.819	Axial length of the left boundary surface, defined as the dimension of the surface in a direction perpendicular to the direction of energy flow within the heat structure. For this situation, CLNL=BNDZL.
HS_RB	IBCR	CalcCoefHS	The right surface has a convective boundary condition
	IBVR	'CV307-Cavity'	The boundary volume for the surface is CV307, which represents the air volume around the vessel upper head
	MTEVAR	NO	No mass transfer is evaluated.
HS_RBP	IFLOWR	EXT	Flow is external
	CPFPR	0.5	Critical pool fraction. See above.
	CPFAR	0.5	Critical pool fraction for atmosphere. See above.
HS_RBS	ASURFL	4.216	Left boundary surface area, equal to $2\pi R_i^2$, where R_i is the inner radius of the HS
	CLNR	0.852	Characteristic length of the right boundary surface, equal to the HS outer radius

	BNDZR	0.852	Axial length of the right boundary surface, defined as the dimension of the surface in a direction perpendicular to the direction of energy flow within the heat structure. For this situation, CLNR=BNDZR.
HS_FT	IFTNUM	OFF	Liquid film-tracking is turned off.

C.6 src-sink.inp

CARD	*WORD*	*VALUE*	*BASIS*
CV_ID	CVNAME	'CoolSource'	Helium source CV name
	ICVNUM	200	Source CV number
CV_THR	ICVTHR	NONEQUIL	Tpool ≠ Tatmos
	IPFSW	FOG	Default
	ICVACT	PROP-SPECIFIED	CV thermodynamic properties are specified as a function of time
CV_PAS	ITYPTH	SEPARATE	Separate pool and atmosphere input
	IPORA	ONLYATM	Only atmosphere is present
	VAPORSTATE	SUPERHEATED	Helium is superheated

CV_VAT	CVZ	-1.009 / -0.552	Altitudes in the altitude/volume table. CV represents the coolant inlet pipe. It is assumed that the inlet diameter is 1/4 of the MHTGR cross duct inner diameter [84]. It is also assumed that the coolant outlet plenum height is equal to the coolant inlet (and outlet) pipe diameter. The top elevation of the outlet duct is assumed to be equal to the bottom elevation of the bottom reflector.
	CVVOL	0.0 / 0.1	Volume at altitude CVZ. Total volume is irrelevant, since the state of the volume is PROP-SPECIFIED.
CV_PTD	PVOL	'SourceP'	Name of CF specifying source pressure
CV_AAD	TATM	'SourceT'	CF specifying source temperature
CV_NCG	RHUM	'Humidity'	CF specifying source relative humidity. 'Humidity' returns 0.0 throughout the calculations.
	NAMGAS	'HE'	CV contains helium

	CFNAME	'Src_HeFrac'	Mole fraction of helium in the source CV. CF returns 1.0 throughout the calculations.
CV_ID	CVNAME	'CoolSink'	Helium sink CV name
	ICVNUM	201	Sink CV number
CV_THR	ICVTHR	NONEQUIL	Tpool $\neq$ Tatmos
	IPFSW	FOG	Default
	ICVACT	PROP-SPECIFIED	CV thermodynamic properties are specified as a function of time
CV_PAS	ITYPTH	SEPARATE	Separate pool and atmosphere input
	IPORA	ONLYATM	Only atmosphere is present
	VAPORSTATE	SUPERHEATED	Helium is superheated
CV_VAT	CVZ	-1.009 / -0.552	Altitudes in the altitude/volume table. CV represents the coolant outlet pipe. It is assumed that the outlet diameter is 1/4 of the MHTGR cross duct inner diameter [84]. The top elevation of the outlet duct is assumed to be equal to the bottom elevation of the bottom reflector.

	CVVOL	0.0 / 1.0	Volume at altitude CVZ. Total volume is irrelevant, since the state of the volume is PROP-SPECIFIED.
CV_PTD	PVOL	'SinkP'	Name of CF specifying sink pressure
CV_AAD	TATM	'SinkT'	CF specifying sink temperature
CV_NCG	RHUM	'Humidity'	CF specifying source relative humidity. 'Humidity' returns 0.0 throughout the calculations.
	NAMGAS	'N2'	The sink CV contains air in order to model air ingress during DLOFC events
	CFNAME	'Sink_N2-Frac'	Mole fraction of nitrogen in the sink CV. CF returns 0.8 throughout the calculations.
	NAMGAS	'O2'	The sink CV contains air in order to model air ingress during DLOFC events
	CFNAME	'Sink_N2-Frac'	Mole fraction of oxygen in the sink CV. CF returns 0.2 throughout the calculations.
FL_ID	FPNAME	'FLfromSource'	Source flow path name
	IFPNUM	200	Source flow path number
FL_FT	KCVFM	'CoolSource'	'FROM' CV name
	KCVTO	'CV160-Gap'	'TO' CV name

	ZFM	-0.7805	'FROM' junction altitude
	ZTO	-0.7805	'TO' junction altitude
FL_GEO	FLARA	0.1642	Flow area. Equal to the inlet duct cross-sectional area.
	FLLEN	0.1	Flow path length. Flow path length is arbitrary and has little impact on the calculation, since the reactor inlet pressure is considered to be the pressure in CV160.
	FLOPO	1.0	Flow path is fully open
FL_SEG	SAREA	0.1642	Segment flow area. Since there is only one segment, SAREA=FLARA.
	SLEN	0.1	Segment length, equal to FLLEN
	SHYD	0.4572	Segment hydraulic diameter, equal to the diameter of the inlet duct
FL_ID	FPNAME	'FLtoSinkLow'	Name of the flow path from the bottom half of the outlet pipe (CV061) to the sink (CV201)
	IFPNUM	201	Flow path number
FL_FT	KCVFM	'CV061-Outlet'	'FROM' CV name
	KCVTO	'CoolSink'	'TO' CV name
	ZFM	-0.895	'FROM' junction altitude
	ZTO	-0.895	'TO' junction altitude

FL_GEO	FLARA	0.08209	Flow area. Equal to half of the outlet pipe cross-sectional area.
	FLLEN	0.25	Flow path length. This value is arbitrary because the outlet pressure is considered to be the pressure in CV061.
	FLOPO	1.0	Flow path is fully open
FL_SEG	SAREA	0.08209	Segment flow area. Since there is only one segment, SAREA=FLARA.
	SLEN	0.25	Segment length, equal to FLLEN
	SHYD	0.4572	Segment hydraulic diameter, equal diameter of the outlet duct
FL_ID	FPNAME	'FLtoSinkHigh'	Name of the flow path from the top half of the outlet pipe (CV062) to the sink (CV201)
	IFPNUM	202	Flow path number
FL_FT	KCVFM	'CV062-Outlet'	'FROM' CV name
	KCVTO	'CoolSink'	'TO' CV name
	ZFM	-0.6665	'FROM' junction altitude
	ZTO	-0.6665	'TO' junction altitude
FL_GEO	FLARA	0.08209	Flow area. Equal to half of the outlet pipe cross-sectional area.

	FLLEN	0.25	Flow path length. This value is arbitrary because the outlet pressure is considered to be the pressure in CV061
	FLOPO	1.0	Flow path is fully open
FL_SEG	SAREA	0.08209	Segment flow area. Since there is only one segment, SAREA=FLARA
	SLEN	0.25	Segment length, equal to FLLEN
	SHYD	0.4572	Segment hydraulic diameter, equal diameter of the outlet duct
FL_VTM	FLNAME	'HeSource'	Name of flow path that will be time-dependent
	NFUN	'HeSource'	Name of CF used to define the flow velocity as a function of time

FL_VLV	VLVNAME	'InletValve'	Name of a valve to be used in the calculation. This valve is in FL161, between CV160 and CV161. The valve is fully open during steady-state calculations and fully closed during an outlet pipe break (the DLOFC event used here as the transient test case). This prevents flow to the inlet during this event.
	FLNAME	'Gap-FL161'	Name of the flow path in which the valve is located
	KEYTRIP	NoTRIP	A trip is not used to control the fraction open. Instead, a CF is used to determine the valve open fraction.
	NVFONF	'InletVlv'	CF used to determine the fraction open

C.7 cavity.inp

C.7.1 HTTF Cavity CVH Input

CARD	*WORD*	*VALUE*	*BASIS*
CV_ID	CVNAME	Table C.18	Control volume name
	ICVNUM	Table C.18	Control volume sequence number

CV_THR	ICVTHR	NONEQUIL	Nonequilibrium thermodynamics switch, meaning Tpool≠Tatmos
	IPFSW	FOG	Default
	ICVACT	ACTIVE	CVs are active, meaning MELCOR advances their thermodynamic state by solving conservation equations
CV_PAS	ITYPTH	SEPARATE	Separate input for pool and atmosphere
	IPORA	ONLYATM	Only atmosphere is present in each control volume
	VAPORSTATE	SUPERHEATED	Atmosphere is superheated
CV_PTD	PTDID	PVOL	Control volume pressure will be specified
	PVOL	1.00E+05	Initial CV pressure in Pa. Equal to 1.0E+05 Pa (atmospheric) for all CVs in the cavity between the HTTF vessel and the RCCS.
CV_AAD	ATMID	TATM	Atmosphere temperature will be specified
	TATM	300.0	Initial CV temperature
CV_NCG	NMMAT	2	Number of NCG materials in CV (nitrogen and oxygen)
	NCGID	RHUM	Relative humidity specified
	RHUM	0.0	Only noncondensible gases are present in the atmosphere

	NAMGAS	N2	Noncondensible present in CV
	MLFR	0.8	Mole fraction of NAMGAS
	NAMGAS	O2	Noncondensible present in CV
	MLFR	0.2	Mole fraction of NAMGAS
CV_VAT	ICVVZP	2	Number of altitude/volume pairs in the volume altitude table
	CVZ	Table C.18	Altitude. Top and bottom elevations for each CV are presented in Table C.18.
	CVVOL	Table C.18	Volume at altitude CVZ. Total volume of each CV is presented in Table C.18.

Table C.18
Elevation and volume of CVs outside of HTTF Vessel

CVNAME	ICVNUM	Bottom El. (m)	Top El. (m)	Volume (m^3)
'CV301-Cavity'	301	-2.166	0.000	7.501
'CV302-Cavity'	302	0.000	0.396	1.372
'CV303-Cavity'	303	0.396	0.792	1.372
'CV304-Cavity'	304	0.792	1.188	1.372
'CV305-Cavity'	305	1.188	1.584	1.372
'CV306-Cavity'	306	1.584	2.230	2.237
'CV307-Cavity'	307	2.230	3.049	2.837

C.7.2 HTTF RCCS HS Input

CARD	*WORD*	*VALUE*	*BASIS*
HS_ID	HSNAME	Table C.19	Heat structure name. RCCS heat structures act as fixed temperature boundary conditions.
	IHSNUM	Table C.19	Heat structure number
HS_GD	IGEOM	CYLINDRICAL	Heat structure has cylindrical geometry.
	ISS	SS	Steady-state initialization of heat structure temperatures is performed by MELGEN
HS_EOD	HSALT	Table C.19	Elevation of the lowest point on the heat structure
	ALPHA	1	Heat structure orientation. '1' indicates a vertical surface.
HS_SRC	ISRC	NO	No internal power source is used for the heat structures in this input.
HS_ND	NP	2	Number of temperature nodes. Each heat structure has two nodes, one at each surface.

	XI	1.352 / 1.362	Location of temperature nodes. Node locations are at the inner and outer boundary surfaces. The distance from the HTTF vessel to the RCCS is assumed to be 0.5 m, which is approximately 1/4 of the distance from the VGM vessel to the RCCS. Thus, the RCCS inner radius used here is reasonable.
	TEMPIN	—	Initial temperature of the node. Since steady-state initialization is chosen, this value is ignored.
	MATNAM	STAINLESS-STEEL-304	Heat structure material.
HS_LB	IBCL	CalcCoefHS	The left surface has a convective boundary condition. The HS package calculates the convective heat transfer coefficient.
	IBVL	Table C.17	The boundary volume associated with the left surface. The gap between the HTTF vessel and RCCS forms the boundary for these heat structures.
	MTEVAL	NO	Mass transfer is not evaluated.
HS_LBP	IFLOWL	EXT	Flow over the surface is external.

	CPFPL	0.5	The minimum value of the pool fraction for which heat transfer to the pool is calculated is set to 0.5. Since there is no pool, this parameter is irrelevant.
	CPFAL	0.5	The maximum value of the pool fraction for which heat transfer to the atmosphere is calculated is set to 0.5. This ensures that heat transfer to the atmosphere will always be considered for this problem.
HS_LBS	ASURFL	—	Left boundary surface area. This parameter is ignored for cylindrical heat structures.
	CLNL	Table C.19	Characteristic length of the left boundary surface, equal to the axial length of the heat structure.
	BNDZL	Table C.19	Axial length of the left boundary surface. For this situation, CLNL=BNDZL.
HS_RB	IBCR	TempTimeCF	The right surface has a fixed temperature boundary condition specified by a control function.

Table C.19
RCCS HS input

HSNAME	IHSNUM	HSALT (m)	IBVL	BNDZL
'RCCS-00'	70000	-2.166	301	1.614
'RCCS-01'	70100	-0.552	301	0.552
'RCCS-02'	70200	0.000	302	0.396
'RCCS-03'	70300	0.396	303	0.396
'RCCS-04'	70400	0.792	304	0.396
'RCCS-05'	70500	1.188	305	0.396
'RCCS-06'	70600	1.584	306	0.646
'RCCS-07'	70700	2.230	307	0.819

	NAMECFTF	'RCCS-T-i'	Control function used to specify the temperature of the outer boundary of the RCCS heat structures. A separate CF is specified for each RCCS HS ('i'=0:7 is the RCCS HS number), so that an RCCS axial temperature profile can be simulated. Currently, all CF's have a constant value of 300 (K).
	MTEVAR	NO	No mass transfer is evaluated.
HS_RBP	IFLOWR	EXT	External flow is selected.
	CPFPR	0.5	See above.
	CPFAR	0.5	See above.
HS_FT	IFTNUM	OFF	Liquid film-tracking is turned off.

C.8 vfhttf.inp

CARD	*WORD*	*VALUE*	*BASIS*
HS_RD	NUMPAIR	25	Number of heat structure pairs for radiation heat transfer calculations.
	IHSRD1	Table C.20	Name of the first heat structure in the pair.
	LRBND1	RIGHT	Heat is transferred from the right side of IHSRD1.
	IHSRD2	Table C.20	Name of the second heat structure in the pair.
	LRBND2	LEFT	Heat is transferred from the left side of IHSRD1.
	VIEW	Table C.20	View factor from the right side of IHSRD1 to the left side of IHSRD2. For this calculation, view factors from directly opposing heat structures (i.e. between the outer face of an inner cylinder and the inner face of an outer cylinder at the same elevations) are set to 1.0. This simplified approach is used because there are large uncertainties in the dimensions of the core barrel, vessel, and RCCS. Once facility geometry has been fully specified, detailed view factors can be calculated using the methodology found in Section 4.2.1.

ICFRD1	—	Name of a control function used to define the emissivity of IHSRD1. 'EmisCB', 'EmisVes', and 'EmisRCCS' are the CFs used to specify core barrel, vessel, and RCCS emissitivies. Currently, all emissivities are set to 0.213, which is 1/3.76 of the emissitivity of the prototype. The prototype emissitivity is assumed to be 0.8, which is the value used for PBMR calculations.
ICFRD2	—	Name of a control function used to define the emissivity of IHSRD2. See above.

Table C.20: View factors for structure to structure radiation heat transfer (HTTF)

IHSRD1	IHSRD2	VIEW
'CB-07'	'RPV-00'	1.0
'CB-08'	'RPV-00'	1.0
'SR_CB-09'	'RPV-01'	1.0
'SR_CB-10'	'RPV-01'	1.0
'SR_CB-11'	'RPV-01'	1.0
'SR_CB-12'	'RPV-02'	1.0
'SR_CB-13'	'RPV-02'	1.0
'SR_CB-14'	'RPV-03'	1.0
'SR_CB-15'	'RPV-03'	1.0
'SR_CB-16'	'RPV-04'	1.0

Table C.20 (continued)

IHSRD1	IHSRD2	VIEW
'SR_CB-17'	'RPV-04'	1.0
'SR_CB-18'	'RPV-05'	1.0
'SR_CB-19'	'RPV-05'	1.0
'SR_CB-20'	'RPV-06'	1.0
'SR_CB-21'	'RPV-06'	1.0
'SR_CB-22'	'RPV-06'	1.0
'CB-23'	'RPV-07'	1.0
'RPV-00'	'RCCS-00'	1.0
'RPV-01'	'RCCS-01'	1.0
'RPV-02'	'RCCS-02'	1.0
'RPV-03'	'RCCS-03'	1.0
'RPV-04'	'RCCS-04'	1.0
'RPV-05'	'RCCS-05'	1.0
'RPV-06'	'RCCS-06'	1.0
'RPV-07'	'RCCS-07'	1.0

C.9 ncg.inp

CARD	*WORD*	*VALUE*	*BASIS*
NCG_ID	MNAME	'HE'	Helium gas is used in this calculation
NCG_PRP	CV0	3130	Constant value for helium specific heat at constant volume. Equal to the specific heat at constant pressure listed in the PBMR-400 benchmark (5195 J/kgK) [71] divided by the specific heat ratio for helium (1.66) [88].

NCG_PRP	MNAME	'H2'	Hydrogen gas. Not used in this calculation, but must still be specified.
NCG_PRP	MNAME	'CO'	Carbon monoxide. Must be listed whenever GRAPHITE is present.
NCG_PRP	MNAME	'02'	Oxygen. Present in reactor cavity CVs.
NCG_PRP	MNAME	'C02'	Carbon dioxide. Must be listed whenver GRAPHITE is present.
NCG_PRP	MNAME	'CH4'	Methane. Must be specified by is not used.
NCG_PRP	MNAME	'N2'	Nitrogen. Present in the reactor cavity CVs.

C.10 mp.inp

CARD	*WORD*	*VALUE*	*BASIS*
MP_ID	MATNAM	'GRAPHITE'	Graphite used in this calculation

MP_PRTF	THC	'THC-GRAPH'	TF specifying graphite thermal conductivity. TF has a constant value of 1.25 (W/m K). This value was obtained by dividing the thermal conductiviy of graphite by 113.7 [60] to account for the scaled reflector resistance, and then multiplying by 4 to account for the model-to-prototype length scale [82]. Thermal conductivity should be changed once the core material has been selected and procured.
MP_ID	MATNAM	'STAINLESS-STEEL-304'	Steel used to represent the RPV and RCCS
MP_ID	MATNAM	'ZIRCALOY'	Zircaloy redefined as the core structural material, which has the same density and heat capacity as graphite but reduced thermal conductivity. Used for supporting structures in the lower reflector because GRAPH cannot be chosen as SS material.

MP_PRTF	CPS	'CPS-GRAPH'	Tabular function (TF) used to define graphite specific heat. TF values correspond to the graphite heat capacity values in the MELCOR Reference manual [6].
	THC	'THC-GRAPH'	TF specifying thermal conductivity. Conductivity is constant at 1.25 ($W/m\,K$).
	RHO	'RHO-GRAPH'	TF specifying graphite density. Density is constant at 1730 (kg/m^3) [6].
	ENH	'ENH-GRAPH'	TF specifying graphite enthalpy. TF values correspond to graphite enthalpy values in the MELCOR Reference manual [6].
MP_PRC	RHOM	1730	Constant value for graphite density [6]
MP_ID	MATNAM	'ALUMINUM'	Steel used to represent the core barrel. Properties are redefined to match those of STAINLESS-STEEL. Property values should be changed once facility design is finalized and materials have been procured.

MP_PRTF	CPS	'CPS-SS'	Tabular function (TF) used to define core barrel specific heat. TF values correspond to the stainless steel heat capacity values in [6].
	THC	'THC-SS'	TF specifying core barrel thermal conductivity. TF values correspond to the stainless steel thermal conductivity values in [6].
	RHO	'RHO-SS'	TF specifying core barrel density. TF values correspond to the stainless steel density values in [6].
	ENH	'ENH-SS'	TF specifying core barrel enthalpy. TF values correspond to the stainless steel enthalpy values in [6].
MP_PRC	RHOM	7930	Constant value for core barrel density [6]
	TMLT	1700	Melting temperature for stainless steel [6]
MP_ID	MATNAM	'URANIUM-DIOXIDE'	UO_2 used as fuel material
MP_ID	MATNAM	'ZIRCONIUM-OXIDE '	Must be listed per COR package requirements but is not used

MP_ID	MATNAM	‘STAINLESS-STEEL ’	Material listed as STEEL in COR package. Used to model SS.
MP_ID	MATNAM	‘STAINLESS-STEEL-OXIDE ’	Must be declared when STAINLESS-STEEL is present
MP_ID	MATNAM	‘ALUMINUM-OXIDE ’	Must be declared when ALUMINUM is present
MP_ID	MATNAM	‘CARBON-STEEL ’	Material used to model the lower head
MP_ID	MATNAM	‘BORON-CARBIDE ’	Must be listed per COR package requirements but is not used

C.11 control-logic.inp

CARD	*WORD*	*VALUE*	*BASIS*
CF_ID	CFNAME	‘Trans-T0’	CF defines the time at the start of a transient
	ICFNUM	001	CF number
	CFTYPE	EQUALS	CF has EQUALS type
CF_SAI	CFSCAL	0.0	CF returns CFSCAL * Function Value + CFADCN. Function value is multiplied by 0.0.

	CFADCN	0.0	0.0 is added to function value. To change 'TransientTime' on a calculation restart, simply change the value of CFSCAL. This will set the CF as a constant equal to CFSCAL, until CFSCAL is modified upon a calculation restart.
	CFVALR	0.0	Initial value for the CF
CF_ARG	NCFARG	1	One argument is required for an EQUALS CF
	CHARG	EXEC-TIME	CF variable argument. The variable used is arbitrary, since it is multiplied by zero. This is done to create a constant CF.
	ARSCAL	0.0	Function value is equal to ARSCAL * Variable + ARADCN. EXEC-TIME is multiplied by zero to create a constant CF.

	ARADCN	0.0	Because the variable is multiplied by zero, and because this quantity is added to zero, the CF will return whatever value is input for CFADCN.
CF_ID	CFNAME	'Trans-dt'	CF returns the time elapsed since the start of the transient (defined by 'TransientTime')
	ICFNUM	002	CF number
	CFTYPE	ADD	CF has type ADD
CF_SAI	CFSCAL	0.0	Function value is multiplied by zero for steady-state calculations to ensure that the thermodynamic state of the inlet and outlet is constant. For transient calculations, CFSCAL should be changed to 1.0 in the MELCOR input deck
	CFADCN	0.0	—
	CFVALR	0.0	CF is initially 0.0

CF_ARG	NCFARG	2	Two arguments are added together for this CF type
	CHARG	EXEC-TIME	The first argument is the problem time
	ARSCAL	1.0	—
	ARADCN	0.0	—
	CHARG	CF-VALU('TransientTime')	The second argument is the value chosen as the transient start time
	ARSCAL	-1.0	'TransientTime' is multiplied by -1.0 so that 'TransientTime' is subtracted from EXEC-TIME
	ARADCN	0.0	—
CF_ID	CFNAME	'Trans-Trip-Time'	CF defines the time at which the HTTF 'trips'. For steady-state calculations, this CF returns a value of 0.0, but the logic is set up so that the reactor will not trip.
	ICFNUM	003	CF number
	CFTYPE	EQUALS	CF has EQUALS type
CF_SAI	CFSCAL	0.0	—

	CFADCN	0.0	0.0 is added to function value. To change 'Trans-Trip-Time' on a calculation restart, simply change the value of CFSCAL. This will set the CF as a constant equal to CFSCAL, until CFSCAL is modified upon a calculation restart.
	CFVALR	0.0	Initial value for the CF
CF_ARG	NCFARG	1	One argument is required for an EQUALS CF
	CHARG	EXEC-TIME	Arbitrary variable
	ARSCAL	0.0	—
	ARADCN	0.0	—
CF_ID	CFNAME	'Trans-Trip'	CF signals reactor trip. This CF is used to signal a change in inlet mass flow, inlet and outlet pressure, and inlet and outlet temperature.
	ICFNUM	004	CF number

	CFTYPE	L-GT	CF has type logical-greater than. TRUE is returned when the time since the start of the transient ('Trans-dt') is greater than the trip time ('Trans-Trip-Time'). CF always FALSE for steady-state calculations.
CF_LIV	LCFVAL	FALSE	CF is initially FALSE
CF_CLS	CLASS	LATCH	CF is classified as LATCH, meaning the CF will change state only once, retaining its new value from that point onward
CF_ARG	NCFARG	2	Two arguments are required
	CHARG	CF-VALU('Trans-dt')	CF variable argument
	CHARG	CF-VALU('Trans-Trip-Time')	CF variable argument
CF_ID	CFNAME	'SS-Mflow'	CF defines the steady-state mass flow rate.
	ICFNUM	050	CF number
	CFTYPE	EQUALS	CF has EQUALS type
CF_SAI	CFSCAL	0.0	—
	CFADCN	0.23	The steady-state mass flow rate is 0.23 kg/s

	CFVALR	0.23	Initial value for the CF
CF_ARG	NCFARG	1	One argument is required for an EQUALS CF
	CHARG	EXEC-TIME	Arbitrary variable
	ARSCAL	0.0	—
	ARADCN	0.0	—
CF_ID	CFNAME	'HeVelocity'	CF calculates the coolant inlet velocity corresponding to the flow rate 'SS-Mflow'
	ICFNUM	051	CF number
	CFTYPE	DIVIDE	CF has type DIVIDE. This CF type divides the second argument by the first argument.
CF_SAI	CFSCAL	1.0	Function value is multiplied by zero for steady-state calculations. For transient calculations, CFSCAL should be changed to 1.0 in the MELCOR input deck.
	CFADCN	0.0	—
	CFVALR	0.0	—
CF_ARG	NCFARG	2	Two arguments are divided for this CF type

	CHARG	CVH-RHO('CV160-Gap',HE)	The first argument is the coolant inlet density. The thermodynamic state of CV160 is used to determine the coolant inlet mass flow rate.
	ARSCAL	0.164	The density is multiplied by the flow area ($v = \dot{m}/(\rho A)$)
	ARADCN	0.0	—
	CHARG	CF-VALU('SS-Mflow')	The second argument is the steady-state mass flow rate 'SS-Mflow'
	ARSCAL	1.0	—
	ARADCN	0.0	—
CF_ID	CFNAME	'HeSource'	CF returns the coolant inlet velocity to the FL package
	ICFNUM	052	CF number
	CFTYPE	L-A-IFTE	CF has type logical-if-then-else. This CF type returns ARG2 if ARG1 is TRUE and returns ARG3 if ARG1 is FALSE
CF_SAI	CFSCAL	1.0	—
	CFADCN	0.0	—
	CFVALR	0.0	—

CF_ARG	NCFARG	3	Three arguments are divided for this CF type
	CHARG	CF-VALU(‘Trans-Trip’)	CF returns ARG2 if ‘Trans-Trip’ is TRUE and ARG3 if ‘Trans-Trip’ is FALSE
	CHARG	EXEC-TIME	CF returns 0.0 for the inlet velocity. This simulates a loss of flow accident.
	ARSCAL	0.0	—
	ARADCN	0.0	—
	CHARG	CF-VALU(’HeVelocity’)	CF returns the steady-state inlet velocity as long as ‘Trans-Trip’ is FALSE
	ARSCAL	1.0	—
	ARADCN	0.0	—
CF_ID	CFNAME	‘SS-Pin’	CF defines the steady-state inlet pressure. The inlet pressure used here is the facility design pressure [61].
	ICFNUM	053	CF number
	CFTYPE	EQUALS	CF has EQUALS type
CF_SAI	CFSCAL	0.0	—
	CFADCN	8.0E+05	The steady-state inlet pressure is 800 kPa

	CFVALR	8.0E+05	Initial value for the CF
CF_ARG	NCFARG	1	One argument is required for an EQUALS CF
	CHARG	EXEC-TIME	Arbitrary variable
	ARSCAL	0.0	—
	ARADCN	0.0	—
CF_ID	CFNAME	'Trans-Pin'	CF defines the transient inlet pressure. During transients, the inlet is at atmospheric pressure.
	ICFNUM	054	CF number
	CFTYPE	EQUALS	CF has EQUALS type
CF_SAI	CFSCAL	0.0	—
	CFADCN	1.0E+05	The transient inlet pressure is 100 kPa
	CFVALR	1.0E+05	Initial value for the CF
CF_ARG	NCFARG	1	One argument is required for an EQUALS CF
	CHARG	EXEC-TIME	Arbitrary variable
	ARSCAL	0.0	—
	ARADCN	0.0	—
CF_ID	CFNAME	'SourceP'	CF returns the coolant inlet pressure to the CVH package
	ICFNUM	055	CF number

	CFTYPE	L-A-IFTE	CF has type logical-if-then-else. This CF type returns ARG2 if ARG1 is TRUE and returns ARG3 if ARG1 is FALSE.
CF_SAI	CFSCAL	1.0	—
	CFADCN	0.0	—
	CFVALR	8.0+05	—
CF_ARG	NCFARG	3	Three arguments are divided for this CF type
	CHARG	CF-VALU(‘Trans-Trip’)	CF returns ARG2 if ‘Trans-Trip’ is TRUE and ARG3 if ‘Trans-Trip’ is FALSE
	CHARG	CF-VALU(’Trans-Pin’)	CF returns the transient inlet pressure if ‘Trans-Trip’ is TRUE
	ARSCAL	0.0	—
	ARADCN	0.0	—
	CHARG	CF-VALU(’SS-Pin’)	CF returns the steady-state inlet pressure as long as ‘Trans-Trip’ is FALSE
	ARSCAL	1.0	—
	ARADCN	0.0	—

CF_ID	CFNAME	‘SS-Pout’	CF defines the steady-state outlet pressure. The outlet pressure used here is the facility design pressure [61].
	ICFNUM	056	CF number
	CFTYPE	EQUALS	CF has EQUALS type
CF_SAI	CFSCAL	0.0	—
	CFADCN	8.0E+05	The steady-state outlet pressure is 800 kPa
	CFVALR	8.0E+05	Initial value for the CF
CF_ARG	NCFARG	1	One argument is required for an EQUALS CF
	CHARG	EXEC-TIME	Arbitrary variable
	ARSCAL	0.0	—
	ARADCN	0.0	—
CF_ID	CFNAME	‘Trans-Pout’	CF defines the transient outlet pressure. During transients, the outlet is at atmospheric pressure.
	ICFNUM	057	CF number
	CFTYPE	EQUALS	CF has EQUALS type
CF_SAI	CFSCAL	0.0	—
	CFADCN	1.0E+05	The transient outlet pressure is 100 kPa
	CFVALR	1.0E+05	Initial value for the CF
CF_ARG	NCFARG	1	One argument is required for an EQUALS CF

	CHARG	EXEC-TIME	Arbitrary variable
	ARSCAL	0.0	—
	ARADCN	0.0	—
CF_ID	CFNAME	‘SinkP’	CF returns the coolant outlet pressure to the CVH package
	ICFNUM	058	CF number
	CFTYPE	L-A-IFTE	CF has type logical-if-then-else. This CF type returns ARG2 if ARG1 is TRUE and returns ARG3 if ARG1 is FALSE.
CF_SAI	CFSCAL	1.0	—
	CFADCN	0.0	—
	CFVALR	8.0E+05	—
CF_ARG	NCFARG	3	Three arguments are divided for this CF type
	CHARG	CF-VALU(‘Trans-Trip’)	CF returns ARG2 if ‘Trans-Trip’ is TRUE and ARG3 if ‘Trans-Trip’ is FALSE
	CHARG	CF-VALU(’Trans-Pout’)	CF returns the transient outlet pressure if ‘Trans-Trip’ is TRUE
	ARSCAL	0.0	—
	ARADCN	0.0	—

	CHARG	CF-VALU('SS-Pout')	CF returns the steady-state outlet pressure as long as 'Trans-Trip' is FALSE
	ARSCAL	1.0	—
	ARADCN	0.0	—
CF_ID	CFNAME	'SS-Tin'	CF defines the steady-state inlet temperature. The inlet temperature used here is the vessel inlet temperature [61].
	ICFNUM	059	CF number
	CFTYPE	EQUALS	CF has EQUALS type
CF_SAI	CFSCAL	0.0	—
	CFADCN	763.0	The steady-state inlet temperature is 490 °C
	CFVALR	763.0	Initial value for the CF
CF_ARG	NCFARG	1	One argument is required for an EQUALS CF
	CHARG	EXEC-TIME	Arbitrary variable
	ARSCAL	0.0	—
	ARADCN	0.0	—
CF_ID	CFNAME	'Trans-Tin'	CF defines the transient inlet temperature. During transients, the inlet is at the initial cavity temperature.
	ICFNUM	060	CF number

	CFTYPE	EQUALS	CF has EQUALS type
CF_SAI	CFSCAL	0.0	—
	CFADCN	300.0	The transient inlet temperature is 27 °C
	CFVALR	300.0	Initial value for the CF
CF_ARG	NCFARG	1	One argument is required for an EQUALS CF
	CHARG	EXEC-TIME	Arbitrary variable
	ARSCAL	0.0	—
	ARADCN	0.0	—
CF_ID	CFNAME	'SourceT'	CF returns the coolant inlet temperature to the CVH package
	ICFNUM	061	CF number
	CFTYPE	L-A-IFTE	CF has type logical-if-then-else. This CF type returns ARG2 if ARG1 is TRUE and returns ARG3 if ARG1 is FALSE.
CF_SAI	CFSCAL	1.0	—
	CFADCN	0.0	—
	CFVALR	763.0	—
CF_ARG	NCFARG	3	Three arguments are divided for this CF type

	CHARG	CF-VALU(‘Trans-Trip’)	CF returns ARG2 if ‘Trans-Trip’ is TRUE and ARG3 if ‘Trans-Trip’ is FALSE
	CHARG	CF-VALU(’Trans-Tin’)	CF returns the transient inlet temperature if ‘Trans-Trip’ is TRUE
	ARSCAL	0.0	—
	ARADCN	0.0	—
	CHARG	CF-VALU(’SS-Tin’)	CF returns the steady-state inlet temperature as long as ‘Trans-Trip’ is FALSE
	ARSCAL	1.0	—
	ARADCN	0.0	—
CF_ID	CFNAME	‘SS-Tout’	CF defines the steady-state outlet temperature. The outlet temperature used here is the vessel outlet temperature [61].
	ICFNUM	062	CF number
	CFTYPE	EQUALS	CF has EQUALS type
CF_SAI	CFSCAL	0.0	—
	CFADCN	1273.0	The steady-state outlet temperature is 1000 °C
	CFVALR	1273.0	Initial value for the CF
CF_ARG	NCFARG	1	One argument is required for an EQUALS CF

	CHARG	EXEC-TIME	Arbitrary variable
	ARSCAL	0.0	—
	ARADCN	0.0	—
CF_ID	CFNAME	'Trans-Tout'	CF defines the transient outlet temperature. During transients, the outlet is at the initial cavity temperature.
	ICFNUM	063	CF number
	CFTYPE	EQUALS	CF has EQUALS type
CF_SAI	CFSCAL	0.0	—
	CFADCN	300.0	The transient outlet temperature is 27 °C
	CFVALR	300.0	Initial value for the CF
CF_ARG	NCFARG	1	One argument is required for an EQUALS CF
	CHARG	EXEC-TIME	Arbitrary variable
	ARSCAL	0.0	—
	ARADCN	0.0	—
CF_ID	CFNAME	'SinkT'	CF returns the coolant outlet temperature to the CVH package
	ICFNUM	064	CF number

	CFTYPE	L-A-IFTE	CF has type logical-if-then-else. This CF type returns ARG2 if ARG1 is TRUE and returns ARG3 if ARG1 is FALSE.
CF_SAI	CFSCAL	1.0	—
	CFADCN	0.0	—
	CFVALR	1273.0	—
CF_ARG	NCFARG	3	Three arguments are divided for this CF type
	CHARG	CF-VALU(‘Trans-Trip’)	CF returns ARG2 if ‘Trans-Trip’ is TRUE and ARG3 if ‘Trans-Trip’ is FALSE
	CHARG	CF-VALU(’Trans-Tout’)	CF returns the transient outlet temperature if ‘Trans-Trip’ is TRUE
	ARSCAL	0.0	—
	ARADCN	0.0	—
	CHARG	CF-VALU(’SS-Tout’)	CF returns the steady-state outlet temperature as long as ‘Trans-Trip’ is FALSE
	ARSCAL	1.0	—
	ARADCN	0.0	—

CF_ID	CFNAME	'Humidity'	CF defines the inlet and outlet CV relative humidity. Relative humidity is 0.0 for all calculations.
	ICFNUM	065	CF number
	CFTYPE	EQUALS	CF has EQUALS type
CF_SAI	CFSCAL	0.0	—
	CFADCN	1.0	—
	CFVALR	1.0	—
CF_ARG	NCFARG	1	One argument is required for an EQUALS CF
	CHARG	EXEC-TIME	Arbitrary variable
	ARSCAL	0.0	—
	ARADCN	0.0	—
CF_ID	CFNAME	'Src_HeFrac'	CF defines the mole fraction of helium in the inlet CV. CF returns 1.0 throughout all calculations.
	ICFNUM	066	CF number
	CFTYPE	EQUALS	CF has EQUALS type
CF_SAI	CFSCAL	0.0	—
	CFADCN	1.0	—
	CFVALR	1.0	—
CF_ARG	NCFARG	1	One argument is required for an EQUALS CF
	CHARG	EXEC-TIME	Arbitrary variable

	ARSCAL	0.0	—
	ARADCN	0.0	—
CF_ID	CFNAME	‘Sink_N2-Frac’	CF defines the mole fraction of nitrogen in the outlet CV. CF returns 0.8 throughout all calculations.
	ICFNUM	067	CF number
	CFTYPE	EQUALS	CF has EQUALS type
CF_SAI	CFSCAL	0.0	—
	CFADCN	0.8	—
	CFVALR	0.8	—
CF_ARG	NCFARG	1	One argument is required for an EQUALS CF
	CHARG	EXEC-TIME	Arbitrary variable
	ARSCAL	0.0	—
	ARADCN	0.0	—
CF_ID	CFNAME	‘Sink_O2-Frac’	CF defines the mole fraction of oxygen in the outlet CV. CF returns 0.2 throughout all calculations.
	ICFNUM	068	CF number
	CFTYPE	EQUALS	CF has EQUALS type
CF_SAI	CFSCAL	0.0	—
	CFADCN	0.2	—
	CFVALR	0.2	—

CF_ARG	NCFARG	1	One argument is required for an EQUALS CF
	CHARG	EXEC-TIME	Arbitrary variable
	ARSCAL	0.0	—
	ARADCN	0.0	—
CF_ID	CFNAME	'InletVlv'	CF returns the valve fraction open for the valve in FL161
	ICFNUM	069	CF number
	CFTYPE	L-A-IFTE	CF has type logical-if-then-else. This CF type returns ARG2 if ARG1 is TRUE and returns ARG3 if ARG1 is FALSE.
CF_SAI	CFSCAL	1.0	—
	CFADCN	0.0	—
	CFVALR	1.0	—
CF_ARG	NCFARG	3	Three arguments are divided for this CF type
	CHARG	CF-VALU('Trans-Trip')	CF returns ARG2 if 'Trans-Trip' is TRUE and ARG3 if 'Trans-Trip' is FALSE
	CHARG	EXEC-TIME	Valve is fully closed
	ARSCAL	0.0	—
	ARADCN	0.0	—
	CHARG	EXEC-TIME	Valve is fully open

	ARSCAL	1.0	—
	ARADCN	0.0	—
CF_ID	CFNAME	‘EmisCB’	CF defines the emissivity of the core barrel
	ICFNUM	080	CF number
	CFTYPE	EQUALS	CF has EQUALS type
CF_SAI	CFSCAL	0.0	—
	CFADCN	0.213	—
	CFVALR	0.213	—
CF_ARG	NCFARG	1	One argument is required for an EQUALS CF
	CHARG	EXEC-TIME	Arbitrary variable
	ARSCAL	0.0	—
	ARADCN	0.0	—
CF_ID	CFNAME	‘EmisVes’	CF defines the emissivity of the vessel
	ICFNUM	081	CF number
	CFTYPE	EQUALS	CF has EQUALS type
CF_SAI	CFSCAL	0.0	—
	CFADCN	0.213	—
	CFVALR	0.213	—
CF_ARG	NCFARG	1	One argument is required for an EQUALS CF
	CHARG	EXEC-TIME	Arbitrary variable
	ARSCAL	0.0	—
	ARADCN	0.0	—
CF_ID	CFNAME	‘EmisRCCS’	CF defines the emissivity of the RCCS

	ICFNUM	082	CF number
	CFTYPE	EQUALS	CF has EQUALS type
CF_SAI	CFSCAL	0.0	—
	CFADCN	0.213	—
	CFVALR	0.213	—
CF_ARG	NCFARG	1	One argument is required for an EQUALS CF
	CHARG	EXEC-TIME	Arbitrary variable
	ARSCAL	0.0	—
	ARADCN	0.0	—
CF_ID	CFNAME	‘CORE-POWER’	CF defines the core power. To simulate decay power, simply change the additive constant.
	ICFNUM	100	CF number
	CFTYPE	EQUALS	CF has EQUALS type
CF_SAI	CFSCAL	0.0	—
	CFADCN	6.0E+05	This is the maximum facility power [60]
	CFVALR	6.0E+05	—
CF_ARG	NCFARG	1	One argument is required for an EQUALS CF
	CHARG	EXEC-TIME	Arbitrary variable
	ARSCAL	0.0	—
	ARADCN	0.0	—

CF_ID	CFNAME	‘FLDIR2’	CF defines the direction of flow through COR ring 2. A negative value indicates that the flow is downward. The negative of the coolant velocity in ring 2 is used to determine the flow direction.
	ICFNUM	102	CF number
	CFTYPE	EQUALS	CF has EQUALS type
CF_SAI	CFSCAL	1.0	—
	CFADCN	0.0	—
	CFVALR	0.0	—
CF_ARG	NCFARG	1	One argument is required for an EQUALS CF
	CHARG	FL-VEL(‘Core-FL126’,’A’)	The velocity of the atmosphere FL126, which is in COR ring 2
	ARSCAL	1.0	—
	ARADCN	0.0	—
CF_ID	CFNAME	‘FLDIR3’	CF defines the direction of flow through COR ring 3. A negative value indicates that the flow is downward. The negative of the coolant velocity in ring 3 is used to determine the flow direction.

	ICFNUM	103	CF number
	CFTYPE	EQUALS	CF has EQUALS type
CF_SAI	CFSCAL	1.0	—
	CFADCN	0.0	—
	CFVALR	0.0	—
CF_ARG	NCFARG	1	One argument is required for an EQUALS CF
	CHARG	FL-VEL(‘Core-FL136’,’A’)	The velocity of the atmosphere FL136, which is in COR ring 3
	ARSCAL	1.0	—
	ARADCN	0.0	—
CF_ID	CFNAME	‘FLDIR4’	CF defines the direction of flow through COR ring 4. A negative value indicates that the flow is downward. The negative of the coolant velocity in ring 4 is used to determine the flow direction.
	ICFNUM	104	CF number
	CFTYPE	EQUALS	CF has EQUALS type
CF_SAI	CFSCAL	1.0	—
	CFADCN	0.0	—
	CFVALR	0.0	—
CF_ARG	NCFARG	1	One argument is required for an EQUALS CF

CHARG	FL-VEL(‘Core-FL146’,’A’)	The velocity of the atmosphere FL126, which is in COR ring 4
ARSCAL	1.0	—
ARADCN	0.0	—

C.12 dlofc.inp

C.12.1 Environmental Data for HTTF Transient Calculations

CARD	*WORD*	*VALUE*	*BASIS*
MEG_DIAGFILE	—	’httfg.dia’	Filename for MELGEN diagnostic output
MEL_DIAGFILE	—	’httf.dia’	Filename for MELCOR diagnostic output
MEG_OUTPUTFILE	—	’httfg.out’	Filename for MELGEN listing output
MEL_OUTPUTFILE	—	’httf.out’	Filename for MELCOR listing output
PLOTFILE	—	’httf.ptf’	Filename for binary plot data
MEG_RESTARTFILE	—	’httf.rst’	Filename for binary file used to restart MELCOR calculation
MEL_RESTARTFILE	—	’httf.rst’	Filename for binary file used to restart MELCOR calculation
	CYCLE	CYCLE	Calculation restarted at cycle specified on NREST

	NREST	18000.0	Calculation restarted at 18,000 s
MESSAGEFILE	—	'httf.mes'	Filename for event message output
STATUSFILE	—	'MELSTT_v2-0'	Filename for MELCOR status file
STOPFILE	—	'MELSTP_v2-0'	Filename for MELCOR stop file
WRITENEWINP	—	'httf.txt'	Filename for echoed input

C.12.2 HTTF DLOFC EXEC Input

CARD	*WORD*	*VALUE*	*BASIS*
EXEC_TITLE	—	'HTTF'	Title of calculation
EXEC_JOBID	—	'httf -'	Job identifier
EXEC_TEND	TEND	2.8E+04	End of calculation time
EXEC_TIME	NTMINV	3	Dimension of timestep table. For the first 5 s after the transient, the plot, edit, and restart intervals are shorter because the thermodynamic state of the HTTF is changing at a much more rapid rate than later in the calculation.
	N	1	The first set of timestep input
	TIME	18000.0	The time this data set goes into effect

DTMAX	0.1	Arbitrary. The actual timestep will be less due to the Courant limit.
DTMIN	1.0E-05	Arbitrary, but should be no more than 1.0E-02, since the maximum timestep due to the Courant limit is $\sim 4.0E-02$
DTEDIT	100.	MELCOR prints an edit to OUTPUTFILE every 100 seconds
DTPLOT	0.01	Plot frequency
DTREST	100.	Restart frequency
DCREST	1.0E+10	Default value. This ensures that restart generation is not a function of CPU time.
N	2	The second set of timestep input
TIME	18005.0	The time this data set goes into effect
DTMAX	1.0	Arbitrary. The actual timestep will be less due to the Courant limit.
DTMIN	1.0E-05	Arbitrary, but should be no more than 1.0E-02, since the maximum timestep due to the Courant limit is $\sim 4.0E-02$
DTEDIT	100.	Edit frequency
DTPLOT	1.0	Plot frequency

	DTREST	100.	Restart frequency
	DCREST	1.0E+10	Default value. This ensures that restart generation is not a function of CPU time.
	N	3	The third set of timestep input
	TIME	18100.0	The time this data set goes into effect
	DTMAX	1.0	Arbitrary. The actual timestep will be less due to the Courant limit.
	DTMIN	1.0E-05	Arbitrary, but should be no more than 1.0E-02, since the maximum timestep due to the Courant limit is $\sim 4.0E-02$
	DTEDIT	10000.	Edit frequency
	DTPLOT	20.0	Plot frequency
	DTREST	50000.	Restart frequency
	DCREST	1.0E+10	Default value. This ensures that restart generation is not a function of CPU time.
EXEC_CPULEFT	CPULEFT	0.30E+02	Minimum number of CPU seconds left at the end of the calculation
EXEC_CPULIM	CPULIM	0.1E+06	Maximum number of CPU seconds allowed for this execution
EXEC_CYMESF	NCYEDD	100	Number of cycles between messages written to the terminal

	NCYEDP	10000	Number of cycles between messages written to OUTPUT-FILE

C.12.3 HTTF DLOFC CF Input

CARD	*WORD*	*VALUE*	*BASIS*
CF_ID	CFNAME	'Trans-T0'	CF defines the time at the start of a transient
	ICFNUM	001	CF number
	CFTYPE	EQUALS	CF has EQUALS type
CF_SAI	CFSCAL	0.0	—
	CFADCN	18000.0	The transient starts at 18,000 s
	CFVALR	18000.0	Initial value for the CF
CF_ID	CFNAME	'Trans-dt'	CF returns the time elapsed since the start of the transient (defined by 'Transient-Time')
	ICFNUM	002	CF number
	CFTYPE	ADD	CF has type ADD
CF_SAI	CFSCAL	1.0	By changing this value from 0.0 to 1.0, the time since the start of the transient is calculated, which allows 'Trans-Trip' to switch state to TRUE at some point during the calculation
	CFADCN	0.0	—

	CFVALR	0.0	—
CF_ID	CFNAME	‘CORE-POWER’	CF defines the core power.
	ICFNUM	100	CF number
	CFTYPE	EQUALS	CF has EQUALS type
CF_SAI	CFSCAL	0.0	—
	CFADCN	3.0E+05	This is the expected maximum decay power [60]
	CFVALR	3.0E+05	—

VITA

Name: James Robert Corson, Jr

Address: Department of Nuclear Engineering, Texas A&M University, 3133 TAMU, College Station, TX 77843-3133

Email: jcorson_08@yahoo.com

Education: M.S., Nuclear Engineering, Texas A&M University, 2010
B.S., Nuclear Engineering, Pennsylvania State University, 2008